IAEA
International Atomic Energy Agency

INDC(NDS)-0530
Distr. SC

INDC International Nuclear Data Committee

Joint ICTP-IAEA Advanced Workshop on Model Codes for Spallation Reactions

International Centre for Theoretical Physics

Trieste, Italy

4 – 8 February 2008

Prepared by

D. Filges[1], S. Leray[2], Y. Yariv[3], A. Mengoni[4], A. Stanculescu[4], G. Mank[4]

[1]Forschungszentrum Jülich GmbH, Germany
[2]CEA-CEN Saclay, France
[3]Soreq Nuclear Research Centre, Israel
[4]International Atomic Energy Agency, Vienna, Austria

August 2008

Selected INDC documents may be downloaded in electronic form from
http://www-nds.iaea.org/indc_sel.html or sent as an e-mail attachment.
Requests for hardcopy or e-mail transmittal should be directed to
services@iaeand.iaea.org
or to:
Nuclear Data Section
International Atomic Energy Agency
PO Box 100
Wagramer Strasse 5
A-1400 Vienna
Austria

Produced by the IAEA in Austria
August 2008

INDC(NDS)-0530
Distr. SC

Joint ICTP-IAEA Advanced Workshop on Model Codes for Spallation Reactions

International Centre for Theoretical Physics

Trieste, Italy

4 – 8 February 2008

Prepared by

D. Filges[1], S. Leray[2], Y. Yariv[3], A. Mengoni[4], A. Stanculescu[4], G. Mank[4]

Abstract

The International Atomic Energy Agency (IAEA) and the Abdus Salam International Centre for Theoretical Physics (ICTP) organised an expert meeting at the ICTP from 4 to 8 February 2008 to discuss model codes for spallation reactions. These nuclear reactions play an important role in a wide domain of applications ranging from neutron sources for condensed matter and material studies, transmutation of nuclear waste and rare isotope production to astrophysics, simulation of detector set-ups in nuclear and particle physics experiments, and radiation protection near accelerators or in space. The simulation tools developed for these domains use nuclear model codes to compute the production yields and characteristics of all the particles and nuclei generated in these reactions. These codes are generally Monte-Carlo implementations of Intra-Nuclear Cascade (INC) or Quantum Molecular Dynamics (QMD) models, followed by de-excitation (principally evaporation/fission) models. Experts have discussed in depth the physics contained within the different models in order to understand their strengths and weaknesses. Such codes need to be validated against experimental data in order to determine their accuracy and reliability with respect to all forms of application. Agreement was reached during the course of the workshop to organise an international benchmark of the different models developed by different groups around the world. The specifications of the benchmark, including the set of selected experimental data to be compared to the models, were also defined during the workshop. The benchmark will be organised under the auspices of the IAEA in 2008, and the first results will be discussed at the next Accelerator Applications Conference (AccApp'09) to be held in Vienna in May 2009.

August 2008

TABLE OF CONTENTS

Foreword

The Joint ICTP-IAEA Advanced Workshop on Model Codes for Spallation Reactions was held at the International Centre of Theoretical Physics (ICTP) in Trieste, Italy, from 4 – 8 February 2008. The workshop was organised in cooperation with co-directors from CEA Saclay (S. Leray), FZ-Jülich (D. Filges) and SOREQ (Y. Yariv); the local organiser was Dr. C. Tuniz. The workshop was opened by the Director of the School, G. Mank, and Dr. C. Tuniz on behalf of the Director of the ICTP, Prof. K. Sreenivasan, who expressed his personal interest in the event.

The workshop consisted of a series of lectures, detailed discussions and a summary session. The lecture sessions were chaired by the directors. All lectures were distributed on a CD-ROM, and are available under the URL of the ICTP. The CD-ROM was finalised during the workshop. Thirty-eight participants and lecturers from Australia, Austria, Armenia, Cameroon, Egypt, France, Finland, Germany, India, Israel, Moldavia, Poland, Russian Federation, Spain, Sudan and Ukraine attended the workshop.

A major objective of workshop was to facilitate experts and competent practitioners to better understand the physical basis, approximations, strengths and weaknesses of the spallation codes. The presentation of relevant basic experimental data with emphasis on accuracies, detector efficiencies, filters and thresholds created a basis for a benchmark exercise and inter-comparison. Specifically the workshop aided in our understanding of the physics of the INC, QMD and de-excitation models. The successes or deficiencies of different models were assessed, and helped define an agreed set of experimental data to be used in the validation and inter-comparison of the models. One main point was to promote the exchange of information among researchers in the field and to identify areas of international cooperation.

This report contains 14 papers that serve as the scientific basis for an international benchmark exercise of the different models developed by leading groups in the world. The IAEA officers responsible for the publication were G. Mank and A. Mengoni from the Division of Physical and Chemical Sciences, and A. Stanculescu from the Division of Nuclear Power.

Introduction and Aim of the Meeting

D. FILGES

Forschungszentrum Jülich GmbH,
Institut für Kernphysik,
Jülich, Germany

Abstract. Particle transport in matter has become increasingly important in many fields of basic science, technology and applications in recent years. The investigation of hadron and electromagnetic cascades is of considerable interest for all aspects of radiation physics. Significant developments include the advent of high intensity spallation neutron sources that possess a proton beam power in the MW range e.g. SINQ, Switzerland, SNS, USA, J-PARC, Japan, with research projects such as the long-pulsed European Spallation Neutron Source (ESS), the 'European Roadmap for Research Infrastructures', accelerator driven systems (ADS) for nuclear waste transmutation and energy production, the application of radioactive beams and experiments at medium- and high-energy accelerators, and cosmic and space applications. These facilities require detailed particle production and transport models to demonstrate feasibility and utilization, to optimize design configurations, and to support the engineering layout. This introduction summarizes the current state-of-the-art of particle transport simulation code systems used in spallation research and in particle transport through matter, and gives a short tabulated overview of which spallation reactions models are in use and are the basis of this workshop.

1. Introduction

With the advent of spallation neutron sources with a proton beam power in the MW range e.g. SINQ, Switzerland [1], SNS, USA [2], J-PARC, Japan [3], with research projects such as the long-pulsed European Spallation Neutron Source (ESS) [4], nuclear waste transmutation and energy production [5, 6, 7], with the application of radioactive beams, with detectors and experiments at medium and high energy accelerators, and with cosmic and space applications, detailed particle production and transport models have to be used to demonstrate feasibility and utilization, to optimize design configurations, and to support engineering layouts. One main goal of the simulation methods is the determination of the particle fluxes for the different applications in a three-dimensional complex multi-material geometry. Particle fluxes and energy deposition influence the engineering design criteria on cooling of targets, windows and containments. Radiation damage produced by different mechanisms as displacements per atom (dpa), gas production, and nuclide transmutation worsen the mechanical properties and limit the lifetime of structure materials and components. Activation and radiation lead to hazards which have an important impact on the different components of the accelerators, target stations and experiments. Shielding in spallation induced reactions is different compared to nuclear reactor systems and fusion devices due to the high energy neutron component which influences the safety protection and the environment. Finally, the uncertainties of the complex simulation methods have to be assessed on the basis of validation against experiments. Comparisons with experiments serve to gain confidence in the complex simulations of the physics processes on the level of a broad range of coincident observables, placing significant constraints on the quality and accuracy of modelling

2. Importance of spallation reactions

Computer simulation opens up new potentials for describing and studying physical and technical issues. In certain circumstances, computer simulation is the only way to understand the complexity of physical phenomena. The classic categories - theory and experiment - are completed or assisted by a third category - computer simulation. The method of this third

category involves realistic simulation by Monte Carlo, and the instrument used is the super computer. In many respects the computer simulation of particle transport in matter resembles an experiment. Not to be misunderstood, computer simulation is not a substitute for experiments, but extends the field of science and represents experiments in a hypothetical world. Vector and parallel computer systems possess tremendous capabilities, and permit the simulation and study of a large number of cases and parameters in a very short period of time. Many complex systems which could not be verified by classic methods are now accessible and can be studied in great detail. Therefore, utilization of super computers in science and technology is an important tool and an advantage in parallel to traditional experimental and theoretical research work.

The particular challenge to particle transport codes in spallation research arises from the description of hadron and electromagnetic phenomena over 10 orders of magnitude, ranging from incident particle energies of some GeV down to the energy of the sub-thermal neutrons in the meV energy range.

One caveat concerns the neutron reaction mechanisms with matter in the low energy region. The complex features of neutron cross sections in the low energy region cannot be calculated from first principles using the properties of the nucleus. Hence, data must be determined empirically as a function of energy for each nuclide and for each reaction. In general these data cannot be interpolated over large energy intervals because of the irregular resonance structure, although the Breit-Wigner resonance parameter or other semi-empirical relations often allow characterization of the cross sections in terms of a few empirical parameters per resonance. Cross sections of neutron-nucleus reactions as well as the energy and angular distributions of the resulting secondary particles for hundreds of isotopes over an energy range from 10^{-5} eV to 150 MeV and neutron scattering kernels with energies in the meV energy range have been evaluated and stored on nuclear data files. These data evaluations are restricted at best to energies of up to about 150 MeV.

Nuclear data for all kinds of applications may be retrieved through the international nuclear data centre links as ANL, LANL, LBNL, LLNL, ORNL and TUNL (USA), IAEA (Austria), NEA (France) and JAEA-Tokai-mura (Japan). The main evaluator and distributor is the National Nuclear Data Center (NNDC), Brookhaven, USA, which is responsible for the evaluation of the ENDF library (Evaluated Nuclear reaction Data File) and ENSDF library (Evaluated Nuclear Structure Data File). A useful index of the available nuclear data libraries which can be retrieved through the nuclear data services of the IAEA is given in Ref. [8].

Where multiple channels on particle production via spallation reactions are opened e.g. above energies of 150 MeV, differential cross sections at higher energies need to be described as a function of the energy and the direction of secondary particles of type j produced when a hadron of type h_i and energy E_i interacts with a target nucleus of A_{target} (see equation (1)).

$$\frac{d\sigma}{dEd\Omega} = \left(E_j, \Omega_j \middle| h_i, E_i, A_{target}\right) \tag{1}$$

This information is not known accurately from measurements over the wide parameter range of interest for practical spallation research applications, nor is it likely to be because of the large amount of data that would be required. For example, for a target calculation of a spallation neutron source one would need correlated energy and angular distributions for about five emitted particles types ($p, n, \pi^{\pm}, \pi^{0}$) produced by four incident particles ($p, n, \pi^{\pm}$), at energy points from about 20 MeV to 3 GeV for over e.g. 10 target nuclei.

Furthermore, to predict the residual nuclei mass and charge distributions for induced radioactivity values, additional cross sections would be required for the multiplicities of the heavier particles produced (d, t, α, etc.), correlated with nucleon and pion production.

Thus, the state-of-the-art approach is to use theoretical nuclear model codes for the generation of the spallation reactions, with model validation for specific sets of parameters. Furthermore, with such models incorporated in particle transport codes to treat the subsequent collisions generated by spallation reactions, and using Monte Carlo techniques, explicit handling of the vast amount of data can be avoided in spallation reaction calculations. Table I gives a short overview of some important applications.

TABLE I. APPLICATIONS FOR SPALLATION REACTIONS

Application	**System or Experiment**
high intensity spallation sources	**SINQ** (Switzerland), E_p = 0.6 GeV, power = 1-1.5 MW, **SNS** (USA), E_p = 1.0 GeV, power = 1-1.5 MW, **J-PARC** (Japan), E_p = 3.0 GeV, power = 1 MW, and 50 GeV hadron facility, **ESS** (Europe), E_p = 1.5 GeV, power = 10 MW
ADS, ADTT, transmutation / benchmark experiments	**MEGAPIE**, **MUSE**, **RACE-ISU**, **YALINA**-booster, etc.
new facilities	**GSI-FAIR**, **SPIRAL**, **EURISOL**, etc.
materials in high intensity particle fields	irradiation facilities, rare isotope production, radiation damage, etc.
safety and radiation protection	shielding, radiation fields, dosimetry, etc.
detector development	for running and future accelerator projects
astrophyics , space science	
IAEA activities for small proton accelerators and their applications	

3. State-of-the-art of particle transport codes and event generators

Summaries of the most advanced Monte Carlo particle transport code systems for beam material interaction studies and the event generators are given in the following tables. Table II gives an overview of the frequently used systems considered in spallation research - mainly MCNPX and PHITS - and in high energy physics detector simulation - mainly FLUKA and GEANT4. The different tallies and analysis strategies of the particle histories are described in the different manuals of the code systems and references therein, which are available usually by internet connections as specified in the last row of Table II.

Table III summarizes the INC-, QMD-, evaporation and fission models, which have been demonstrated and discussed during the workshop. The details of the implemented physics of the models and their assumption are described in detail in the following contributions given in this report.

TABLE II. GENERAL OVERVIEW OF THE MOST ADVANCED PARTICLE TRANSPORT CODES

system	**MCNPX -2.6** LANL	**PHITS -2.09** RIST, GSI	**FLUKA - 2006.3** CERN, INFN	**GEANT4 -4.9.1** CERN, INFN, KEK, SLAC	**MARS -15** FNAL
cost	free	free	free	free	free
language	Fortran90 / C	Fortran77	Fortran77	C++	Fortran90 / C
parallel processing	yes	yes	yes	yes	yes
models	ABLA, Bertini, ISABEL, CEM, LAQGSM, FLUKA89	GEM, JAM, JQMD > 3 GeV	PEANUT, DPMJET, GLAUBER, neutrinos	ABLA, Bertini, INCL, GEM, GHEISHA	CEM, LAQGSM, DPMJET
Web Site http://	mcnpx.lanl.org	rcww.kek.jp/research/shield/phits.html	fluka.org	geant4.web.cern.ch/geant4/	www-ap.final.gov/MARS/

TABLE III. A SUMMARY OF IMPORTANT PARTICLE EVENT GENERATORS

INC (intra-nuclear-cascade) < 3 GeV	**QMD** (quantum-molecular-dynamic)	**evaporation plus fission**	**intra-nuclear-cascade plus evaporation**
Bertini, CEM, INCL, ISABEL	JQMD, QMD-SDM, BUU, SMM	ABLA/ABRABLA, ALICE/ASH, EVAP-versions, GEM, GEMINI, JULIAN, PACE,.ORNL-fission, RAL-fission	BRIC, DISCA, MICRES

4. Aim of the workshop

The aim of the workshop is to demonstrate and discuss the state-of the-art of the INCE / QMD event generators e.g. model-dependent critical parameters, their validity and deficiencies. Presentations of the recent ‘thin’ target experiments, e.g. double-differential cross section, reaction rates, excitation function and residual measurements complement the talks about the models, and provide the code developers with a set of verified experimental data to be benchmarked. The availability of the models and the experimental data will also be discussed.

Finally, a benchmark exercise should be defined for spallation reactions of ‘thin’ targets to be presented at a follow-up workshop during the AccApp09 conference, Vienna, 2009.

REFERENCES

[1] W. Wagner et al., Status of SINQ, the only {MW} spallation neutron source-highlighting target development and industrial applications, Nucl. Instrum. Methods Phys. Res. (Section A), Vol. 562, 541-547, 2005.

[2] T. E. Mason, The Spallation Neutron Source: Facility Status Report, ICANS-XVIII, Proc. of the Seventeenth Meeting of the International Collaboration on Advanced

Neutron Sources, April 24-29, Santa Fe, USA, Editors: G. J. Russell, J. J. Rhyne, B V. Maes, Vol. I, 82-83, 2005.
[3] Y. Oyama, J-PARC and a new era of science, Nucl. Instrum. Methods Phys. Res. (Section A), Vol. 562, 548-552, 2005.
[4] European Roadmap for Research Infrastructures - ESFRI, Report of the European Commission, ISBN 92-79-02694-1, page 55, 2006.
[5] Accelerator driven systems: Energy generation and transmutation of nuclear waste, International Atomic Energy Agency, Vienna, Austria, IAEA-TECDOC-985, 1997.
[6] Actinide and Fission Product Partitioning and Transmutation, Sixth Information Exchange Meeting, Madrid, Spain, 11-13 December, OECD-Nuclear Development, EUR 19783 EN, 2000.
[7] Accelerator and Spallation Target Technologies for ADS Applications, OECD-Nuclear Science, NEA No. 5421, 2005.
[8] O. Schwerer, Index of Nuclear Data Libraries available from the IAEA Nuclear Data Section, International Atomic Energy Agency, Vienna, Austria, IAEA-NDS-7, 2007.

ISABEL – INC Model for High-Energy Hadron-Nucleus Reactions

Y. YARIV

Soreq Nuclear Research Center,
Yavne, Israel

Abstract. A detailed description of the ISABEL INC model developed in 1978-1980 is given with emphasis on the physical assumptions, actual implementation and parameters of the INC Monte Carlo code.

1. Introduction, Motivation

The recent activities in production of Rare Isotope Beams and Spallation Sources led to revival of interest in reliable and predictive simulation of collisions of hadron-nucleus and nucleus-nucleus in the energy range of few hundred MeV to few GeV per particle, to be embedded in transport codes (e.g. MCNPX, GEANT). Owing to the complexity of the quantum-mechanical many-body problems, the processes are often approximately described by Intra-Nuclear Cascade (INC) models followed by de-excitation (sometime, two-step, pre-equilibrium - evaporation) models.

ISABEL belongs to the chain of INC models which started from the original idea of Serber [1], continued with the (based on manual calculations) implementation of Goldberger [2] and (the first computerized calculations) of Metropolis [3] through the VEGAS [4] and ISOBAR [5] codes.

INC models reproduce successfully wide variety of experimental data of hadron and pion induced reactions, using a small number of adjustable parameters, most with clear physical meaning. The main purpose of the INC models is to fill the high-energy gap in existing experimental cross-section libraries, which are limited to incident energies of 150 MeV or even, for some isotopes, 20MeV. For calculations of residua there is a need to use models already above 20MeV.

In the first part of the present paper the basic assumptions of the INC models are presented and the applicability and limitations, important for the evaluation of reliability of transport calculations used in wide variety of applications, are discussed. In the second part, the "time like basis" Monte Carlo method is described. Finally detailed description of its implementation in the ISABEL code is given.

2. Basic assumptions and applicability of INC

The INC models treat the interaction of incoming projectile with the nucleus as a series of independent collisions using on-mass-shell free particle-nucleon cross sections. The colliding particles are treated as classical point-like objects moving between collisions on well defined trajectories in the target potential well. The collision processes are treated as classical, energy and momentum conserving, scatterings. Collisions violating the Pauli Principle are not allowed – this is the single significant “quantum” property of the models.

In order to determine the applicability of the INC models at low energies we shall “revisit” their basic assumptions [1, 6, 7]:

i. The reactions are “deep inelastic” - the energy transferred into internal energy of the target is large in comparison with the binding energy of nucleons in the target

- the many body scattering can be approximately formulated in terms of on-shell single-particle scattering probabilities.

ii. The "reduced" de Broglie wavelength, $\lambda\!\!\!^{-}$, is much smaller than the inter-nucleon distance, d. In language of quantum mechanics [8] - the wave-packets representing the particles have good enough definition of position, energy and momentum to be followed on classical trajectories.

iii. $\lambda\!\!\!^{-}$ is much smaller than the mean-free-path between collisions, Λ, - the scattered wave reaches approximately its asymptotic value before the next scattering and classical treatment of scattering becomes reasonable.

iv. The radius of the target nucleus, R, is large with respect to Λ. There will be many scatterings inside the nucleus and the interference terms between different scattered waves will tend to cancel out.

v. Λ is larger than d, and the time between interactions, Δt, is much longer than the time of an interaction, T - the scattering from different nucleons in the nucleus can be assumed to be approximately independent of each other

Summarizing, we have:

$$\lambda\!\!\!^{-} << d < \Lambda < R \tag{1a}$$

$$\Lambda/\beta c > T \approx 10^{-23}\ \text{sec} \quad => \quad \Lambda/3\beta \approx> 1\ \text{fm} \tag{1b}$$

Fig. 1 shows the behaviour of the relevant quantities for proton on ^{208}Pb reaction as a function of incident proton energy, E_{inc}. Calculating $\lambda\!\!\!^{-}$ we took into account that proton entering the nucleus gains ≈40 MeV kinetic energy.

$$\lambda\!\!\!^{-} = \hbar / \sqrt{(E+40)^2 - m_p^{\,2}} \tag{2}$$

where m_p is the proton mass.

The mean free path, Λ, was calculated using the Isabel INC code [9] (which includes the Pauli Principle) for central collisions:

$$\Lambda = -2R/Ln(N_{tranp}/N_{tot}), \tag{3}$$

where R=6.63 fm, N_{transp} is the number of "transparencies" (events when the proton traversed the diameter of the nucleus without interacting) and N_{tot} is the total number of events. For comparison also shown is $1/\rho\sigma$, with ρ=.16 fm^{-3} being the central nucleon density and σ the average proton-nucleon cross section (in fm^2). This is an estimate of the mean-free-path without Pauli Principle effect.

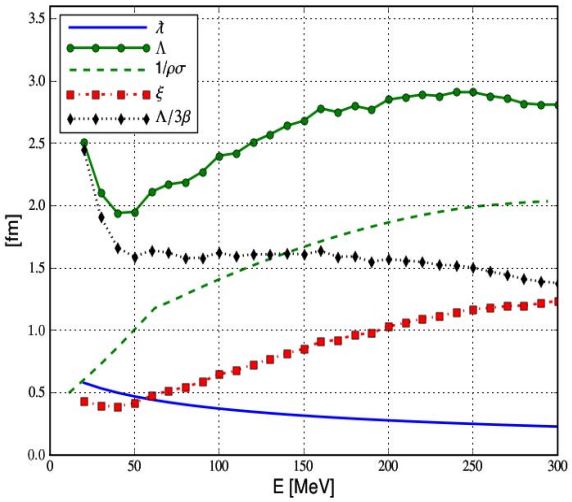

Fig. 1. Central collision proton on ^{208}Pb: $\lambda\!\!\!^{-}$, Λ, $\xi=\Lambda/\lambda\!\!\!^{-}/10$, $1/\rho\sigma$ and $\Lambda/3\beta$ as a function of incident proton energy.

The effect of Pauli Principle is very important and is especially pronounced at $E_{inc} < 40$ MeV causing Λ to rise even though the nucleon-nucleon cross section is strongly increasing. In collisions of high energy particle with the Fermi Sea, the momentum transfer is small, and Pauli Principle limits the interaction to small fraction of the Fermi Sea close to its surface, thus increasing the mean free path.

From eq. (1a) with $d\approx 2$ fm, requiring, very conservatively, that $d,\Lambda > 5\lambda\!\!\!^{-}$, INC is applicable only for $E_{inc}\approx>60$ MeV. Requiring $d,\Lambda > 10\lambda\!\!\!^{-}$, moves the applicability of INC to $E_{inc}\approx>200$ MeV. No additional restrictions follow from (1b).

Most of the collisions are not central. Isabel calculations show that in the energies of few tens to few hundred MeV about 60% of the collisions leading to inelastic reactions occur at impact parameters at which the nuclear density is less than a half of the central density. However, in the region of low nuclear density the degenerate Fermi gas potential is low, so the particle gains less kinetic energy entering the nucleus. 50 MeV proton has $\lambda\!\!\!^{-}=0.6$ fm and cannot be "localized" on nuclear periphery. On the other hand, proton of 250 MeV has $\lambda\!\!\!^{-}=0.25$ fm and starts to be sensitive to the details of nuclear surface. Still, the lower density of the surface is expected to extend the applicability range of INC to lower energies due to growing d and Λ.

It is clear that the applicability range of INC depends strongly on the specific reaction property to be calculated and the desired accuracy.

Thus, considering the total nucleon yields from nucleon induced reactions one may use INC starting from just a few tens of MeV. Using the original Serber's arguments [1], the incident particle will lose in each collision ≈10-20 MeV. Particle with energies of ≈<30 MeV will be absorbed in the target nucleus (their probability to interact with the target nucleons is large, and they will "thermalize") unless they are on far periphery of the nucleus. The "thermalized" by INC nucleus has the right excitation energy and momentum (since INC conserves energy and momentum) and may be properly treated by the de-excitation models. In the peripheral collisions the number of emitted particles is expected to be correct in the low energy regime, being determined by energy conservation and the ability of particles to escape the nucleus.

INC may be justified for low energies ($E_{inc}\approx$ >50 MeV) considering reactions which take place primarily on nuclear periphery (e.g. "quasi-elastic", "low multiplicity"). Here, however, the results may strongly depend on the target periphery modelling. We may expect discrepancies, especially when looking in forward direction, due to violation of assumption iv. For "quasi elastic" reactions we may expect distortion of forward angle cross sections due to interference with the elastic channel, which is not accounted for in INC.

Considering "violent" (high multiplicity, high excitation energy) events, which involve the inner parts of the target nucleus the reliability of INC is expected to degrade for energies below 100-200MeV, though it may be used, with caution, according to the original Serber's argument. [1].

Until now we have considered the energy limitations on the incident particle. However, an energetic projectile will give little momentum transfer to its Fermi Sea collision partners, and create low energy "participants". Inside the nucleus those should be "absorbed" contributing their energy to the excitation of the "remnant" target, on nuclear periphery they may some chance to escape. The target periphery is modelled in all the INC implementations, but each has a different way to deal with the low energy "participants" chosen considering agreement with the experimental data rather than from basic physical considerations.

High energy cluster (α, d, ^{3}He…) production is out of the scope of INC models. In order to calculate those "extra prescriptions" are used. In the "coalescence" model [10,11] the vicinity (configuration, momentum or phase space) of escaping particle is searched for potential particles to share its energy and form a cluster. An alternative "kick-out" process [6] assumes existence of "virtual" clusters in the nucleus which elastically scatter with the cascading particles and then, taking into account their survival probability, escape the nucleus.

3. The Time-Like Basis Cascading for Particle-Nucleus Reaction

In order to explain the Time-Like Basis Monte Carlo method introduced in the VEGAS model [4], consider a single bombarding particle entering the target nucleus. The Lorentz invariant probability per unit path length of the particle to interact with the nucleons of the nucleus (the inverse of particle's mean free path, Λ) is:

$$Q \equiv \Lambda^{-1} = \frac{1}{v_1}\int \sigma_{12} v_{12} \frac{\partial \rho_2}{\partial \vec{p}_2} d\vec{p}_2 \approx \frac{1}{v_1}\sum \sigma_{12} v_{12} \frac{\partial \rho_2}{\partial \vec{p}_2}\Delta\vec{p}_2 , \qquad (4)$$

where v_1 is the laboratory velocity of the bombarding particle, σ_{12} , v_{12} are the cross section and relative velocity of the incident particle and the particles with momentum p_2 and density ρ_2 . The probability of the particle to interact at the distance between a and $a+da$ is given by:

$$dN(a) = e^{-Qa} Q da . \qquad (5)$$

If the nucleon distribution in the target is assumed to be that of a degenerate Fermi gas, a convenient method of calculation is to divide the Fermi sphere of momentum into n parts of equal volume and calculate the mean cross section, σ_{12}, and the mean velocity, v_{12}, for each sub-volume. If Q is calculated in the rest system of the nucleus, the momentum distribution is the "undistorted" Fermi gas distribution (contrary to the "velocity distorted" distribution of eq. (4)) for each sub-volume

$$\frac{\partial \rho_2}{\partial \vec{p}_2} \Delta \vec{p}_2 = \frac{\rho}{n} \quad , \tag{6}$$

and

$$Q = \frac{\rho}{n} \sum_{i=1}^{n} \frac{v_{12_i}}{v_1} \sigma_{12_i} \equiv \frac{\rho}{n} \sum_{i=1}^{n} \sigma_i' \tag{7}$$

The probability that a collision takes place in an interval a is calculated by integrating Eq. (7)

$$N(a) = 1 - \exp(-Qa) = 1 - \prod_{i=1}^{n} \exp(-\frac{a}{n} \rho \sigma_i') \,. \tag{8}$$

Each term of the product of the right hand side of Eq. (8) is formally equivalent to the probability of no collision between the incident particle and a beam of particles of momentum $\boldsymbol{p}_i$ and density ρ occurring in an interval a/n. In other words, the probability of collision of a cascade particle in the interval a may be calculated by dividing the interval a into n equal parts and calculating for each interval $\delta a = a/n$ the probability of collision between the cascade particle and a hypothetical nucleon gas having a density ρ and nucleon momentum $\boldsymbol{p}_i$. For each interval δa a different momentum $\boldsymbol{p}_i$ is chosen out of the undistorted momentum distribution in a completely arbitrary sequence. A test is made to see if the collision occurs in that step by the comparison of a random number to the quantity

$$N(\delta a) = 1 - \exp(-\rho \sigma_i' \delta a) \approx \rho \sigma_i' \delta a \tag{9}$$

The interval a is the path length over which a good estimate of Q is required. We may choose a to be an estimate of the mean free path, Λ, and $\delta a = \Lambda/n$. The value of n depends on the accuracy required and on the type and energy of the interacting particles. It must be large enough so that: (a) the sampling method of Fermi sea momentum is a sufficiently accurate, and (b) the interval $\delta a = \Lambda/n$ is small enough for the approximation (9) to hold.

4. ISABEL implementation of INC

ISABEL [9] is a "time like basis" Monte Carlo realization of an INC model for hadron-nucleus and nucleus-nucleus collisions. Hadrons included are nucleons, pions, anti-nucleons and kaons (the cross sections used for anti-nucleon and kaons are "ad-hoc", and will not be discussed in the following). It is a direct descendant of the original implementations of Serber's model [1-3] and a generalization of the VEGAS [4] and ISOBAR [5] INC codes. The general idea of Serber [1] is to follow the energetic projectile as it classically scatters in the target. On its way it excites particles pulling them out of the Fermi sea. Those particle either leave the target volume, or if they are not energetic enough (below certain "energy cutoff", in VEGAS language) contribute to the residual excitation of the target, to be de-excited by some evaporation (or pre-equilibrium process).

As in ISOBAR [4] pion production and absorption modes are included in ISABEL via the Δ_{33} resonance (pion-nucleon isobar) formation in nucleon-nucleon scattering

$$N_1 + N_2 \Leftrightarrow \Delta_{3,3} + N_3 \tag{10a}$$

$$\Delta_{3,3} \Leftrightarrow \pi + N \,. \tag{10b}$$

No additional modes of pion production or capture are included.

4.1. Nuclear model

The original VEGAS [4] code uses the nuclear charge distribution as measured by Hofstadter [12] represented by Fermi distribution:

$$\rho(r) = \rho_0 /[1 + \exp(r - c)/a], \tag{11}$$

with the "sharp radius" c=1.07A$^{1/3}$ fm and "skin thickness" a= 0.55 fm. ISABEL includes additional options for density distribution such as folded-Yukawa [13] or arbitrary, user defined, distribution.

A step–function distribution is used to approximate the nuclear charge distribution. The nucleus is divided into several (usually 8 or 16) concentric regions, each of constant density. The ratio of proton to neutron density is assumed to be Z/(A-Z) in all the regions.

The momentum distribution of nucleons in the nucleus is assumed to be that of degenerate Fermi gas with the Fermi energy given by:

$$E_{F_i} = (\hbar^2 / 2m)(3\pi^2 \rho_i)^{2/3}, \tag{12}$$

where the subscript i stands for either protons or neutrons, m is the nucleon mass, and ρ_i is the density of protons and neutrons, respectively.

Due to the variation of the Fermi energy, the nuclear potentials of the protons and neutrons differ in the various density regions.

$$V_i = E_{F_i} + (Separation\_Energy)_i \tag{13}$$

The average pion potential is uncertain, and may be set to a constant, but because of the short pion mean free path, is generally ignored in ISABEL calculations.

The average potential that the Δ feels is even more uncertain, and is taken after [7] as:

$$V_{\Delta^{++}} = V_p; V_{\Delta^{+}} = V_p + \frac{(V_p + V_n)}{3}; V_{\Delta^{0}} + \frac{(V_p + V_n)}{3} = V_n; V_{\Delta^{-}} = V_n \tag{14}$$

Conservation of energy and momentum requires that the kinetic energy of the particles and their direction change as they cross density region boundary (refraction). If the impact angle at the region boundary is greater that the critical angle the particle is reflected. However, as already pointed out in [4], "full" refraction gives generally worse results than particle kinetic energy correction without direction change. It was speculated [4] that in order to treat properly the refraction one should introduce energy dependence of the nuclear potential, as indicated by optical potential models. ISABEL may be used with the option of "full refraction" or just proper kinetic energy corrections on region boundaries. There is no option for energy dependant potential.

The Coulomb interactions between the target nucleus and the incident or emitted charged particle is explicitly considered in one way only: The refraction, or simple energy correction,

of the particles entering or leaving the nuclear boundary is calculated taking into account the Coulomb potential there.

4.2. Elementary (hadron-hadron) cross sections

4.2.1. Elastic nuleon-nucleon scattering

The nucleon-nucleon cross sections used in ISABEL are the on-mass-shell free nucleon-nucleon cross sections. Parameterization of [5] is used for the total, σ_{tot}, elastic, σ_{el}, and inelastic (pion production), σ_{inel}, cross sections. Parameterization of [14] is used for the elastic scattering angular distribution, $d\sigma_{el}/d\omega$.

4.2.2. Inelastic (pion production)

The types of outgoing nucleon and Δ in inelastic scattering, $N_1+N_2 \rightarrow \Delta + N_3$, are determined by isotopic spin considerations [15]. The mass of the $\Delta_{3,3}$ is chosen, according to [7], from the (normalized) distribution:

$$P(m_\Delta, E_{cm}^{N+N}) = const.* \sigma_{tot}^{\pi^+ + p}(E_{cm}^{N+N}) * F(m_\Delta, E_{cm}^{N+N})$$
$$m_\pi + m_N < m_\Delta < m_\pi + m_N + 500MeV \qquad (15)$$

where F is the two body phase factor for the produced N+Δ.

The angular distribution of the outgoing (N,Δ) is uncertain, and is taken, tentatively, from the distribution $P(cos_{cm})=.25+.75*(cos_{cm})^2$.

4.2.3. Δ capture

The types of outgoing nucleons in "pion capture" scattering, $\Delta+N_1 \rightarrow N_2 + N_3$, are determined by isotopic spin considerations [15]. The capture cross sections used were calculated from the inverse process with the aid of the principle of detailed balance [15], using the one-pion-exchange model for Δ production process [16].

4.2.4. Δ "charge exchange"

The Δ charge exchange process, $\Delta+N \rightarrow \Delta'+N'$, is considered as a two step process: first Δ decays into pion and nucleon and another nucleon absorbs the pion to become a "charge exchanged" Δ as shown schematically in Fig 2.

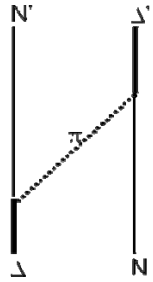

$\Delta \rightarrow \pi + N'$,

$\pi + N \rightarrow \Delta'$

Fig. 2. Δ "charge exchange".

The types of outgoing particles, are determined by isotopic spin considerations and the cross sections were calculated using the experimental π-N cross sections [15, 16]. Though, in

principle, both the mass and charge of the Δ may change in this process, the assumption is made that the mass of the Δ does not change.

4.2.5. π-N resonant scattering

The process involves intermediate Δ, π+N→ Δ→ π'+N' and the relevant cross sections were calculated from the experimental πN scattering data [17]. If, after being created, Δ "charge exchanges" – it decays isotropically. However, if the Δ decays without intermediate interaction – the code calculates correctly the π+N→ π'+N' kinematics.

4.2.6. Δ decay

The energy dependant Δ width is parameterized according to [7].

4.3. Cascading process

Following the ideas of the time-like basis Monte Carlo simulation, ISABEL cascading process is described in Fig. 3.

The ***general initialization*** includes calculation of the parameters of the nuclear model. The nuclear density distribution (e.g. Eq.11) is approximated by a step function of N_{reg} (usually 8 or 16) regions of constant density. The outermost radius of the targer nucleus is fixed, generally as *c+4a* of Eq. 11. Proton and neutron separation energies are determined from the experimental mass tables and Coulomb repulsion potential is determined for the outermost region of the target nucleus. The region boundaries are usually determined so that the difference of average densities in adjoining regions is constant [4]. Proton and neutron Fermi energies (Eq. 12), momenta, and potentials (Eq. 13) in the various regions are calculated.

The total cross sections $\sigma_p(E'_{inc})$ and $\sigma_n(E'_{inc})$ of the incoming particle, E'_{inc} being the incident energy corrected by the Coulomb energy (for charged projectiles), with a stationary proton and neutron are determined and an approximate mean free path of the incoming particle is calculated

$$\Lambda = (A/\rho_{\max})[Z\sigma_p + (A-Z)\sigma_n]^{-1} \tag{16}$$

ρ_{max} is the total nucleon density in the center of the nucleus. The first time interval, $\delta\tau$, is

$$\delta\tau = \Lambda / n\beta \tag{17}$$

where β is the velocity of the incoming particle. Generally n=30 is used in our calculations.

In ***event initialization*** an impact parameter, b, is chosen randomly from $P(b)\sim b^2$ distribution and the projectile particle is brought to the target boundary. It becomes the first (and at this point the only) "active" particle. It is refracted by the Coulomb and nuclear potentials in the outermost region (or its energy is corrected without changing its directions) and its velocity, β, is determined. The first random number of the event is picked out. It is extremely important to choose the right random number generator, to avoid correlated results from different events and ensure the correct sampling in a single event.

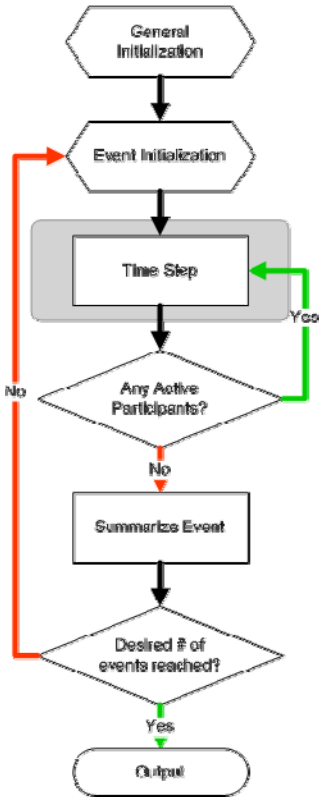

Fig. 3. ISABEL cascading scheme.

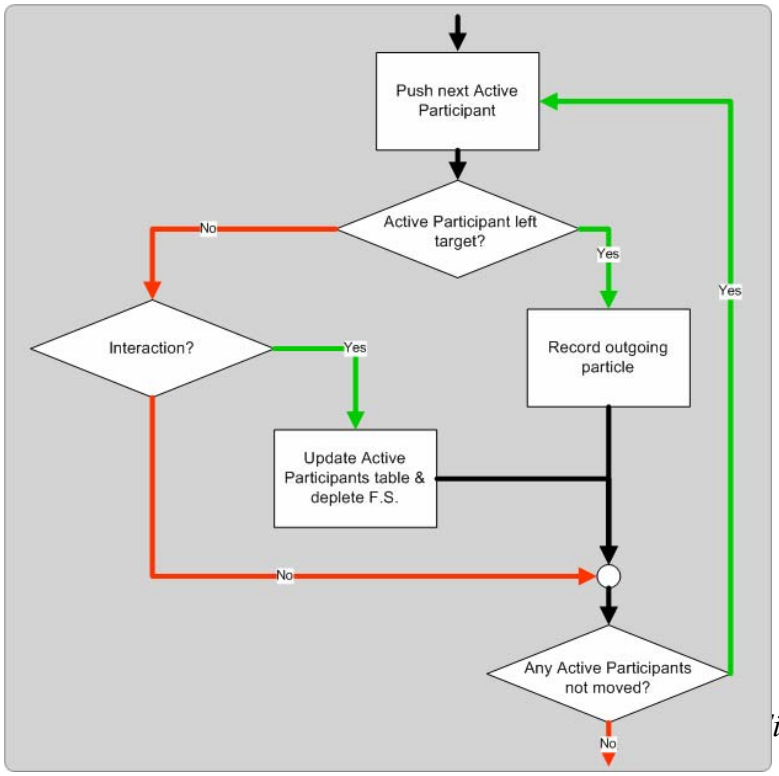

Fig. 4. ISABEL time step.

According to the general idea of the time-like Monte Carlo cascading, each event is realized by considering a series of small time steps. A general structure of a time step is described in Fig.4.

1. The next "active" particle, having velocity β_i, is pushed, in the direction of its momentum, by a small distance $\delta a=\beta_i*\delta\tau$. If it leaves the target volume its properties (type, momentum, position, time relative to the beginning of the event) are recorded in vector of escaping particles, and it ceases to be "active". Δ's are not allowed to escape the target volume, and are forced to decay or be captured on the target boundary.

2. A potential interaction partner is chosen to be a proton or a neutron according to the densities in the Fermi sea at the position of the "active" particle, and its momentum, $\boldsymbol{p}_2$ is chosen from the Fermi sphere

3. A random number $0<\zeta\leq 1$ is chosen. $N(\delta a)$ is calculated according to Eq. (9). If $\zeta\leq N(\delta a)$, an interaction is assumed to have occurred. Otherwise, go to (6), below.

4. If the interaction between the incoming particle and the partner from the Fermi sea of the target occurred – the type of the interaction (e.g. elastic, inelastic, pion absorption) and the identity of outgoing, "cascade" particles is determined by comparing the relevant branching ratios to a random number, and the calculation of reaction kinematics is performed. Outgoing nucleons are checked for Pauli principle violation (more about it later), and only allowed reactions take place. The "cascade" particles become the "active" particles for the next time intervals. However, "cascade" nucleons which fall below a certain "energy cutoff" are considered "absorbed" by the target and cease to be "active".

5. For each of the "cascade" particles a new time interval, $\delta\tau_i=\Lambda_i/n\beta_i$, is calculated and the smallest of those $\delta\tau=min[\delta\tau_i]$ is chosen for the next time interval. The Fermi sea is "depleted" (see later), and the cascading continues from (1) above.

6. If not all "active particles" moved in the current time interval, pick the next "active" particle and go to (1). If all "active particles" moved in the current time interval, start a new time interval, pick the first "active" particle and go to (1). If there are no "active particles" – the event is finished.

The cascading event stops when all the "cascade" particles leave the target volume or fall below a certain "energy cutoff". This "energy cutoff" sets the limit between the INC fast stage and the "pre-equilibrium" and "evaporation" stages. We must make sure that particles that cannot escape from the potential well fall below cutoff – otherwise they will wander "infinitely" sharing their energy with others, without changing the global residual target proprties. This means that our "cutoff energy" for neutron must be at least its separation energy and for proton the separation energy plus Coulomb barrier.

A pictorial example of an event is shown on Fig. 5.

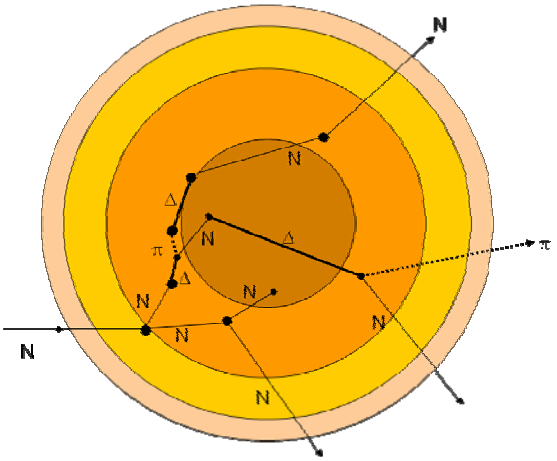

Fig. 5. An example of ISABEL event.

The residual excitation energy of the target is the sum of the hole (in the particle-hole sense) energies and the energies of the particles which fell below cutoff. The residual linear and angular momenta are calculated in a similar fashion. Those quantities may be processed by evaporation codes.

ISABEL repeats the cascading process for a prescribed number of events. Finally the results are recorded for further processing by evaporation (or pre-equilibrium) codes.

4.4. Density and Pauli blocking depletion

The most important advantage of the timelike basis Monte Carlo procedure is the possibility of changing the global properties of the system as the interaction proceeds.

As a cascade develops the density in the participating Fermi seas is depleted. Since the detailed nature of the density rearrangement is unknown, we have applied two extreme prescriptions:

- ***Fast rearrangement*** - After each collision with a target partner, the density distribution ρ_i of the "partner type" (i denotes proton or neutron) in the target is instantaneously and uniformly reduced for the whole nucleus. In addition "distance restriction" is usually applied – any given particle is not allowed to interact within a distance smaller than some $r_{min,i}$ from its last interaction. There are few options for $r_{min,i}$, that should be close to d_i, the average (local) interparticle distance in the Fermi sea, and may depend on the local density of protons or neutrons.

- ***Slow rearrangement*** - After each collision a hole of radius r_{min} is punched in the density distribution configuration space around the position of the interaction. No more interactions are allowed in this hole. The holes may be either isospin dependant or isospin independent, i.e. we may punch them for protons and neutrons independently, with possibly different $r_{min,i}$ or punch holes for nucleons using common r_{min}.

The slow rearrangement prescription with isospin dependant holes and $r_{min,i}$ =1.1fm was found to be best.

The depletion of the Fermi seas affects the Pauli blocking. Two options for dealing with Pauli blocking are included in ISABEL:

- ***Full Pauli blocking*** – After each interaction cascade nucleons are tested for Pauli principle violation. If cascade nucleon energy is lower than the target Fermi energy – the interaction is forbidden.

- ***Partial Pauli blocking*** – After each interaction proton and neutron Fermi sea depletion factors (ratio of actual to original number of particles in the Fermi sea) is calculated. If the energy of a cascade proton (neutron) generated in an interaction is lower than the target Fermi energy, a random number is compared to the depletion factor, and only if it is smaller – the reaction is forbidden. Intuitively, as we deplete the Fermi sea, cascade particle are allowed to fill the "empty" states below the Fermi energy. In our approximation, this depletion of the Fermi sea is "global" – it does not depend on position or energies of the particles lifted from the Fermi sea or those trying to fall into it.

Pauli blocking contributes to extension of the mean free path, Λ , of the nucleons and to prolongation of the lifetime of a the Δ in the nucleus (since it is forbidden to decay into a nucleon violating the Pauli principle).

4.5. Total Reaction Cross Section

The INC calculation may, quite accurately, estimate the total reaction cross section of hadron-nucleus collisions. For the radius R of the outermost region of the target the geometric cross section is $\sigma_{geom}=\pi*R^2$. If out of N_{tot} events N_{transp} were transparencies – events when the projectile did not interact within the target, we may estimate the total reaction cross section by $\sigma_{geom}=\pi*R^2*(N_{tot}-N_{transp})/N_{tot}$.

For charged projectile a correction for Coulomb deflection should be applied [4], and the total reaction cross section is estimated by

$$\sigma_R = \pi R^2 * \frac{N_{tot} - N_{transp}}{N_{tot}} * (1 - \frac{V_{Coul}(R)}{E_K^{Proj.}}) \qquad (18)$$

where $E_k^{Proj.}$ is the projectile kinetic energy and $V_{Coul}(R)$ is the Coulomb potential at radius R.

5. Extension to Nucleus-Nucleus Collisions

In the *particle-nucleus* collision the Fermi sea of the target nucleus is treated as a continuous density distribution, whereas the incoming and the "cascade" particles are discrete particles of well defined position and momentum. In the *nucleus-nucleus* collision one has two Fermi seas interacting with each other and hence the following prescription is used: For the purpose of calculating the interactions between nucleons of the *projectile* Fermi sea and the nucleons in the *target* Fermi sea the *projectile* Fermi sea is assumed to consist of a gas of *discrete particles* whose positions in space and momenta are randomly chosen from the appropriate distribution. However for the purpose of calculating interaction between the (discrete) "cascade" particles and the Fermi sea of the projectile or target, the latter two distributions are considered *continuous*. This procedure was chosen in order to calculate the collision in the same manner as was done in the particle-nucleus INC calculation. It ensures the equal treatment of projectile and target, i.e. the Lorentz invariance of the calculation.

The INC model of *nucleus-nucleus* collisions involves a large number of "cascade" particles. The evolving particle density outside the target and projectile Fermi seas in such an interaction is high, and the relative distances between the energetic particles are quite small. The scattering between pairs of "cascade" particles, neglected in VEGAS model [4] and early version of ISABEL, cannot be justified, and may lead to disagreement with experiments. The introduction of "cascade-cascade" interactions [9] led to significant improvement of the model.

The "cascade-cascade" interactions are treated, once again, as interactions of a discrete particle with continuous density. Each cascade particle is represented, in its rest-frame, by a spherical Gaussian density distribution $\rho(r)$ centered at its discrete position with standard deviation of 1 fm. Each cascade particle may thus interact with the continuous Fermi sea of the target and projectile and the continuous distribution of its fellow cascade particles. The only restriction is that two given cascade particles cannot interact more than once, until at least one of them interacted with a third particle. The interacting cascade particles are brought to common position and the reaction kinematics is calculated with "zero range". This procedure conserves energy and momentum in each cascade-cascade interaction, but only "on the average" conserves angular momentum in cascade-cascade interactions.

In ISABEL the projectile and target nucleons are initially bound in their respective nuclei by real potential wells (approximated by step-function distributions) that are uniquely determined for a degenerate Fermi gas by the nuclear density. Since the potential energy of a particle can not be transformed covariantly from one Lorentz frame to another, the *projectile nucleons* (i.e. projectile Fermi sea nucleons and cascade nucleons with momentum lower in the projectile frame of reference than in the target frame of reference) are assumed to feel the *projectile potential* while they are in the projectile volume and are treated as free nucleons outside this volume. They do not feel the target potential. Similarly, the *target nucleons* feel the *target potential* while they are in the target volume and are treated as free nucleons outside this volume. After an interaction between target and projectile nucleons, the identity of the outgoing nucleons is determined according to their momentum relative to the projectile and target frames. This procedure might be considered a crude approximation to a velocity dependent potential that vanishes for high velocities.

Schematically the step by step process of building a nucleus-nucleus cascade proceeds as follows:

1. In the projectile frame of reference a set of discrete coordinates and momenta are randomly chosen from appropriate distributions. Impact parameter is chosen randomly and the set is Lorentz transformed to the target frame of reference.
2. The first time interval, $\delta\tau$, is obtained from $\delta\tau=\Lambda/n\beta$, where β is the velocity of the projectile. The projectile particles are translated by a distance Λ/n in the direction of projectile motion. Some of them may cross the target boundary and travel distances δa_i through the target Fermi sea. For each of them interaction partner is chosen to be a proton or a neutron according to the densities in the Fermi sea, and its momentum, $\boldsymbol{p}_2$ is chosen from the Fermi sphere. A random number $0<\zeta_i\leq 1$ is chosen. If $\zeta_i\leq N(\delta a_i)$, an interaction is assumed to have occurred. If none of the particles interacted the projectile particles are translated again and the testing for interactions repeated.
3. If one or more particles interacted - the identity of outgoing, "cascade" particles is determined and the calculation of reaction kinematics is performed. Outgoing nucleons are checked for Pauli principle violation in the target and projectile. Only allowed reactions take place. The momentum of a cascade particle is determined in the target

and projectile frames of reference, and it is decided whether it is a "projectile" particle (it feels the projectile potential) or "target" particle (it feels the target potential.)

4. A new time interval $\delta\tau_i=\Lambda_i/n\beta_i$ is chosen for each of the "cascade" particles and the smallest of those $\delta\tau=min[\delta\tau_i]$ is chosen for the next time interval. Both projectile and target Fermi seas are depleted.

5. The projectile particles that did not interact yet ("virgin" particles) are translated by $\beta_i*\delta\tau$ in the direction of projectile motion. The cascade particles are pushed by distances $\beta_i*\delta\tau$ in the direction of their momenta. A test is made for interaction of all particles. However whereas the "virgin" particles are checked for interaction with target Fermi sea only (like in (2) above), the cascade particles are tested for interaction with both the projectile and target Fermi seas. First a test is made in the target frame of reference, and then the particle is Lorentz transformed into the projectile frame of reference and tested there for interaction. If the result shows interaction in both Fermi seas a decision where it actually took place is made based on the probabilities of the two interactions.

6. Cascading continues by repeating step (5) above. In every m's time interval (usually m=3) the "cascade" particles are scanned for cascade-cascade interactions.

7. The particles are followed until they leave the target-projectile volume or fall below projectile or target energy cutoff. Particles can fall below cutoff only outside the overlap region between projectile and target, since in the overlap a particle below cutoff in the projectile (target) will be generally above cutoff in the target (projectile), and therefore eligible for interaction with the target (projectile) Fermi sea.

The residual excitation energies, linear and angular momenta of the target and projectile are calculated summing the hole and "below cutoff particle" energies and momenta and may be processed by evaporation code. The projectile velocity is kept constant during the collision, the recoil being calculated at the end.

REFERENCES

[1] R. Serber, Phys. Rev. 72, 1114 (1947)
[2] M.L.Goldberger, Phys. Rev. 74, 1269 (1948)
[3] N.Metropolis et al., Phys. Rev. 110, 185 (1958); Phys. Rev. 110, 204 (1958)
[4] K.Chen et al., Phys. Rev. 166, 949 (1969).
[5] G.D.Harp et al., Phys. Rev. C6, 581 (1973); Phys. Rev. C8, 581 (1973); Phys. Rev. C10, 2387 (1974)
[6] V.S. Barashenkov, V.D. Toneev, Interaction of High Energy Particles and Atomic Nuclei (Atomizdat, Moscow, 1972) 268-325 (in Russian)
[7] J.N. Ginocchio, Phys. Rev. C17, 195 (1978)
[8] A. Messiah, *Quantum Mechanics Vol. I* (North-Holland, Amsterdam, 1964) 372-376
[9] Yariv Y., Fraenkel Z., Phys. Rev. C20, 2227 (1979), Phys. Rev. C24, 448 (1981).
[10] J. Gosset *et al*., Phys. Rev. C16, 629 (1977)
[11] A. Boudard *et al*., Nucl. Phys. A740, 195 (2004)
[12] Hofstadter R., Ann. Rev. Nucl. Sci. 7, 295 (1957).
[13] Krappe H. J., Nix J. R. and Sierk A. J., Phys. Rev. C20, 992 (1979).
[14] P.C.Clements, L.Winsberg, UCRL 9043 (1960), unpublished
[15] Z.Fraenkel, Phys. Rev. 130, 2407 (1963), Nuovo Cimento 30, 512 (1963)
[16] S.Lindenbaum and R. Sternheimer, Phys. Rev. 105, 1874 (1957); 109, 1723 (1958); 123, 333 (1961)
[17] G.Giacomelli et al., CERN/HERA 69-1 (1969)

INCL4 – The Liège INC Model for High-Energy Hadron-Nucleus Reactions

A short description of the INCL4.2 and INCL4.4 versions

A. BOUDARD[1], J. CUGNON[2]

[1] CEA Saclay,
IRFU/SPhN,
Gif-sur-Yvette, France
[2] Department AGO,
University of Liege,
Liege, Belgium

Abstract. The details of the standard INCL4.2 version of the Liège Intranuclear Cascade model for spallation reactions are reviewed. Emphasis is put on the physics features which are incorporated and on their practical implementation in the numerical code. New developments, bearing on the production of clusters, on the properties of the nucleon and pion mean fields and on the behaviour of the model at low incident energy, are briefly presented and discussed. They will be part of the forthcoming INCL4.4 version.

1. Introduction

This report is a short explanatory account of the latest versions of the Liège intranuclear cascade model (INCL) for high-energy nuclear collisions induced by nucleons, pions or light clusters.

The Liège Intranuclear Cascade (INC) model has been built about twenty years ago in order to describe heavy-ion collisions in the GeV range [1]. Afterwards, specific versions have been built to describe reactions induced by antiprotons, pions, nucleons or light clusters. Due to the renewed interest for spallation reactions, in relation to transmutation studies, the early version for nucleon-induced reactions [2] has been improved to give birth to the INCL3 version a few years ago [3] and to the INCL4 version a little bit later [4]. Thanks to the HINDAS collaboration [5], this model was shown to be, when coupled to the ABLA evaporation-fission code, quite successful in describing an extensive set of experimental data in the 200 MeV to 2 GeV energy range [6]. This model, known as INCL4.2, has been included in LAHET [7] and MNCPX [8], and is considered as the standard version of the INCL4 model. It is basically a parameter free model. Yet it suffers from some limited but systematic deficiencies. Further improvements have been studied in the meantime. They bear on the introduction of light charged cluster emission in the cascade stage [9], on the introduction of energy-dependent potentials for nucleons [10], on the introduction of an average potential for pions[11] and on the improvements of the code at low incident energy (below 200 MeV) [12-14]. The inclusion of these developments to the INCL model constitute the version INCL4.4, which is not yet available to the public, some aspects being still under study in the frame of the EUROTRANS collaboration [14]. A version consisting of INCL4.2 plus the production of clusters, as defined in Ref. [9], is available under the label INCL4.3.

The purpose of this note is to describe the standard version of INCL4.2 and to give a short account of the additional features contained in INCL4.4. However, due to lack of space, only the main features of INCL4.2 will be given. For a comprehensive description, we refer to Ref. [15].

2. Description of the standard INCL model (INCL4.2)

2.1. Introduction

The basic premises of the INCL model are schematically illustrated in Fig. 1. Particles are moving freely between instantaneous events that we call "avatars" (to distinguish from the usual meaning of "event", namely a complete simulation or “realization” of the reaction). These avatars can be of three types: two-body collision, decay and transmission or reflection at the nuclear periphery. In INCL4.2 only three types of particles are considered: nucleons *(n, p)*, Δ-isobars (4 charge states) and pions (3 charge states). The target is composed of point-like particles. All particles are followed in space-time and are propagated in single steps between avatars, on a manner described below. The simulation is stopped according to a self-consistent criterion, which constitutes a unique feature of INCL. The properties of the exit channel are recorded and are transferred to an evaporation module.

In this presentation, we will refer to the nucleon-nucleus case, indicating when necessary the variants for incident pions or incident light clusters.

2.2. Description of the model

A. *Target preparation*

Nucleons are positioned at random, according to a distribution *f(r)* which follows nuclear density (i.e. with the same shape), taken from electron scattering measurements. For target mass $A>27$ a Woods-Saxon distribution is used up to a maximum distance R_{max}, fixed to $R_0 + 8a$. For $6<A<27$, a "modified harmonic oscillator" distribution is adopted and for $A<6$, Gaussian density distributions are used. See Ref. [15] for the values of the parameters of these distributions.

Nucleon momenta are taken at random in a sphere of radius *pF* , the Fermi momentum, equal to 270 MeV/c, a value corresponding to normal nuclear matter. The same distribution is used for protons and neutrons.

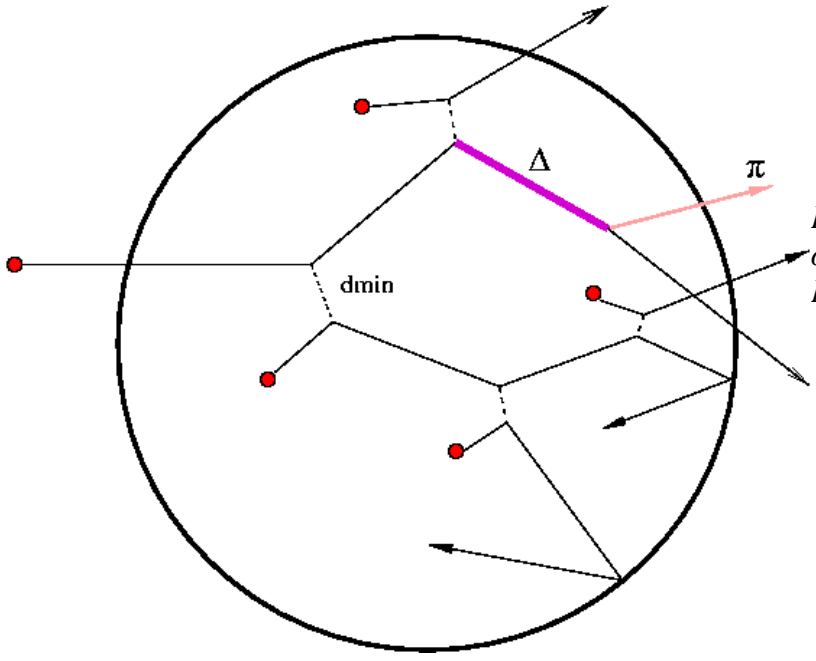

Fig. 1. Schematic illustration of the main features of the INCL model.

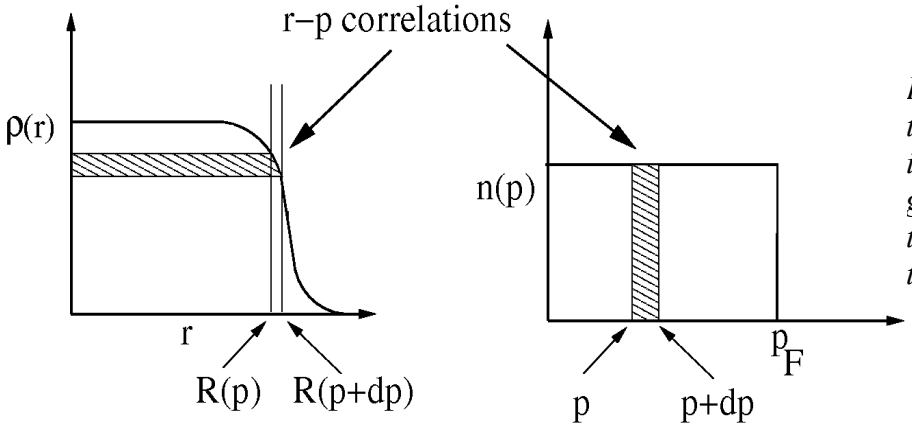

Fig. 2. Illustration of the r-p correlations introduced in the generation of the target initial state. See text for detail.

Actually, momentum and position are not taken independently. Momentum p is generated first at random and the position is taken at random inside a sphere of radius $R(p)$, which is implicitly given by:

$$\left(\frac{p}{p_F}\right)^3 = -\frac{1}{3N}\int_0^{R(p)} \frac{df(r)}{dr} r^3 dr \tag{1}$$

where N is a normalization constant

$$N = \int_0^{R_{\max}} f(r) r^2 dr \tag{2}$$

It is easy to check that $R(p)$ is an increasing function going from 0 at p=0 to Rma_X at p=pF. It is shown in Ref. [4] that this procedure amounts to requiring that the nucleons with momentum contained in the interval [p, p+dp] are contributing to the density profile by a horizontal slab corresponding to the vertical coordinates $R(p)$ and $R(p+dp)$, as shown in Fig. 2, or equivalently that nucleons with momentum p do not propagate farther than $R(p)$. The procedure is also equivalent to a phase space joint distribution function of the form

$$\frac{dn}{d^3\vec{r}\,d^3\vec{p}} \propto \frac{\theta(R(p)-r)\theta(p_F-p)}{R(p)^3} \tag{3}$$

where $\theta(x)$ is the Heaviside function. Although this distribution obviously generates correlations between r and p coordinates, it nevertheless yields the constant Fermi gas distribution and the r-space distribution $f(r)$ after integration over $\vec{r}$ and $\vec{p}$, respectively, as demonstrated in Ref. [4]. There are no other correlations. There is no attempt to have zero total momentum ($\sum \vec{p} = 0$), location of the barycenter at the origin ($\sum \vec{r} = 0$) nor zero total angular momentum ($\sum \vec{r} \times \vec{p} = 0$).

All target particles are sitting in a (fixed and constant) attractive square potential well, with a momentum-dependent radius $R(p)$ and a depth $V0$. The function $R(p)$ is such that, in absence of collisions, nucleons are moving while the average (over events) spatial and momentum distributions remain unaffected. This is demonstrated in Ref. [4]. But it is almost clear from Fig.2 that nucleons can be divided into groups of particles with the same momentum

occupying given spheres in *r*-space. In absence of collisions, the distribution in *r*- and *p*-space remains the same on the average (this is a well-known property of a system of billiard board particles with initial momentum and directions at random bouncing elastically on the interior surface of a sphere). We anticipatively indicate that particles with momentum larger than *pF* experience a potential well with radius $R_{\max}$ (as for $p = pF$).

The *r-p* correlations introduced in this model are not of the conventional type. They comply with the fact that high (kinetic) energy particles can propagate farther out than low energy particles, as they should, in accordance with the standard shell-model. In contrast with the latter, particles keep the same momentum, be they in the centre or in the (allowed) surface region of the nucleus. The procedure that is adopted here has the advantage of straight-line motion between collisions, an advantage that will become clearer when we will be discussing the propagation of the particles.

B. Projectile preparation

The nucleon is incoming along the *z*-direction and is given at random in the *xy*-plane an impact parameter *b* inside a circle of radius $R_{\max} = R_0 + 8a$. A sphere of the same radius centered on the middle of the target is defined as the "volume of calculation". Nothing happens to the particles outside this volume. At *t*=0 (beginning of the calculation), the incoming nucleon is positioned at the surface of the volume of calculation. As described above, this is also the surface of the potential well felt by this particle. It is considered that at *t*=0, the incident nucleon has just entered the well. Therefore its total energy has increased by the value of the potential depth *V0* and its momentum has been increased accordingly (direction is not changed; no reflection, no refraction in the entrance channel). The choice of *bmax* guarantees a good compromise between computational efficiency and accurate evaluation of the total reaction cross section. Indeed only a small fraction (10-4) of the interacting events beyond *bmax* is missed.

For an incident pion, the procedure is the same, except that the pion does not experience any average potential. For an incident light ion, the procedure is more involved. First the incident ion has to be generated. In the rest frame of the latter, nucleons are given positions and momenta at random according to Gaussian laws, with rms values given in Table 1 below.

TABLE I. PARAMETERS OF THE GAUSSIAN FORMS USED TO DESCRIBE RADIAL DISTANCE AND MOMENTUM DISTRIBUTIONS IN LIGHT IONS

Light ion	***d***	***t***	***3 He***	***4 He***
$\sqrt{\langle r^2 \rangle}$ (fm)	1.91	1.8	1.8	1.63
$\sqrt{\langle p^2 \rangle}$ (MeV/c)	77	110	110	153

The values of the parameters are either taken from the Paris potential for the deuteron, and from experiment or from realistic wave functions, for the other ions. In this case, $\sum \vec{r} = 0$ and

$\sum \vec{p} = 0$ are imposed, simply by choosing the values for the last nucleon appropriately, possibly after a renewed generation of the first ones. The maximum impact parameter is taken as *bmax* defined above plus the rms radius of the ion. The transverse position of the ion centre of mass is taken randomly in a circle of radius equal to this new value. The ion is then Lorentz-contracted along the collision axis and the longitudinal position of the ion is chosen in such a way that one of the nucleons is just touching the "interaction volume", the other ones being outside. The ion is then "boosted": 4-momenta undergo the Lorentz transformation corresponding to the velocity of the incident ion. They are finally corrected in order to comply with the energy content of the incoming ion. Because of the generation of the internal motion of the nucleons, the total energy is larger than the nominal incident energy *Winc=Tlab+Minc*. Let us denote by ε_i and $\vec{p}_i$ the total energy and the momentum of the ion nucleons, respectively. The momenta of the nucleons are scaled by a common factor such that the sum $\sum \varepsilon_i$ is put equal to *Winc* . Let us notice that for very slow ions, this operation may not be possible, because the minimum value of $\sum \varepsilon_i$ is *AincMN*, the mass number of the incident ion times the nucleon mass, whereas the minimum value of *Winc* is equal to that quantity minus the binding energy of the ion. To circumvent this drawback, the following procedure if adopted: if *Winc – AincMN* < 0, all nucleons are given the same kinematics as the velocity as the incident ion, neglecting so internal motion and binding energy. Finally, as in the nuclear case, the nucleon located at the surface of the interaction volume is supposed to sit inside the nuclear potential, with appropriate energy and momentum.

C. Propagation of the particles

At t=0, all nucleons are set in motion with their initial velocity and are assumed to follow straight-line trajectories until an avatar occurs, i.e. until two of them achieve their minimum distance of approach, or until one of them hits the nuclear surface, or until a Δ–resonance decays. Due to the straight-line trajectories, the times at which these events occur can be predicted. The smallest of these times is selected and the particles are propagated in a single step. The simplicity of this propagation is a particular feature of the Liège INC model. After the occurrence of an avatar, straight-line motion is resumed until the next avatar, and so on. The process is followed up and terminated according to a criterion explained below.

Let us elaborate a little bit on the procedure. At the beginning, a table of times for the possible avatars is constructed. For a possible collision between a pair of nucleons *a* and *b*, with initial relative position $\vec{r}_{ab}^{\,0}$ and relative velocity $\vec{\beta}_{ab} = \vec{\beta}_a - \vec{\beta}_b$, the time at which. the relative distance is minimum is given by

$$t_{ab} = -\frac{\vec{r}_{ab}^{\,0} \cdot \vec{\beta}_{ab}}{\beta_{ab}^2} \tag{4}$$

and the square of this minimum relative distance is equal to

$$d_{\min}^2 = \left(\vec{r}_{ab}^{\,\min}\right)^2 = \left(\vec{r}_{ab}^{\,0}\right)^2 - \frac{\left(\vec{r}_{ab}^{\,0} \cdot \vec{\beta}_{ab}\right)^2}{\beta_{ab}^2}, \tag{5}$$

where $\vec{r}_{ab}^{\,\min}$ is the minimum relative position vector. It is also easy to verify that a nucleon *a* will encounter the radius *R* of the potential well (which depends on its momentum) at time

$$t_a = \frac{1}{\beta_a^2}\left[-\vec{r}_a^{\,0} \cdot \vec{\beta}_a + \sqrt{\left(\vec{r}_a^{\,0} \cdot \vec{\beta}_a\right)^2 + \left(R - r_a\right)^2 \beta_a^2} \right] \quad (6)$$

See later for Δ-decay. Not all times need to be considered. They are disregarded:

- if they are larger than the stopping time *tstop* of the cascade (see Section 2.F)

- if nucleons *a* and *b* are spectators; nucleons are divided into participants and spectators; a nucleon is a participant if it is an incident nucleon or if it has participated to an avatar (Deltas and pions are participants)

- if *tab* is negative (diverging trajectories)

- if nucleons *a* and *b* are passing too far away from each other to make a real collision, i.e. if $\pi d_{\min}^2 > \sigma_{NN}^{tot}$

- if the c.m. energy of the collision is smaller than 1925 MeV (*2MN+cutNN* , *cutNN* = 48.5 MeV)

The last point needs a word of clarification. Soft collisions are so neglected, for three reasons. First, a soft collision does not change very much the momentum content of the target. Second, most of the time, soft collisions involve nucleons with momenta not far from the Fermi momenta and, therefore, these collisions are expected to be suppressed efficiently by the Pauli principle. The third reason is more practical: taking these soft collisions, whose effect is presumably not important, into account would multiply the number of times *tab*, due to the very large *NN* cross sections at low energy. There are theoretical arguments supporting this procedure, indicating that "soft interactions" are rather taken into account by the average potential, whereas hard interactions contribute to the collisions. See Ref. [16] for a discussion of these matters.

After the list of times for the occurrence of possible avatars is completed, the smallest time of the list is selected. If the corresponding avatar is a collision, a test for the possible realisation of the latter is performed. If

$$\sqrt{s} > 2M_N + cut_{NN} \quad (7)$$

and

$$\pi d_{\min}^2 < \sigma_{NN}^{tot}(s), \quad (8)$$

the avatar is accepted. Otherwise the time *tab* is removed from the list, and the next smallest time is selected. The same test is done and the same procedure is repeated until the avatar is accepted (avatars corresponding to decay or reflection/transmission are always accepted at this stage). Particles are then propagated until the selected time, in a single step.

At this stage, the first avatar is considered for realisation. It may be realized or not (due to Pauli blocking of collisions for instance, see later). If it is realized, the list of times is updated. Let us consider for instance a collision between particles *a* and *b*. We refer here to the labels of the particles. Their nature may have changed during the collisions. All the times involving *a* and *b* are removed. New times are added, corresponding to possible further collisions between either *a* or *b* with other particles (not between *a* and *b* to avoid repeated interactions)

or to possible reflection/transmission of *a* and *b*). For other kinds of avatars, it is easy to list the operations needed to update the list of times. Of course, in the addition of new times, the same criteria of selection as described above are applied.

Then, the smallest time of the updated list is selected and the same set of operations is performed, and so on.

The process is terminated on a manner described later.

D. Description of the avatars

D.1 Collisions

Inelastic nucleon-nucleon collisions are dominated by the production of pions. In the energy range mentioned in the introduction, there are good indications that pion production results from the production of a Δ-resonance followed by its decay. Although the Δ-resonance is short-lived, it has a good chance to interact with another nucleon before decaying. The philosophy of the standard INCL model is to propagate the Δ-isobars (instead of describing the *NN* inelastic collisions by the asymptotic channels in free space). Therefore, the following possible reactions are considered

$$NN \to NN\,, \quad NN \to N\Delta\,, \quad N\Delta \to N\Delta\,, \quad \Delta\Delta \to \Delta\Delta\,, \quad \pi N \to \Delta \tag{9}$$

We treat the two-body reactions first.

(a) Selection of the final channel. For any of the incident channels (*NN, N*$\Delta, \Delta\Delta$), the final channel is selected at random, by the standard method of comparing a random number with the ratio between elastic and inelastic cross sections. The relevant cross sections, as parametrized in INCL4.2, as well as the angular distributions, are given in Refs. [4,17]. Elastic *NN* cross sections are of course taken directly from experiment. The $NN \to N\Delta$ cross section is taken as equal to the experimental inelastic *NN* cross section (*pp* and *np*, the *nn* cross section is taken equal to the *pp* cross section). The $N\Delta \to NN$ cross section is taken from the previous one by detailed balance:

$$\sigma_{N\Delta\to NN}(s) = f_{corr}\,\frac{1}{2}\left(\frac{p_{NN}}{p_{N\Delta}}\right)^2 \frac{1}{1+\delta_{NN}}\,\sigma_{NN\to N\Delta}(s)\,. \tag{10}$$

In this equation, valid for definite charge states of the particles, *pab* is the momentum of the particles in the c.m.

$$p_{ab} = p_{ab}(s) = \frac{\left[\left(s-(m_a+m_b)^2\right)\left(s-(m_a-m_b)^2\right)\right]^{1/2}}{2\sqrt{s}}\,, \tag{11}$$

the ½ factor comes from the spin degeneracies and the Kronecker symbol applies to the isospin states of the nucleons. In INCL4, a definite value of the mass is ascribed to the Δ-isobar (see below), which makes *pNΔ* well defined. However, detailed balance breaks down for unstable particles. Arguments are given in Ref. [4], which show that the effect of the unstable isobar can be approximated by the use of a correction factor $f_{corr} = \exp(t_{coll}/\tau_\Delta)$ involving the collision time and the Δ lifetime. The former is not well known, but is of the order of 1-2 fm/c. More or less accordingly, in INCL4.2, f_{corr} is put equal to 3.

The $N\Delta \to N\Delta$ and $\Delta\Delta \to \Delta\Delta$ cross sections are taken as equal to the *NN* elastic cross section at the same cm energy.

(b) Generation of the final state. The collision is realized in the cm frame. The 4-momenta of the initial particles are Lorentz-transformed in the cm frame. The cm relative momentum *q* in the final state is calculated by Eq. (11) for the two outgoing particles. For Δ-creating reactions, the mass of the isobar should be determined first. It is taken at random according to the following distribution

$$f(m_\Delta) = F_N \frac{q^3}{q^3 + q_0^3} \frac{1}{1 + 4\left(\frac{m_\Delta - m_\Delta^0}{\Gamma_0}\right)^2}, \tag{12}$$

subject to kinematical constraints: the Δ-mass should be larger than $mN + m\pi$ and smaller than $\sqrt{s} - mN$ (otherwise the available energy is not sufficient). If these conditions are not fulfilled, new random generations are performed repeatedly, until they are satisfied. In Eq. (12), F_N is a normalization constant, q_0=180 MeV/c, m_Δ^0= 1215 MeV and Γ_0=130 MeV. The introduction of the *q*-dependent factor can be justified as follows: a Δ resonance can be viewed as a πN correlated system and the phase space of the latter is considerably reduced when the cm energy is low. The form of *q*-dependent factor is also inspired from the πN elastic cross section.

The direction of the outgoing particles (in the cm) are determined according to the experimental angular distributions, as far as possible. The polar angle, relative to the incident direction is taken at random according to distributions which parametrize cm differential cross sections (see Refs. [15,17]). The azimuthal angle is determined at random. The 4-momenta of the outgoing particles are Lorentz-transformed back in the target frame.

For the $NN \to N\Delta$ reaction, the description of the final state is completed with the determination of the Δ-lifetime and of its helicity. The intrinsic lifetime *t0* is determined stochastically according to an exponential law with a mean of $\tau_\Delta = \hbar / \Gamma_0$. The actual lifetime t_Δ is corrected as

$$\frac{1}{t_\Delta} = \frac{1}{\gamma} \frac{q^3}{q^3 + q_0^3} \frac{1}{t_0} \tag{13}$$

where the first factor is the inverse of the Lorentz factor for the motion of the isobar in the target frame and where *q* is the relative momentum of the pion and the nucleon in the rest frame of the isobar (given by Eq. (11)). The second factor is motivated by the reduction of phase space. The helicity $h = \vec{p} \cdot \vec{s} / |\vec{p}| \cdot |\vec{s}|$ (involving momentum and spin), considered as a classical quantity, is taken at random with a distribution proportional to $\cos^2\theta$, where θ is the angle between the incident direction and the one of the outgoing isobar. The helicity, which is not supposed to change in further (elastic) collisions, will govern the eventual decay of the isobar.

Let us turn to the treatment of the $\pi N \to \Delta$ reaction. The cross section is taken as the experimental πN total cross section and parametrized as follows. The $\pi + p$ cross section is given (in mb) by

$$\sigma_{\pi^+ p} = \frac{326.5}{1+4\left(\frac{\sqrt{s}-1215}{110}\right)^2}\frac{q^3}{q^3+180^3}, \qquad (14)$$

where q (in MeV/c) is the cm relative momentum, given by Eq. (11), and where the cm energy is in MeV. The other πN cross sections are derived by isospin symmetry. Here the generation of the final state is very simple. It consists in creating an isobar with a 4-momentum equal to the sum of the 4-momenta of the pion and the nucleon. Its 3rd component of the isospin is also the sum of the ones of the two incident particles. Finally, its lifetime is generated in exactly the same way as described above and its helicity is taken equal to 1. In INCL4, the $\pi N \to \Delta$ reaction is allowed if the cm energy is larger than 1117 MeV (slightly above the physical threshold) and is smaller than 3 GeV. It is supposed to be elastic only. Above 1500 MeV, the intrinsic average lifetime is taken $\hbar/200\,\mathrm{MeV}$.

D. 2 Reflection/Transmission

At the time foreseen for this kind of avatar, the particle (nucleon or Delta) is sitting on the boarder of its potential well (whose radius depends upon its energy). If its kinetic + potential energy is negative, the particle is reflected. If it is positive, the particle will be transmitted with a probability equal to

$$T = \frac{4kk'}{(k+k')^2}e^{-2G}, \qquad (15)$$

with

$$G = \frac{mzZ_N e^2}{\hbar^2 k'}\left(ar\cos x - x\sqrt{1-x^2}\right), \quad x = \frac{T'}{B}, \qquad B = \frac{zZ_N e^2}{R_0}, \qquad (16)$$

if $x<1$ (below the barrier B) , and $G=0$, if $x>1$ (above the barrier B). In these equations, k and k' are the momenta of the particle before and after transmission, m and z are the mass and charge of the particle, Z_N is the current charge of the target (at the time of the avatar), T' is the asymptotic kinetic energy after transmission and R_0 is the radius of the density distribution. The transmission probability (Eq. (15)) is taken as the product of the transmission of a Schrödinger (plane) wave on a potential step and of the semi-classical (JWKB) transmission probability through a Coulomb barrier $V(r) = B\,R_0/r$, for $r > R_0$, $V(r) = 0$ for $r < R_0$.

When the particle is transmitted, it keeps its direction of motion (there is no refraction). The kinetic energy is changed as $T' = T - V_0$, and the momentum is changed accordingly. Once it is transmitted, the particle is "frozen": it leaves the "interaction volume". Actually, it receives a tag which tells that it should not be considered for further interaction: it will not be accepted any more for the evaluation of the times for future avatars. That is why it receives its asymptotic kinetic energy T' readily. If the particle does not succeed the test for transmission, it is reflected. The times corresponding to this particle are removed from the list of times and new ones (for future avatars involving this particle) are added. See Ref. 5 for a discussion about reflection and refraction.

When the incident particle is a light ion, one can find a slightly different type of avatar, corresponding to the entrance of a nucleon in the "interaction volume". It is reminded that at t=0, only one nucleon is at the boarder of this volume, the other ones being outside. For the latter ones, the time for the entrance is calculated by Eq. (10), where the plus sign is replaced by a minus sign. Reflection is not considered for this kind of avatar. When entering the "interaction volume", the kinetic energy of the nucleon is changed by adding the depth of the potential. The direction is not changed and the momentum is modified accordingly. After the entrance, the list of times is re-actualized in exactly the same way as for the escape of a particle.

D.3 Decay of a Δ particle

At the end of its foreseen lifetime, a Δ-isobar is forced to decay. The decay is performed in the rest frame of the isobar: the pion and the nucleon have opposite momenta (absolute value given by Eq. (11) with $\sqrt{s} = m_{\Delta}$) and the direction is taken at random with the probability law $P(\theta) \propto 1 + 3h\cos^2\theta$, where θ is the angle between the direction of the isobar (in the lab frame) and the direction of the outgoing pion (the azimuthal angle is chosen completely at random). The 4-momenta of the outgoing particles are Lorentz-transformed back in the target frame. The charge states of the pion and the nucleon are determined in agreement with the isospin Clebsch-Gordan coefficients. The list of the times is updated as described before.

E. Pauli blocking

Due to the fermionic nature of the particles, the collision probability may be diminished as a consequence of the Pauli principle. Although it is a purely quantum effect, the reduction may fortunately be expressed in terms of phase space density. In INCL4, Pauli blocking is implemented in this spirit.

Let us discuss first the case of two body collisions $a + b \rightarrow c + d$ with two nucleons in the final state and let $\vec{r}_i$ and $\vec{p}_i$, $i = c, d$, the positions and momenta of the nucleons just after the realization of the collision (the avatar). Phase space occupation probabilities *fi* are estimated by counting the nucleons lying in phase space in a small test volume centered of the representative point of nucleon *i* in phase space. They are given by:

$$f_i = \frac{1}{2}\frac{(2\pi\hbar)^3}{\frac{4\pi}{3}r_{PB}^3\frac{4\pi}{3}p_{PB}^3}\sum_{k\neq i}\theta\left(r_{PB} - \left|\vec{r}_k - \vec{r}_i\right|\right)\theta\left(p_{PB} - \left|\vec{p}_k - \vec{p}_i\right|\right), \qquad (17)$$

where the summation runs over nucleons of the same isospin state as nucleon *i* and where θ is the Heaviside function. The factor ½ stands for spin degeneracy (nucleon spin is not considered). The parameters r_{PB} and p_{PB} define the size of the test volume (an hypersphere) in phase space. They should not be too small, otherwise the estimated occupation probability can be vanishing almost all the time and they should not be too large, otherwise the variations of the occupation probability in the occupied phase space can be missed. In INCL4, r_{PB} and p_{PB} have been taken just large enough for results (in typical cases) to be more or less insensitive to moderate modifications on these parameters: r_{PB} =3.18 fm and p_{PB} = 200 MeV/c, which corresponds to ~2.3 natural units of phase space. We remind that in the ground state of normal nuclear matter there is one nucleon (of given spin and isospin) per natural unit. It is generally considered that there cannot be more than one particle per unit phase space in

any circumstance and that this density is more or less achieved in the ground state of actual (at least heavy) nuclei.

The collision will be allowed stochastically with a probability $P = (1 - f_c)(1 - f_d)$. Pauli blocking is not applied to Δ-isobars (for a collision with a Δ and a nucleon in the final state, there is only one blocking factor). On the other hand, it is enforced for nucleons issued from Δ-decays.

The interplay between this stochastic implementation of the Pauli blocking, the evaluation of the phase space density by Eq. (17) and the fluctuations of the phase space occupancy, inherent to any model with a stochastic generation of the initial state, may introduce unphysical effects, unless sufficient care is exercised. In any particular event, the initial phase space is not uniformly populated and displays "clumps" and "holes". If several nucleons are clumped in a test volume, the quantity f_i may be larger than 1. In such a case, it is put equal to unity. Let us consider the possible effect of a hole in the momentum Fermi sphere. With the procedure described above, the first collision may bring a nucleon into this hole from a higher energy occupied state, creating so a *negative* excitation energy. In order to avoid such an annoying feature, a procedure referred to in Ref. [4] as CDPP (for Consistent Dynamical Pauli Principle) has been implemented. The latter centers on the energy content of the current Fermi sphere. As shown in Section 2.3, the excitation energy of the target may be written as a sum of two terms: one which corresponds to the nucleons which have been promoted above the Fermi level (and which therefore is positive) and a term *ECDPP* which corresponds to the rearrangement of the remaining Fermi sphere and can be considered as the excitation of this remaining Fermi sphere. At each possible collision, after the test on the Fermi blocking is passed successfully, the quantity *ECDPP* is checked for the possible final state. The collision is blocked if *ECDPP* is negative (this check is also done after a Δ-decay, but not after a reflection/transmission, the energy content of the Fermi sphere being not changed in that case). Doing so, the remaining Fermi sphere can only have positive excitation energy. A fortiori, the remaining target (i.e. the baryons inside the "interaction volume") can only have positive excitation energy, in spite of the deficiencies of the implementation of the "statistical" Pauli blocking.

F. End of the cascade

An original feature of INCL4 is the consistent determination of the stopping time, i.e. the time at which the cascade should be stopped. A criterion has been adopted which is based on physical results concerning the time-dependence of several key physical quantities when averaged over events. Examples are given in Fig. 3 below.

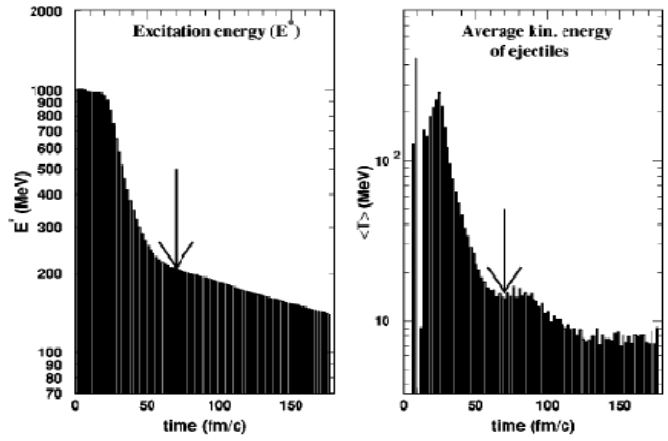

Fig. 3 Time evolution of the excitation of the target nucleus (left) and of the average kinetic energy of the ejectiles (right), as given by averaging over a few thousand events. The results correspond to collisions of 1 GeV protons with 208Pb nuclei at an impact parameter of 4 fm.

One can see that both the excitation energy of the target nucleus and the average kinetic energy of the ejectiles assume large values at early times, decrease rapidly until some time, after which they vary much more slowly. Other quantities (not shown), in particular the anisotropy of the momentum distribution of the participants sitting inside the target, offer a similar pattern with a rapid variation followed by a much slower one. For all of them, the change of regime occurs *at the same time*, defined within a few fm/c. This observation suggests that the regime of fast variation, typical of a cascade, gives place at a rather well-defined time to a regime of softer variation, typical of an evaporation. This feature is also in strong support of skipping an pre-equilibrium module between cascade (at least INCL4.2 with its proper stopping time) and evaporation. We refer to Refs. [4,15,18] for elaboration on this point. In INCL4, the cascade is stopped at this common time, called the stopping time t_{stop}. It has been sampled once for all and parametrized as

$$t_{stop} = f_{stop} t_c \left(\frac{A_T}{208} \right)^{0.16} \tag{18}$$

with f_{stop} =1 and t_c =70 fm/c. This parametric form seems reasonable for the range of energy and target mass under interest, but may be improved at the border of this range, by using another value for f_{stop}. All the results labelled as "INCL4.2" correspond to the standard value of this parameter.

An event is stopped when the clock for a foreseen avatar gives a time larger than t_{stop}. Some events may be stopped earlier. An event may be stopped at the very beginning, if the initial time list for the collision avatars is empty. This happens mainly for peripheral events. Such a event is named a *void event*. An event may also terminate at a time earlier than t_{stop} if the list of times becomes empty when it is updated. In a no-void event, it may happen that no collision has taken place (due to Pauli blocking for instance) and that the incident particle has left the interaction volume with its incident energy. Such events, together with the void events are named "transparent event". The other events are called "interacting events".

Transparent events are just disregarded (but they are counted for cross section evaluation, see later). The other events, after they are stopped, may possibly be completed by the decay of the

remaining Δ-isobars, if any. The Pauli blocking is not applied in this case and the resulting nucleons are considered as belonging to the remnant.

The description of the final state is delayed to Section 2.4

2.3. Conservation laws

It is instructive to detail how INCL4 handles conservation laws. In the energy range of interest, the most important conservation laws can in general be formulated as follows:

$$A_P + A_T = A_{ej} + A_{rem} \tag{19}$$

$$Z_P + Z_T = Z_{ej} + Z_\pi + Z_{rem} \tag{20}$$

$$\vec{p}_P + \vec{p}_T = \vec{p}_{ej} + \vec{p}_\pi + \vec{p}_{rem} \tag{21}$$

$$T_P = K_{ej} + W_\pi + T_{rec} + E^* + S \tag{22}$$

$$\vec{l}_P = \vec{l}_{ej} + \vec{l}_{rem} + \vec{l}^* \tag{23}$$

for baryon number, charge, momentum, energy and angular momentum, respectively. We consider a projectile *P* colliding with a target *T* and generating baryonic ejectiles, pions and a remnant (the remaining nucleus at the end of the cascade). For the sake of simplicity, we have assumed that the interaction between the several bodies at the end of the cascade is negligible. In addition, we have disregarded intrinsic spins and we have neglected the production of other particles than those introduced in INCL4. In Eq. (22), K_{ej} is the kinetic energy of the ejectiles, W_π is the total energy of the pions, T_{rec} is the recoil energy of the remnant, E^* is the excitation energy of the remnant and *S* is the separation energy (i.e. minus the *Q*-value of the reaction). Strictly speaking, energy conservation law should include rest mass energies. They have been eliminated from Eq. (22) owing to the use of Eq. (19). The other notations are self-explanatory.

In INCL4.2, conservation laws (19) and (20) are exactly fulfilled. Eq. (20) is strictly equivalent to the conservation law for the 3rd component of the isospin. Eqs. (21,22) need be commented. Let us for the moment neglect the recoil energy. The different terms of the rhs of Eq. (22) have a well-defined meaning within the INCL4.2 model, in terms of the quantities handled by this model. In addition, since there is no interaction energy in INCL4.2 between the ejectiles, the baryons inside the interaction volume and the pions, decomposition (22) holds at any moment during the cascade. Indeed, one can write, for any time during the cascade

$$T_P + \sum_{i \in A_T} \left(T_i^0 - V_0 \right) = \sum_{j}^{A_{ej}} \overline{T}_j + W_\pi + \sum_{i \in A_{rem}} \left(\overline{T_i} - V_0 \right), \tag{24}$$

where the sums run over the target nucleons in the initial state, the ejectiles and the baryons remaining in the interaction volume, respectively, and where the bar means that the Δ-nucleon mass difference has been added to the kinetic energy for the isobars (which are supposedly not present any more at the end of the cascade, when Eq. (22) applies). The

quantities T_i^0 are the initial kinetic energies of the target nucleons. In INCL4.2, the interaction volume is fixed and there is no recoil energy. Eq. (24) can be rewritten as

$$T_P = \sum_k^{A_{ej}} \overline{T_k} + W_\pi + \left\{ \sum_{j \in A_{rem}} \overline{T}_j - \left[\sum_{i \in A_T} T_i^0 - \left(A_T - A_{rem}\right) T_F \right] \right\} + \left(A_T - A_{rem}\right)\left(V_0 - T_F\right), \qquad (25)$$

where *TF* is the Fermi kinetic energy. The last term is the minimum energy required to extract $AT - Arem$ nucleons and can be identified as the separation energy *S* (in the model). Consequently, the term inside the curly bracket is nothing but the excitation energy E* (in the model). This term can still be rewritten as

$$E^* = \sum_{j \in A_{rem}, p_j > p_F} \left(\overline{T}_i - T_F\right) + \left\{ \left(\sum_{j \in A_{\min}, p_j \le p_F} \overline{T}_i \right) - \left[\sum_{i \in A_T} T_i^0 - \left(A_T - A_{rem}^F\right) T_F \right] \right\}, \qquad (26)$$

where A_{rem}^F is the number of nucleons in the remnant with momentum less than the Fermi momentum. The quantity in the square bracket is the ground state energy of the current Fermi sea. The term in the curly bracket is identified as the excitation energy of the current Fermi sea, i.e. the quantity *ECDPP* discussed above.

In the INCL4.2 model, energy is conserved exactly, since it is conserved during the collisions and at the entrance and the exit of the interaction volume (but without recoil energy). On the contrary, momentum and angular momentum is not conserved. Momentum is conserved during collisions but not at the entrance or exit of particles. Angular momentum is not conserved, even at the level of the collisions. See however Ref. [3] for a discussion of this topic. However, the results of the cascade can be used to evaluate with reasonable accuracy the momentum, angular momentum and recoil energy of the remnant. The lack of momentum conservation mainly arises from the treatment of transmission of particles at the surface. Suddenly, a particle is emitted with (sometimes a large) momentum $\vec{p}$, without any counterpart. It is not easy to know how to correct for this since it may depend very much upon the dynamics leading to the emission. The simplest thing would be to give an opposite recoil momentum to the nucleus, keeping the same available energy. The momentum of the ejectile relative to the nucleus will then be $\simeq \left(1 - 1/\left(2A_{rem}\right)\right)\vec{p}$. Recoiling the whole remnant (plus the average potential) is technically difficult. But, one can see that the momentum of the ejectiles is estimated in the model with an error of the order of 1/(2A). Therefore, the quantity

$$\widetilde{\vec{p}}_{rem} = \vec{p}_p - \vec{p}_{ej} - \vec{p}_\pi \qquad (27)$$

evaluated with the results of the model yields the remnant momentum with an accuracy of the order of 1/(2A). The corresponding recoil energy

$$\widetilde{T}_{rem} = \sqrt{\widetilde{\vec{p}}_{rem}^{\,2} + M_{rem}^2} - M_{rem} \qquad (28)$$

gives already a good evaluation of the recoil energy of the remnant. It should be stressed that even if $\widetilde{\vec{p}}$ can be large part of $\vec{p}_p$, $\widetilde{T}_{rem}$ (of the order of 1 MeV) is always very small compared to the other terms of Eq. (22). Nevertheless, in INCL4.2, an effort has been done to include the approximate recoil energy, still managing the energy balance. The recoil energy is first evaluated through Eqs. (27,28). This quantity is then included in the rhs of Eq. (26) and the

momenta of the ejectiles and the pions are multiplied by a factor *f0* in order to balance the two sides of the equation. The modified momenta are then used to re-evaluate $\tilde{\vec{p}}_{rem}$ and $\tilde{T}_{rem}$ through Eqs. (27,28). The new recoil energy is introduced in the final energy and the momenta of the ejectiles and pions are multiplied by *f1* in order to balance the two sides of Eq. (26) again, and so on. Two iterations are performed, which is largely sufficient.

The internal angular momentum of the remnant is also evaluated by difference:

$$\tilde{\vec{l}}^{*} = \vec{l}_P - \vec{l}_{ej} - \vec{l}_{\pi} - \vec{l}_{rem} \tag{29}$$

where the last term is evaluated as $\vec{l}_{rem} = \vec{R}_{rem} \times \tilde{\vec{p}}_{rem}$, $\vec{R}_{rem}$ being the position of the barycenter of the remnant. It is argued in Ref. [4] that Eq. (29) provides a good estimate, which follows to some extent from the accuracy of the calculated momentum transfer.

2.4. Description of the final state

The output data of a cascade event contain:

1. the type of event: transparent event, absorption (no outgoing particle), non-transparent event (with the number of emitted particles)

2. for each of the emitted particles, the following quantities are recorded:

    1. type of emitted particle

    2. kinetic energy (in MeV)

    3. the three direction cosines

    4. for the remnant: mass number, charge, excitation energy, recoil energy, direction cosines and intrinsic angular momentum (in units of ħ; absolute value and direction cosines).

When coupled to an evaporation model, the output of a (complete) event contains in addition the same information for the evaporated particles and the properties of the final residue. These information are recorded in an *n-tuple*. *n-tuples* can be handled "off-line" by PAW++ to generate physical results.

Evaluation of cross sections is done by standard means. The total inelastic (reaction) cross section is given by:

$$\sigma_R = \pi b_{\max}^2 \left(1 - N_{transp} / N_{run}\right) \tag{30}$$

where N_{run} is the total number of runs and N_{transp} the number of transparent events. Differential cross sections can be formulated as:

$$\frac{d\sigma}{d\varpi} = \pi b_{\max}^2 \frac{N_{i \in d\varpi}}{N_{run} d\varpi}, \tag{31}$$

where $d\varpi$ is the relevant element of phase space and $N_{i \in d\varpi}$ is the cumulated number of relevant particles belonging to this element.

3. A short account of the INCL4.4 model

Here we turn to the recent developments of the INCL4 model that has been added to INCL4.2 to form the INCL4.4 model, as explained in the introduction. Due to lack of space, we only give a sketchy description of the most important features.

3.1. Isospin and energy-dependent potential for nucleons

The motivation for this development is rooted in the phenomenology of the optical model (and of the shell model), which indicates that the depth of the average nuclear potential depends upon the isospin of the nucleons and decreases more or less linearly when the energy of the nucleon increases until it reaches roughly 200 MeV (kinetic energy). At this value, the potential basically vanishes. Above, it remains very small. Accordingly, an isospin and energy-dependent potential for nucleons has been introduced. Square wells with momentum-dependent radius are still used, as before. Inside this radius, the value of the potential is a function $V(\tau,E)$ of the isospin and the total energy E. One now has:

$$E = T + V(\tau,E) = \frac{\hbar^2 k^2}{2M} + V(\tau,E) \tag{32}$$

Following Refs. [19,20], the following form is used

$$V(\tau,E) = V_0(\tau) + \alpha_\tau \left(E - E_F^\tau\right), \qquad \text{for } E < E_0^\tau,$$

$$V(\tau,E) = 0, \qquad \text{for } E > E_0^\tau, \tag{33}$$

where E_F^τ is the Fermi energy and E_0^τ is the energy at which the rhs in the first line vanishes. For the sake of consistency, the Fermi momentum should also depend upon isospin, in order to have roughly the same Fermi energy for protons and neutrons, which is required by β-stability. The Fermi momenta are determined by

$$\left(\frac{k_F^n}{k_F^p}\right)^3 = \frac{N}{Z}, \quad \frac{1}{3\pi^2}\left[\left(k_F^n\right)^3 + \left(k_F^p\right)^3\right] = \rho_0 \tag{34}$$

translating the fact that neutron and proton densities are proportional to neutron and proton mass numbers and sum to ordinary nuclear density. The parameters α_τ in Eq. (33) are taken as $\alpha_p = \alpha_n = 0.23$, following Ref. [19]. Finally, the quantities $V_0(\tau)$ are determined by requiring

$$E_F^\tau + T_F^\tau + V_0(\tau) = -S_\tau, \tag{35}$$

where *S* is the separation energy. The potential for Δ-isobars is kept energy-independent but does depend upon the isospin, with a linear dependence which matches the one for protons and neutrons. The potential depth for the Δ-isobars is determined by assuming that, for the same isospin, it is equal to the nucleon potential at the Fermi energy.

The implementation of such a potential somehow complicates the realization of collisions. Indeed, for collisions $a + b \to c + d$, the energy conservation now writes

$$E_a + V_a + E_b + V_b = E_c + V_c + E_d + V_d \tag{36}$$

in the rest frame of the potential (or the target). It is proceeded as follows. The initial free 4-vectors $(E, \vec{p})$ are Lorentz-transformed into the usual cm frame (as before). The corresponding final 4-vectors in this frame are determined, as usual, i.e. conserving momentum and free (kinetic) energy. This would be the normal procedure if there were no potential. Let p* be the momentum of the particles in the cm. Let us consider now these 4-vectors after multiplication of p* by a factor f* (and, of course, after modification of the energy component to be consistent with the cm energy). These modified 4-vectors are Lorentz-transformed back in the target frame and inserted in Eq. (36), which appears then as an algebraic equation for f*. So the new energy conservation law is fulfilled owing to solution of this algebraic equation. It turns out that f* is always rather close to unity. This may suggest that the energy-dependence of the potential has minor effects. Actually, the effect may be significant when, in a collision, nucleons changes substantially their individual energy. Of course, it is expected that there are compensating effects in other collisions. It is therefore no surprise that the effect of the energy-dependence is noticeable for charge-exchange quasi-elastic and quasi-inelastic events (see ref. [18]).

3.2. Average potential for pions

A difficulty arises here. The phenomenological optical-model potential for pions is badly determined in the nuclear volume, because of the strong pion absorption. Propagating pions are not therefore good quasi-particle excitations. Furthermore, what is needed is the potential energy of a pion created at any moment of the multiple scattering process (involving successive creations and absorptions of pions), which of course cannot be revealed by elastic scattering experiments to which the optical model applies. Finally, the largest part of the pion-nucleon interaction proceeds to Delta formation, which is explicitly accounted for in INCL. In view of these considerations, a pragmatic approach has been adopted. A square well potential is chosen with a radius of $R_c = R_0 +$ 2fm, a range somehow consistent with the properties of the empirical pion potentials. More precisely, the following form is used:

$$V(r,\tau) = V_t(\tau) = V_N(\tau) + \overline{V_C}\,, \qquad \text{for } r < R_c\,, \tag{37}$$

$$V(r,\tau) = V_C = \frac{Z_T \tau e^2}{r}\,, \qquad \text{for } r > R_c\,,$$

where τ is the 3rd component of the pion isospin. The nuclear part VN and the average Coulomb part $\overline{V_C}$ are given by

$$V_N(\tau) = V_N^0 + V_N^1 \tau\xi\,, \qquad \overline{V_C} = 1.25\frac{Z_T \tau e^2}{R_0} \tag{38}$$

where $\xi = (N\text{-}Z)/A$ is the asymmetry parameter of the target.

The parameters V_N^0 and V_N^1 have been determined by a rough fit to experimental data concerning reactions with pions as incident or produced particles. The following values have been so obtained: V_N^0 = -30.6 MeV and V_N^1 = -71.0 MeV, rather consistently with the phenomenological values of the pion potential in the nuclear surface.

Pions are now considered as participants. They are subject to transmission or reflection at the boarder of their nuclear potential (using formulae (15,16)) and they do not interact any more after leaving this potential.

The introduction of the pion potential considerably improves the predictions of INCL4 for the pion production cross sections, but also, to a lesser extent, for other observables. See Refs. [11,18] for more detail.

3.3. Production of light charged clusters

The introduction of this production is based on the idea that a nucleon escaping from the nucleus can drag with him other nucleons which are sufficiently close (in phase space), and form an emitted light charged cluster. The following procedure has been introduced:

1. When a nucleon hits the surface and satisfies successfully the test for emission (sufficient energy), it is checked to see whether it can belong to a cluster. A candidate cluster is constructed, starting from the considered nucleon, by adding a second, then a third, etc, nucleons which are sufficiently close in phase space. The following proximity criterion is adopted:

$$r_{i,[i-1]}\, p_{i,[i-1]} \leq h \quad , \tag{39}$$

   where the quantities in the lhs are the Jacobian coordinates, i.e. the relative spatial and momentum coordinates of nucleon *i* with respect to the subgroup consisting of the first *i-1* nucleons, and where *h* is a parameter. The following light clusters are considered for the moment: *d, t,* ^{3}*He,* ^{4}*He*. Δ-isobars are not supposed to be included in clusters.

2. Fast nucleons being checked for emission at *R(pF)*, in the very outskirts of the nuclear surface, where the density is practically vanishing, they are moved back along their direction of motion until they sit at a radial distance $R_0 + D$ (One is forced to check for emission of nucleons at large radial distance, because possible collisions even in the periphery of the nucleus cannot be precluded). In order to avoid problems with tangential emission, clusters are considered only if the cosine of the angle between their emission direction and the radial direction is larger than a certain value, taken as 0.7.

3. The cluster with the lowest "excitation energy" is selected. The relevant parameter is $\left(\sqrt{s} - B\right)/A$, where $\sqrt{s}$ is the c.m. energy of the cluster, *B* its nominal binding energy, and *A* its mass number.

4. For being emitted, the selected cluster should fulfil two requirements. First, its total kinetic plus potential energy, corrected by the nominal binding energy should be positive, owing to which a cluster with positive kinetic energy can be emitted. Second, it has to succeed the test for penetration through the Coulomb barrier, given by Eqs. (16,17). If these conditions are not met, the "leading" nucleon is emitted, provided it succeeds the Coulomb penetration test.

Let us notice that this procedure is slightly different from the one described in Ref. [9] and used in INCL4.3. In the latter, only one cluster for each species was constructed and a hierarchy for the possible emission was established, favoring emission of heavier clusters. See Ref. [9] for more detail.

The procedure described above looks like a surface coalescence model and retains some well established features: the small probability for existence of clusters in the nuclear volume and the necessary dynamical generation of clusters in the surface from "pre-existing" clusters. It contrasts with the ordinary coalescence model: clusters can be emitted at any time and their properties are not directly linked with the final nucleon spectra. It contains two parameters: *D* and *h*. They have tentatively been determined by a rough fit to experiment. The extracted values are *D*=2fm and *h*=387 MeV fm/c.

This model cures evidently a serious shortcoming of INC models. Furthermore, it gives surprisingly good results, at least for sufficiently high enough incident kinetic energy. See Ref. [9] for detail. To extend this model at lower energy, variation of the parameters and modification of the scenario are presently envisaged [14].

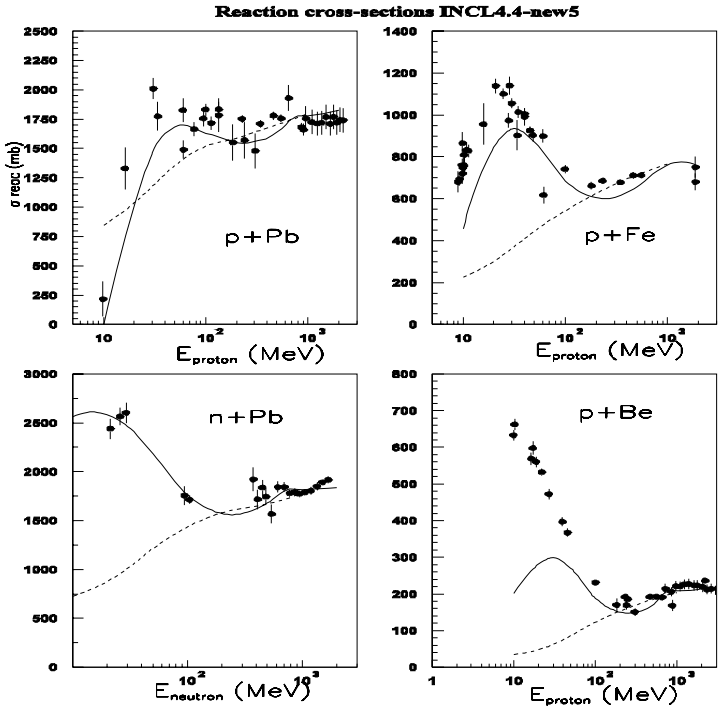

Fig. 4. Comparison of the predictions of INCL4.2 (dashed-lower lines) and of INCL4.4 (full upper lines) with the experimental total reaction cross sections (collected from Refs.[23,24]).

3.4. Extension to low energy

The conventional wisdom expresses that the INC approach is valid in the classical (non quantum) independent collision regime, which roughly requires that the following condition is fulfilled:

$$\lambda\!\!\!^{-}_{B} << r_s < d \,, \tag{40}$$

where $\lambda\!\!\!^{-}_{B}$ is the de Broglie wavelength for the relative motion, r_s is the range of the nuclear forces and *d* is the average distance between neighbouring nucleons. These conditions are only marginally satisfied (and for the first collisions only) for incident energy above 200 MeV. Yet, INC models do not seem to yield crazy results at lower energy. Even, it was shown in Refs. [12,21] that INCL4.2 can reproduce surprisingly well neutron and proton spectra at as low incident energy as 50 MeV, where important quantum motion effects are expected. There is no real explanation to this paradox. See however Ref. [22] for an interesting discussion.

The most important deficiency of INC4.2 at very low energy lies in the fact that it is unable to reproduce the rise of the total cross section just above the Coulomb barrier. The latter is

usually interpreted as due to the interplay between the rise of the *NN* cross section and the variation of the penetration through the Coulomb barrier. Several ways of curing this defect have been investigated recently [14], resulting in a much better prediction of the total reaction cross section, as shown in Fig.4. Because of lack of space and because these developments are still under investigation, we cannot give much detail here. Let us just mention that the quantity cut_{NN} has been removed (set to zero) for the first collision, Coulomb distortion in the entrance channel has been introduced and corrections have been introduced to compensate for the too large momentum content of the target surface (see Section 2.2.A). One may wonder why cut_{NN} has been removed whereas we have insisted on cutting soft collisions. In fact, soft collisions do not perturb very much the nucleon motion and it is then natural (or acceptable) to consider that their effect is mainly taken into account by the average potential. However, the total reaction cross section is determined by the first collision inside any event. Whether the first collision is soft or hard does not matter, inasmuch a soft collision can be followed by a harder one. It is then indicated to consider first soft collisions totally.

The last modification deals with collisions occurring in the nuclear surface. As we said in Section 2.2.A, the target nucleons moving in this region have a large energy (in the allowed [*0, TF*] interval). They have also a large momentum. This results from the use of square well potentials. It is generally considered that, in reality, these nucleons have a large energy but a low momentum, in accordance with the shell-model, which uses a smooth Saxon-Woods-like potential. Let us now consider the collision between an incident low-energy nucleon and one of these surface target nucleons. If the cross section depends upon the relative momentum, the latter is probably overestimated in INCL4.2 and the cross section is consequently underestimated. To compensate for this, a new procedure have been introduced, which realizes the collision with the momenta of the particles in a smooth potential, defined as having the same classical turning points as the one used in INCL4.2. The latter is implicitly given by

$$V(r) = V(r = R(p)) = -V_0 + \frac{\left[p = R^{-1}(r)\right]^2}{2m}, \tag{41}$$

where R^{-1} is the inverse of the function *R(p)*. In practice, the modified momenta are calculated, by using this potential. The collision is realized with this kinematics, including the evaluation of the cross section, and the final momenta and energies are calculated after restauration of the original INCL4.2 potential, guaranteeing so the conservation of energy. It is easy to see that this modification has no effect when the collisions occurs in the interior (the potential defined by Eq. (41) is practically equal to $-V_0$ in this region) or when the collision occurs at high energy. One should also realize that this procedure has to do with the extrapolation of the experimental cross sections to off-shell particles. The original procedure of INCL4.2 supposes that the cross sections should be extended according to the cm energy, whereas the new procedure is better suited if they have to be extended according the momenta of the particles. More details are given in Ref. [15].

One has to stress that, even if the modifications described in this subsection are motivated by the behaviour of INCL4.2 at low incident energy, they have been implemented for any incident energy. It is easy to see that they are only effective at low energy.

3.5. Other modifications

Other minor modifications have also been introduced in the meantime. Let us mention two of them:

1. The strict Pauli blocking has been introduced on the first collision. This seems to be the best compromise which minimizes the problems inherent to the statistical implementation, partly cured by the CDPP procedure (see Section 2.2.E), and accounts nevertheless for the depletion of the Fermi sphere. More detail can be found in Ref. [21].

2. Events are terminated at t_{stop} (see Section 2.2.F) or when all the particles have energies below the Fermi energy plus a constant energy, taken as 10 MeV, if this occurs earlier. In such a situation, it is expected that the system will basically evolves by evaporation. This new procedure has been adopted because the results are basically unchanged, while the computation time is reduced by 25%.

4. Outlook

We have presented an analytical description of the recent versions of the INCL model, trying to present the features of the physics included in this model, the various assumptions and some technical points, which are nevertheless important to understand how the numerical simulations are working.

The standard version INCL4.2 is basically a parameter free version. In the numerical code, there are only two physical parameters: the potential depth *V0* and the nucleon separation energy. These are not really free parameters, as it is indicated to use phenomenological values for these parameters. There are also options allowing to use a more or less diffuse surface, to vary the stopping time (through the parameter *fstop*) and to adopt alternative versions of the Pauli blocking (like the strict Pauli blocking), enabling the user to have an idea of variations of the model. But it should be stressed that what is referred to as the INCL4.2 model corresponds to the standard choice described in this paper.

We did not discuss the performances of INCL4.2. For this, we refer to Ref. [4]. One has to keep in mind that if some observables constrain the INCL model alone (total reaction cross section, high-energy particle spectra), many others constrain INCL and the de-excitation model to which it is coupled, at the same time. The good performances of INCL4.2 for the second kind of observables have been obtained thanks to the coupling to the standard version of the ABLA model (named KHSv3p, see Ref.[4]). They have to be confirmed with the new version of ABLA [6] or with another evaporation-fission model.

Model INCL4.4 has been developed to cure some shortcomings of INCL4.2 (lack of cluster emission), to introduce mandatory features of nuclear dynamics (energy-dependent average potential for nucleons and average potential for pions) and to improve the performances, especially at low energy. Inclusion of new features was done by relying as much as possible on known physics rather than on free parameters. Developments are still in progress, but it is likely that achieving a good description of more and more observables in a more and more extended domain will not be possible with a little dose of free parameters. We have particularly in mind the production of clusters, which is expected to proceed differently at high or low incident energy and in heavy or light nuclei. Preliminary results seems to indicate that the goal could be reached with a satisfactorily low level of fitting procedure [14,25].

We did not really discuss the justification of the assumptions of the model, nor the general theoretical foundation of the model, which is still in embryo for the time being. See Ref. [15] for a discussion of this point.

ACKNOWLEDGEMENTS

We want to thank all the people with whom we had the pleasure to collaborate on the developments of the Liège Intranuclear Cascade model since the beginning and, in particular, those who have contributed to INCL4 in the recent years: Thierry Aoust, Pierre Henrotte, Sylvie Leray, Sophie Pedoux, Claude Volant and Yair Yariv.

This work has been done in the frame of the EU IP EUROTRANS project (European Union Contract N° FI6W-CT-2004-516520). We acknowledge the EU financial support.

REFERENCES

[1] J. Cugnon, T. Mizutani and J. Vandermeulen, Nucl. Phys. **A352** (1981) 505
[2] J. Cugnon, Nucl. Phys. **A462** (1987) 1987
[3] J. Cugnon, C. Volant and S. Vuillier, Nucl. Phys. **A620** (1997) 475
[4] A. Boudard, J. Cugnon, S. Leray and C. Volant, Phys. Rev. C**66** (2002) 044615
[5] J.-P. Meulders et al, *HINDAS Detailed Final Report*, EU Report, 2005
[6] K.-H. Schmidt, these proceedings and references therein
[7] R.E. Prael and H. Liechtenstein, report LA-UR-89-3014, Los Alamos National Laboratory, (1989)
[8] J.S. Hendricks et al, ORNL Report ORNL-TM-196 (2003)
[9] A. Boudard, J. Cugnon, S. Leray and C. Volant, Nucl. Phys. **A740** (2004) 195
[10] Th. Aoust and J. Cugnon, Eur. Phys. J. **A21** (2004) 79
[11] Th. Aoust and J. Cugnon, Phys. Rev. C. **74** (2006) 064607
[12] J. Cugnon and P. Henrotte, Eur. Phys. J. **A16** (2003) 393
[13] Th. Aoust, A. Boudard, J. Cugnon, J.-C. David, P. Henrotte, S. Leray and C. Volant, NIM Phys. Res. **A562** (2006) 806
[14] A. Boudard, Proceedings of the *Nice Nuclear Data 2007 Conference*, to be published
[15] J. Cugnon, http://www.theo.phys.ulg.ac.be/~cugnon/
[16] J. Cugnon, Ann. Phys. Fr. **21** (1996) 537
[17] J. Cugnon, D. L'Hôte and J. Vandermeulen, NIM **B111** (1996) 215
[18] Th. Aoust, PhD thesis, University of Liège, 2007
[19] C. Mahaux and R. Sartor, Adv. Nucl. Phys. 2**0** (1991) 1
[20] P.E. Hodgson, "*The Nucleon Optical Potential*", World Scientific, Singapore, 1994
[21] P. Henrotte, PhD thesis, University of Liège, 2005
[22] Y. Yariv et al, Proceedings of the *Nice Nuclear Data 2007 Conference*, to be published
[23] R.E. Prael and M.B. Chadwick, report LA-UR-97-1744, Los Alamos National Laboratory, (1997)
[24] B.C. Barashenkov, *Cross Sections of Interactions of Particles and Nuclei with Nuclei, JINR Publications*, Dubna, (1993)
[25] Th. Aoust et al, NIM Phys. Res. **A562** (2006) 806

CEM03.03 and LAQGSM03.03 Event Generators for the MCNP6, MCNPX, and MARS15 Transport Codes

S.G. MASHNIK[1], K.K. GUDIMA, R.E. PRAEL, A.J. SIERK, M.I. BAZNAT, N.V. MOKHOV

[1]Los Alamos National Laboratory,
Applied Physics Division,
Los Alamos, United States of America

Abstract. A description of the IntraNuclear Cascade (INC), preequilibrium, evaporation, fission, coalescence, and Fermi breakup models used by the latest versions of our CEM03.03 and LAQGSM03.03 event generators is presented, with a focus on our most recent developments of these models. The recently developed "S" and "G" versions of our codes, that consider multifragmentation of nuclei formed after the preequilibrium stage of reactions when their excitation energy is above 2A MeV using the Statistical Multifragmentation Model (SMM) code by Botvina et al. ("S" stands for SMM) and the fission-like binary-decay model GEMINI by Charity ("G" stands for GEMINI), respectively, are briefly described as well. Examples of benchmarking our models against a large variety of experimental data on particle-particle, particle-nucleus, and nucleus-nucleus reactions are presented. Open questions on reaction mechanisms and future necessary work are outlined.

A 94 page detailed lecture as presented at the workshop, with 5 tables, 51 color figures, and 216 references is available on the Web as E-print: arXiv:0805.0751 [nucl-th] (LANL Report LA-UR-08-2931), or, if not accessible, in hard copy from the authors.

We thank the Organizers of this workshop, especially Dr. Sylvie Leray, for inviting us to present these lectures and for financial support. We are grateful to ICTP and IAEA for kind hospitality. These lectures were written with support from the US Department of Energy.

Proton induced spallation reactions investigated within the framework of BUU model

Z. RUDY[1], A. KOWALCZYK[2]

[1] Jagiellonian University,
Cracow, Poland

[2] Forschungszentrum Jülich,
Jülich, Germany

Abstract. Major progress of contemporary research in the natural sciences can no longer be imagined without model simulations. Particularly demanding are cases when one wants to investigate a real dynamic system. The simulation of nuclear reaction forms such a case where one is compelled to introduce essential simplifications in order to make truly quantum N-body problem calculable. Sure, the simplifications should be chosen carefully, if not they can distort the time evolution of dynamic system. Essential for nuclear reaction is diffusion of interacting particles, therefore it is natural to expect that approach based on Boltzman equation of transport is promising one. The Boltzmann-Uehling-Uhlenbeck model, which includes Fermi motion of nucleons, the mean field of their interaction, individual N-N interactions and quantum mechanical Pauli blocking effect can be used for calculations of properties of hot residual system – its distributions of excitation energy, mass, charge and angular momentum. Such a model is presented, starting from derivation of transport equation. Feasibility of the collision term of the transport equation which is constructed in specific way in order to respect the Pauli blocking is discussed. BUU model supplemented with statistical evaporation code (i.e. statistical evaporation code as “afterburner” of hot residual nuclei) describes well e.g. the sample neutron data.

1. Introduction

The following definition of spallation process can be found in Nuclear Physics Academic press: "Spallation - a type of nuclear reaction in which the high-energy of incident particles causes the nucleus to eject more than tree particles, thus changing both its mass number and its atomic number." So, the term spallation means a kind of nuclear reactions, where hadron with high kinetic energy (100 MeV up to several GeV) interacts with a target. First, this term was connected with observation of residuum of reaction corresponding to losses of mass of target nucleus from few up to several dozen nucleons. Nowadays, it means mechanism, in which high energy light particle causes production of numerous secondary particles from target nucleus, leaving cold residuum of spallation. As a result of such process also various Intermediate Mass Fragments (IMF), i.e. fragments with masses in range $4 < M_{IMF} < 20$, are observed. From a historical point of view, the possibility of heating a nucleus via bombarding by neutrons was suggested for the first time in 1936 by N. Bohr [1]. Studies of similar reactions were possible due to development of accelerator techniques. It was at the end of the forties, when accelerators could provide projectiles with energies higher than 100 MeV [2]. Experimentally, two - component spectra of emitted particles are observed: anisotropic high energy part, which dominates in forward angles (i.e. the high energy tail decreases at backward angles) and isotropic, low energy part. These general features of spallation process are established experimentally. A theoretical picture of an incident particle colliding successively with several nucleons inside target nucleus, losing a large fraction of its energy was proposed by Serber in 1947 [3]. Before, in 1937 Weisskopf considered possibility of emission of neutron from excited target nucleus [4]. In the end of fifties, Metropolis [5] and Dostrovsky [6] (who used the ideas of Serber and Weisskopf) suggested description of spallation as two step process involving energy deposition and subsequent evaporation. They formulated and performed first Monte Carlo calculations of the reactions. Such treatment of spallation reactions is used from that time up to now. In more details, the first, so-called fast

stage of the spallation is highly non-equilibrated process. High energy proton causes an intra-nuclear cascade on a time scale 10^{-22} s.

The incident projectile goes through the target nucleus and deposits a significant amount of excitation energy and angular momentum, while ejecting only a few high energy nucleons and, with a minor yield, pions and light ions. The result of the first stage is excited residual nucleus in thermodynamical equilibrium (totally or partly equilibrated), with excitation energy of a few MeV/nucleon. In case of thick target, i.e. system of several nuclei, the ejectiles, as secondary projectiles can cause so-called inter-nuclear cascade, placing individual nuclei into excited states, as illustrated in Fig. 1.

The second, so-called slow stage of the spallation, consists in deexcitation of the residuum by evaporation of particles. The isotropic emission (in the system of nucleus) of nucleons (mainly neutrons), light and heavy ions (d, t, He, Li, Be, B, ...,) takes place on a time scale 10^{-18}- 10^{-16} seconds.

Since many years spallation reactions of medium and high energy protons with atomic nuclei are still of interest for many reasons. First of all, because knowledge of the reaction mechanism is still not complete. This is interesting both from theoretical and experimental point of view. Experimental data of double differential cross sections of emitted particles in the reactions are necessary for testing, validation and developing of theoretical models. It means, experimentally measured cross sections for exclusive elementary reactions (e.g. NN, N_, ...) are implemented in theoretical models. Then, results of calculations are compared with results of inclusive measurements. It is reasonable to study the reaction mechanism on the base of proton – nucleus rather than nucleus - nucleus collisions, where all processes start to be much more complicated (e.g. presence of distortions due to collective processes like compression, deformation, high spin [8]).

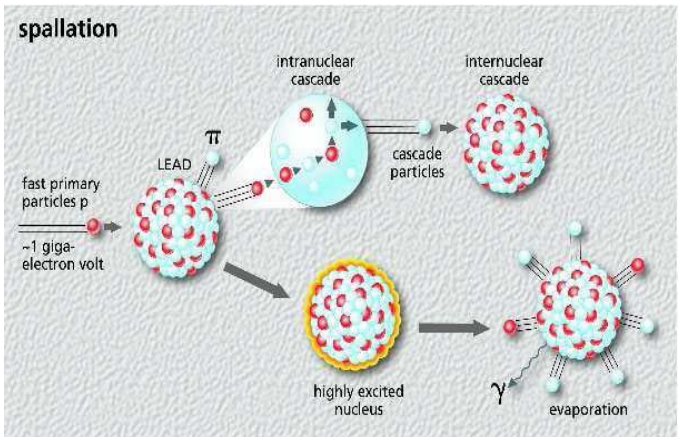

Fig. 1

Moreover, proton – nucleus reactions are important and indispensable also for experiments of nucleus - nucleus collisions (e.g. HADES [9], CHIMERA [10]). Results of proton-nucleus reactions facilitate extraction and interpretation of results of nucleus-nucleus reactions. Other reasons concern very broad range of applications (e.g. in medicine (radiation therapy), cosmology, accelerator technology). Relatively huge number of produced neutrons suggested the idea of using spallation reactions as neutron sources. Nowadays, neutron beams are produced in nuclear reactors. Reactors dedicated for such production generate also a lot of heat; about 190 MeV of energy is dissipated for single produced neutron. In accelerator based sources, neutrons are produced in a spallation process, with only about 30 MeV of energy dissipated for one generated neutron. During the last decade several spallation sources (IPNS [11], ISIS [11], LANSCE [12], SINQ [13]) became operational.

Spallation reactions are very important in accelerator technology (e.g. activation of detectors, radiation protection). The reactions are used for energy amplification, also for production of energy from nuclear waste and furthermore, transmutation of long - lived radioactive nuclei of nuclear waste to stable or short - lived, in order to avoid their long term storing [14]. Astrophysical models have to include spallation processes. If one compares abundances of cosmic rays and solar system elements, it is seen that Li, Be and B in cosmic rays are enriched by more than 6 orders of magnitude [15, 16]. They were evidently produced in spallation reactions of hydrogen nuclei (which consist about 87 % of cosmic rays) with heavy elements (produced due to stars explosions). For more informations see [15, 16]. Theoretical predictions of the process are important in each of the above mentioned cases. Several models have been constructed in order to describe the spallation process. First stage of the reaction is described by a class of microscopic models, e.g. [17, 18, 19]. For the second stage statistical models are used, described e.g. in [20, 21].

2. Modelling

Our understanding of physical phenomena is expressed as modelling. At present, the broadest platform for such modelling is quantum mechanics approach. Unfortunately, many - body systems are usually an extreme challenge for existing methods of quantum mechanics. One has to rely on rather simple, much more straight formed concepts – they are ingredients of typical models of nuclear reaction. Several microscopic models have been constructed in order to describe the first stage of proton - nucleus reaction. All of them have the same basis, they describe the reaction as a cascade of nucleon - nucleon collisions, but employing different assumptions. The main difference concerns implemented potential of nucleon - nucleus interaction. One can distinguish the simplest models, which neglect features of the mean field dynamics and employ constant static potential, like a class of Intra - Nuclear Cascade (INC) models. Other, more sophisticated approaches comprise dynamically changing field and minimal fluctuations obtained due to use of test particle method, i.e. models based on Boltzmann - Uehling - Uhlenbeck (BUU) transport equation. There are also models, which include real fluctuations and particles correlations, employing two- and three-body potentials, e.g. Quantum Molecular Dynamics models.

Simulations are closely related to dynamic models. In short, a simulation results when the equations of the underlying dynamic model are solved. This model is designed to imitate the time-evolution of a real system. To put it another way, a simulation imitates one process (real) by another process (evolving in computerized environment). In this definition, the term “process” refers solely to some object or system whose state changes in time. As the simulation run on a computer, it is called a computer simulation - a computer simulation is any computer-implemented method for exploring the properties of mathematical models where analytic methods are unavailable.

The following is what inspires scientists to run simulations:

1. Investigations of the detailed dynamics of a system; one develops an understanding of the relevant processes by means of calculating macroscopic properties (like cross sections) from assumed microscopic properties.

2. Development of hypotheses, models and theories; e.g. theorists can investigate singularities or regularities by varying the model parameters.

3. Simulations as a substitute for an experiment i.e. numerical experiments; particularly useful when experiment is impossible or very costly, e.g. in case of research concerning formation and development of stars.

4. Simulations as a tool for experimentalists – coarse and fine tuning of experiments; detailed simulations performed in advance are used to determine the best experimental setup or help to compromise between the cost and the experimental effectiveness.

5. Simulations as a pedagogical tool for understanding of a process, e.g. simulation of what is just irrelevant background in measured spectrum: what is left after subtraction of background is due to nontrivial process that can be scrutinized in detail. Sure, there is the following potential high risk in usage of computers in science – people spend less and less time thinking about essential features of investigated process, they tend to complicate the model in order to increase the model ability to reproduce accumulated data.

3. BUU model

Historically, the transport equation originates from classical Boltzmann equation for one-body phase-space distribution function $f(\vec{r},\vec{v},t)$ normalized so that $f(\vec{r},\vec{v},t)d^3vd^3r$ is the number of particles at time t positioned in element volume d^3r around vector $\vec{r}$, which have velocities in volume element of velocity space d^3v around vector $\vec{v}$.

Let us consider particles of mass m under influence of an external force $\vec{F}$ and assume initially that no collisions take place between the particles. In time t + δt the velocity $\vec{v}$ of each particle will change to $\vec{v}+(\vec{F}/m)\delta t$ and its position $\vec{r}$ will change to $\vec{r}+\vec{v}\delta t$. Thus the number of $f(\vec{r},\vec{v},t)d^3vd^3r$ is equal to the number of particles $f(\vec{r}+\vec{v}\delta t,\vec{v}+(\vec{F}/m)\delta t,t+\delta t)d^3v'\,d^3r'$ what is explained by the Liouville theorem:

The volume of phase-space element is constant, if movement of all particles inside is consistent with canonical Hamilton equation of motion.

and written as:

$$f(\vec{r}+\vec{v}\delta t,\vec{v}+(\frac{\vec{F}}{m})\delta t,t+\delta t)-f(\vec{r},\vec{v},t)=0$$

If collisions occur between the particles, an additional element, i.e. collision term is needed. This gives the following equation describing evolution of the distribution function:

$$f(\vec{r}+\vec{v}\delta t,\vec{v}+(\frac{\vec{F}}{m})\delta t,t+\delta t)-f(\vec{r},\vec{v},t)=(\partial f/\partial t)_{coll}\partial t$$

Letting δt → 0 and expanding into the Taylor series gives the Boltzmann equation:

$$((\partial/\partial t)+\nabla_r\cdot\vec{v}+(\frac{\vec{F}}{m})\nabla_v)f(\vec{r},\vec{v},t)=(\partial f/\partial t)_{coll}$$

An apparent form of the collision term (i.e. right hand of the equation above) can be found considering an element volume A at time t, around position $(\vec{r},\vec{v})$ and an element volume B at time $t+\delta t$, around position $(\vec{r}+\vec{v}\delta t, \vec{v}+(\vec{F}/m)\,\delta t)$.

These two element volumes are so similar, that letting $\delta t \to 0$, particles knocked out from A, due to collisions, will not get into B. Particles being outside A, during time δt, will get into travelling A, and they will be inside B. So, the number of particles inside B, at time $t+\delta t$, at $\delta t \to 0$, is equal to the initial number of particles inside A, at time t plus relative modification of number of particles due to collisions, during time δt. Therefore, the collision term can be calculated as a difference between the number of collision in a time range (t; $t+\delta t$), when one of particles after collision is situated in element volume $d^3r d^3v$ around position $(\vec{r},\vec{v})$, and the number of collision in a time range (t; $t+\delta t$), when one of particles before collision is situated in the same element volume $d^3r d^3v$ around position $(\vec{r},\vec{v})$. It can be done by assuming that the density of particles is low enough, that only binary collisions need to be considered. It is also assumed that the velocity of particle is uncorrelated with its position in the space. It means that in element volume d^3r the number of particles pairs with velocities in volume elements of velocity space d^3v_1 around $\vec{v}_1$ and d^3v_2 around $\vec{v}_2$ is equal to:
$\left[f(\vec{r},\vec{v}_1,t)\,d^3v_1\,d^3r\right]\left[f(\vec{r},\vec{v}_2,t)\,d^3v_2\,d^3r\right]$.

The number of binary collisions ($\vec{v}_1$, $\vec{v}_2$ $\to \vec{v}_3, \vec{v}_4$) inside element d^3r, in time range (t; $t+\delta t$) is equal to: $\left[f(\vec{r},\vec{v}_2,t)\,d^3v_2\right] \mid \vec{v}_1 - \vec{v}_2 \mid \sigma(\Omega)\,d\Omega\,\delta t$, where:
$\vec{v}_1$ and $\vec{v}_2$ are the velocities of the two particles before collision,
$\vec{v}_3$ and $\vec{v}_4$ are their velocities after the collision,
$\sigma(\Omega)$ is the differential cross section for a reaction, in the centre of mass reference frame,
Ω is the solid angle the particles are scattered into (the angle between vectors $\vec{v}_1-\vec{v}_2$ and $\vec{v}_3-\vec{v}_4$),
$\mid \vec{v}_1-\vec{v}_2 \mid$ is the magnitude of the particles relative velocity before the collision,
$\left[f(\vec{r},\vec{v}_2,t)\,d^3v_2\right]|\vec{v}_1-\vec{v}_2|$ is the density of particles flux equal to the product of particles density and their velocity.

The total number of collisions, where one of the particle before collision is situated inside element $d^3v_1\,d^3r$ around ($\vec{r}$, $\vec{v}_1$) is obtained multiplying the number of binary collisions by number of particles with velocity $\vec{v}_1$, inside element d^3r and integrating over all possible $\vec{v}_2$ and Ω:

$$\int d^3v_2 \int d\Omega\,\sigma(\Omega) f(\vec{r},\vec{v}_2,t)\,|\vec{v}_1-\vec{v}_2|\left[f(\vec{r},\vec{v}_1,t)\,d^3r d^3v_1\right]\delta t$$

Using analogical method as above, the total number of collisions, where one of the particle **after** collision is situated inside element $d^3v_1\,d^3r$ around ($\vec{r}$, $\vec{v}_1$) is obtained:

$$\int d^3v_4 \int d\Omega\,\sigma'(\Omega) f(\vec{r},\vec{v}_4,t)\,|\vec{v}_3-\vec{v}_4|\left[f(\vec{r},\vec{v}_3,t)\,d^3r d^3v_3\right]\delta t$$

One can easily justify that $\sigma(\Omega)$ and $\sigma(\Omega')$ are equal and that because of Liouville theorem $d^3v_1\ d^3v_2 = d^3v_3\ d^3v_4$.

The BUU model provides an equation for the phase space density $f(\vec{x},\vec{p})$ of the nucleons, the constituents of the colliding nuclei. Having the phase-space density one can subsequently work out all interesting observables that can later be compared to experimental data. Particles can be scattered into another phase-space cell (leakage) or scattered into considered cell, respectively. The process can be described as process of diffusion of interacting particles-nucleons.

$$\left[\partial_t + \left(\vec{\nabla}_p U\right)\vec{\nabla}_x - \left(\vec{\nabla}_x U\right)\vec{\nabla}_p\right] f(\vec{x},\vec{p}) = \frac{4}{(2\pi)^3}\int d^3p_1 d^3p'\, d\Omega\, v\frac{d\sigma}{d\Omega}\,\delta(\vec{p}+\vec{p}_1-\vec{p}'-\vec{p}'_1)$$
$$\left[f(\vec{x},\vec{p}')f(\vec{x},\vec{p}'_1)(1-f(\vec{x},\vec{p}))(1-f(\vec{x},\vec{p}_1)) - (f(\vec{x},\vec{p})f(\vec{x},\vec{p}_1)(1-f(\vec{x},\vec{p}'))(1-f(\vec{x},\vec{p}'_1))\right]$$

This BUU transport equation depicts the time evolution of the phase space density $f(\vec{x},\vec{p})$ in the presence of the mean field potential U and two-particle collisions. The term on the right side is called collision term. $d\sigma/d\Omega$ is the corresponding two-particle collision cross section. The factors of the form $(1-f)$ in the collision term take the Pauli principle into account - two particles cannot occupy the same phase-space cell. f factors in the above equation are normalized so that $f=1$ means that phase-space is fully occupied. Through these Pauli factors quantum mechanics is explicitly taken into account (not fully, as quantum mechanical interference is not considered in BUU !) Next, a question appears how reliably the Pauli factors are calculated; this will be considered soon. It is important to point out the essential constituents of the BUU transport equation. These are:

- The basic structure of the BUU equation is on "responsibility" of statistical physics that acts as a background theory, i.e. the exact form of the BUU equation was obtained using statistical physics method, as discussed e.g. in [22], the same equation with collision term set to zero gives for gas in equilibrium Maxwell-Boltzmann distribution, $f(v) = n(m/(2\pi kT))^{3/2}\exp(-mv^2/(2kT))$.

- The collision term is modelled in order to respect features of quantum mechanics: Pauli blocking.

- Two components of the BUU model are delivered by other models:

1) Mean-field potential U of the form

$$U(\vec{x},\vec{p}) = A\left(\frac{\rho(\vec{x})}{\rho_0}\right) + B\left(\frac{\rho(\vec{x})}{\rho_0}\right)^{\sigma}$$

is taken from physics of nuclear structure. The parameters A, B, σ describe static properties of the nuclei. One can conclude that it is necessary, indispensable to have good description of the relevant nuclei (i.e. targets in case of proton-induced reactions) at rest. If not, the time evolution of the nuclear system would be invalid.

2) The elementary cross section $d\sigma/d\Omega$ is typically taken from experimental data.

The BUU equation describes the full dynamics of the model system. The equations can not be solved analytically. In order to solve them, one approximates the continuous phase-space density $f(\vec{x},\vec{p})$ by a phase space density of a large number of test-particles. Every real nucleon is substituted by N such test-particles; every of the test-particles imitates $1/N$ of real nucleon.

Nuclear density and phase-space density $f(\vec{x},\vec{p})$ can be calculated using following formulas:

$$\rho(\vec{r}_g) = \frac{1}{N}\sum_{i=1}^{NA} \frac{1}{(2\pi\Delta^2)^{3/2}} \exp\left(\frac{-(\vec{r}_g - \vec{r}_i)^2}{2\Delta^2}\right)$$

$$f(\vec{r},\vec{p},t) = \frac{6}{N}\frac{1}{N}\sum_{\vec{r}_g}\int d^3p \sum_{j=1}^{NA} \Theta(q_0 - |\vec{p}_j - \vec{p}|)(2\pi\Delta^2)^{-3/2} \exp\left(\frac{-(\vec{r}_g - \vec{r}_j)^2}{2\Delta^2}\right)$$

(points $\vec{r}_g$ are distributed over three-dimensional grid of size 1 fermi, q_0 is equal to 0.45 fm^{-1}, in the lower formula sum runs over $\vec{r}_g$ that are inside 3 fm times 3 fm times 3 fm cube). Please notice that here again some quantum mechanical effect is simulated – every test particle contributes to nuclear density and to phase-space density in some area rather then in specific point ("Gaussian smearing of test particle").

The test particles move between collisions according to classical Hamilton equations of motion.

$$\dot{\vec{p}}_i = -\vec{\nabla}_r U(r_i), \qquad \dot{\vec{r}} = \vec{p}_i / \sqrt{m^2 + p^2}$$

(dot in the above formulas means differentiation over time). Please consider that sufficiently large number of test particles is required in order to reproduce well e.g. nuclear density (and further Pauli blocking factors); a good choice is to have number of test particles as high as 10000 – 20000 or even more.

Logistics of BUU calculations

- initialization of nucleus (nuclei); positions of test particles (according to Saxon-Woods formula of nuclear density)
- initialization of incoming proton; positions of its test particles are distributed on disk (i.e. averaging on impact parameters)
- initialization of momenta for test particles of incoming proton; they are all set to momentum equivalent to kinetic energy of proton
- initialization of momenta for test particles of nucleus (nuclei): they are chosen for every test particle randomly, from 0 to local Fermi momentum p_F; it depends on local nuclear density ρ

  $$p_F = (3\pi^2\ \rho)^{1/3}$$

- beginning of time loop; typical time step 0.5 fm/c

- at every time step:

  1. nuclear density is calculated on three dimensional grid, d = 1 fermi
  2. it is checked whether given pair of particles (nucleons) is close enough to interact
  3. if particles (nucleons) will come closer in next time step postpone collision
  4. if given test particle does not collide, propagate it (i.e. modify its position, momentum) using Hamilton equation

- if given pair of test particles (only binary collision are considered) collides, specific reaction is chosen using branching ratios; Pauli blocking phase space densities f_1, f_2 are calculated; $g_1 = (1 - f_1)$, $g_2 = (1 - f_2)$ are calculated; two random numbers r_1, r_2 from [0,1] are chosen via random number generator; if $r_1 > g_1$ and $r_2 > g_2$ then reaction is allowed, if it is not this case it is blocked

- at the end of time loop all Delta resonances are forced to decay; typically time loop lasts 35 fm/c

- from BUU calculations, by exploring the conservation of total energy, mass number, momentum and angular momentum one can calculate the properties of hot residual nuclei as function of time, according to formulas:

$$\left\langle E_R^* \right\rangle(t) = E_{tot} - \sum_{i=1}^{N_p(t)} \sqrt{p_i^2 + m_i^2} - M_R - E_C$$

$$\left\langle A_R \right\rangle(t) = A_T + A_P - N_p(t),$$

$$\left\langle \vec{p}_R \right\rangle(t) = \vec{p}_{tot} - \sum_{i=1}^{N_p(t)} \vec{p}_i(t),$$

$$\left\langle L \right\rangle(t) = L_{tot} - \sum_{i=1}^{N_p(t)} \vec{r}_i(t) \times \vec{p}_i(t),$$

These calculated properties of hot residual system (excitation energy, mass, charge, angular momentum) can be further fed into statistical evaporation model, like PACE2 or GEM [20,21]. In this way the mass distribution of cold residues as well as spectra of nucleons and pions can be evaluated for time scales of 10^{-10} s.

4. Sample simulations

As example on Fig. 2 below time evolution of maximal nuclear density for reaction of incoming proton with ^{197}Au is presented, for proton kinetic energy from 0.5 to 5 GeV. The presented nuclear density is normalized to standard nuclear density ρ^0_{MAX}. It is evident from the Figure that the incoming proton causes negligible modification of nuclear density. The fluctuations of presented ratio of densities is of order of few percent, what proves that proton induced reactions are quite non-invasive processes.

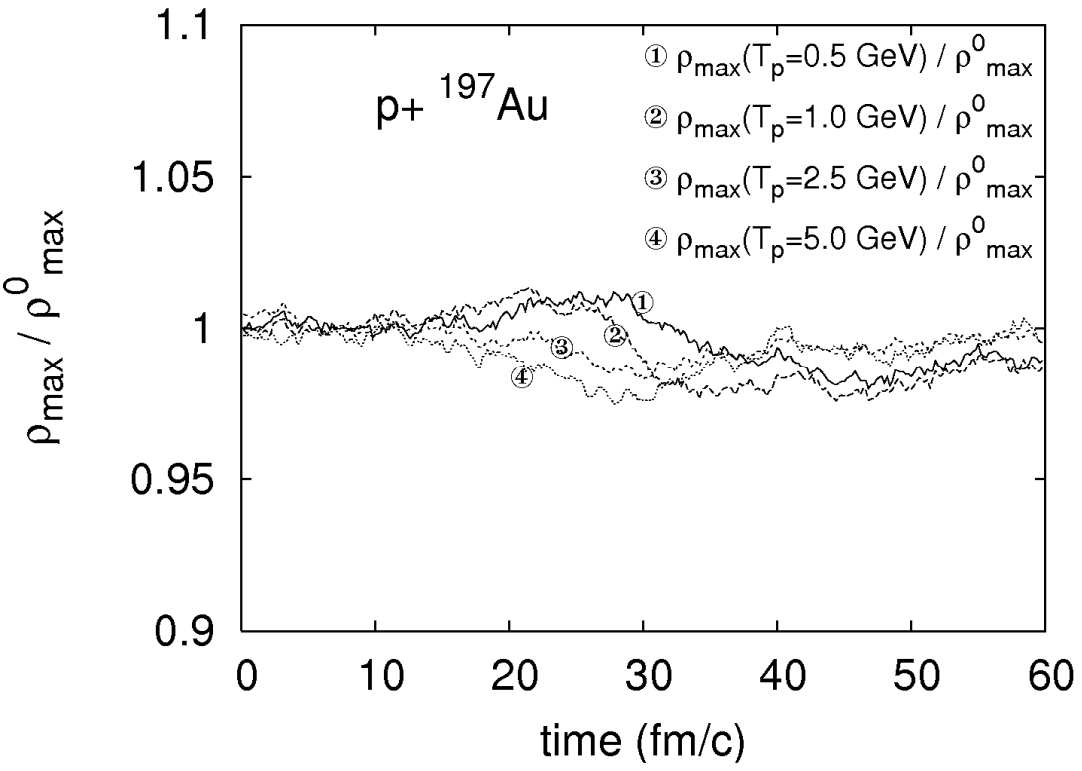

Fig. 2

On Fig. 3 average values of excitation energy per nucleon for hot residual nuclei produced after the first stage of proton – nucleus reactions are shown (BUU transport calculations). One observes that the simulations predict visibly higher value of excitation energy per nucleon for lighter targets. Still, even for p + ^{28}Si reaction the value is far below 5 MeV/nucleon, this value is usually considered as necessary for fragmentation to take place.

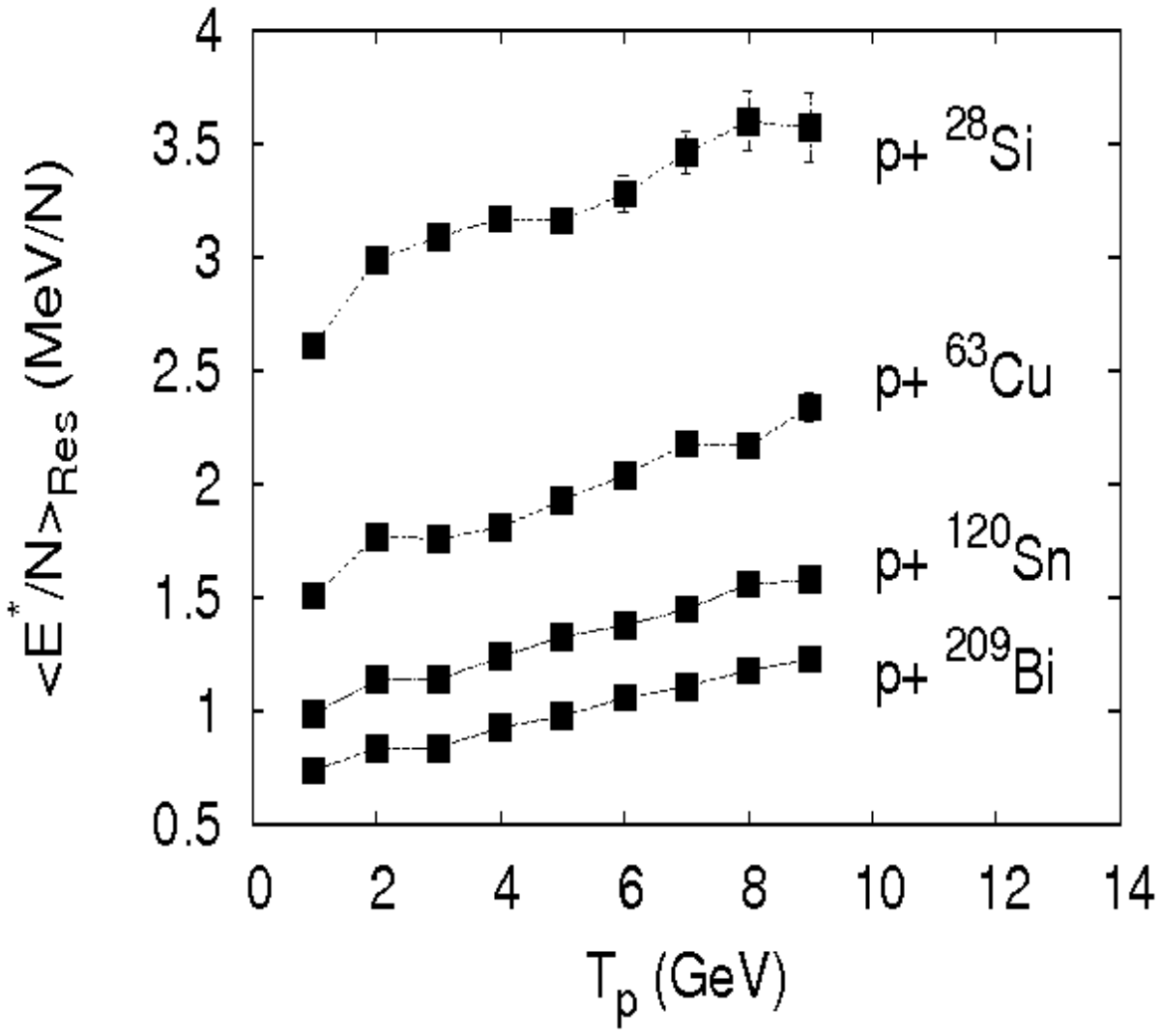

Fig. 3

On Fig. 4 double differential neutron production cross sections for p + ^{91}Zr reaction, at 1.2 GeV proton beam energy are presented. Lines show results of the BUU + GEM [21] model calculations (dashed and dotted lines are contributions of first and second stage of reaction, solid line is their sum), symbols indicate the experimental data [23]. The agreement between simulations and experimental data is really good, however, it should be mentioned that for heavier targets calculations underestimate the data in the central part of the distributions, around 50 MeV kinetic energy of neutrons. The effect increases monotonically with mass of the target. It is a hint that apart from the two stages of spallation reaction, there must be an additional intermediate stage probably preequilibrium emission. It seems that the neutron emission from the considered preequilibrium stage would be rather negligible for reactions with light targets.

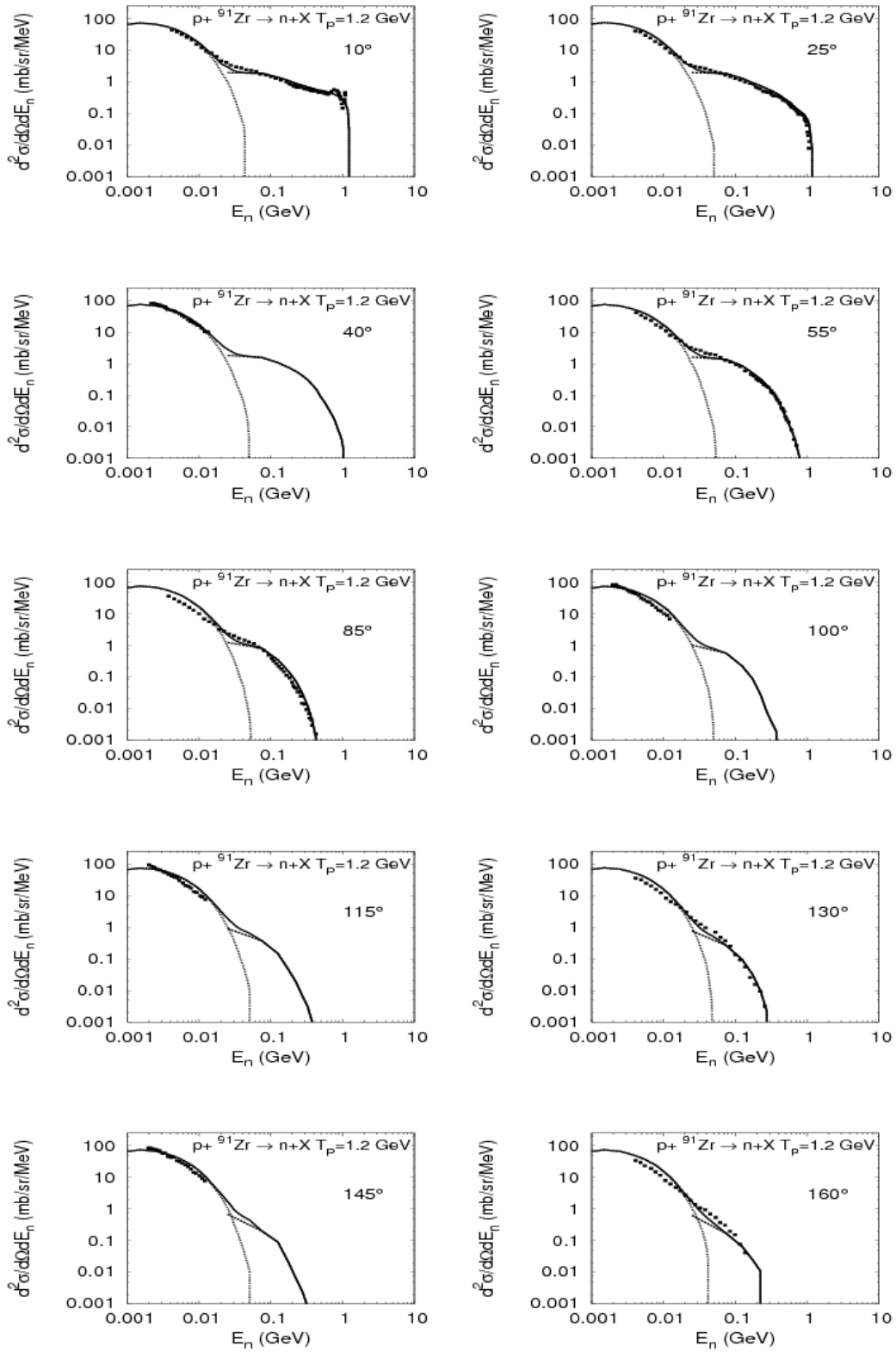
p+ ^{91}Zr → n+X T_p=1.2 GeV
10°
25°
40°
55°
85°
100°
115°
130°
145°
160°
$d^2\sigma/d\Omega dE_n$ (mb/sr/MeV)
E_n (GeV)

Fig. 4

REFERENCES

[1] N. Bohr, Nature 137(1936)344
[2] B. B. Cunningham et al., Phys. Rev. 72(1947)739
[3] R. Serber, Phys. Rev. 72(1947)1114
[4] V. Weisskopf, Phys. Rev. 52(1937)295
[5] N. Metropolis et al., Phys. Rev. 110(1958)185
[6] I. Dostrovsky et al., Phys. Rev. 111(1958)1658
[7] A. Bubak et al., Non-equilibrium emission of complex fragments from p+Au collisions at 2.5 GeV proton beam energy, accepted for publication in Phys. Rev. C, 2007.
[8] F. Goldenbaum et al., Phys. Rev. Lett. 77(1996)1230
[9] W. Przygoda et al., Nucl. Phys. A 783(2007)583
[10] S. Aiello et al., Nucl. Phys. A 583(1995)461
[11] B. S. Brown, A. D. Taylor, ICANS XIII, 13th Meeting of the International Collaboration on Advanced Neutron Sources, Report PSI-Proc. 95-02, November 1995, ISSN 1019-6447
[12] R. Pynn, ICANS XI, 11th Meeting of the International Collaboration on Advanced Neutron Sources, Report KEK 90-25
[13] G. S. Bauer, ICANS XIV, 14th Meeting of the International Collaboration on Advanced Neutron Sources, Report ANL-98/33, ISSN 1560-859X
[14] C. D. Bowman et al., Nucl. Inst. Meth. in Phys. Res. A 320(1992)336
[15] R. Silberberg, C. H. Tsao, Phys. Rep. 191(1990)351
[16] S. G. Mashnik, On Solar System and Cosmic Rays Nucleosynthesis and Spallation Processes, LANL, Report LA-UR-00-3658, (2000)
[17] J. Cugnon et al., Nucl. Phys. A, 620(1997)475
[18] K. Niita, W. Cassing and U. Mosel, Nucl. Phys. A, 504(1989)391
[19] J. Aichelin, Phys. Rep. 202(1991)233
[20] A. Gavron in Computational Nuclear Physics 2, Nuclear Reactions, edited by K. Langanke et al., Springer-Verlag 1993, p. 108
[21] S. Furihata, Nucl. Inst. Meth. in Phys. Res. B 171(2000)251
[22] Kerson Huang, “Statistical mechanics”, John Wiley and Sons, Inc., New York 1963
[23] S. Leray et al., Phys. Rev. C, 65(2002)044621

Description of Nuclear Collisions within the Isospin Quantum Molecular Dynamics (IQMD) Model

C. HARTNACK

SUBATECH,
Ecole des Mines de Nantes, CNRS/IN2P3,
Université de Nantes,
Nantes, France

Abstract. This article presents the major features of the Isospin Quantum molecular dynamics model (IQMD), a microscopic simulation model based on semi-classical N-body theory which is used to describe heavy ion collisions on an event-by-event level. The ingredients of the simulation model namely, the initialization, the transport with potential and the stochastic scattering including Pauli blocking and their numerical realization are discussed. The influence of technical and physical parameters is sketched and the choice of the default values is motivated.

1. Introduction

The Isospin Quantum molecular dynamics model (IQMD) is a microscopic simulation model based on semi-classical N-body theory. It is used to describe heavy ion collisions on an event-by-event level in an energy range from about 60 MeV/nucleon to about 2 GeV/nucleon. It was mainly applied for the study of collective effects like transverse, elliptic and radial flow, fragmentation and the production of secondary particles like pions, kaons or di-leptons (see e.g. [1-6]).

This article will only give a brief sketch on the realization of the model and refers for a more detailed discussion of the ingredients to [2,4]. A good introduction into the derivation of the basic transport equations and the use of Skyrme type potentials and their relation to the nuclear equation of state can be found in [7]. More general informations on microscopic models of heavy ion collisions using potentials and collisions and on different numerical realizations can be found in [8-12]

2. Description of the IQMD model

2.1. Theoretical background

The following paragraphs cite rapidly the relevant theoretical founding of QMD-type models. For more details see [7-9].

2.2. The VUU transport equation

The underlying equation used for the description of heavy ion collisions is a modified Boltzmann-equation with a two-body collision term supplemented by Uehling-Uhlenbeck factors taking into account the fermionic nature of the nucleons:

$$\begin{aligned}\frac{\partial f}{\partial t} + \vec{v}\cdot\nabla_r f - \nabla_r U\cdot\nabla_p f \quad = \quad & -\frac{4\pi^3(\hbar c)^4}{\hbar(mc^2)^2}\int \frac{\mathrm{d}^3p_1'}{(2\pi\hbar)^3}\frac{\mathrm{d}^3p_2'}{(2\pi\hbar)^3}\mathrm{d}^3p_2\frac{\mathrm{d}\sigma}{\mathrm{d}\Omega}\\ & \times [f f_2(1-f_1')(1-f_2') - f_1' f_2'(1-f)(1-f_2)]\\ & \times \delta^4(p+p_2-p_1'-p_2').\end{aligned} \tag{1}$$

This equation is known under a various number of names like Vlasov-Uehling-Uhlenbeck (VUU), Boltzmann-Uehling-Uhlenbeck (BUU), Landau-Vlasov (LV), Vlasov-Nordheim … (the list is surely not exhaustive). It is an integro-differential equation for the one particle distribution function *f(r,v,t)*.

The left hand side describes its total derivative with respect to the time *df/dt*. The right hand side describes the violation of its conservation due to binary collisions. The additional factors *(1-f)* take into account that the transition rate does not only depend on the phase space densities in the incoming states but also on the occupation of the final states. Since the particles are fermions, it has to be assured that no final state is overpopulated *f<1*.

2.3. The QMD distribution function

In IQMD particles are represented by the 1-particle Wigner density:

$$f_i(\vec{r},\vec{p},t) = \frac{1}{\pi^3\hbar^3} \mathrm{e}^{-(\vec{r}-\vec{r}_i(t))^2 \frac{2}{L}} \mathrm{e}^{-(\vec{p}-\vec{p}_i(t))^2 \frac{L}{2\hbar^2}} \tag{2}$$

The total 1 particle Wigner density is the sum of the Wigner densities of all nucleons. The particles move according to Hamiltons equations of motion

$v=dr/dt=\partial H/\partial p$ and $F/m=dp/dt=-\partial H/\partial q$.

Insertion of these equations into the VUU equation (1) yields the governing transport equation of IQMD. The Hamiltonian density H can be described by a sum of a kinetic and a potential term containing the kinetic energies of the particles and the potential interactions convoluted with the distribution functions of the interacting particles. Its expectation value reads:

$$\begin{aligned} \langle H \rangle &= \langle T \rangle + \langle V \rangle \\ &= \sum_i \frac{p_i^2}{2m_i} + \sum_i \sum_{j>i} \int f_i(\vec{r},\vec{p},t)\, V^{ij}\, f_j(\vec{r}',\vec{p}',t)\, d\vec{r}\, d\vec{r}'\, d\vec{p}\, d\vec{p}' \end{aligned} \tag{3}$$

2.4. Potentials in QMD

The baryon-potential consists of the real part of the *G*-Matrix which is supplemented by the Coulomb interaction between the charged particles. The former can be further subdivided in a part containing the contact Skyrme-type interaction only, a contribution due to a finite range Yukawa-potential, a momentum dependent part and a symmetry term between protons and neutrons.

$$
\begin{aligned}
V^{ij} &= G^{ij} + V^{ij}_{\mathrm{Coul}} \\
&= V^{ij}_{\mathrm{Skyrme}} + V^{ij}_{\mathrm{Yuk}} + V^{ij}_{\mathrm{mdi}} + V^{ij}_{\mathrm{Coul}} + V^{ij}_{sym} \\
&= t_1\delta(\vec{x}_i - \vec{x}_j) + t_2\delta(\vec{x}_i - \vec{x}_j)\rho^{\gamma-1}(\vec{x}_i) + t_3\frac{\exp\{-|\vec{x}_i - \vec{x}_j|/\mu\}}{|\vec{x}_i - \vec{x}_j|/\mu} + \\
& \quad t_4 \ln^2(1 + t_5(\vec{p}_i - \vec{p}_j)^2)\delta(\vec{x}_i - \vec{x}_j) + \frac{Z_i Z_j e^2}{|\vec{x}_i - \vec{x}_j|} + \\
& \quad t_6\frac{1}{\varrho_0}T_3^i T_3^j \delta(\vec{r}_i - \vec{r}_j)
\end{aligned}
\tag{4}
$$

The local Skyrme term contains an attractive term linear in the baryonic density ρ and a repulsive term of higher order in ρ which simulates effectively many particle correlations. For more details see e.g. [7].

The finite range Yukawa term with t_3=-6.7 MeV and μ=1.5 fm serves especially in stabilizing the surface of a finite size nucleus.

In the description of the Coulomb interaction Z_i, Z_j are the charges of the baryons.

The momentum dependence of the nucleon interaction, which may optionally be used in QMD, is fitted to experimental data on the real part of the nucleon optical potential obtainingt_4=1.57 MeV and t_5=5· 10^{-4} MeV^{-2}.

The asymmetry energy is linear in the difference of proton and neutron densities (where T_3^i and T_3^j denote the isospin projection T_3 of the nucleons i and j, i.e. 1/2 for protons and -1/2 for neutrons)

with a strength of t_6 =100 MeV.

2.5. Ground state properties and the nuclear equation of state

For a nucleus at ground state the expectation value of the total Hamiltonian should correspond to its total binding energy. When comparing to the Bethe-Weizsaecker mass formula we will find that the kinetic energy, the Skyrme potential and the momentum dependent interactions contribute to the volume energy, while the Yukawa interactions effect the surface energy and the volume energy, the Coulomb interactions define the Coulomb energy and the symmetry interactions the symmetry energy.

There is no term corresponding to the pairing energy since this corresponds to a global property of the nucleus which would be difficult to be described by microscopic local forces.

The nuclear equation of state describes the properties of infinite isospin saturated nuclear matter (without Coulomb interactions) and is therefore related to the term of the volume energy.

It describes the change of this energy when changing the nuclear density to values different than the saturation density ρ_0. Its potential part resulting from the convolution of the distribution

functions f_i and f_j with the local interactions (including momentum dependence) reads

$$U = \alpha \cdot \left(\frac{\rho_{int}}{\rho_0}\right) + \beta \cdot \left(\frac{\rho_{int}}{\rho_0}\right)^{\gamma} + \delta \cdot \ln^2\left(\varepsilon \cdot (\Delta\vec{p})^2 + 1\right) \cdot \left(\frac{\rho_{int}}{\rho_0}\right) \quad (5)$$

where ρ_{int} is the interaction density obtained by integrating the convolution of the distribution function of a particle with the distribution function of all other particles of the surrounding medium.

Δp is the relative momentum of a particle with respect to the surrounding medium.

The parameters t_1 ... t_5 are uniquely related to the corresponding values of α, β, γ, δ and ε resulting from the convolution integrals which serve as input. The standard values of these parameters can be found in the following table:

	α (MeV)	β (MeV)	γ	δ (MeV)	ε $\left(\frac{c^2}{\mathrm{GeV}^2}\right)$	κ (MeV)
S	-356	303	1.17	—	—	200
SM	-390	320	1.14	1.57	500	200
H	-124	71	2.00	—	—	376
HM	-130	59	2.09	1.57	500	376
INT	-157	103	1.58	—	—	284
VH	-110	56	2.40	—	—	456

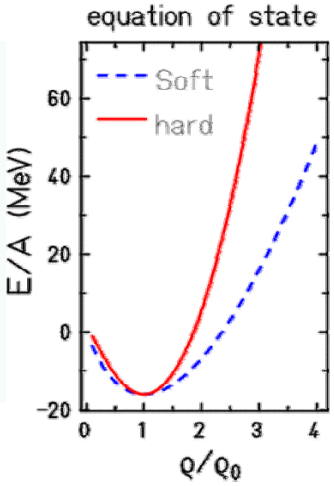

The parameters of the momentum dependent interactions δ and ε are obtained from a fit to the optical potential. Optionally, these interactions can be switched on (denoted "with mdi", parametrization HM and SM) or off (denoted "no mdi", other parametrizations).

The choice of the parameters α, β, γ is constrained by the condition
that the the volume energy of the nucleus (including kinetic energy, Skyrme potential and momentum dependent interactions) should have a minimum of *E/A*=-16 MeV at ground state density $\rho=\rho_0$. The remaining degree of freedom is related to the compression modulus *K* of the nucleus, which corresponds to the curvature of the volume energy at $\rho=\rho_0$ (for *T=0*). A hard eos (full line) yields a higher compression modulus and a stroner repulsion at high densities than a soft eos (dashed line). It should be noted that actual experimental data on heavy ion collisions around 1 AGeV favour a soft equation of state [6].

2.6. Binary collisions

Particles interact not only by the potential (left hand part of the VUU equation (1)) but also via binary hard collisions (right hand side of the VUU equation). These collisions may be elastic (NN→NN) but also inelastic. At energies around 1 GeV the inelastic channel is dominated by the production of a Δ.

This Δ may be reabsorbed or decay into a nucleon and a pion. The cross sections for these reactions are taken from experiment. The particles considered for collisions are nucleons, deltas and pions. Kaons can be produced as virtually propagating particles.

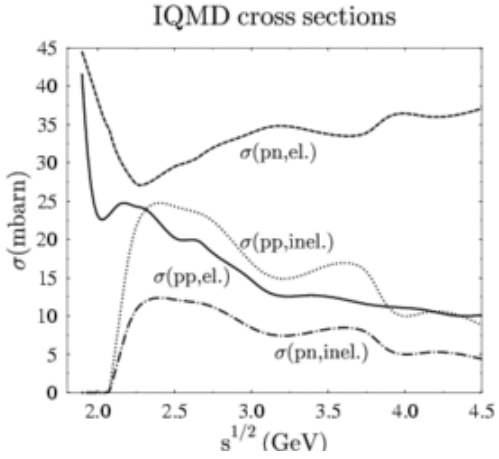

2.7. Numerical realization

The numerical solution of the VUU equation (1) is done by propagation of test-particles as sketched below. The nuclei are initialized as ensembles of nucleons. The potential part (left hand side) is solved by a propagation according to Hamiltons equation of motion. The collision integral (right hand side) is solved by a Monte Carlo integration. The final states are tested to be allowed by Pauli's principle.

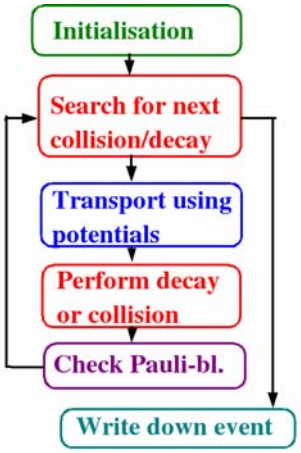

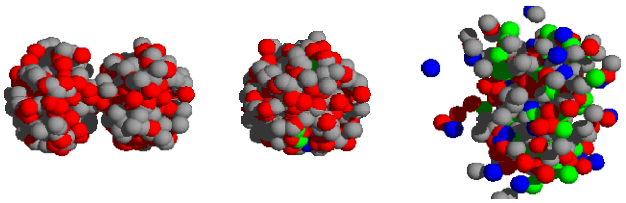

The different parts shall now be discussed in detail.

2.8. Propagation

The particles in IQMD are moving on curved trajectories using a leapfrog algorithm. The whole reaction time (typically 50-200 fm/c) is divided into time-steps of typically 0.2-0.5 fm/c. At each time-step the potentials are updated and a list of collisions susceptible to happen in the time-step is created.

This list is sorted according to the clock of the used reference frame (which usually is nucleon-nucleon centre-of-mass frame, also called equal-speed frame). Then the whole system is propagated to the time of the next collision. This collision is executed as detailed in the next paragraph. The new momenta of the colliding particles are checked for their compatibility with Pauli's principle. If the collision is allowed, the collision list will be

updated taking into account the new momenta of the particles. If not the momenta of the particles will be reset to their values before the collision was tested. Afterwards, the next collision in the list will be taken and the system will be propagated to that time.

Concerning the potentials, different parametrizations representing different equations of state are available. The standard parametrization is a soft equation of state including momentum dependent interactions (SM). It is possible to use only Skyrme-forces or add Yukava and Coulomb forces.

The asymmetry potential can be switched on and off explicitly. Its potential value can be adjusted

2.9. Initialization

The particles are represented by Gaussian wave functions as described in equation (2) using a Gaussian width L in the range of about 4-9 fm^2. For Au the standard value is $L=8.66$ while for small systems $L=4.33$ is used. Their centroids are initialized within a sphere in coordinate and momentum space. The radius in momentum space is given by

$$R_{max} = R_0 A^{1/3} \quad R_0 = 1.12\ fm$$

while the radius in momentum space depends on the coordinate radius parameter by the condition

of a limited phase space density. The standard value of $R_0 = 1.12\ fm$ yields $p_{Fermi} = 268\ MeV$ for $\rho=\rho_0$.

It is possible to choose an overall value for the whole nucleus (global Thomas-Fermi) or to choose the maximum momentum as a function of the local density (local Thomas Fermi). The latter option reduces the maximum momentum at the surface and stabilizes the nucleus versus evaporation of nucleons. It should be noted that, although the centroids are distributed in a hard sphere, the density profile of the nucleus is smooth due to the superposition of the Gaussians. The profile itself is influenced by the Gaussian width as it can be seen in the following figure showing the initial distributions in coordinate and momentum space: a smaller width yields a sharper profile.

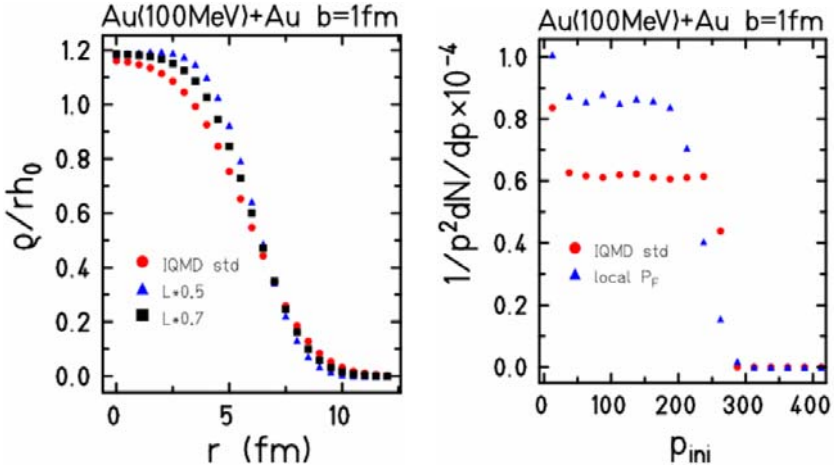

2.10. Collisions

Two particles collide if their minimum distance *d*, i.e. the minimum relative distance of the centroids of the Gaussians during their motion, in their CM frame fulfils the requirement:

$$d \leq d_0 = \sqrt{\frac{\sigma_{\text{tot}}}{\pi}}, \qquad \sigma_{\text{tot}} = \sigma(\sqrt{s},\ \text{type}). \tag{6}$$

where the cross section is assumed to be the free cross section of the corresponding type (N-N. N-Δ).

The time of this nearest point is taken in the clock of the global reference frame of the system, which as default is assumed to be the nucleon-nucleon centre-of-mass-frame. The collision is assumed to happen at the point of nearest contact even if condition (6) is already fulfilled at earlier times.

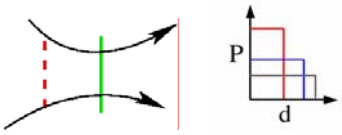

This description corresponds to the image of a black disc with a collision probability *P=1* inside the disc and *P=0* outside. Other parametrizations for P(d) are possible.

The total cross section is the sum of the elastic cross section and all inelastic cross sections.

$$\sigma_{\text{tot}} = \sigma_{\text{el}} + \sigma_{\text{inel}} = \sigma_{\text{el}} + \sum_{\text{channels}} \sigma_i \tag{7}$$

The cross sections for the different channels are given by experiment, if available. Different isospin selections can be weighted by isospin coefficients, e.g. $\sigma(pp \rightarrow n\Delta^{++}) = 3\sigma(pp \rightarrow p\Delta^{+})$. Inaccessible reactions like $N\Delta \rightarrow NN$ are calculated from their reverse reactions (here $NN \rightarrow N\Delta$) using detailed balance. For the latter case corrections are used taking into account the spectral function of the Δ as done in [13]. It is possible to scale the cross sections with a global or a density dependent factor which allows to simulate in-medium modifications. The possibility of reaching a channel in a collision is given by its contribution to the total cross section:

$$P_{\text{channel}} = \frac{\sigma_{\text{channel}}}{\sigma_{\text{tot}}} \qquad \text{e.g.} \quad P_{pp \rightarrow p\Delta^+} = \frac{1}{4}\frac{\sigma_{\text{tot}} - \sigma_{\text{el}}}{\sigma_{\text{tot}}} \tag{8}$$

In the numerical simulation, the choice of the channel is done randomly using the weight of the probability of the channel. Also the final momenta of the outgoing particles are chosen randomly obeying energy-momentum conservation and s-dependent angular distributions. The acceptation of the final state with respect to the Pauli principle is done randomly taking the final state phase space occupancy as weight factor.

3. Application range and the influence of parameters

This section is dedicated to review critically the application range of IQMD as well as the influence of the choice of several parameters on observables.

3.1. Application range

3.1.1. System Size and Beam Energy

The IQMD model is majorly intended for the simulation of heavy ion collisions. However, it should be kept in mind that like for most of particle-particle type models the calculation time increases by the square of the number of involved particles. For reasons of the internal dimensioning of arrays the total number of nucleons (projectile and target) is not allowed to exceed 500.

Small systems (like p+A) do not carry problems on the numerical side. However, it should be noted that the philosophy of IQMD relies on the idea of collisional chaos. Since the full covariant relativistic microscopic description of a N body system is not possible and the time ordering of the collisions depends on the used reference frame, a sufficiently large number of collisions may decrease the effect. Thus, small systems like p+A are rather limiting cases of the application.

IQMD is intended to work in the range of several hundred MeV/nucleon incident energy in the laboratory frame. At very low energies quantum effects in the interactions play an increasing role. Concerning the collisions most of the attempted collisions will be blocked. Since the efficiency of the Pauli-blocking in IQMD is in the range of about 95%, there will be some collisions taking place that are not consistent with the Pauli blocking. This overestimation of collisions shows a stronger effect at low incident energies. Therefore, a lower energy limit of around 70 AMeV should be assumed, even if IQMD was successfully applied at 45 MeV at KVI.

At high incident energies, the production of nucleon resonances plays an increasing role. In IQMD the only resonance implemented is the $\Delta(1232)$. This resonance dominates the energy range of several hundred MeV, but other resonances arise at energies between 1-2 AGeV. Therefore, an upper limit of around 2 GeV may be assumed, even if IQMD was able to describe experimental data at 2.5 GeV in a satisfactory way.

3.1.2. Physical observables

One fundamental problem for semi-classical models like IQMD is the description of the ground state energy of the nucleons in the nucleus. In IQMD, this Fermi-energy is assumed to be a kinetic energy of the nucleons moving in a potential formed by the other nucleons. However, a complete stability of the nucleus cannot be assured. A spurious evaporation of nucleons from the nucleus is found in the range of around 100 fm/c. Also the creation of fragments in heavy ion collisions at a few hundred AMeV is underestimated by IQMD in default version. This behaviour can be improved by changing some parameters in IQMD. However, these changes decrease the available Fermi-energy and cause spurious breathing modes of the nuclei. The diminution of the available energy effects other physical observables like collective flow and particle production. Since the latter observables were of special interest in the development of IQMD, the default parametrizations have been chosen in the actual way.

It has however to be noted, that the choice of a parametrization implies a focalization on a better description of particle production or of multifragmentation. For details see [4].

Concerning the description of p+A collisions, IQMD is rather successful in describing the production of secondary particles like kaons. However, the description of multifragmentation is less satisfactory. It was found that IQMD does not describe correctly the heat capacity of nuclei. The tendency towards spurious neutron emission should also be kept in mind.. However, it should be reminded, that the philosophy of IQMD was based on the idea of collisional chaos, which might not be assumed to happen in p+A collisions.

3.2. Influence of parameters

In this section the influence of several parameters on observables and the choice of the default parametrizations are discussed. For further details see [4].

3.2.1. Reference frame

In the reference frame, the system clock is synchronized. The time-ordering of the collisions is done with respect to the eigentime of the reference frame. Also the potential interactions are assumed to be instantaneous in the reference frame. Therefore, the choice of the reference frame may effect the number of collisions and of the produced particles. The choice of the reference frame should be done in such a way that γ of the focused reaction is minimized.

In IQMD different reference frames may be chosen: the laboratory frame (which may be interesting for neutron emission in p+A), the centre-of-mass frame of projectile and target nucleus (which might be interesting for multifragmentation) and the reference frame of a corresponding nucleon-nucleon system. In the latter one the absolute value of the momentum per nucleon is the same for projectile and target, therefore this reference frame is also called equal-speed-system. It is interesting for effects related to the first energetic collisions, e.g. particle production.

3.2.2. Equation of state

The nuclear equation of state (eos) describes the repulsion of nuclear matter under compression. Several parametrizations of the nuclear eos are available. A hard eos yields a stronger repulsion than a soft eos. Thus lower densities are reached for a hard eos yielding less particle production. The collective flow in plane and out-of-plane are stronger for a hard eos than for a soft one.

Momentum dependent interactions (mdi) yield additional repulsion of particles with high relative momenta and enhance the collective flow. Frequently, IQMD is applied using a soft eos with mdi.

3.2.3. Gaussian width

The Gaussian width influences the interaction range of the nucleon-nucleon potentials but also their gradients (which enter into the forces). A smaller Gaussian width sharpens the potential gradients, enhances the yield of fragments and the strength of collective flow but reduces the number of secondary particles. For small systems, a Gaussian width of L=4.33 is used, while for Au+Au a width of L=8.66 yields better results concerning stability, flow and particle production. However, fragment production in Au+Au collisions are better described when using L=4.33.

3.2.4. Initialization of the nucleus

In IQMD the nucleons of a nucleus are distributed in a sphere of radius $R_{max} = R_0 A^{1/3}$ with $R_0 = 1.12\ fm$. A larger value of R_0 yields less density in the centre and reduces the flow and the particle production.

The momenta are distributed in a sphere with $p_{Fermi} = 268\ MeV$. A reduction of this value enhances the stability versus spurious evaporation of nucleons, but reduces flow and particle production and causes spurious breathing modes.

3.2.5. Cross section modifications

In IQMD the cross sections are assumed to be the free elementary cross sections as measured by experiment. It is possible to scale these cross sections with a global or density dependent factor.

An enhancement of the cross sections yields smaller rapidity distributions, higher flow and higher yields of secondary particles.

The cross section is effectively reduced by Pauli-blocking. At low beam energies the suppression of the Pauli blocking shows similar effects than an enhancement of the cross section. At higher beam energies the Pauli blocking becomes less important and its suppression becomes less significant.

The cross section is interpreted as a black disk (see eq. (6)) with a probability 1 inside and 0 outside the disk. It is possible to enhance the area, where a collision is possible, and to reduce the probability (e.g. double the area and take only half probability). This modification does not effect the observables. A slight change of the fragment yield may be observed.

REFERENCES

[1] C. Hartnack, Li Zhuxia, L. Neise, G. Peilert, A. Rosenhauer, H. Sorge, J. Aichelin, H. Stoecker, W. Greiner, Nucl. Phys. A495 (1989) 303
[2] C. Hartnack, PhD thesis, GSI report 93-05 (1993)
[3] S.A. Bass, C. Hartnack, H. Stoecker, W. Greiner, Phys. Rev. C 51 (1994) 3343
[4] C. Hartnack et al. Eur. Phys. J. A1 (1998) 151
[5] C. Hartnack, J. Jaenicke, L. Sehn, H. Stoecker, J. Aichelin, Nucl. Phys. A580 (1994) 643
[6] C. Hartnack, H. Oeschler and J. Aichelin, Phys.Rev. Lett. 96 (2006) 012302
[7] H. Stoecker and W. Greiner, Phys. Rep. 137 (1986) 277
[8] W. Cassing, V. Metag, U. Mosel, K. Niita, Phys. Rep. 188 (1990) 361
[9] J. Aichelin, Phys. Rep. 202 (1991) 233
[10] S.A. Bass et al. Prog. Part. Nucl. Phys. 41 (1998) 225
[11] C. Fuchs, Prog. Part. Nucl. Phys. 56 (2006) 1
[12] M. Bleicher et al. J. Phys. G25 (1999) 1859
[13] P. Danielewic and G. Bertsch, Nucl. Phys. A533 (1991) 712[

Appendix: Input parameters of IQMD

A typical input file may look as the following (the text behind the ! was only inserted for making it more comprehensible but is not at all necessary to be read in by the program):

```
arca                          ! IQMD-type output, title=arca
40, 18, 40, 20,               ! A,Z proj    A,Z target      /Ref.Syst.
300, 150, 10,99999.,  1, 800.0,' NN' !#timest., pr.out, #runs,??,#par, Elab
3,      1.12          ! radius parameter                  === default
8,      1.0000              ! cross section parameter          === default
11,     0.0           ! b=0fm
12,  0.200000               ! timestep width                    default=0.25
13,    1.0            ! multiplier to Delta decay width === default
14,     128.00              ! switches
15,     1.0                 ! factor to Fermi momentum        ==== default
16,    12.2000              ! 11=full Coulomb nomdi 12=+mdi .1=hard eos .2=soft
19,   -1.10000              ! w. asymetry energy
20,    33.00                ! random number initialisator
 0,  0.0000000E+00      ! end of da()-changes  2nd loop   ->dasup()
 1, 0.5                ! Gaussian width  L=0.5*8.66 = 4.33
 2, 1.0                ! factor to cross section=1          === default
 3, 0.0                ! normal Gaussian normalization === default
 6,  0.0               ! no density dependent cross sections
 8  -11.032                  ! c.3-body, p-n Pauli seperate  Esym=32meV
11   1.0              ! global Thomas-Fermi,              === default
12   0.0              ! no Formation time                 === default
13   1.0              ! with det-bal. correction          === default
14 -20.0              ! pi+N-D normal, 20mb at high E=== default
15  10.0              ! ND-switches                       === default
0,  0.0000000E+00      ! end of Dasup()-changes
```

The lines marked with === default could be dropped off the input file, since these values are already assumed by default. An explicit definition overwrites the default values. Now the lines step by step:

```
          arca                          ! IQMD-type output
```

The first line has 4 characters as a heading. They will show up in the IQMD-output file. Any character is allowed (even unphysical ones like "nuts"). Only some special exceptions should be noted

$TST (test run) will give no output to the data-file
$GED (GEDEON p+A runs) will use a reduced IQMD-output format
$BQM (BQMD format) will write a BQMD type output format

```
          40, 18, 40, 20,               ! A,Z proj    A,Z target
```

The A and Z of projectile and target, here Ar+Ca; 1,1, 197, 79 will give you a p+Au collision

```
          300, 150, 10,99999.,  1, 800.0,' NN' !#timest.,pr.out, #runs,??,#par, Elab
```

300 : number of timesteps that are calculated for each run
150 : number of printout-steps, here all 150 steps, this means an output after 150 and after 300 steps
90 yields an output after 90,180, 270 steps, a negative number allows for an explicit notation .
10 : number of runs to be calculated, here 10 runs
99999. this was a CPU-time regulator, now it is useless, but has not been removed for compatibility
1 : number of parallel events, for IQMD this should be 1, in VUU events take between 15 and 100
800.0 incident lab energy/nucleon in MeV, here Ar(800 AMeV)+Ca
' NN' the reference frame, where the calculation is done (3 characters, one may be a blank)
' NN' or 'NN ' is the equal speed or 'N-N center of mass' frame
' CM' or 'CM ' is the center of mass frame of projectile and target
'LAB' is the laboratory frame, i.e. the target frame
'PRO' is the projectile frame

in case that the number N_P of printout-steps is negative, a line with - N_P printout-steps follows:
300, -4, 10,99999., 1, 800.0,' NN' ! For N_P <0 a line follows, but not for N_P >0
100 150 200 300
-4 means that 4 explicit printout-steps will follow, they are effected after 100,150,200, 300 steps

Now there comes a free cycle of the type N, X which will attribute the values of the data-block DA to DA(N)=X . The length of this cycle is of arbitrary length, it is closed by the statement 0 0.
The values for N=1,2,5,6,7,10 are already defined by the values above and should not be modified.
The major values are already described in the example file:

3, 1.12 ! radius parameter of the initialization for projectile and target $R_{max} = R_0 A^{1/3}$
8, 1.0000 ! cross section parameter ,one may change parameters to the cross section tables.
11, 0.0 ! b=0fm impact parameter *b* in fermi. *b> 0* gives a fixed impact parameter.
b>100 gives a percentage of the maximum impact parameter, e.g. 125 will give you 0.25 b_{max}
b<0 gives a range, e.g. -3 yields $0<b<3$ with bdb weighting, -100 yields $0<b<b_{max}=R_{proj}+R_{target}$
12, 0.200000 ! timestep width , the size of a timestep in fm/c, default is 0.25
The reaction time is the number of timesteps x timestep width, in our example 300x0.2 =60 fm/c
13, 1.0 ! Here you can apply a factor to the Delta decay width, 1 is normal, 0 will force your deltas to stay alive, a large number like 1000 will cause practically an instantanious decay
14, 128.00 ! There are a lot of switches. For 128 we only note, that the first collision to be allowed for a nucleon is a collision with one of the other nucleus or one that has already collided
A cascade without Pauli but with frozen Fermi may be addressed by a value of 104
15, 1.0 ! one may modify the Fermi momentum by a factor , default=1.0
16, 12.2000 ! Values for the nuclear equation of state, practically we use
QMD 11.1 = hard no mdi, 11.2=soft no mdi, 12.1=hard+mdi, 12.2=soft+mdi
for a value <0 we do VUU-type calculations, standard values are -1 soft eos -2 hard eos
17, 1.0 ! if >0 factor to preselection area for collisions (time saver) , default=1.0
If <-1 enhancement of cross section area, e.g. -2 means double area with P=0.5
18, 0.05 ! energy cutoff in GeV in case that Pauli blocking is disabled, default=0.05
19, -1.10000 ! To switch the asymmetry energy off use -0.1
20, 33.00 ! Seed for random number generator, now made by the clock
0, 0.0000000E+00 ! end of da()-changes 2nd loop ->dasup()
here we end the loop on changing the DA-Block and enter a loop for changing the DASUP()-Block.
Idem: arbitrary loop length, to be finished by 0 0.0
1, 0.5 ! factor to the Gaussian width *L*: 1.0→*L*=8.66 0.5→ *L*=4.33
2, 1.0 ! factor to the total (elastic and inelastic) cross sections
3, 0.0 ! here we could do same special stuff for the normalization of the Gaussians
6, 0.0 ! one may modify the cross sections with a factor: $\sigma_\rho=\sigma(1-a\cdot\rho/\rho_0)$
8 -11.032 ! c.3-body, p-n Pauli separate Esym=32MeV
for VUU use 0 for QMD 2.0 means cascade mode, no eos, otherwise use 1 or 11.xyz
<0 means separate Pauli blocking for protons and neutrons
>0 means average Pauli blocking of protons and neutrons
11.xyz means an asymmetry energy of xyz MeV, here 032 MeV
when switching off the asymmetry energy set this value to 1.0
11 1.0 ! global Thomas-Fermi, for setting it to local (density dependent) use 10
12 0.0 ! no Formation time , here one could implement a fomation time of the particles
13 1.0 ! Delta decay with Randrup-Parametrization and detailed balance modification
14 -20.0 ! pi+N-D normal, 20mb at high E , a positive value disables the pi absorption
another negative value would give another high energy limit of piN→D
15 10.0 ! ND-switches just leave this like it is
19 0.0 ! no lower threshold for kaons , touches f19-file output default=0
20 0.0 ! no kaon propagation , this touches only iqmd8020 , default=0
0, 0.0000000E+00 ! end of Dasup()-changes

Nuclear Reaction Models, JAM and JQMD, in PHITS

K. NIITA

Research Organization for Information Science & Technology,
Tokai, Ibaraki, Japan

Abstract. In the particle and heavy ion transport code system PHITS, we have used two simulation codes JAM and JQMD to describe the intermediate and high energy nuclear reactions. JAM is a simulation code based on INC (intra-nuclear cascade) model, which explicitly treats all established hadronic states including resonances with explicit spin and isospin as well as their anti-particles. We have parametrized all hadron-hadron cross sections based on the resonance model and string model by fitting the available experimental data. JQMD is a simulation code based on the molecular dynamics. A typical feature of QMD compared with that of the INC model is that QMD can describe not only nucleon-nucleus reactions but also nucleus-nucleus reactions in the same framework. Though the QMD model has been used mainly for the heavy-ion physics, we have applied JQMD code intensively to nucleon-nucleus reactions and checked its validity. In this paper, physical ideas and the details of these two models are discussed.

1. Introduction

The cross sections of intermediate and high energy nuclear reactions are strongly required in design study of many facilities such as accelerator-driven systems, intense pulse spallation neutron sources, and also in medical and space technology. There is, however, few evaluated nuclear data of intermediate and high energy nuclear reactions. Therefore, we have to use some models or systematics for the cross sections, which are essential ingredients of high energy particle transport code to estimate neutron yield, heat deposition and many other quantities of the transport phenomena in materials.

In the particle and heavy ion transport code system PHITS [1], we have used two simulation codes JAM [2] (Jet AA Microscopic Transport Model) and JQMD [3] (JAERI Quantum Molecular Dynamics) to describe the intermediate and high energy nuclear reactions.

JAM is a simulation code based on INC (intra-nuclear cascade) model, which explicitly treats all established hadronic states including resonances with explicit spin and isospin as well as their anti-particles. We have parametrized all hadron-hadron cross sections based on the resonance model and string model by fitting the available experimental data.

JQMD is a simulation code based on the molecular dynamics. A typical feature of QMD compared with that of the INC model is that QMD can describe not only nucleon-nucleus reactions but also nucleus-nucleus reactions in the same framework. The JQMD code has been widely used to analyze various aspects of heavy ion reactions as well as of nucleon-induced reactions [4], and has shed light on several exciting topics in heavy ion physics, for example, the multifragmentation, the flow of the nuclear matter, and the energetic particle production [5].

In this paper, physical ideas and the details of these two models are discussed.

2. Overview of PHITS

A reliable and accurate particle and heavy ion transport code is an essential implement in the design study of accelerator facilities as well as for various applications such as radiotherapy

and space technology. We have therefore developed a multi-purpose particle and heavy ion transport Monte Carlo code system, PHITS.

In PHITS, neutrons can be transported from thermal energies up to 200 GeV, and the same method as in the MCNP4C code [6] is employed for neutrons with energies below 20 MeV down to 1 meV based on the Evaluated Nuclear Data such as the ENDF-B/VI [7], JENDL-3.3 [8], and LA150 libraries [9]. Above 20 MeV, the simulation model JAM. For protons and other hadrons, JAM is also used above 1 MeV up to 200 GeV, but for charged particles below 1 MeV only the ionization process is considered until the particles are stopped.

PHITS also uses Evaluated Nuclear Data for photon and electron transport below 1 GeV in the same manner as in the MCNP4C code based on ITS version 3.0 code [10]. The energy range of electron and photon is restricted to the energy region 1 keV - 1 GeV at the present, but the extension of the maximum energy of these particles is in progress.

PHITS can also transport nuclei in materials. Below 10 MeV/n, only the ionization process for the nucleus transport is taken into account, but above 10 MeV/n the nucleus-nucleus collisions up to 100 GeV/n is described by the simulation model JQMD. The QMD simulation, as well as the JAM simulation, describes the dynamical stage of the reactions. At the end of the dynamical stage, excited nuclei are created and must be forced to decay in a statistical way to get the final observed state. In PHITS the GEM model [11] (Generalized Evaporation Model) is employed for light particle evaporation and fission process of the excited residual nucleus.

When simulating the transport of charged particles and heavy ions, the knowledge of the magnetic field is sometimes necessary to estimate beam loss, heat deposition in the magnet, and beam spread. PHITS can provide dipole and quadrupole magnetic fields in any direction and any region of the setup geometry. In contrast to other beam transport codes, PHITS can simulate not only the trajectory of the charge particles in the field, but also the collisions and the ionization process at the same time. This is a great advantage of PHITS when designing high intensity proton and heavy ion accelerator facilities, where one must estimate radiation damage of the magnets and the surrounding materials and the radiation shielding, as well as perform trajectory calculations.

For the ionization process of the charged particles and nuclei, the SPAR code [12] is used for the average stopping power dE/dx, the first order of Moliere model for the angle straggling, and the Gaussian, Landau and Vavilov theories for the energy straggling around the average energy loss according to the charge density and velocity. In addition to the SPAR code, the ATIMA package [13] developed at GSI group has recently been implemented as an alternative code for the ionization process.

The total reaction cross section, or the life time of the particle for decay is an essential quantity in the determination of the mean free path of the transport particle. According to the mean free path, PHITS chooses the next collision point using the Monte Carlo method. It is therefore very important that reliable data of total non-elastic and elastic cross sections is used for the particle and heavy ion transport. In PHITS, the Evaluated Nuclear Data is employed for neutron-induced reactions below 20 MeV. For neutron-induced reactions above 20 MeV a parameterization is used [14]. As for the elastic cross sections, the Evaluated Nuclear Data is also used for neutron-induced reactions below 20 MeV, and a parameterization is used above 20 MeV [14]. Parameterizations are also used for proton induced reactions for all energies, and for the double differential cross sections of elastic nucleon-nucleus reactions [14].

Recently we have also adopted the NASA systematics developed by Tripathi et al., [15] for the total nucleus-nucleus reaction cross section, as an alternative to the Shen formula [16].

3. High energy intra-nuclear cascade code; JAM

Below the energy in the center-of-mass system (c.m.) $\sqrt{s} < 4\,\mathrm{GeV}$, the inelastic hadron-hadron collisions are described by the resonance formations and their decays, and at higher energies, string formation and their fragmentation into hadrons are assumed.

We have parameterized the resonance formation cross sections in terms of the extended Breit-Wigner form and used the established data [17] for its decay channels and probabilities. At an energy range above $\sqrt{s} < 4 \sim 5$ GeV, the (isolated) resonance picture breaks down because the width of the resonance becomes wider and the discrete levels get closer. The hadronic interactions at the energy range $4 \sim 5 < \sqrt{s} < 10 \sim 100$ GeV where it is characterized by the small transverse momentum transfer is called "soft process", and string phenomenological models are known to describe the data for such soft interactions well. The hadron-hadron collision leads to a string like excitation longitudinally. In actual description of the string formation, we follow the prescription adopted in the HIJING model [18]. The strings are assumed to hadronize via quark-antiquark or diquark-antidiquark creation. As for the fragmentation of the strings, we adopted the Lund fragmentation model PYTHIA6.1 [19].

For nuclear reactions in JAM, we use the full cascade method described in the following. Each hadron has its position and momentum and moves along a straight line until it meets the next hadron-hadron collision, decay or absorption. The initial position of each nucleon is sampled by the parameterized distribution of nuclear density. Fermi motion of nucleons is assigned according to the local Fermi momentum as a function of the density. We do not take into account the mean field effects except for the initial nucleons. The initial nucleons in the target nucleus stay in the initial positions until the collision with the other hadrons. The interaction probabilities of hadron-hadron are determined by the method of so-called "closest distance approach", if the minimum relative distance for any pair of particles becomes less than the interaction range specified by $\sqrt{\sigma(\sqrt{s})/\pi}$, where $\sigma(\sqrt{s})$ is the total cross section for the pair at the c.m. energy $\sqrt{s}$, then particles are assumed to collide. This cascade method has been widely used to simulate high energy nucleus-nucleus collisions. However, geometrical interpretation of the cross section violates causality and the time ordering of the collisions in general differs from one reference-frame to another. These problems have been studies by several authors [20, 21]. We have adopted the similar procedure as that in ref.[20, 22] for the collision criterion to mimic the reference-frame dependence. Pauli-blocking for the final nucleons in two-body collisions is also considered. For the comparison with the alternative methods of the cascade, we have compared the results of JAM with that of Glauber type calculations in ref.[2]. It is found that the rescattering effect, which is not considered in Glauber type calculations, is of importance both for the explanation of the high transverse momentum tail and for the multiplicity of produced particles.

3.1. Elementary cross sections of Hadron-Hadron

There are a lot of adjustable parameters in the resonance model and string model in JAM. However, the number of the adjustable parameters in the models is relatively small compared with the number of final channels at high energy, because the number of final channels even in a proton-proton scattering increases drastically as a function of energy. Furthermore, they are not completely free parameters but restricted by the basic physical observables and

arguments as the mean energies and widths of the resonances, the detailed balance principle, and the kinematical conditions of the scattering. The detail of the parameterization of hadron-hadron cross sections in JAM is described in ref.[2]. Here, we demonstrate typical examples of the elementary hadron-hadron cross sections obtained by JAM and compare results with the experimental data.

In Fig. 1, we show the calculated rapidity y distributions and the transverse momentum distributions of protons, and positive and negative pions for proton-proton collisions at 12 GeV/c and also the data from ref.[23]. It is found that the proton stopping behavior and the pion yields are well described by JAM. In the JAM model at this energy, fast protons mainly come from resonance decays and mid-rapidity protons from string fragmentation.

Fig. 2 shows the energy dependence of the exclusive pion production cross sections in pp reactions. We compare the results obtained from the simulation with the experimental data [24]. Overall agreement is achieved in these exclusive pion productions. Smooth transition from the resonance picture to the string picture at $E_{cm} = 3 \sim 4$ GeV is realized since no irregularity of the energy dependence is present in the calculated results.

For another example of hadron-hadron cross sections, we plot, in Fig. 3, the total and elastic $\pi^- p$ and $K^+ p$ cross sections parameterized by JAM (upper panel), and the energy dependence of the exclusive cross sections of $K^- p \to \pi^0 \Lambda$ and $K^- n \to \pi^- \Sigma^0$ (lower panel). Data are taken from ref.[25]. It is recognized that JAM shows a good capability for calculating the cross sections even for the K, Λ, Σ.

These examples indicate that the parameterization of the elementary hadron-hadron cross sections in JAM is accurate enough for the high energy particle transport calculations.

3.2. Results of thin target

For validation, we compare the results of the JAM code with experimental data of thin targets. In Fig.4, we plot the invariant transverse mass distribution of proton (left panel) and π^+ (right panel) from proton on thin Au target reaction at 13.7 GeV. The results of JAM (histograms) and data [26] are plotted for each rapidity y bin quoted in the figure. For both ejectiles, the results of JAM agree well with the experimental data [26]. The agreements are also shown in the other targets of Be, Al, and Cu and the other ejectiles of π^-, K^+ in ref.[2].

3.3. Results of thick target

For validation of JAM in the PHITS calculations for the neutron flux produced by the mercury spallation target, we have applied PHITS to the experiments under the ASTE (AGS Spallation Target Experiment) collaboration [27]. One of the experiments was carried out using a bare mercury target, which is a 20 cm diameter and 130 cm long cylinder, and detecting the reaction rate distributions along the cylindrical surface of the target by activation techniques at incident proton energies of 1.6, 12 and 24 GeV. Various activation detectors such as the ^{115}In(n,n')^{115m}In, ^{93}Nb(n,2n)^{92m}Nb and ^{209}Bi(n,xn) reactions with threshold energies ranging from 0.3 to 70.5 MeV were employed to obtain the reaction rate data for estimating spallation neutron source characteristics of the mercury target. Fig.5 shows the distribution of the ^{27}Al(n,□)^{24}Na reaction rates along the cylindrical surface of bare mercury target bombarded with 1.6, 12, and 24 GeV protons. The threshold of this reaction is 3.3 MeV, while the most effective neutron energy for this reaction is roughly 10 MeV. The

results of PHITS, denoted by the solid histograms in these figures, reproduce the experimental distribution quite well for all positions and all energies.

4. Heavy-ion reaction code; JQMD

4.1. Basic formulation

The QMD method is a semi-classical simulation method in which each nucleon state (denoted by a subscript *i*) is represented by a Gaussian wave packet. The total wave function is assumed to be a direct product of these wave functions. Thus the one-body distribution function is obtained by the Wigner transform of the wave function,

$$f_i(\vec{r},\vec{p}) = 8\cdot\exp\left[-\frac{(\vec{r}-\vec{R}_i)^2}{2L}-\frac{2L(\vec{p}-\vec{P}_i)^2}{\hbar_2}\right], \tag{1}$$

where L is a parameter representing the spatial spread of a wave packet, $\vec{R}_i$ and $\vec{P}_i$ corresponding to the centers of a wave packet in the coordinate and momentum space, respectively. The equation of motion of $\vec{R}_i$ and $\vec{P}_i$ is given, on the basis of the time-dependent variational principle, by the Newtonian equations:

$$\dot{\vec{R}}_i = \frac{\partial H}{\partial \vec{P}_i}, \qquad \dot{\vec{P}}_i = -\frac{\partial H}{\partial R_i}, \tag{2}$$

and the stochastic N-N collision term [3]. We have adopted the Hamiltonian H consisting of the relativistic energy and the Skyrme-type effective N-N interaction plus Coulomb and symmetry energy terms:

$$\begin{aligned} H = & \sum_i \sqrt{m_i^2+\vec{P}_i^2} \\ & + \frac{1}{2}\frac{A}{\rho_0}\sum_i <\rho_i> + \frac{1}{1+\tau}\frac{B}{\rho_0^{\tau}}\sum_i <\rho_i>^{\tau} \\ & + \frac{1}{2}\sum_{i,j(\neq i)}\frac{e_i e_j}{|\vec{R}_i-\vec{R}_j|}\,erf\left(|\vec{R}_i-\vec{R}_j|/\sqrt{4L}\right) \\ & + \frac{C_s}{2\rho_0}\sum_{i,j(\neq i)} c_i c_j \rho_{ij}, \end{aligned} \tag{3}$$

where "erf" denotes the error function, the e_i is the charge of the *i*-th particle, and the c_i is 1 for proton , -1 for neutron and 0 for the other particles. With the definition

$$\begin{aligned} \rho_i(\vec{r}) \equiv & \int \frac{d\vec{p}}{(2\pi\hbar)^3} f_i(\vec{r},\vec{p}) \\ = & (2\pi L)^{-3/2}\exp\left[-(\vec{r}-\vec{R}_i)^2/2L\right] \end{aligned} \tag{4}$$

the other symbols in eq.(3) are given as:

$$
\begin{aligned}
<\rho_i> &\equiv \sum_{j\neq i}\rho_{ij} \equiv \sum_{j\neq i}\int d\vec{r}\,\rho_i(\vec{r})\rho_j(\vec{r}) \\
&= \sum_{j\neq i}(4\pi L)^{-3/2}\exp\left[-(\vec{R}_i-\vec{R}_j)/4L\right]
\end{aligned}
\tag{5}
$$

The symmetry energy coefficient C_s is taken to be 25 MeV. The four remaining parameters, the saturation density ρ_0, the Skyrme parameters *A*, *B* and τ are chosen to be 0.168 fm^{-3}, -124 MeV, 70.5 MeV and 4/3, respectively. These values give the binding energy/nucleon of 16 MeV at the saturation density ρ_0 and the compressibility of 237.7 MeV (soft EOS) for nuclear matter limit. The only arbitrary parameter in QMD is the width parameter *L*, which is fixed to be 2 fm^2 to give stable ground states of target nuclei in a wide mass range.

In addition to the Newtonian equation eq.(2), the time evolution of the system is affected by the two-body collision term. In the QMD model, the stochastic two-body collision process is described in the same method as in the intra-nuclear cascade model except for the Pauli blocking factor. The final blocking probability is determined by $\left[1-f(\vec{r},\vec{p},t)\right]$ which is obtained by summing up the each one-body distribution function given by eq.(1).

The ground state of the target and/or projectile is generated by packing $\vec{R}_i$ and $\vec{P}_i$ randomly based on the Woods-Saxon type distribution in the coordinate space and corresponding local Thomas-Fermi approximation in the momentum space, seeking a configuration to reproduce the binding energy included in the nuclear data table within a certain uncertainty. The ground state obtained by this procedure is a self-bind system and rather stable up to the time 200 fm/c, which is enough time for the dynamical stage of the reaction.

The QMD simulation, as well as the JAM simulation, describes the dynamical stage of the reactions. At the end of the dynamical stage, excited nuclei are created and must be forced to decay in a statistical way to get the final observed state. In PHITS, the GEM model [28] (Generalized Evaporation Model) is employed for light particle evaporation and fission process of the excited residual nucleus. The switching time, when we switch the QMD calculation to the SDM, is an arbitrary parameter in the model. We have checked the dependence of the final results on the switching time and found that the final results are not sensitive to the switching time if we use the switching time from 100 fm/c to 150 fm/c [3, 29].

4.2. Results of nucleon induced reactions

We have applied the JQMD code intensively to nucleon-nucleus reactions and checked its validity [3,29,30]. First we show the results of the JQMD code for the particle spectra emitted from proton induced reactions. Fig. 6 shows the neutron energy spectra for the reaction p + ^{208}Pb at 256 MeV [31] and 3 GeV [32]. The JQMD results of the neutron energy spectra agree well with the data from 1 MeV up to the beam energy.

In Fig. 7 we plot the invariant cross sections of the proton (left-hand-side) and negative pion (right-hand-side) emission for the reaction p (3.17 GeV) + ^{27}Al [33]. These figures indicate the JQMD code can reproduce quit well the overall features of the outgoing protons and pions as well as neutrons without assuming any reaction mechanism, and without changing the parameter set.

Next we have analyzed the fragment production from the proton induced reaction. In Fig.8, we show the production cross sections of various fragments for p (1.5 GeV) + ^{56}Fe reaction

[34]. It is clearly concluded that the JQMD code reproduces well the fragment production cross sections in the whole mass region, including the light clusters such as α and intermediate mass fragments (IMF) (A ~ 20 to 30) except for ^{7}Be where the results of JQMD underestimate the data by approximately 2 order of magnitude.

4.3. Results of heavy-ion reactions

So far the QMD model has shed light on several exciting topics in heavy-ion physics, e.g. the multi-fragmentation, the flow of the nuclear matter, and the energetic particle productions [35]. Here we show two examples of the basic observables from heavy-ion reactions calculated by the JQMD code.

In Fig.9(a) we represent the results of π^- energy spectra for the reaction ^{12}C + ^{12}C at 800 MeV/nucleon. The result of JQMD reproduces the experimental data [36]. We notice that this calculation has been done in the same formulation and also with the same parameter set as used in the nucleon-induced reactions.

Next example is the neutron energy spectra from the reaction ^{12}C + ^{208}Pb at 400 MeV/nucleon, which is shown in Fig.9(b). The neutron produced in heavy-ion reactions is very important in the shielding design of new facilities because of its large attenuation length in shielding materials. Recently, secondary neutrons from heavy-ion reactions have been systematically measured using thin and thick targets by HIMAC of NIRS (National Institute of Radiological Sciences), Japan [37,38]. Fig,9(b) shows that the QMD code roughly reproduced the measured cross sections for the C beams.

From these comparisons for nucleus-nucleus reactions, the predictive power of the QMD code seems to be less than that for nucleon induced reactions. Furthermore, it is reported that the results of the fragment production cross section are not so good particularly for the intermediate mass fragments [39]. Another problem of the QMD model is the calculation time, which is about ten to hundred times longer than that of the intra-nuclear cascade codes. In spite of these problems, there are two reasons that we should develop the QMD model further. First, many simulation codes based on the intra-nuclear cascade and evaporation model have been developed with including new parameters and ingredients. However, most of them are not designed to treat nucleus-nucleus collisions. Second, the improvement of the QMD model is focused on that of the effective interactions, which is closely related to the fundamental nuclear physics [40]. This is a very nice opportunity for the collaboration of the fundamental nuclear physics and the application field.

5. Summary

We have described two simulation codes JAM and JQMD which describe the intermediate and high energy nuclear reactions in the particle and heavy ion transport code system PHITS. By using these nuclear reaction models, PHITS can simulate various phenomena including hadron-nucleus reactions with energies up to 200 GeV, nucleus-nucleus collisions from 10 MeV/u up to 100 GeV/u and transports of heavy-ions in the materials as well as the neutrons down to 10^{-5} eV and leptons.

ACKNOWLEDGEMENT

The author wishes to acknowledge the other members of the PHITS development team: Hiroshi Iwase (KEK), Tatsuhiko Sato, Yosuke Iwamoto, Norihiro Matsuda, Yukio Sakamoto, Hiroshi Nakashima (JAEA), and Davide Mancusi, Lembit Sihver (Chalmers Univ.).

REFERENCES

[1] H. Iwase, K. Niita and T. Nakamura, *J. Nucl. Sci. Technol.* **39**, 1142 (2002); K. Niita, T. Sato, H. Iwase, H. Nose, H. Nakashima, L. Sihver, *Radiat. Meas.* **41**, 1080 (2006).

[2] Y. Nara, N. Otuka, A. Ohnishi, K. Niita and S. Chiba, *Phys, Rev.* **C61**, 024901 (2000).

[3] K. Niita, S. Chiba, Toshiki Maruyama, Tomoyuki Maruyama, H. Takada, T. Fukahori, Y. Nakahara, A. Iwamoto, *Phys. Rev.* **C52**, 2620 (1995).

[4] S. Chiba, O. Iwamoto, T. Fukahori, K. Niita, Toshiki Maruyama, Tomoyuki Maruyama, A. Iwamoto, *Phys. Rev.*, **C54,** 285 (1996), S. Chiba, M.B. Chadwick, K. Niita, Toshiki. Maruyama, Tomoyuki. Maruyama, A. Iwamoto, *Phys. Rev.*, **C53**, 1824 (1996).

[5] J. Aichelin, *Phys. Rep.* **202**, 233 (1991).

[6] J. F. Briesmeister, et al., "MCNP General Monte Carlo N-Particle Transport Code", Los Alamos National Laboratory report; LA-12625-M (1997).

[7] V. McLane, et al., "ENDF/B-VI Summary Documentation", BNL-NCS-17541 (1996).

Shibata, K., et al., "Japanese Evaluated Nuclear Data Library Version 3 Revision-3: JENDLE-3.3", *J. Nucl. Sci. Technol*. **39**, 1125 (2002).

[9] M. B. Chadwick, et al., "LA150 Documentation of Cross Sections, Heating, and Damage", Los Alamos National Laboratory report; LA-UR-99-1222 (1999).

J. A. Halbleib, et al., "ITS Version 3.0: The Integrated TIGER Series of Coupled Electron/Photon Monte Carlo Transport Codes", *SAND91-1634* (1992).

S. Furihata, *Nucl. Instr. and Meth*. **B171,** 251 (2000).

T. W. Armstrong and K. C. Chandler, "A Fortran program for computing stopping powers and ranges for muons, charged pions, protons, and heavy ions". *ORNL-4869*, Oak Ridge National Laboratory, (1973).

[13] C. Scheidenberger and H. Geissel, *Nucl. Instr. Meth.* **B136**, 114 (1998).K. Niita, H. Takada, S. Meigo and Y. Ikeda, *Nucl. Instr. and Meth.* **B184,** 406 (2001).[15] R. K. Tripathi, F. A. Cucinotta, and J. W. Wilson, *Nucl. Instr. and Meth*. **B117**, 347 (1996); R. K. Tripathi, J. W. Wilson, and F. A. Cucinotta, *Nucl. Instr. and Meth*. **B129**, 11 (1997); R. K. Tripathi, F. A. Cucinotta, and J. W. Wilson, *Nucl. Instr. and Meth*. **B155**, 349 (1999).

[16] W. Shen, B. Wang, J. Feng, W. Zhan, Y. Zhu and E. Feng, *Nucl. Phys*., **A491**, 130 (1989).

[17] W.-M.Yao et al. (Particle Data Group), *J. Phys.* **G 33**, 1 (2006).

[18] X.N. Wang and M. Gyulassy, *Phys. Rev*., **D44**, 3501 (1991); X.N. Wang, *Phys. Rep.*, **280**, 287 (1997); X.N. Wang and M. Gyulassy, *Comp. Phys. Comm.,* **83**, 307 (1994).

[19] T. Sjostrand, *Comp. Phys. Comm.,* **82**, 74 (1994).

[20] B. Zhang, *Comp. Phys. Comm.,* **109,** 70 (1997); B. Zhang and Y. Pang, *Phys. Rev.,***C56**, 2185 (1997); B. Zhang, M. Gyulassy and Y. Pang, *Phys. Rev.,* **C58**, 1175 (1998).

[21] G. Kortemeyer, W. Bauer, K. Haglin, J. Murray and S. Pratt, *Phys. Rev.*,**C52**, 2714 (1995).

[22] B. Andersson, A. Tai and Ben-Hao Sa, *Z. Phys.*, **C70**, 499 (1996).

[23] Bonn-Hamburg-München Collaboration, V. Blobel, *et al*., *Nucl. Phys.*, **B69**, 454 (1974).

[24] A. Baldni, V. Flaminio, W.G. Moorhead and D.R.O. Morrison, "Total Cross-Sections for Reactions of High Energy Particles,", Springer-Verlag, Berlin, vol. 12a and vol. 12b, 1988.

[25] High Energy Reactions Analysis Group, CERN Report CERN-HERA 83-01 and 83-02, 1983.

[26] E802 Collaboration, Abbott T., *et al*., *Phys. Rev.*, **D45** 3906 (1992)

[27] H. Nakashima, *et.al*., "Research Activities on Nuetronics under ASTE Collaboration at AGS/BNL", *Proc. of Int. Conferece on Nuclear Data for Science and Technology,*

Tsukuba, Japan, 2001.; "Current Status of the AGS Spallation Target Experiment", *Proc. of the 6th meeting of the Task Force on SATIF*, SLAC, 2002.
[28] S. Furihata, *Nucl. Instr. and Meth.,* **B171**, 251 (2000).
[29] S. Chiba, O. Iwamoto, T. Fukahori, K. Niita, Toshiki Maruyama, Tomoyuki Maruyama, A. Iwamoto, *Phys. Rev.*, **C54**, 285 (1996).
[30] M.B. Chadwick, S. Chiba, K. Niita, T. Maruyama, A. Iwamoto, Phys. Rev., C52, 2800 (1995); S. Chiba, M.B. Chadwick, K. Niita, Toshiki. Maruyama, Tomoyuki. Maruyama, A. Iwamoto, Phys. Rev., C53, 1824 (1996).; S. Chiba, K. Niita, O. Iwamoto, Phys. Rev., C54, 3302 (1996).
[31] W. B. Amian, B. C. Byrd, C. A. Goulding, M. M. Meier, G. L. Morgan, C. E. Moss, and D. A. Clark, Nucl. Sci. and Eng., 112, 78 (1992).
[32] K. Ishibashi, et al., J. Nucl. Sci. Technol., 32, 827 (1995).
[33] H. En'yo, et al., Phys. Lett., B159, 1 (1985).
[34] R. Michel, et al., Nucl. Instr. and Meth., B103, 183 (1995).
[35] J. Aichelin: Phys. Rep., 202, 233 (1991).
[36] I. Tanihata et al., Phys. Lett., B87, 349 (1979).
[37] Y. Iwata et al., Phys. Rev., C64, 054609 (2001).
[38] T. Kurosawa, et al., Nucl. Sci. and Eng., 132, 30 (1999); Journal of Nucl. Sci. and Technol. 36-1, 42 (1999); Nucl. Instr. and Meth. A430, 400 (1999); Phys. Rev. C62, 044615 (2000).
[39] Toshiki Maruyama, K. Niita, Tomoyuki Maruyama, A. Iwamoto, Prog. Theor. Phys., 98, 87 (1997).
[40] Toshiki Maruyama, K. Niita, K. Oyamatsu, Tomoyuki Maruyama, S. Chiba, A. Iwamoto, Phys. Rev., C57, 655 (1998).

FIGURES

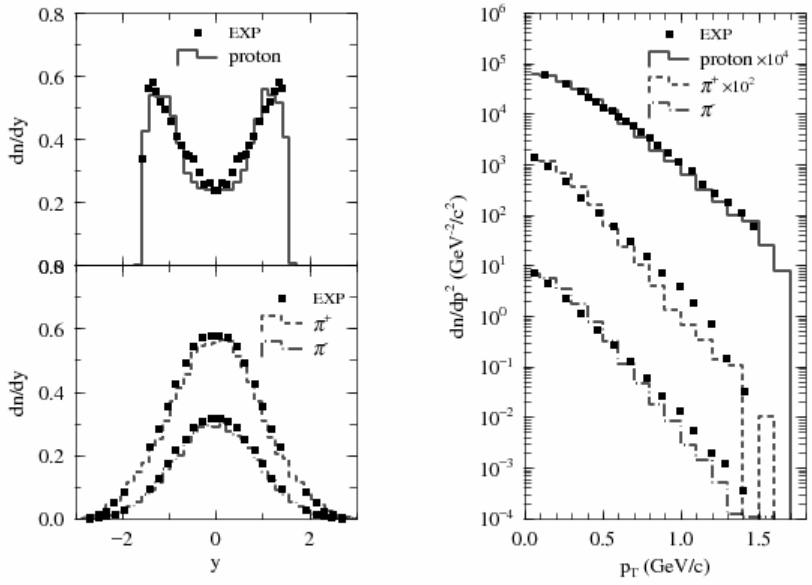

Fig. 1. Rapidity y distributions (left panel) and the transverse momentum distributions (right panel) of proton, π^+ and π^- in pp collisions at 12 GeV/c. Histograms are the results obtained from JAM, while the data are from [23].

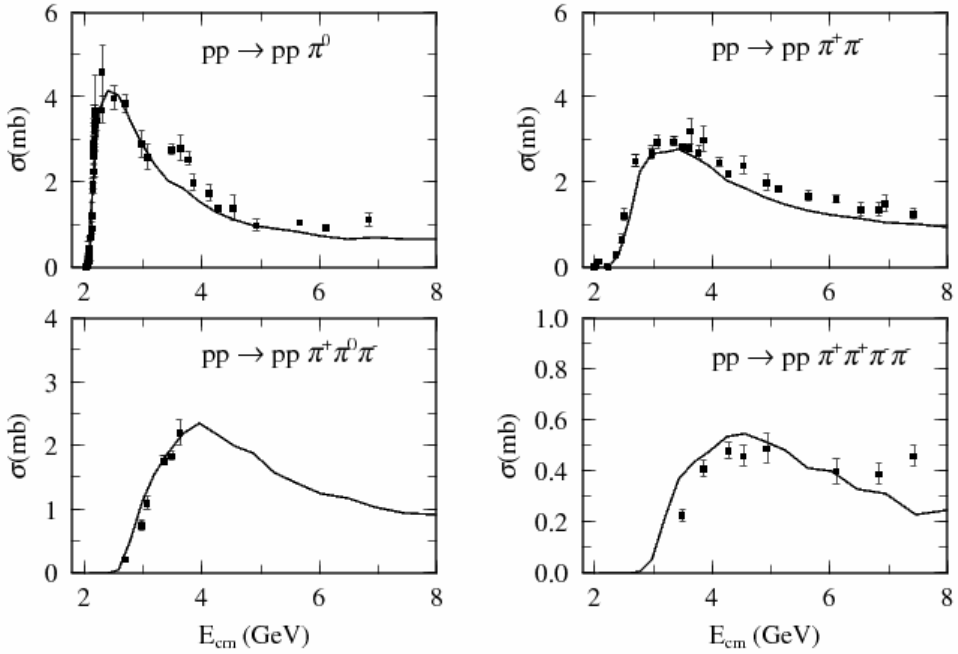

Fig. 2. Energy dependence of the exclusive pion production cross sections for proton-proton reactions as a function of c.m. energy. Solid lines are the results obtained from JAM, while the data are from ref.[24].

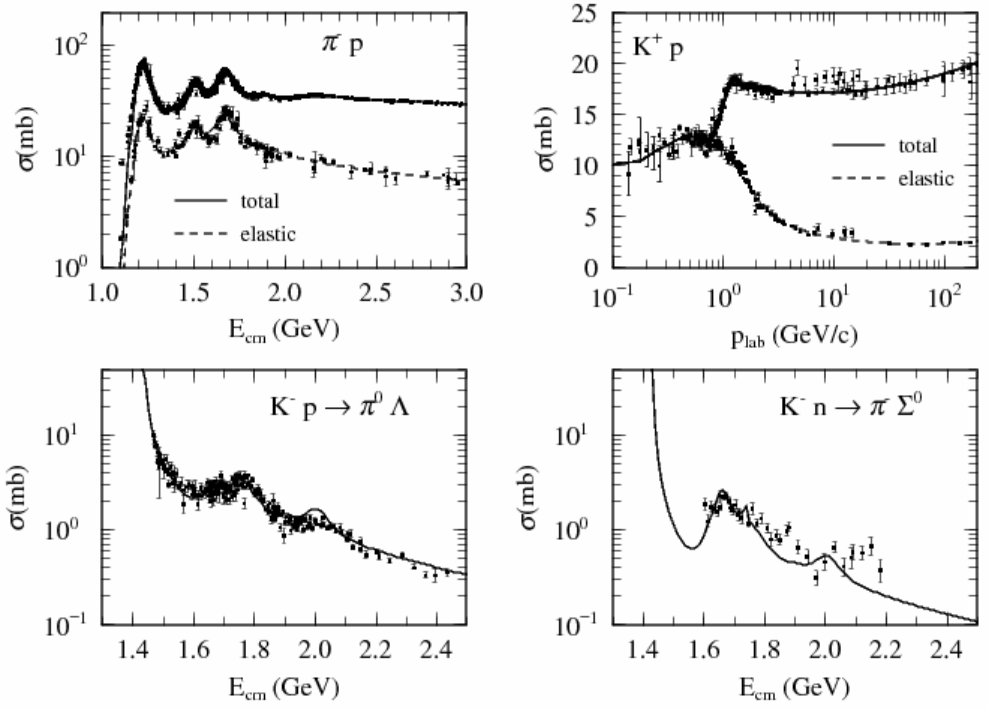

Fig. 3. Parameterization of the total and elastic $\pi^- p$ and $K^+ p$ cross sections (upper panel), and the energy dependence of the exclusive cross sections of $K^- p \to \pi^0 \Lambda$ and $K^- n \to \pi^- \Sigma^0$ (lower panel). Data are taken from ref.[25].

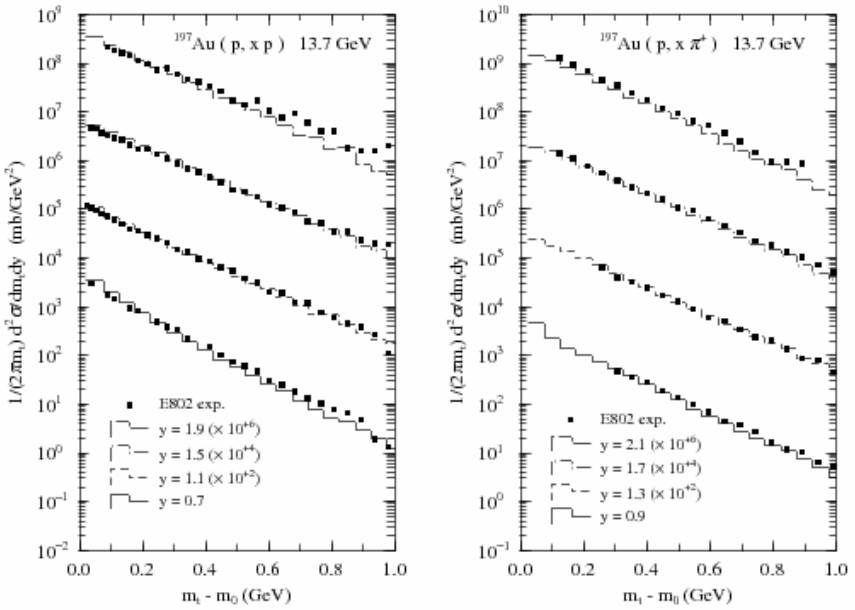

Fig. 4. Invariant transverse mass distribution of proton (left panel) and π^+ (right panel) from proton on thin Au target reaction at 13.7 GeV. The results of JAM (histograms) and data [26] are plotted for each rapidity y bin quoted in the figure.

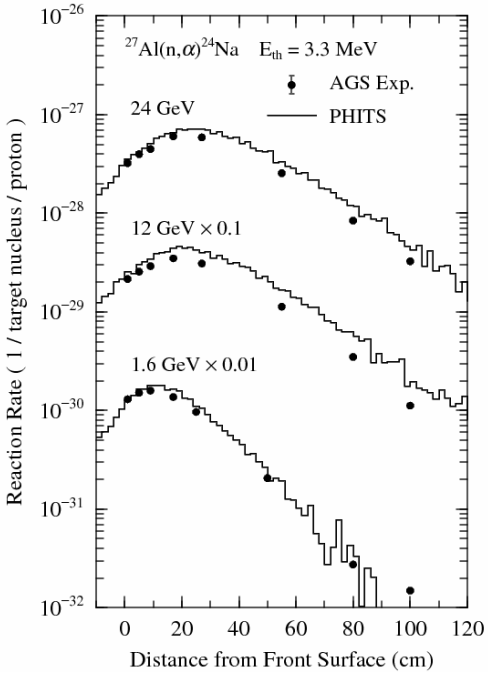

Fig. 5. Distribution of the $^{27}Al(n,\square)^{24}Na$ reaction rates along the cylindrical surface of a mercury target bombarded with 1.6, 12 and 24 GeV protons. The solid histograms denote the results of PHITS.

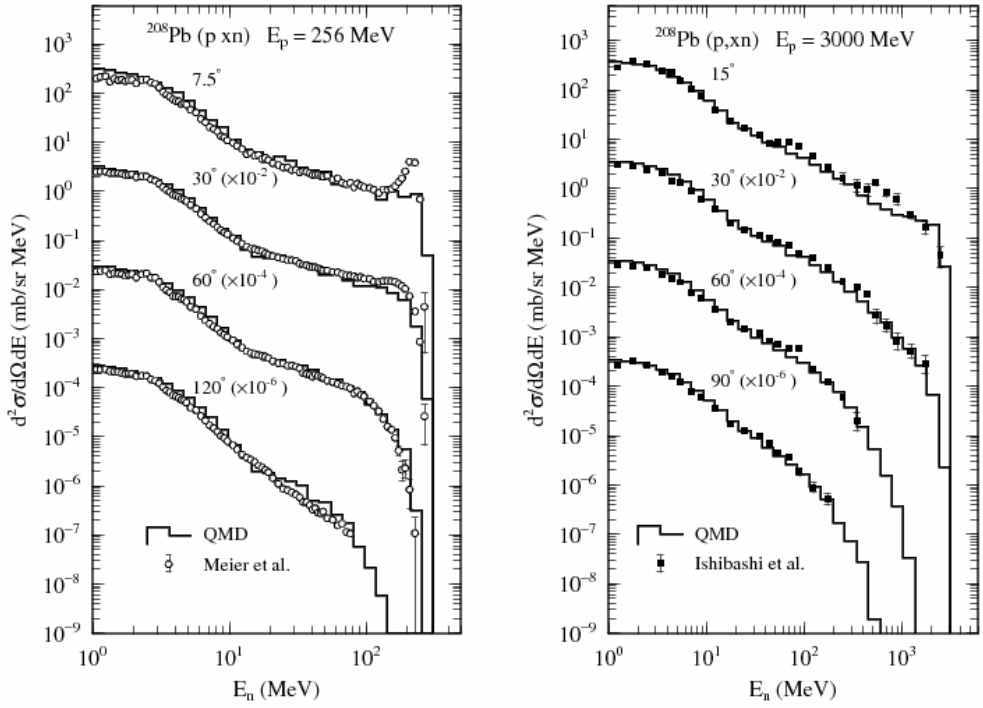

Fig. 6. Neutron energy spectra for the reaction p + ^{208}Pb at different laboratory angles as indicated in the figure. The incident energy is 256 MeV (left-hand-side) and 3 GeV (right-hand side). The solid histograms are the results of QMD and the open circles and the full boxes with error bars denote the experimental data taken from refs.[31,32].

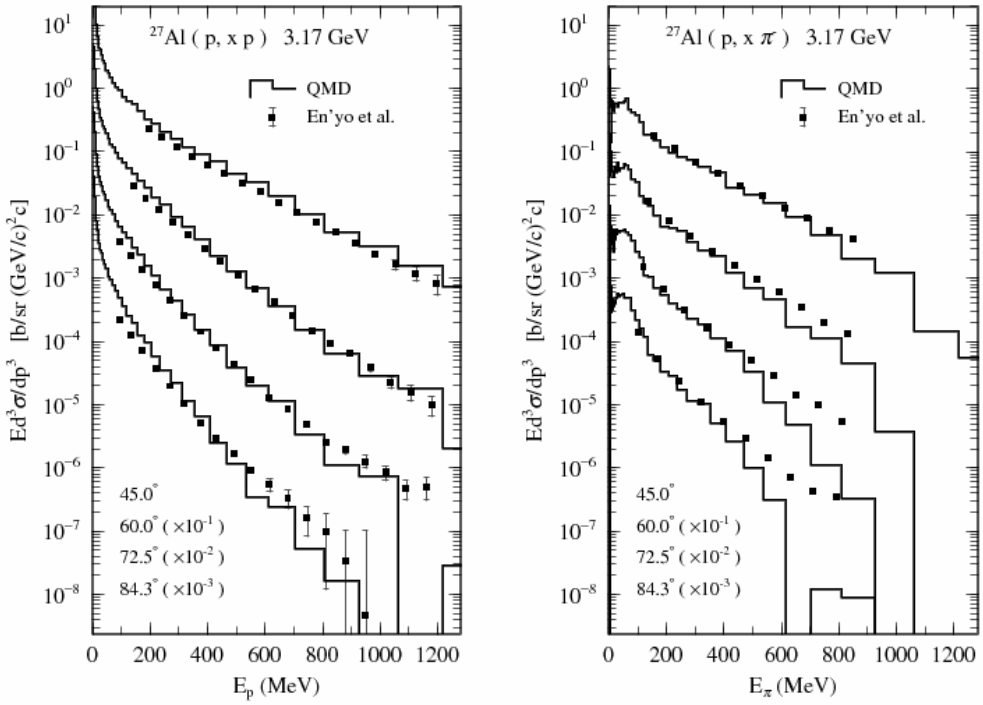

Fig. 7. Invariant cross sections of the proton (left-hand-side) and negative pion (light-hand-side) emission for the reaction p (3.17 GeV) + ^{27}Al at different laboratory angles as indicated

in the figure. Full boxes with error bars are the experimental data taken from ref.[33] and the results of QMD are denoted by solid histograms.

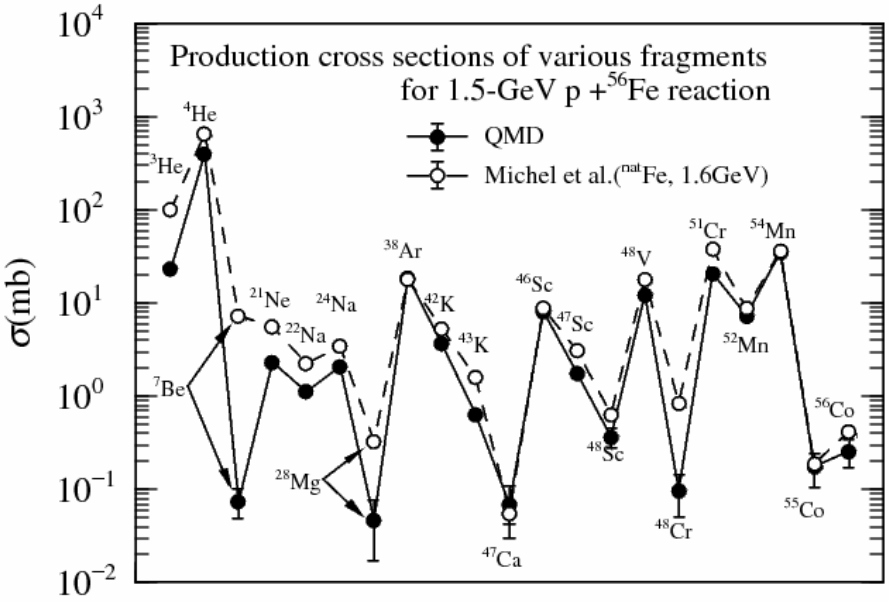

Fig. 8. Production cross sections of various fragments for p (1.5 GeV) + ^{56}Fe reaction. The full circles connected by a solid line denote the results of QMD, while the open circles connected by a dashed line are obtained experimentally by Michel et al. measured at 1.6 GeV for ^{nat}Fe [34].

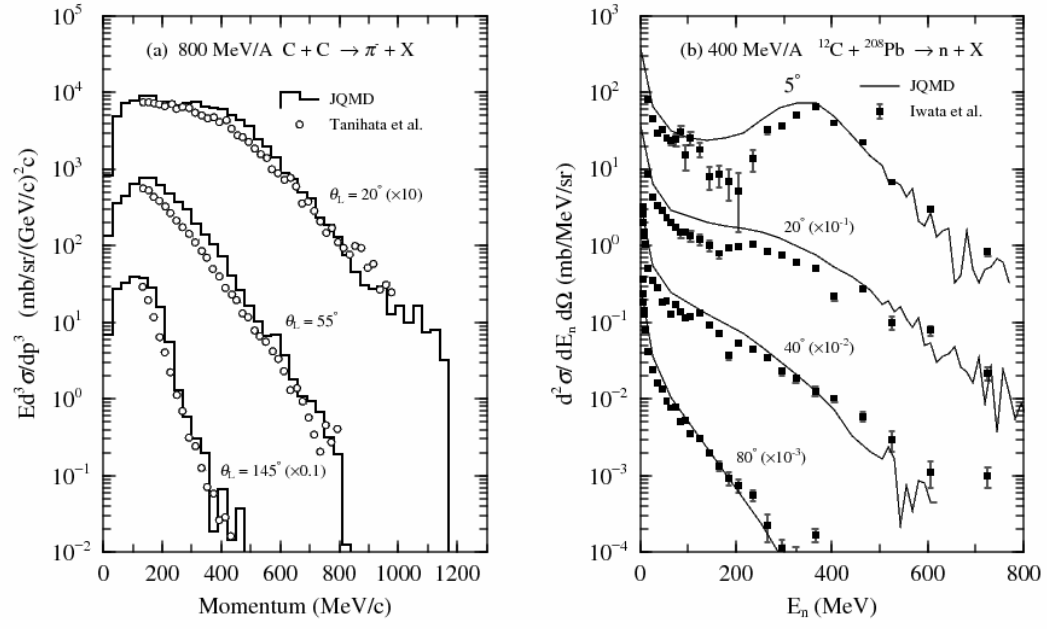

Fig. 9. (a) (left panel) π^- energy spectra for the reaction ^{12}C (800 MeV/nucleon) + ^{12}C and (b) (right panel) neutron energy spectra for the reaction ^{12}C (400 MeV/nucleon) + ^{208}Pb at different laboratory angles as indicated in the figure. The solid histograms and the solid lines are the results of the QMD and the open circles and solid squares denote the experimental data taken from ref.[36,37].

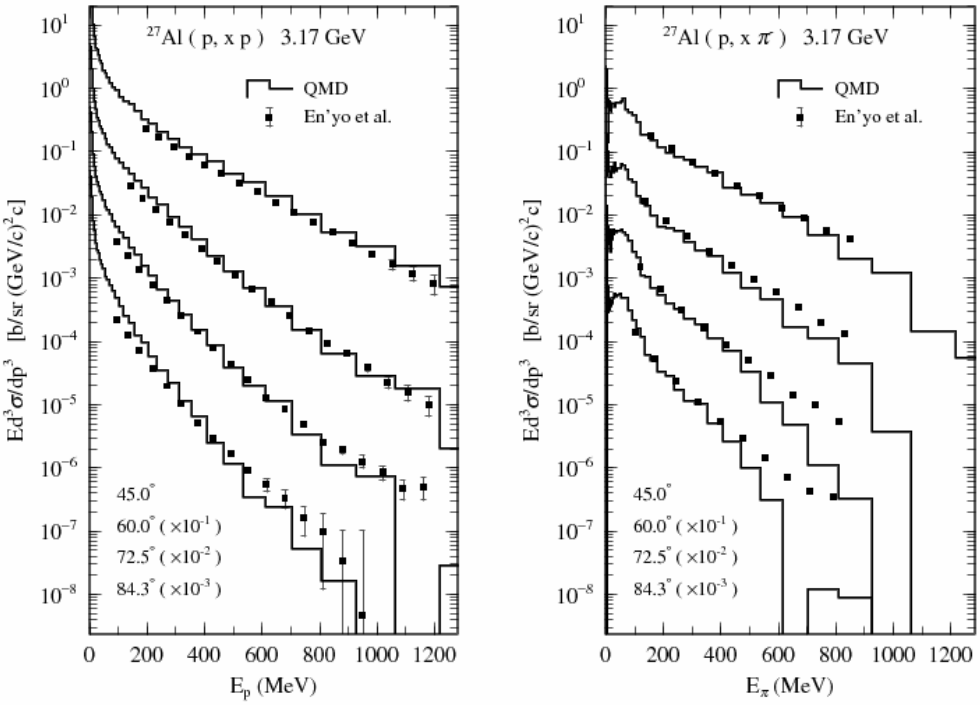

Fig. 7. Invariant cross sections of the proton (left-hand-side) and negative pion (light-hand-side) emission for the reaction p (3.17 GeV) + ^{27}Al at different laboratory angles as indicated in the figure. Full boxes with error bars are the experimental data taken from ref.[33] and the results of QMD are denoted by solid histograms.

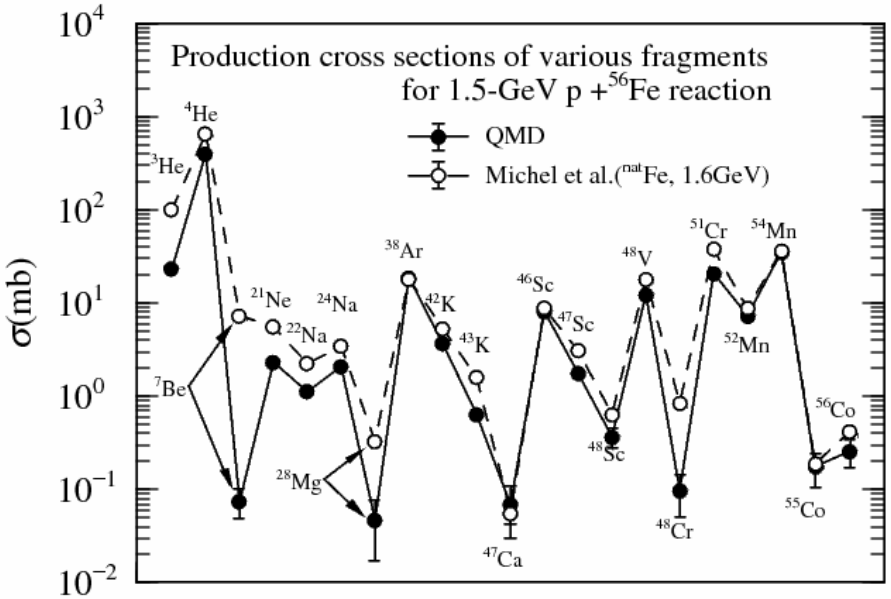

Fig. 8. Production cross sections of various fragments for p (1.5 GeV) + ^{56}Fe reaction. The full circles connected by a solid line denote the results of QMD, while the open circles connected by a dashed line are obtained experimentally by Michel et al. measured at 1.6 GeV for ^{nat}Fe [34].

Experimental data on evaporation and pre-equilibrium emission in GeV p-induced spallation reactions

NESSI@COSY & PISA@COSY experiment (data up to 2.5 GeV)

F. GOLDENBAUM

Forschungszentrum Jülich GmbH,
Institut für Kernphysik,
Jülich, Germany

Abstract. This contribution will focus on the latest progress on data analysis of two experiments both being performed at the Cooler Synchrotron Juelich, Germany and partly being subject of nuclear data achieved in the NUDATRA domain of the FP6 IP EUROTRANS. The objective of this contribution is to provide reliable and comprehensive experimental data serving as benchmarks for code development and validation in the 200-2500 MeV energy range. To scrutinize the codes under consideration of the current spallation workshop smr1930 and to calculate as reliably as possible quantities related to high energy reactions, hadronic interaction lengths, reaction cross sections, average particle multiplicities, particle multiplicity and double differential energy distributions are investigated. In this context the latest results of crutial experiments performed at COSY essentially on helium and intermediate mass production will be presented and compared to model predictions. The model comparision here is just shown as an exemplary sample and shall by no means be understood as an "a priori" bias.

1. Introduction

In the following, the emphasis will be on the description of nuclear data taken by the NESSI (NEutron Scintillator and SIlicium detector) and the PISA (Proton Induced SpAllation) experiment installed at the Cooler Synchrotron in Juelich, Germany as shown in Fig. 1. The typical energy range of incident protons is 150 MeV – 2.5GeV with luminosities for the internal experiment PISA up to $6x10^{34}$ $cm^{-2}s^{-1}$.

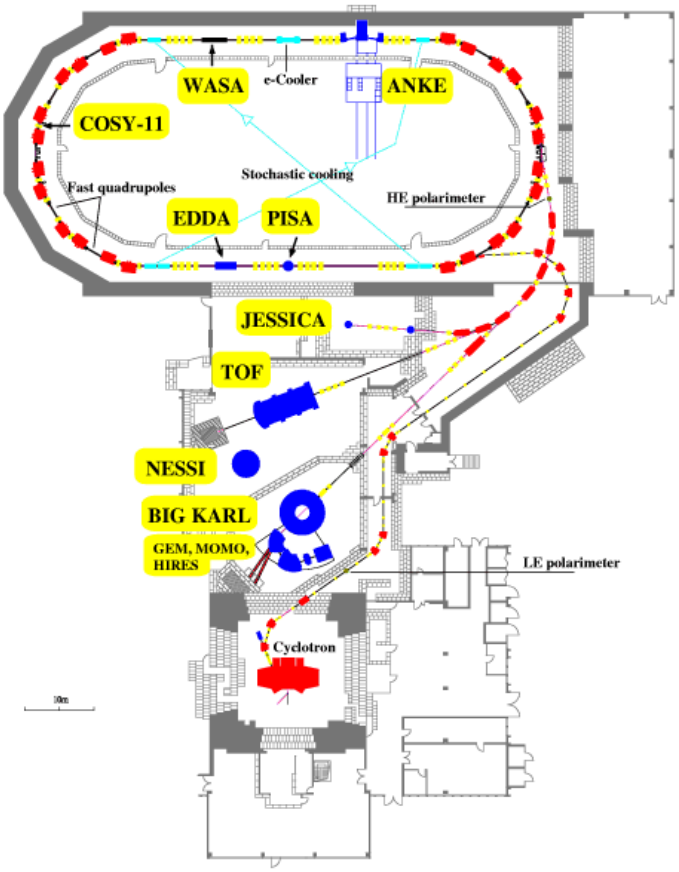

Fig. 1. Location of NESSI and PISA experiment at the Cooler Synchrotron COSY.

Whenever possible the numerical data shown in the following are made available for all participants of this spallation workshop on the smr1930 devoted webpage. For a detailed description of the experiment the interested reader is referred to the references given there, respectively. The data are at the same time also relevant for the EU- FP6 integrated project EUROTRANS – (DM5 NUDATRA Nuclear data for transmutation of nuclear waste). The goal of that domain is to improve nuclear data evaluated files and models which involves sensitivity analysis and validation of simulation tools, low and intermediate energy nuclear data measurements, nuclear data libraries evaluation at low and medium energies, and high energy experiments and modeling. In the following the focus is on NUDATRA WP5.4---High energy experiments and modeling. This workpackage aims at the investigation of:

- pA (spallation) reactions in the GeV regime
- data measured from exclusive experiments for testing, validating and developing theoretical models
- double differential cross sections (DDXS) $d\sigma /dEd\Omega$ of light charged particles (LCP=p,d,t,^{3}He,^{4}He,...) and intermediate mass fragments (IMFs, $Z \leq 16$) in spallation and fragmentation p-induced reactions (0.1-2.5 GeV, C to Au)
- reaction mechanism of pN reactions in terms of time scales, simultaneous or sequential emission of IMFs, origin of pre-equilibrium and evaporation processes

2. Light charged particle and IMF production

An example of the capability of the NESSI experiment is presented in Fig.2. It shows the eventwise correlation of neutron versus charged particle multiplicities measured with the two almost 4π devices. The best description of the coincidence data for multiplicities LCP vs Mn can be found in Ref.[Let02].

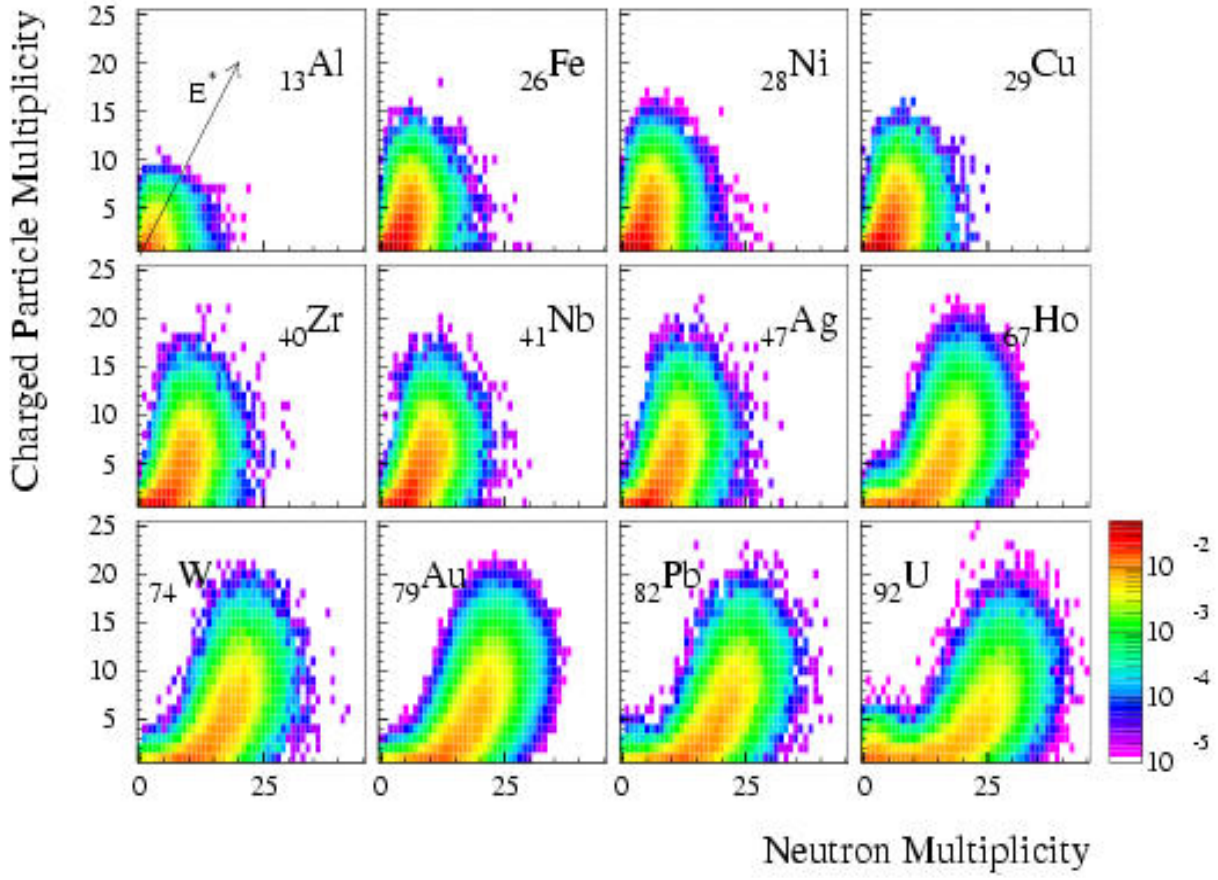

Fig. 2. Correlation of measured (NESSI) light charged particle(LCP)-vs. neutron-multiplicity for 2.5 GeV proton-induced spallation reactions on various targets from Al to U. The color scale gives the relative yield for each target per multiplicity bin, the thermal excitation is following indicated arrow.

In figure 7 of Ref.[Let02] there is even given the comparison of such a correlation between experiment and filtered INC+GEMINI calculation. The particular advantage of the presentation in Fig.7 of Ref.[Let02] is that the correlation is shown both for GEMINI (evaporation only) as well as for the full calculation (INC+ GEMINI). The z-scale in that figure presents the production cross section expressed in mbarn per M_n and M_{LCP} units as a function of LCP and neutron multiplicity. The filter applied for the neutrons i.e. the effciency for detecting a neutron in the 4π neutron Ball NESSi is parameterized by the following polynomial function which could easily be implemented in any code:

$$efficiency(E_{kin}) = 0.820652 + 0.00689154\ E_{kin} - 0.00423934\ E_{kin}^{\ 2} + 0.000370167\ E_{kin}^{\ 3}$$
$$-1.80244E-05\ E_{kin}^{\ 4} + 5.2007E_{kin}^{\ 5} - 8.97261E-09\ E_{kin}^{\ 6} + 9.06944E-11\ E_{kin}^{\ 7} - 4.95096E$$
$$-13\ E_{kin}^{\ 8} + 1.12679E-15\ E_{kin}^{\ 9}$$

i.e. low energy neutron are detected with an efficiency about 82% while for higher energetic neutrons (>100MeV) the efficiency drops down to 12-15%. This parameterization is published in ref.[Let00] and shown in graphical presentation in Fig.17.

As an example for light charged particle production, double differential energy spectra of ^{1,2,3}H and ^{3,4}He ejectiles following 1.2 GeV p-induced reactions on Ta target as measured by the NESSI collaboration at COSY-Juelich is shown for different angles in respect to the incident proton in Fig. 3.

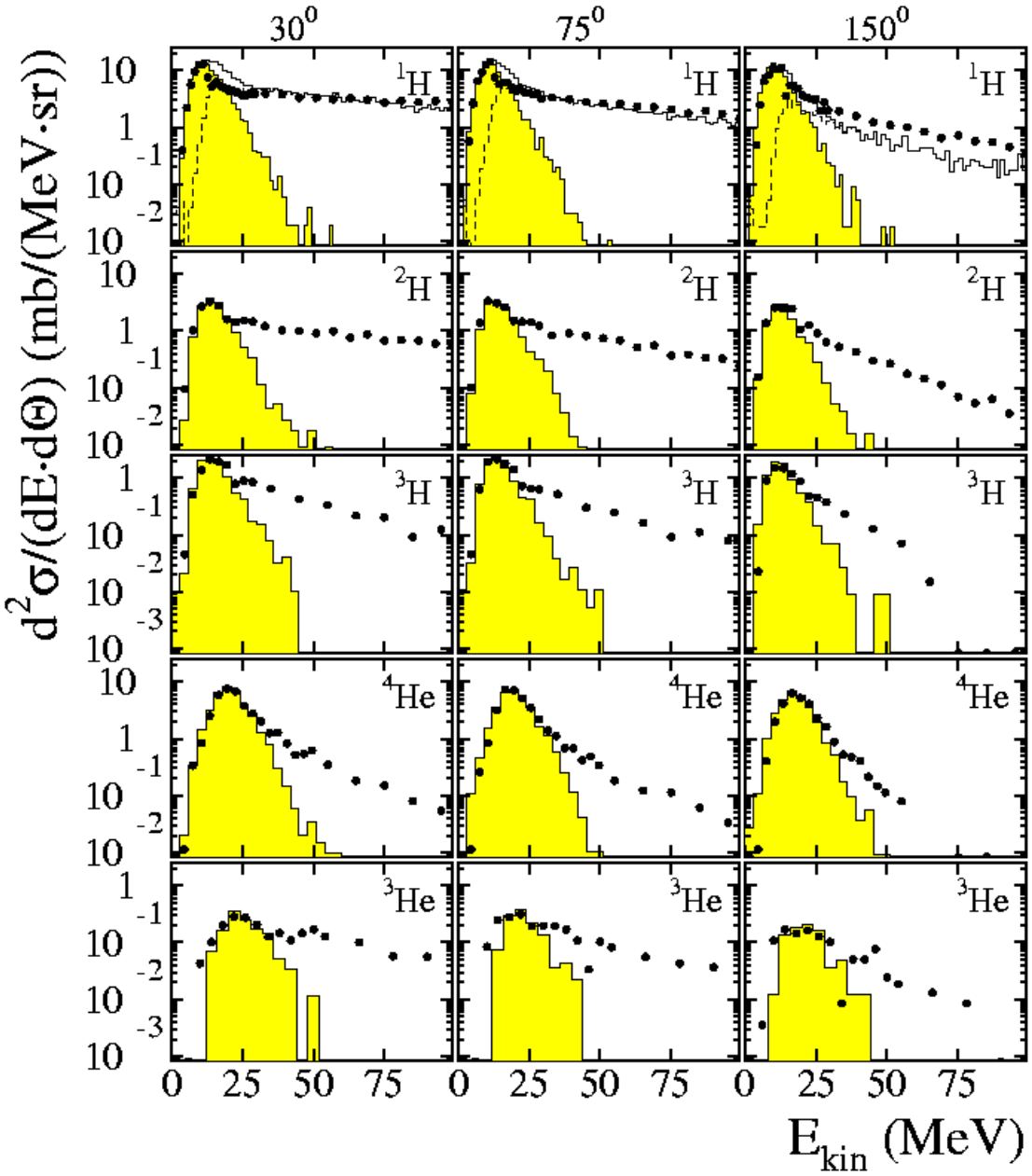

Fig. 3. Energy spectra of ^{1,2,3}H and ^{3,4}He for 1.2 GeV p+Ta. dots: experimental data, shaded histogram: calculated evaporation spectra, dashed histogram: pre-equilibrium protons as calculated by INCL2.0 [Her06].

The experimental data clearly feature two components, an evaporation component dominant for all angles and at low kinetic energies and a high energy component all the more pronounced the smaller the angle of the ejectile in respect to the incident proton is. Here [Her06] for the theoretical description the INCL2.0 [Cug97] intranuclear cascade code is

coupled to the evaporation code GEMINI [Cha88]. Only for protons both components can be well described. Due to the lack of composite particle emission in the early phase of the reaction in the INCL2.0 model, the high energy tails of the spectra for d, t, ^{3,4}He are not described by the calculations. The shape of the calculated *evaporation* component (shaded yellow histogram in Fig.3) however is well reflected also for composite particles.

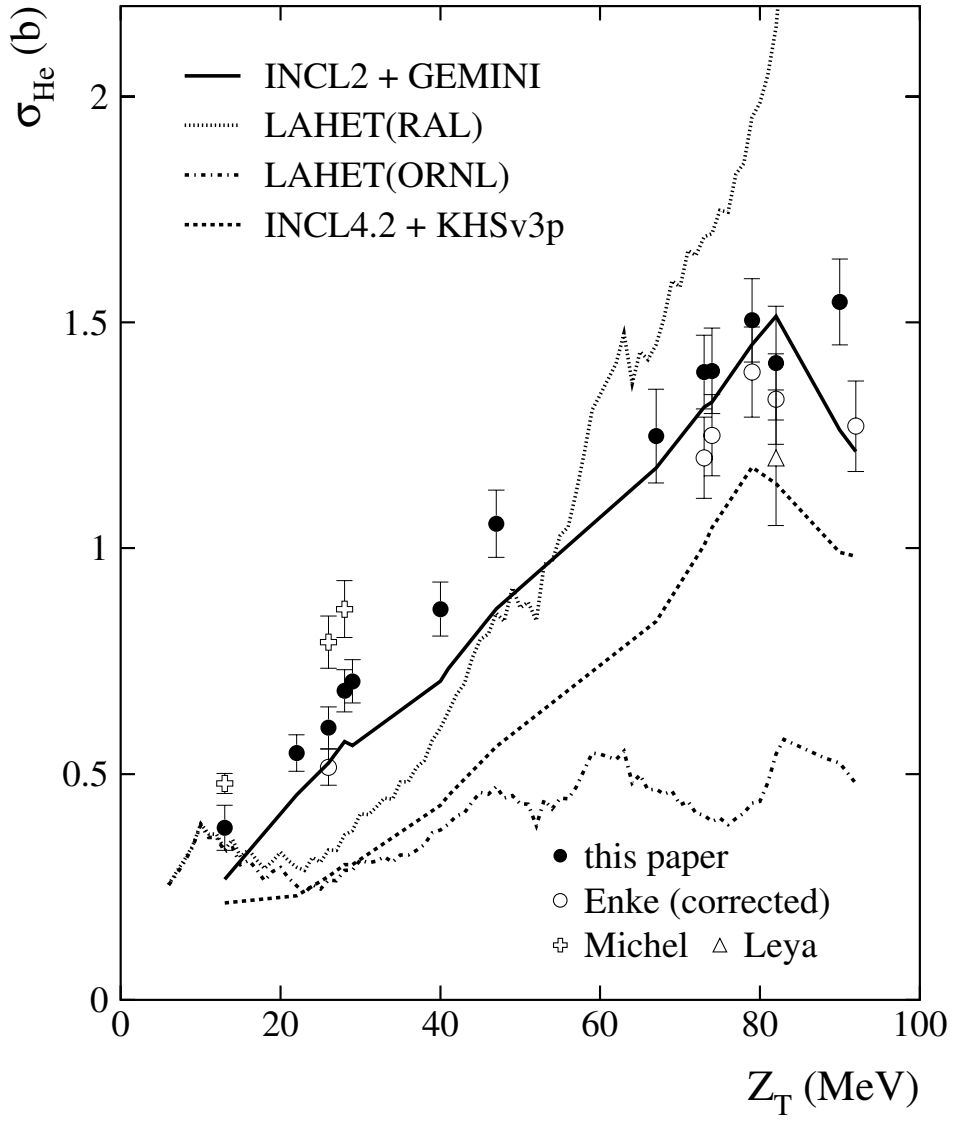

Fig. 4. Total He (^{3}He+^{4}He) production cross sections for 1.2GeV p+X (NESSI) symbols: experimental data, lines calculation by INCL2.0+GEMINI, LAHET and new version of INCL [Her06].

The calculations confronted with the measured total He (^{3}He+^{4}He) production cross sections as shown in Fig.4 generally tend to underestimate the experimental data, because of 5-20% pre-equilibrium emission (not taken into account in INCL+GEMINI). Although it is obvious that there is some discrepancies between different sets of data, Fig. 4 clearly exhibits the need to solve deficiencies or discrepancies of the different models.

For 1.2 GeV p+Au in Fig. 5, the angular distribution of disentangled evaporation (left panel) and pre-equilibrium (right panel) components are shown (details see [Her06]). For all particle species the evaporation exhibits an isotopic behaviour, while more directly emitted particles show larger forward/backward asymmetry. Note that for pre-equilibrium protons the angular dependence is well described in the INCL2.0 model. It would be certainly worth to compare the current experimental data [Her06] with e.g. the latest version of INCL4.3 [Bou04] including a coalescence formalism allowing for the cluster emission of composite nucleons (d, t, ^{3,4}He) in the early phase of the reaction (partly done already, cf. contribution of Alain Boudard et al.).

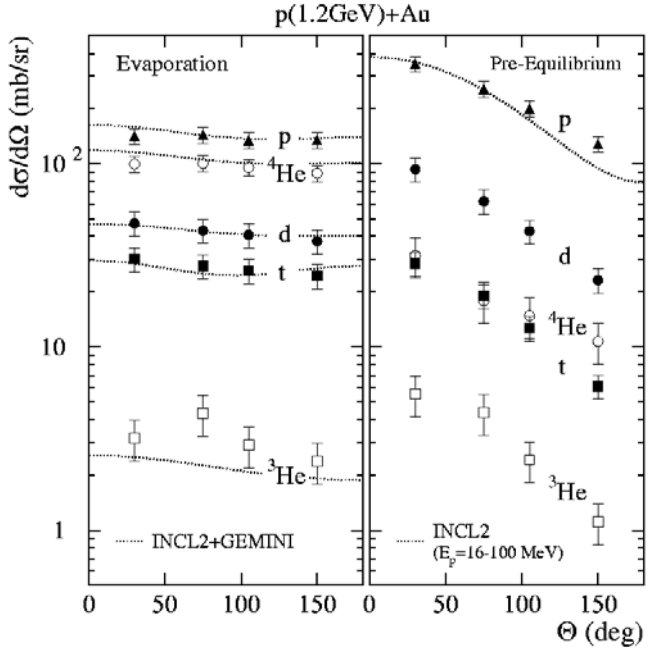

Fig. 5. Angular distributions of ^{1,2,3}H and ^{3,4}He for 1.2 GeV p+Au. symbols: experimental data, lines calculation by INCL2.0+GEMINI [Her06].

The production cross sections of ^{6,7,8,9}Li and ^{7,9,10}Be isotopes for 1.2 GeV protons on different targets (C to Au) as well as the total production cross sections σ_{Li} and σ_{Be} are shown in Fig.7. The production of all individual isotopes does not strongly depend on Z, respectively. When looking more carefully at the energy spectra of IMFs (shown in Fig.8), ones more as expected the combination of INCL2.0+GEMINI fails to describe the high energy tails of the energy spectra. Nevertheless in Fig.7 the calculated angle and energy integrated production cross sections agree generally rather well with the NESSI [Her06,Mic95,Dos65] data, because the pre-equilibrium component may amount to the total cross section only on the percent level. The lines representing the model prediction are reflecting the ejectiles coming from evaporation model only, i.e. GEMINI. The experimental data on ^{7}Be and ^{10}Be ejectiles measured for low Z-targets by mass spectrometry [Mic95] coincide with the systematics of the NESSI experiment [Her06]. In a similar presentation one observes the multiplicity/production cross sections of the neutron rich ^{6}He isotope strongly increasing with atomic number Z of the bombarded target (see Fig.6) -- a very similar behavior as the one which is observed for the "neutron rich" triton. In contrast to the ^{3,4}He isotopes, for ^{6}He the INCL2.0+GEMINI calculations *overestimate* the experimental results of Herbach et al.[Her06] by approximately 30%.

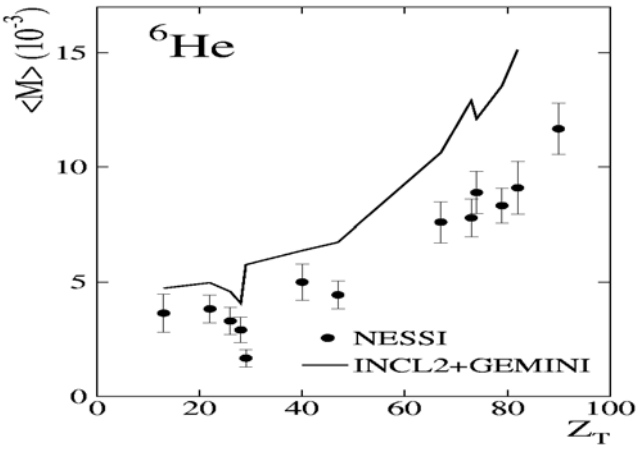

Fig. 6. Multiplicity of ^{6}He isotopes as function of target Z, bullets •: [Her06], line: INCL2.0+GEMINI.

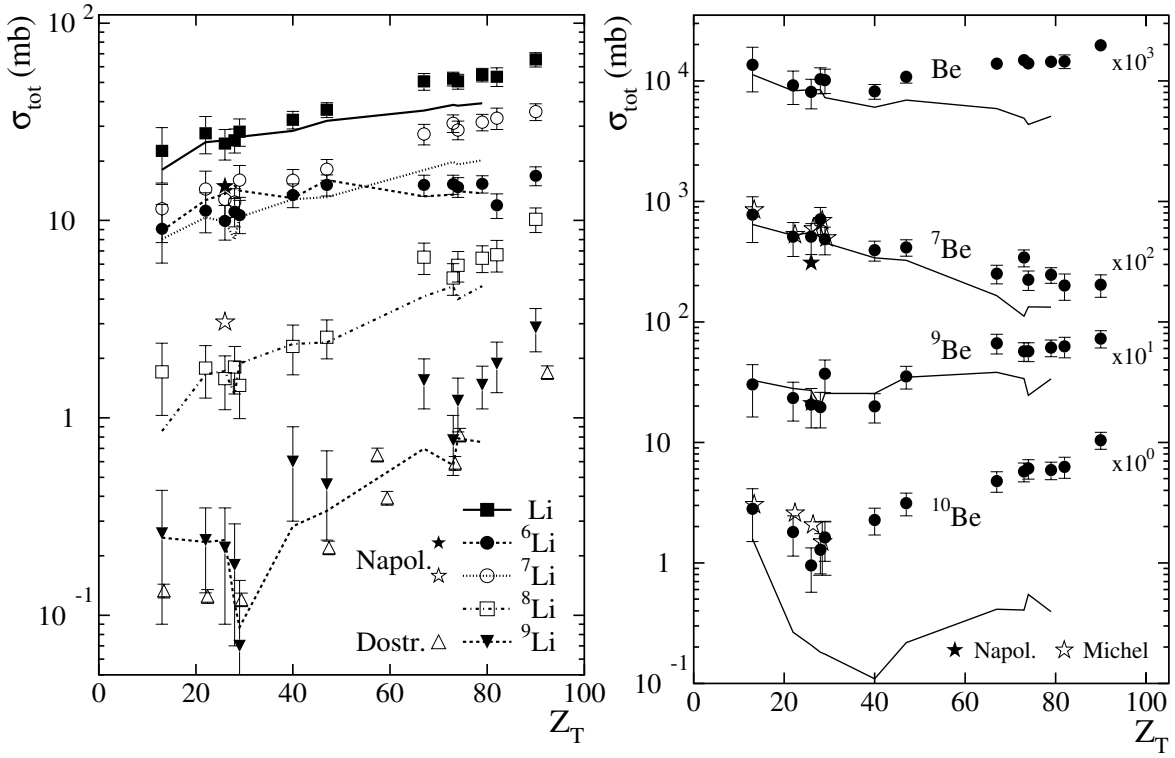

Fig. 7. Production cross section of ^{6,7,8,9}Li and ^{7,9,10}Be isotopes for 1.2 GeV p+X. bullets •: NESSI [Her06], triangle: Dostrovsky [Dos65], stars: R. Michel [Mic95] data, lines: calculation by INCL2.0+GEMINI.

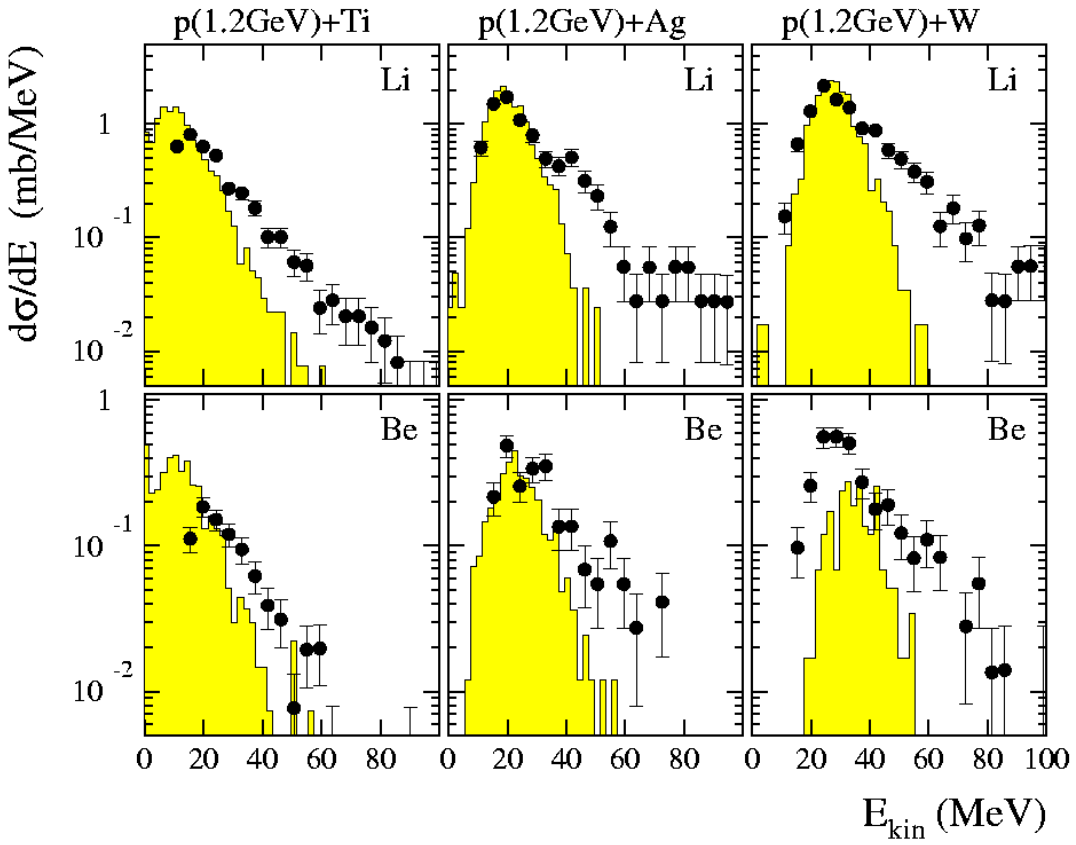

Fig. 8. Energy spectra of Li and Be for 1.2 GeV p+Ti, Ag and W; bullets •: [Her06], histogram: calculation by INCL2.0+GEMINI.

The international collaboration PISA (Proton Induced SpAllation) [pisa-web,Gol05,Bar03,Bub04} is aiming at a quite similar physics program as NESSI, however with a completely different setup and at an internal beam location. At the internal beam of COSY the investigation of the reactions induced by protons on thin targets (50-200 μg/cm^2) enables us to get the cross sections without the absorption and energy loss involved with the propagation of reaction products in the material of the target. The multiple circulation of the beam in the COSY ring is used to compensate for the small reaction rate of beam-protons with the thin targets. The advantage being higher statistics and more precise information on the very tails of double differential energy spectra---important in particular for rare decay channels and low production cross sections of i.e. IMFs. Typical very low energy thresholds and the upper detection limits for different ejectiles are given in the following table:

TABLE I: LOWER (E_{min}) AND UPPER (E_{max}) DETECTION THRESHOLD FOR VARIOUS ISOTOPES IN PISA EXPERIMENT

Particle	p	d	t	3He	4He	6Li	7Be	10B	11C	14N	16O
E_{min} [MeV]	2.0	2.6	3.0	2.0	2.5	4.0	4.5	9.0	11	14	16
E_{max}[MeV]*	160	215	250	580	650						

Isotope separation of the ejectiles was done by combining the information from multi-channel-plates (time-of-flight), silicon detector telescopes and Bragg curve spectroscopy (energy deposited inside Bragg curve detectors) allowing for the separation of following isotopes: ^{6}Li, ^{7}Li, ^{8}Li - ^{7}Be, ^{9}Be, ^{10}Be - ^{10}B, ^{11}B - ^{11}C, ^{12}C, ^{13}C, ^{14}C and ^{13}N, ^{14}N [Bub04]. In [Bub07], the double differential cross sections ($d\sigma^2/d\Omega dE$) were for the first time measured with good statistics for isotopically identified intermediate mass fragments produced by interaction of 2.5-GeV protons with the gold target. For that measurement the following individual isotopes of the elements from hydrogen to boron were resolved: ^{1,2,3}H, ^{3,4,6}He, ^{6,7,8,9}Li, ^{7,9,10}Be, ^{10,11,12}B, whereas for heavier ejectiles (from carbon to aluminium) only elemental identification was done. Measurements of these double differential cross sections (here for 9 angles 12, 15, 20, 35, 50, 65, 80, 100, 120 degree) and the investigation of the interaction of medium and high energy protons with atomic nuclei are important for providing benchmark data in the GeV incident p- energy range, understanding the complex reaction mechanism itself and testing the reliability of physical models describing the fast intranuclear cascade (INC) phase as well as the subsequent statistical decay from an equilibrated or thermalized hot nucleus. As already mentioned, a particular focus is on developing new models for the description of highly energetic composite particles [Bou04].

As discussed in detail in Ref.[Bub07], the energy spectra for all nuclear fragments, determined at several scattering angles---representatively shown for ^{4}He and ^{7}Li fragments in 2.5 GeV p-induced reactions on Au in Fig.9, appear to be of Maxwellian shape with exponential, high energy tail. The low energy part of the distribution is almost independent of angle, but the slope of high energy tail of the spectrum increases monotonically with the angle. The contribution strongly varying with angle is present at higher energy in all experimental spectra. The slope of this anisotropic energy contribution increases with the angle, what may be interpreted as effect of fast motion of an emitting source in the forward direction. The shape of the angle independent part of spectra can be reproduced by the two-stage model of the reaction, i.e. intranuclear cascade of the nucleon-nucleon and meson-nucleon collisions followed by statistical emission from an equilibrated residual nucleus. However, the absolute magnitude of the spectra predicted by two-stage model, using Boltzmann-Uehling-Uhlenbeck program (see contribution of Z.Rudy) for the intranuclear cascade and Generalized-Evaporation-Model (GEM) [Fur00] for statistical emission of fragments, is in agreement with the experimental data only for the light charged particles (H and He ions). Furthermore, the theoretical cross sections underestimate significantly the yield of heavier fragments at high kinetic energies for all ejectiles. This indicates that another mechanism plays an important role besides the standard two-stage mechanism.

The nice agreement shown in Fig.9 of the NESSI data [Let02] confronted with the PISA data [Bub07] on an absolute normalization scale(!) clearly give confidence to the completely independently analysed experimental data.

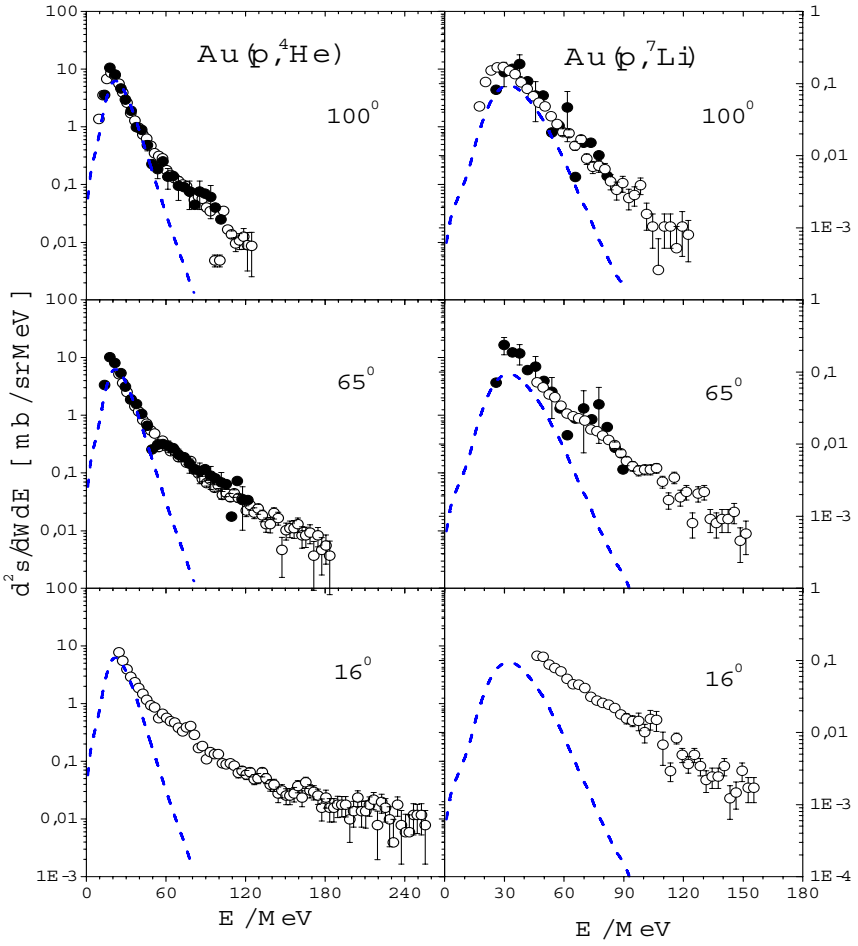

Fig. 9. Energy spectra of ^{4}He (left column) and ^{7}Li particles (right column) for 2.5 GeV p+Au; bullets•: [Let02] (NESSI-exp.), circ° [Bub07] (PISA-exp.) for corresponding emission angles; The lines show the prediction of evaporation of ^{4}He and ^{7}Li evaluated by means of GEM program [Fur00] from excited residual nuclei of the first stage of the reaction with properties extracted from BUU calculations.

In Fig.10 (left panel), open circles represent typical spectra of protons, deuterons and tritons measured in the PISA experiment [Bub07] by telescope consisted of silicon semiconductor detectors and 7.5 cm thick scintillating detector CsI placed at scattering angle of 65 degree in respect to the proton beam. The dashed lines show evaporation contribution evaluated by means of the BUU and Generalized Evaporation Model whereas the full lines correspond to phenomenological model of two emitting sources described in detail in Ref.[Bub07]. Note the change of the scale for the triton spectrum. The right panel of Fig.10 showns typical energy spectra of helium ions ^{3,4,6}He measured by telescope consisted of silicon semiconductor detectors placed at scattering angle of 35 degree in respect to the proton beam - open circles. Note different vertical scales for each spectrum. The lines have the same meaning as for H-isotopes in the left panel of Fig.10.

Fig. 11 shows the typical spectra of lithium ions ^{6,7,8,9}Li (left panel) and $^{7,9.10}$Be particles (right panel) for 2.5 GeV p+Au measured in the PISA experiment. The lines have the same meaning as those of Fig.10. Finally Fig. 12 exhibits the spectra of boron ions ^{10,11,12}B (left panel) and spectra of carbon, nitrogen and oxygen ions without isotopic separation measured in the PISA experiment [Bub07] for 2.5GeV p+Au at 35° in respect to the incident proton beam.

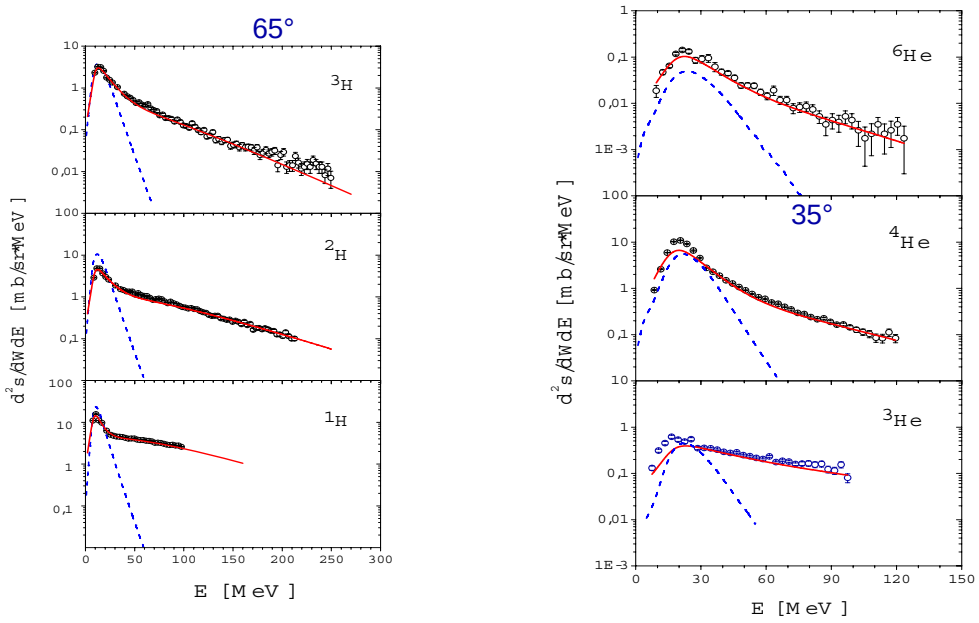

Fig. 10. Energy spectra of [1,2,3]H (left column) and [3,4,6]He particles (right column) for 2.5 GeV p+Au; circ° [Bub07] (PISA-exp.) for corresponding emission angles; The dashed lines show the prediction of evaporation of H- and He-isotopes evaluated by means of GEM program [Fur00] from excited residual nuclei of the first stage of the reaction with properties extracted from BUU calculations; full lines correspond to phenomenological model of two emitting sources as described in ref. [Bub07].

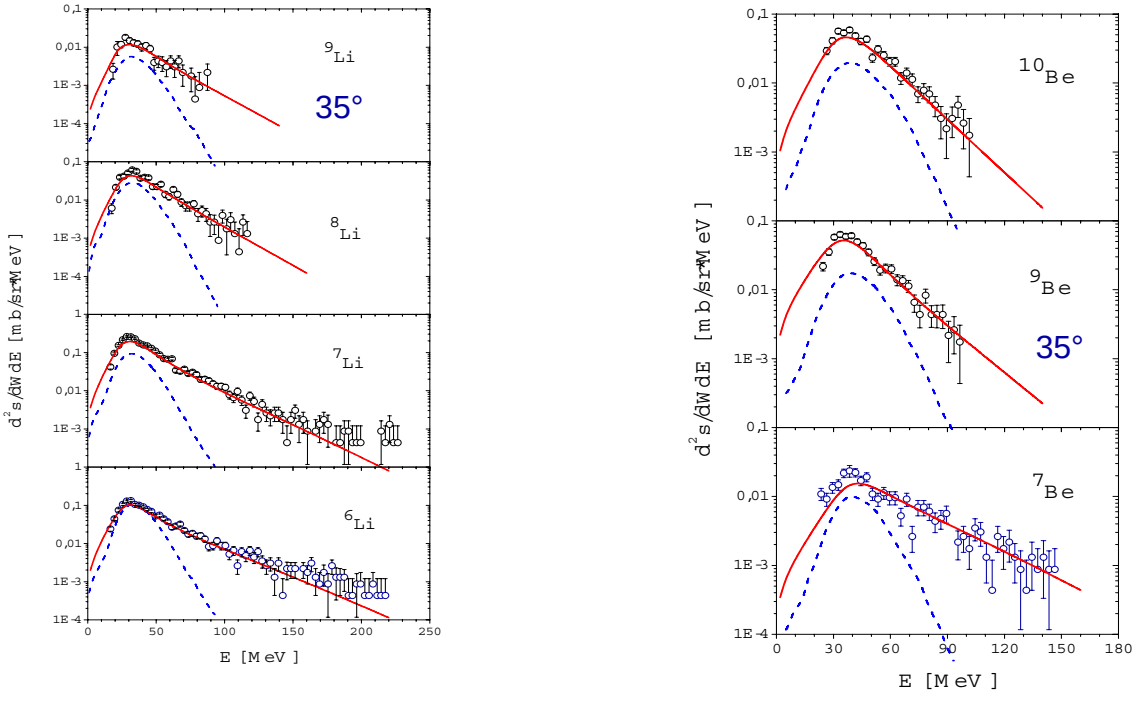

Fig. 11. Energy spectra of [6,7,8,9]Li (left column) and [7,9.10]Be particles (right column) for 2.5 GeV p+Au; circ° [Bub07] (PISA-exp.) for 35° in respect to p-beam; The dashed and full lines have the same meaning as in Fig.10.

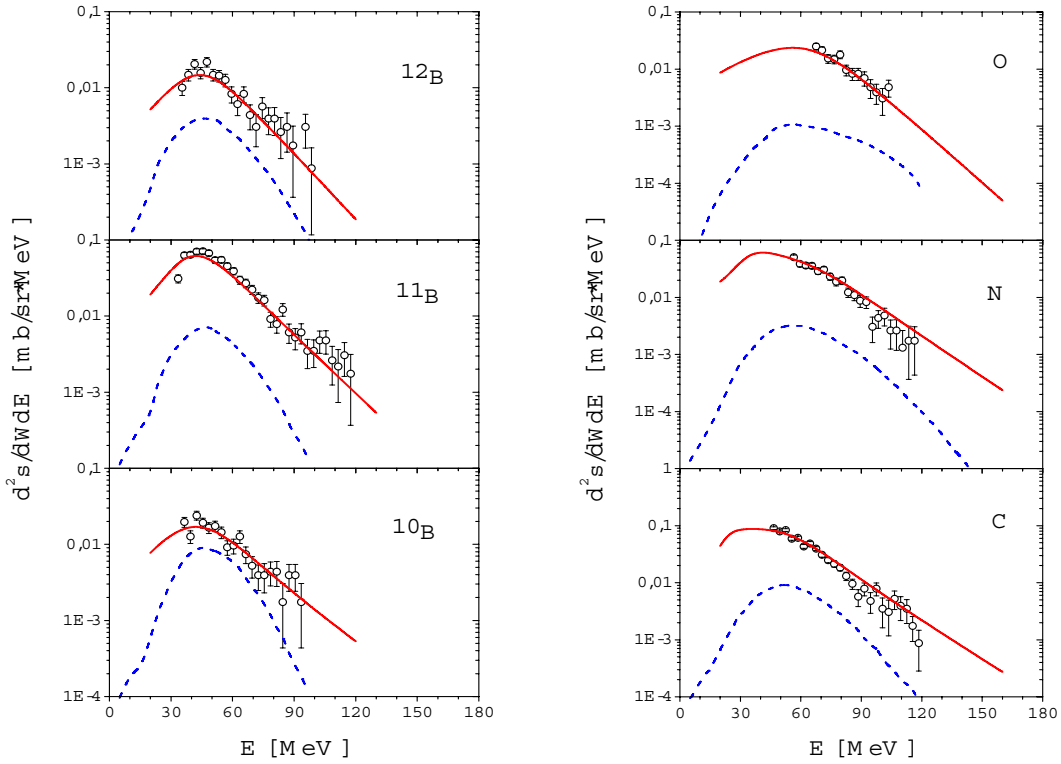

Fig. 12. Energy spectra of ^{10,11,12}B (left column) and C,O,N particles (right column) for 2.5 GeV p+Au; circ° [Bub07] (PISA-exp.) for 35° in respect to p-beam; The dashed and full lines have the same meaning as in Fig.10.

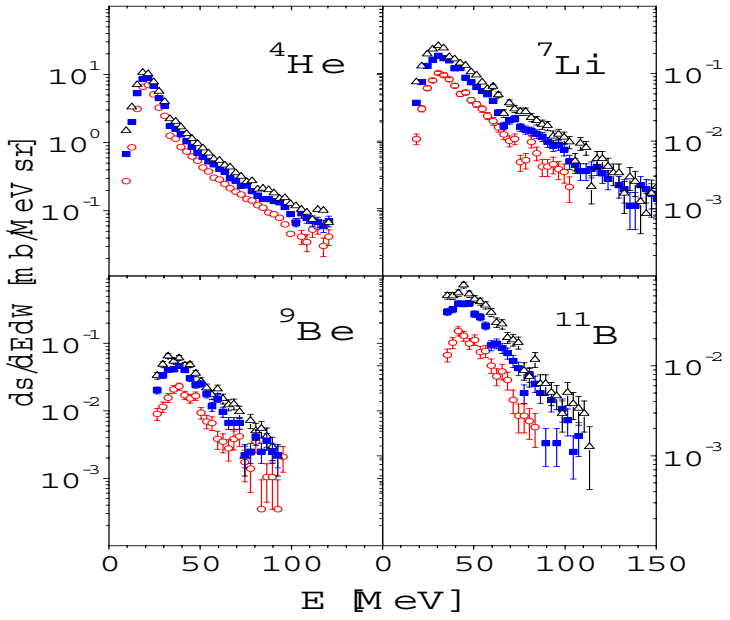

Fig. 13. Typical spectra of ^{4}He, ^{7}Li, ^{9}Be, and ^{11}B ejectiles measured at 35° in respect to incident beam for three energies of protons: 1.2(open circles), 1.9(full squares), and 2.5 GeV(open triangles), impinging on to Au. The cross sections at 2.5 GeV proton beam energy were published in ref.[Bub07] and the data at 1.2 and 1.9 GeV are currently in press in Phys.Rev C Journal.

Double differential cross sections $d^2\sigma/d\Omega dE$ as a function of scattering angle and energy of ejectiles, were also measured as a function of incident kinetic energy of the protons. This allows to study the incident particle energy dependence of the light charged particles production. A detailed analysis of the energy dependence of intermediate mass fragments will be published in a forthcoming contribution. Typical spectra of isotopically identified ejectiles obtained in the PISA experiment as a function of bombarding energy are shown in Fig. 13. As can be seen in the figure the shape of spectra does not vary significantly with beam energy. The main effect, present for all products is monotonic increase of the absolute value of the cross sections with beam energy. Furthermore, all the spectra for all bombarding energies are –as described above-- bell shaped with two components; low energy component of the Gaussian shape - attributed to evaporation from an equilibrated, excited nucleus, and high energy exponential component - interpreted as nonequilibrium mechanism contribution. The data for LCP's, represented in Fig. 13 for alpha-particles, have similar character and energy dependence as those for IMF's, however, the nonequilibrium component is more pronounced. The final PISA double differential cross section experimental data files including ejectiles up to Z=13 (with poor statistics for heavier elements) for 1.2 and 2.5 GeV p+Au are made available on the smr1930 web page. A detailed analysis and interpretation of the 2.5GeV p+Au data can be found in ref.[Bub07]. The 1.2GeV (and 1.9, 2.5 GeV) p+Au data and explanations are published/in print at Phys.Rev.C (2008).

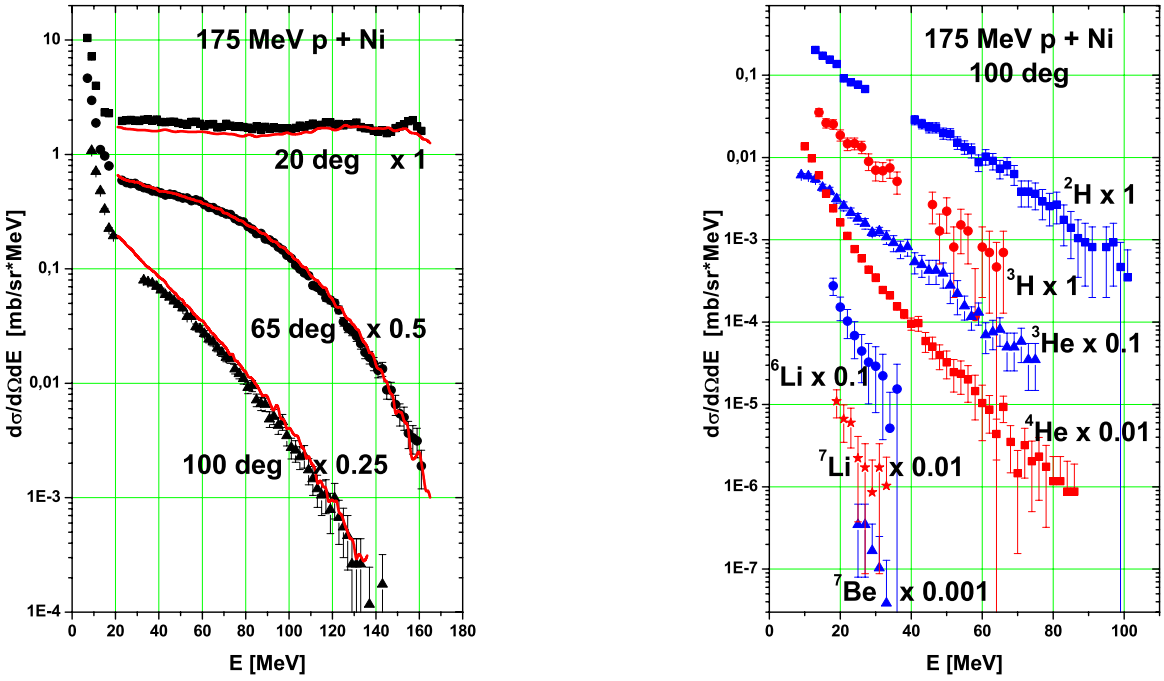

Fig. 14. Kinetic energy spectra for protons at 20, 65, and 100° following 175 MeV p+Ni (left panel). Symbols are data of PISA experiment, lines are from ref.[For91]. Right panel: PISA data of d, t, ^{3}He, ^{4}He, ^{6,7}Li, ^{7}Be spectra for 175 MeV p+Ni and ejectiles measured at 100° in respect to incident beam.

The final PISA experimental data for 175 MeV proton induced reactions on Ni target are shown in Fig.14. Absolute normalization of the data was done by comparing double differential cross section of protons measured by PISA experiment with the cross sections published by Foertsch at al. [For91]. In that paper the energy spectra of protons were determined for many angles, i.e. from 15 to 70 degrees in 5 degree steps and for 80, 90, 100,

120 degrees, thus it was possible to compare the PISA data at several angles (15, 20, 65 and 100 degrees) with those of ref.[For91]. It was found that the shapes of all compared spectra agree very well and, moreover, the ratio of our data to those of Foertsch et al. is the same for all angles. Therefore the normalized cross sections for all products observed in the 175 MeV p+Ni experiment rely on the absolute normalization of proton data found by Foertsch et al.. The Normalization factor was found using the method of weighted least squares for each angle separately and then mean value of four angles were used as normalization factor. The statistical error of normalization factor was found to be close to 3%. Additionally systematic error of data of Foertsch (as authors claimed it is close to 10%) should be taken into consideration.

The second method of normalization for the 175 MeV p+Ni reaction was performed independently. It consisted in comparing the experimental total cross section for emission of ^{7}Be with results of parameterization of ^{7}Be data published in the literature [Bub04]. This method is less accurate as comparing proton spectra with results of Foertsch et al. because of two reasons:

(i) Statistics of ^{7}Be spectra in reaction Ni(p,^{7}Be) is much poorer than statistics of proton spectra,

(ii) The experimental total cross sections should be derived from the spectra by integration over angle and energy what is biased with virtually large error because the experimental spectra are not measured at very low ^{7}Be energies, where the cross sections are relatively large.

Nevertheless, both methods gave normalization factors which agreed with accuracy of about 20% what is quite good results taking into account the fact of 10% error of normalization, quoted by Foertsch et al., inaccuracy of total ^{7}Be cross sections extracted from the spectra, and the error of parameterization of Bubak et al.[Bub04]. The good agreement gives additional confidence in the absolute normalization. The files including the data for ejectiles up to Z=6 (C, but with poor statistics however for heavier ejectiles) for 175MeV p+Ni are placed on the smr1930 webpage.

As a function of incident proton beam energy the He-production cross sections on Fe measured by NESSI [Her06], Hannover [Mic95], SPALADIN [Gen06], and PISA [Pis07] are compiled in Fig.15. The latest data points of SPALADIN at 1 GeV and PISA at 175 MeV are also included. The SPALADIN result obtained in inverse kinematics of Fe on p at GSI shows a value slightly above the NESSI data, but is definitely still smaller than the systematics of R.Michel et al.[Mic95]. The data shown here for PISA are for Ni reaction, but a comparison should be legitimate, because Fe and Ni are very close in terms of atomic number. Note, that for the PISA data [Pis07] the cross sections for the individual of ^{3,4,6}He isotopes are given at 175 MeV. The Monte Carlo calculation getting closest to the available experimental He data is the INCL4-Clus-GEMINI version (dashed line in Fig.15), which accounts-using a coalescence approach-for cluster (here composite He particles) emitted in the first fast phase of the reaction. The two solid lines in Fig.15 take into account only the He particles being emitted during the slow evaporation phase and therefore as expected the abundance of production cross sections is underestimated in INCL4+ABLA or INCL4+GEMNI, respectively.

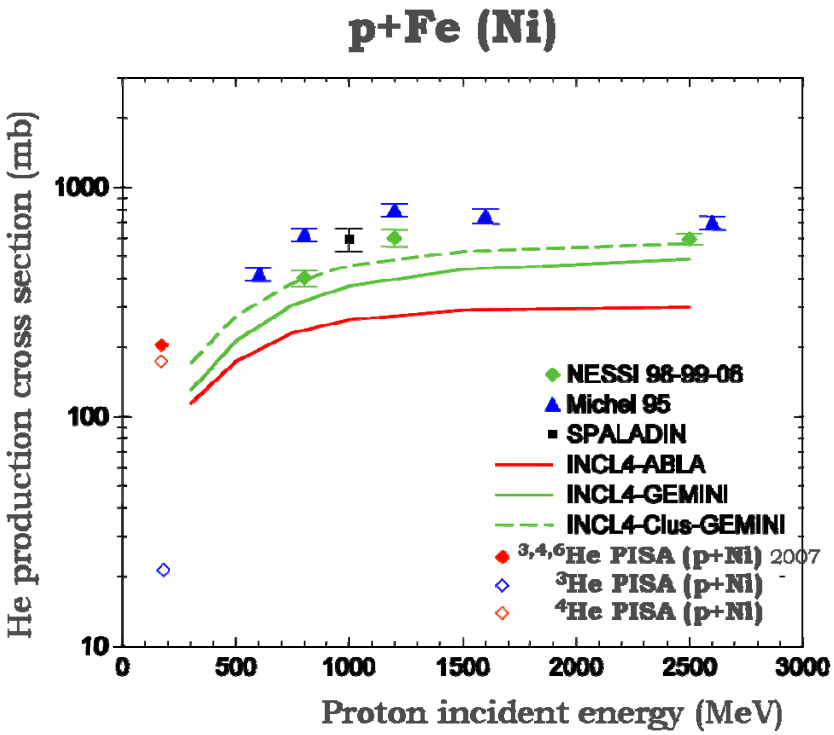

Fig. 15. Production cross section of ^{3,4,6}He isotopes as a function of incident proton beam energy. symbols: NESSI, Hannover, SPALADIN, PISA data, curves: calculation by INCL4.3+ GEMINI/ABLA.

In the following the XS data p,d,t, ^{3}He, ^{4}He, for Fe, Pb targets at 1.2 and 1.8 GeV of NESSI for our benchmark are listed. As discussed and requested during Trieste workshop, the data are optional, therefore I take the freedom to just guide the interested reader / code developer to our NESSI publication [Enk99].

For **1.2 GeV** p-induced reactions I would like to refer to Table 1 (page 326 of ref.[Enk99]) for the measured hydrogen and helium cross section data on Fe and Pb (among Fe, Ta, W, Au, Hg, Pb, U).

In summary for the two targets under consideration the cross sections are:

Fe:

σ_H=1.32 b (H means p+d+t isotopes)

σ_{He}=0.44 b (He means ^{3}He+^{4}He isotopes)

Pb:

σ_H=2.27 b (H means p+d+t isotopes)

σ_{He}=1.22 b (He means ^{3}He+^{4}He isotopes)

The lower detection thresholds for the cross section measurements is 2.2 MeV, which corresponds also to an upper energy threshold for p, d, t as follows:

$\sigma_H=\sigma_p(2.2\text{-}26MeV)+ \sigma_d(2.2\text{-}49MeV)+ \sigma_t(2.2\text{-}76MeV)$

$\sigma_{He}=\sigma_{He}(2.2\text{-}120MeV)$

For **2.5 GeV** p-induced reaction I would like to refer to Table 2 (page 331 of ref.[Enk99].) for the measured cross hydrogen and helium section data on Au and Pb (among Ni, Ag, Ta, Au, Pb, U).

In summary for the two targets under consideration the cross sections are:

Pb:

$\sigma_H=3.13$ b (H means p+d+t isotopes)

$\sigma_{He}=1.64$ b (He means $^3He+^4He$ isotopes)

For Au we have also measurements on individual isotopes:

Au:

$\sigma_p=2.10\pm0.2$ b

$\sigma_d=1.0\pm0.2$ b

$\sigma_t=0.60\pm0.14$ b

$\sigma_{3He}=0.2\pm0.08$ b

$\sigma_{4He}=1.78\pm0.2$ b

same lower detection thresholds for the cross section measurements as above.

Please note, that all cross sections for 1.2 and 1.8 GeV are visualized in figures in ref. [Enk99].

Please note that in the NESSI data for 1.2 GeV proton induced reactions mentioned above [Her06] all cross sections have been corrected not only for double hits, geometrical efficiencies, background as measured with empty frames and dead times, but also for the contribution below the lower energy threshold (see Table2, page 434 of [Her06]) of the Si-detectors. Indeed this had been done by extrapolating to zero energy for the cross section contribution. The hydrogen and He production cross sections --including errors-- are given for Al, Ti, Fe, Ni, Cu, Zr, Ag, Ho, Ta, W, Au, Pb, Th, U in Table 3 (page 441) of ref.[Her06]. Thresholds are specified in Table 3, respectively.
Table 4 and Table5 give the cross sections for the individual p,d,t and He3, He4 and He6 isotopes, respectively. Table 6 provides for the very same targets the production cross sections for Li6, Li7, Li8, Li9, Be7, Be9, Be10.

Of great value and particular interest are the measurements performed by mass spectrometry [Mic95,Ley05]. The authors provide excitation functions in the whole energy range of interest, however in particular for light targets typically the measured He production cross

sections do not coincide. The discrepancies between the two experimental methods for light targets are not yet understood. The huge amount of data collected for proton induced reactions here and elsewhere (R.Michel et al.) will be valuable for the identification of deficiencies of existing INC/evaporation codes.

3. Neutron production

Of significant interest for a wide range of applications and fundamental research, in particular at the crux of spallation neutron sources, transmutation of nuclear waste in accelerator driven systems [Nif01], and shielding issues are also neutron production double differential cross sections in GeV proton-induced spallation reactions. Although generally described satisfying by e.g. INC+evaporation codes, neutrons are more difficult to detect than protons or LCP. Experimental double differential neutron production spectra represent a valuable observable also for validating new model developments or improvements [Bou04,Cug97b,Dua07,Bou02]. It is also interesting to look at neutron multiplicities M_n, global properties of neutron spectra which are not easily revealed by their inspection. An extensive overview on the observable M_n for thin targets is compiled in Refs.[Bou02,Fil01,Let00,Hil98].

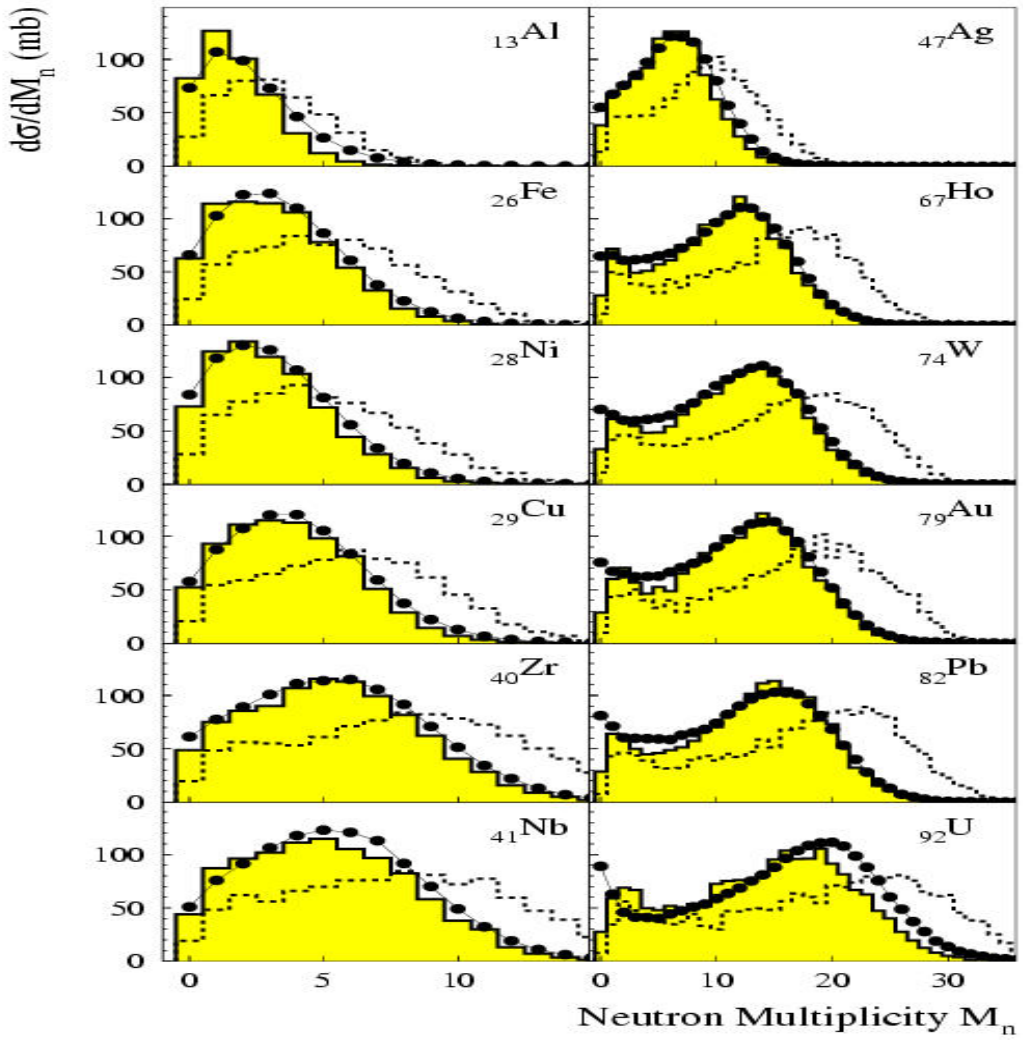

Fig. 16. Measured (symbols) and calculated (histograms) neutron multiplicity distributions of NESSI for 1.2 GeV p+Al,...,U. Note different M_n scales for the left and the right panels.

Fig. 16 shows calculated (INCL2.0+GEMINI) M_n distributions before (dashed histogram) and after (shaded histogram) folding with the neutron energy dependent detector efficiency. Numerical values of this plot are available on the smr1930 website. The neutron detection efficiency of the Ball needed for correcting the model calculations is also given on the web page as well as presented in Fig. 17.

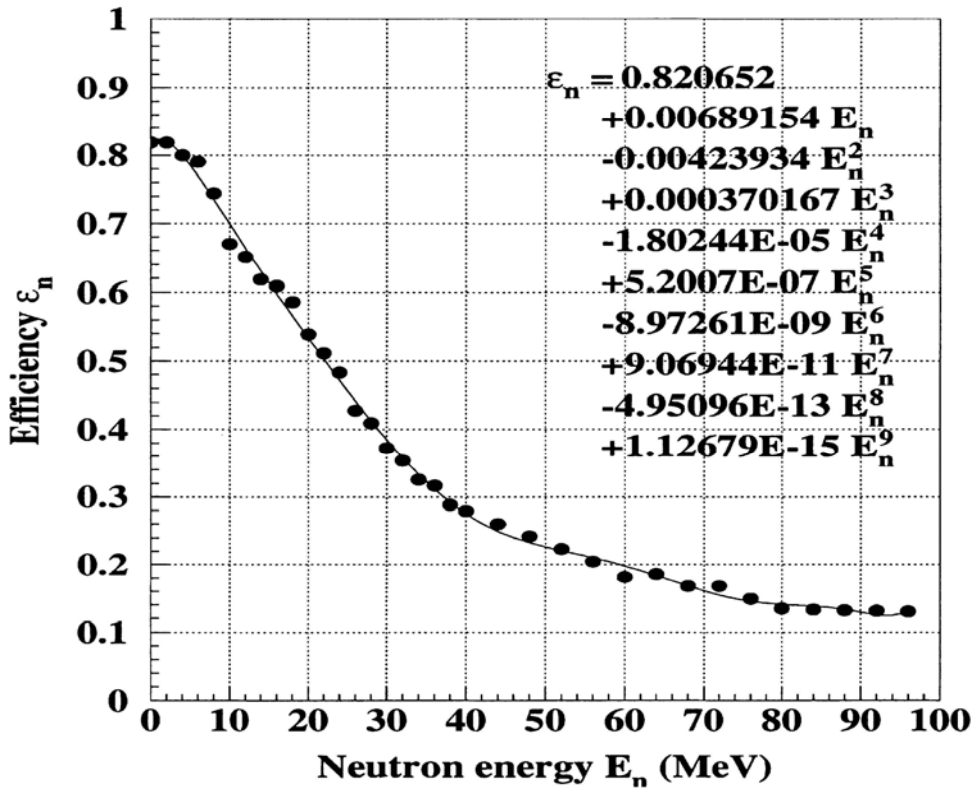

Fig. 17. Monte Carlo simulated neutron detection efficiency as a function of kinetic energy.

4. Conclusion

Two experiments (NESSI,PISA) have been consulted to validate models with regard to reaction cross-sections or reaction probabilities, neutron- and charged particle production cross-sections and angular- and energy- distributions for GeV proton induced reactions on various thin targets. PISA experiment e.g.~has showm to be able to measure the products of pA collisions with Z-identification up to at least Z=16 and isotope identification to masses up to 13-14% with a particularly low energy threshold of less than 1 MeV/A. In very brief summary the two experiments PISA and NESSI contribute the following information

- NESSI:
  - 4π detection system for LCP and neutrons, neutron multiplicity spectra,
  - DDXS for p,d,t, ^{3,4,6}He, ^{6,7,8,9}Li
  - Targets Al-U (with emphasis on Au),
  - incident proton beam energies 0.8, 1.2, 2.5 GeV
  - literature & references: NuclPhysA765, 426(2006), PhysRevLett95,162701(2005), NIMA508, 295(2003), NIMA508,315(2003), Nucl.Phys.A712,133(2002),
- PISA:
  - no neutron detection, but due to internal beam operation high statistics, very good Z and A identification of reaction products,

- DDXS for p,d,t, ^{3,4,6}He, ^{6,7,8,9}Li, ^{7,9,10}Be, ^{9,10,11,12}B, ^{11,12,13,14}C, N, O,…
- *targets: Al, Ni, Nb, Ag, Au*
- *incident proton beam energies: 175 MeV (Ni), 1.2, 1.9, 2.5 GeV* .
- literature & references: NIMA519,610(2004), Phys.Rev.C 76 014618(2007), Phys.Rev.C in press 2008

- →completely independently performed and analysed experiments NESSI/PISA are in good agreement, a set of experimental benchmark data is provided for the development and test of models capable of describing (among other features also) the emission of the high energy component of composite particles

The experiments presented here provide an important set of benchmark data for the development and test of reliable new models capable of describing the emission of the high energy component of composite particles produced in GeV reactions.

ACKNOWLEDGEMENTS

The author acknowledges gratefully the support of the European Community-Research Infrastructure Activity under FP6 "Structuring the European Research Area" programme (CARE-BENE, contract number RII3-CT-2003-506395 and HadronPhysics, contract number RII3-CT-2004-506078). The NESSI/PISA collaboration appreciates the financial support of the European Commission through the FP6 IP-EUROTRANS FI6W-CT-2004-516520.

REFERENCES

[Let02] A. Letourneau et al, Nucl.Phys.A712, 2002, 133
[Her06] C.-M.Herbach et al., Nucl.Phys.A765, 2006, 426
[Cug97] J. Cugnon et al., Nucl.Phys.A620 (1997), 475
[Cha88] R.J. Charity et al., Nucl.Phys.A483 (1988), 371
[Bou04] A. Boudard et al., Nucl.Phys.A740 (2004), 195
[Mic95] R. Michel et al., NIM B103, (1995) 183
[Dos65] Dostrovsky et al. Phys.Rev.139, B1513(1965)
[pisa-web] http://www.fz-juelich.de/ikp/pisa
[Gol05] F. Goldenbaum et al., NIM A562, Issue 2, (2005) 733
[Bar03] R. Barna et al., NIM A519, (2003) 610
[Bub04] A. Bubak, PhD-thesis, Juel-4138, ISBN 0944-2952, (2004)
[Gen06] E. Le Gentil, PhD-thesis, Evry University, France, (2006)
[Pis07] B. Piskor-Ignatowicz, priv. communication (2007)
[Bub07] A. Bubak et al. Phys.Rev.C76, 014618 (2007)
[Fur00] S. Furihata et al., NIM Res.B 71 (2000), 251
[Ley05] I. Leya et al., NIM Phys.Res.B229 (2005) 1
[Nif01] H. Nifenecker et al., NIM A463 (2001) 428
[Cug97b] J. Cugnon et al., Nucl.Phys.A625 (1997), 729
[Dua07] H. Duarte, Phys.Rev.~C75 (2007) 024611
[Bou02] A. Boudard et al., Phys.Rev.C66 (2002) 044615
[Fil01] D. Filges et al., Eur.Phys.Jour.~A11 (2001) 467
[Let00] A. Letourneau et al., NIM B170 (2000) 299
[Enk99] M. Enke et al., Nucl.Phys.A657 (1999) 317
[Hil98] D. Hilscher et al., NIM A414 (1998) 100
[For91] S. Foertsch et al., Phys.Rev.C 43 (1991) 691

Detailed Investigations on Residual Nuclei Production in Spallation Reactions at GSI

J. BENLLIURE

Universidade de Santiago de Compostela,
Santiago de Compostela, Spain

Abstract. During the last years intense efforts have been deployed by several European laboratories to deeply investigate the production of residual nuclei in spallation reactions. The combination of the inverse kinematics technique together with the use of a high resolving power magnetic spectrometer made it possible to measure with high accuracy the production cross sections and kinematic properties of more than 7000 residual nuclei in 16 different spallation reactions. These experiments provide a comprehensive data collection on spallation reactions induced on target nuclei spread all over the chart of the nuclides with different size, neutron excess and with projectile energies covering the range between 200 and 1500 MeV.

1. Introduction

Spallation reactions are considered as the most efficient and clean source for neutrons. Spallation sources are proposed for fundamental and applied research with neutrons (e.g. SNS in USA [1], NSP in Japan [2] ISIS in UK [3] or the ESS project in Europe [4]) or as a neutron source for the transmutation of radioactive nuclear waste in accelerator-driven systems (ADS) [5-7]. The neutron fluxes produced by the next generation of spallation sources require the use of multi-MW targets being the design and operation of these targets a real challenge. Among others, activation, long-term radio-toxicity or corrosion problems in the spallation target due to the production of spallation residues should be considered. Structural materials, in particular the window between accelerator and target, will also suffer due to high intensities and long irradiation periods.

Indeed, two main factors that influence the design and construction of such a target are neutron yields and the nature and kinematic properties of residual nuclei produced in the reaction. Neutron production has to be described in terms of neutron multiplicity and its spatial and energy distribution. Neutron multiplicity determines both, the current and the beam energy of the proton-driver accelerator, while their energy and spatial distribution will shape the geometry of the spallation target and the shielding to high-energy neutrons. As already mentioned, the production and kinematic properties of residual nuclides are of interest with respect to activation and radiation damage. However, the present knowledge about this reaction mechanism is not accurate enough to fulfill the standards used for the design and operation of next-generation spallation targets.

The main consequence of the present qualitative understanding of spallation reactions is that most of the existing codes used to describe these reactions have a limited predictive power [8]. This was the motivation for a large experimental program initiated in Europe few years ago aiming at improving our knowledge on these reactions. These modern experiments are expected to provide accurate data to develop and benchmark more reliable model calculations. While other contributions to the present report discuss the progress on new data on neutron production in spallation reactions [9], in this paper we will concentrate on some the experiments aiming at accurate measurements of residual nuclei produced in spallation reactions.

Residue production in spallation reactions can be investigated using two different experimental approaches. In the standard one, the reaction is induced by light energetic projectiles impinging on heavy targets. As the recoil velocity of the residual nuclei produced in this reaction is not sufficient to make them leave the target, the spectroscopy of γ-rays or masses is used to identify them. The main limitation of this technique is that for most of the residues the measurement is done after β-decay and consequently only isobaric identification is possible. However, this technique is relatively fast allowing for the measurement of many different reaction systems, in particular excitation functions (see Refs [10,11] for details).

Reactions investigated using inverse kinematics are better suited to unambiguously identify spallation residues. In this case, a heavy nucleus is accelerated to relativistic energies and impinges on a light target nucleus. Due to the kinematic conditions, the reaction residues leave the target easily and can be identified in flight combining a magnetic spectrometer with position, time-of-flight and energy-loss measurements.

During the last years a collaboration of research institutes and universities from Germany, France and Spain has developed an intense research program at GSI (Germany) to identify and measure with high accuracy the production cross sections and kinematic properties of residual nuclei produced in spallation reactions taking advantage of the inverse kinematic technique. In this paper we describe the experimental technique used in these measurements, including a detailed description of the experimental setup and the data analysis methods, the results obtained as well as their main impact in the theoretical description of spallation reactions and model benchmarking.

2. Experimental technique

2.1 Experimental setup

The experiments were conducted at the SIS18 synchrotron at GSI. The synchrotron delivered beams of ^{56}Fe, ^{136}Xe, ^{197}Au, ^{208}Pb and ^{238}U with energies between 200 and 1000 A MeV, intensities between 10^7 and 10^8 ions/s and a pulsed time structure with a typical spill length of 3 seconds and a spill frequency of 10 seconds. These beams were extracted from the synchrotron and driven to the FRS target area where a secondary electron monitor SEETRAM measured in permanence the beam current for normalization purposes [12]. The beams impinged then on a liquid target filled with hydrogen or deuterium, contained in a cryostat with two thin titanium windows (18.1 mg/cm^2) [13]. The thicknesses of the hydrogen and deuterium were 87.3 mg/cm^2 and 201 mg/cm^2, respectively.

The separation and identification of the heavy nuclei with good resolution, A/ΔA~400 for A~238, is experimentally very demanding, being possible using a high resolving-power magnetic spectrometer like the Fragment Separator (FRS) [14]. This is a 70 meter long, zero-degree magnetic spectrometer, with an angular acceptance of 15 mrad around the central trajectory, a longitudinal momentum acceptance Δp/p~3%, and a nominal resolving-power value of 1500. This symmetric two-stage spectrometer was used in its achromatic mode with an intermediate dispersive focal plane. In Fig.1 we plot a schematic view of the FRS setup used in these experiments, where only the dipole magnets, among many other magnetic elements, are shown.

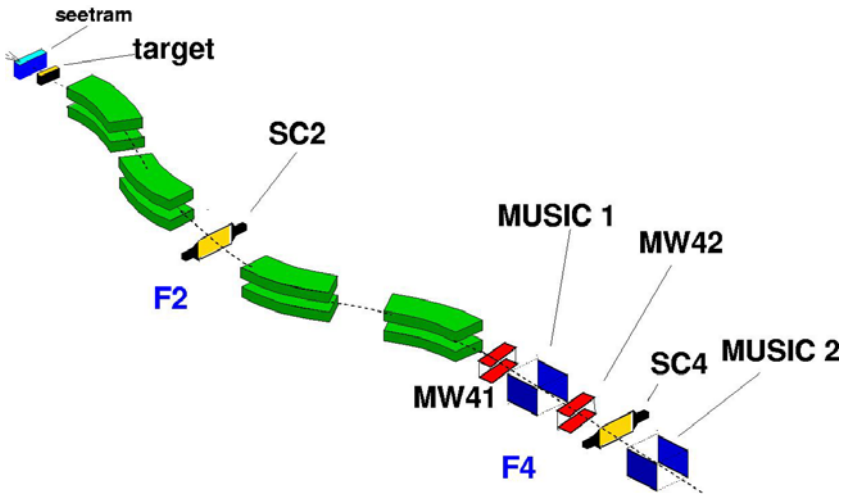

Fig. 1. Schematic representation of the FRS, where only the dipole magnets and main detectors are depicted. The intermediate (F2) and final (F4) focal planes are indicated. The degrader is placed just after the plastic scintillator SC2.

The residual nuclides produced in the reaction, keeping the kinematic properties of the projectile, flew forward through the FRS and were identified in mass and atomic number by a dedicated setup of detectors, see Fig.1. The short times of flight involved, below 300 ns, allowed to observe the primary production from the spallation reaction. Only a few extremely short-lived alpha emitters with 128 neutrons, having half-lives around 100 ns, partly decayed inside the spectrometer. For all other nuclides, the production cross sections were determined prior to their radioactive decay.

The FRS provides the separation of the particle fragments from their magnetic rigidity calculated according to the following equation:

$$B\rho = \frac{p_L}{Q} = A \cdot u \cdot c \cdot \frac{\beta\gamma}{Q \cdot e} \qquad (1)$$

being p_L the longitudinal momentum, A the mass number, Q the ionic charge, u and e the atomic mass and charge units respectively, c the speed of light, and β and γ the relativistic parameters. The measurement of the position of the fragments in the magnetic dispersive coordinate x at the intermediate and final focal planes of the FRS (F2 and F4, respectively, in Fig.1), defines the magnetic rigidity Bρ of each residual nucleus according to $\Delta B\rho = \Delta x / D$, where D is the dispersion of the spectrometer, and $\Delta B\rho$, Δx are the differences in rigidity and position, respectively, with respect to a nucleus following the central trajectory along the FRS. The positions were determined with two plastic scintillators [15] placed at the intermediate focal plane of the FRS (SC2), and at the final focal plane (SC4), located about 2 m after the exit of the FRS vacuum pipe. Additionally, the drift-times measured in the multi-sampling ionization chambers (MUSIC) [16] were used to define the tracking angle. The position calibration of the plastic scintillators was obtained with multi-wire proportional chambers (MW) placed next to the plastic scintillators, and independently calibrated. The values of the dispersion D and the dipole radii ρ were calibrated with the primary beam and its charge states. The magnetic fields B of the FRS were determined by Hall probes. The final resolution (FWHM) for $\Delta B\rho/B\rho$ was $4 \cdot 10^{-4}$.

The time of flight (ToF) measurement was also provided by the two plastic scintillators placed at the focal planes, and defined the relativistic reduced momentum $\beta\gamma$. The ToF calibration was determined from measurements of the beam ToF when passing through the FRS at different energies. That procedure allowed also the calibration of the thicknesses of the layers of matter placed along the FRS, and the length of the flight path for the central trajectory along the second half of the FRS, about 35 m. Any other trajectory was corrected in length according to the tracking angle measured at the exit of the FRS with the MUSIC chambers. The use of different detectors guaranteed a detection efficiency higher than 99% for the rates observed during the experiment: typically below 10^4 particles per second.

2.2. Data analysis

The separation and isotopic identification of the residues produced in these experiments represents a real challenge. In particular, for the heavier residual nuclei where the contribution of different ionic charge states can not be neglected, affecting the separation in magnetic rigidity, as well as the atomic-number identification with the ionization chambers. To overcome this problem, we used the momentum-loss achromat technique [17,18], based in the use of an achromatic energy degrader to improve the separation of heavy residues. A combined measurement of the energy loss of the residues in the intermediate energy degrader and in two ionization chambers allowed us to separate the contributions of the different ionic charge states [19]. Since the contamination due to ionic charge states decreases with the atomic number, we applied two different methods for the identification of residues with Z above and below 70.

2.3. Isotopic identification of residues with Z<70

In this interval of atomic number and energies above 500 A MeV, the expected contribution of charge states is below few percent. In this case, the identification in atomic number can be obtained directly from the energy-loss measurements with the ionization chambers placed at the exit of the FRS with a resolution better than $7 \cdot 10^{-3}$ (FWHM). Although the contamination of ionic-charge states is expected to be small, it can be suppressed from the correlation between the position of the transmitted nuclei at the final image plane of the FRS and their energy loss in the ionization chamber as shown in Ref. [20].

The selection of fully stripped ions ($Z=Q$), makes it possible to determine the A/Z value of the transmitted nuclei from the $B\rho$ and ToF measurements and construct identification matrices as the one shown in Fig. 2. The identification matrix shown in Fig. 2 corresponds to all fission products identified in the reaction ^{238}U(1 A GeV)+d [21]. Due to the limited acceptance of the FRS $\Delta p/p \sim 3\%$, 33 different tunings of the magnetic fields of the FRS were summed up to produce this identification matrix. The resolution in mass separation achieved is better than $A/\Delta A \sim 325$ (FWHM) for A=160.

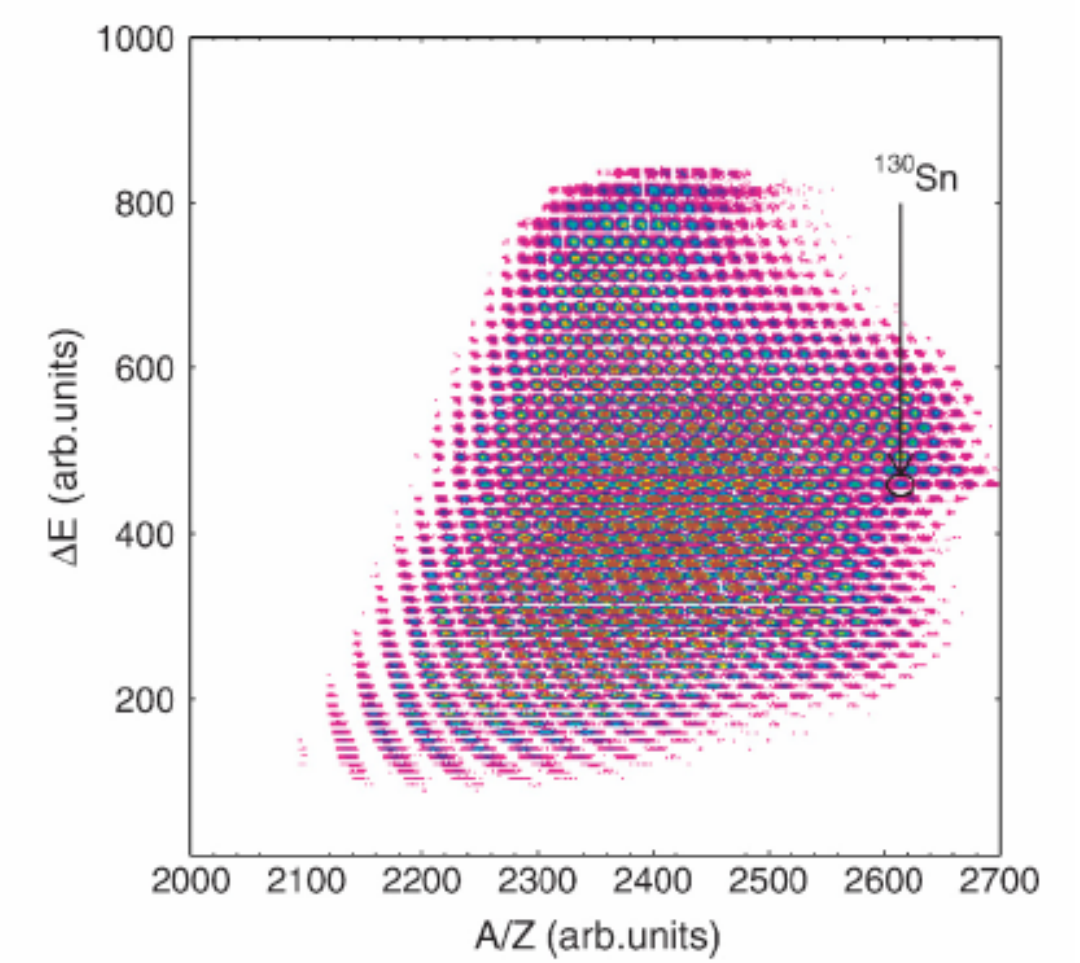

Fig. 2. Identification matrix corresponding to all fission residues identified in the reaction ^{238}U(1 A GeV)+d [21]. Due to the limited acceptance of the FRS this matrix was obtained by summing up 33 different tunings of the magnetic fields of the FRS.

2.4. Isotopic identification of residues with Z>70

Two problems have been faced to obtain an unambiguous identification of residues with Z above 70: the contamination due to ionic-charge states produced at the different layers of matter inside the FRS, and the loss in energy-loss resolution with the MUSIC chambers due also to stochastic charge-state changes within the gas. Following Ref. [19], to overcome this problem we used a profiled achromatic energy degrader made of aluminum, placed at the intermediate focal plane of the FRS, several niobium foils acting as strippers and a combined measurement of energy losses in two MUSIC chambers.

The niobium foils acting as strippers and placed behind the target, the energy degrader and in between the two MUSIC chambers limit the number of possible ionic charge states, enhance the population of fully stripped ions but also force the change in charge state between the two sections of the FRS and the two MUSIC chambers. The measurement of the energy loss in two identical MUSIC chambers with a stripper foil in between made it possible to select the signal corresponding to fully stripped ions improving considerably the resolution in the energy-loss measurement and hence in the atomic number identification (see Ref. [20] for details).

To overcome the ambiguities in the isotopic identification due to ionic-charge states inside the FRS, we use the additional information provided by the energy degrader [19]. The energy loss of one ion in the energy degrader is given by the equation:

$$\Delta E_d = (\gamma_1 - \gamma_2) \cdot u \cdot \frac{A}{Q} \qquad (2)$$

Being γ the relativistic factor, where *1* and *2* represents the first and second stages of the FRS, and *A* is the mass number of the ion and *Q* its atomic charge. Both, γ_2 and the ratio *A/Q* are determined from the values of $B\rho_2$ and *ToF* measured in the second section of the FRS. Under the assumption that *A/Q* is the same in both stages of the FRS, the $B\rho_1$ value is also determined in the first stage, thus γ_1 and ΔE_d are defined.

This quantity ΔE_d is sensitive to changes in the atomic charge of the ion between the two sections of the FRS. In Fig.3 we represent the energy loss obtained with the degrader (ΔE_d) versus the combined energy-loss measurement in the two MUSIC chambers Q_{eff}^{max} for a magnetic setting of the FRS centered on ^{195}Pb. In this figure we observe spots lying in three tilted parallel lines. The most populated spots, in the central tilted line, correspond to those nuclides which are bare along the spectrometer. For a given *Z* value, the spots above and below the former ones correspond to those nuclides with one electron before the energy degrader and bare after and vice-versa, respectively. A nuclide keeping one electron along the FRS but being fully stripped in one of the MUSIC chambers will lie on the smaller spots next to the main ones, marked as *+1e*. Those *+1e*-spots are also populated by nuclides which carried one electron in both ionization chambers, but were fully stripped within the FRS. The most unfavorable case in our setup is the one of a nuclide with one (or two) electron(s) unchanged in the whole setup line. The identification procedure would fail in the assignation of both *Q* and *Z*, thus also for *A*. Fortunately, those events amount to less than 1% in the most unfavorable case, ^{238}U.

In our analysis we have used only those events corresponding to fully stripped ions (*Z=Q*) along the experimental setup, identified using the method explained above. The drawback of this method is the large thickness of the energy degrader, corresponding to about 50% of the range of the residual nuclei. Such a thickness reduces the number of nuclides accepted in a single magnetic setting, to about 20, and induces secondary reactions. On the other hand, this method provides an unambiguous pattern for the atomic number identification, and an improved resolution to separate the different elements. These advantages largely overcome all related drawbacks and define the quality of the applied technique.

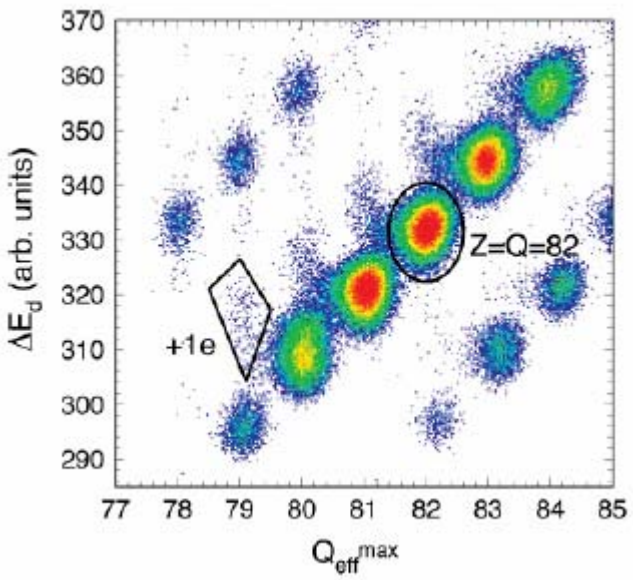

Fig. 3. Identification of charge states using the energy loss in the energy degrader ΔE_d and the combined measurement of the energy loss in the two MUSIC chambers Q_{eff}^{max} (see text for details).

Once we have identified the atomic number of the transmitted nuclei their mass number can be obtained using equation (1). In the present case, the degrader is a key element for the identification of heavy nuclides, since it allows the unambiguous separation of the different ionic charge states of a nucleus. The resolution achieved in this case is typically A/ΔA~330 (FWHM) for A=215, and Z/ΔZ~160 (FWHM) for Z=88.

2.5. Production cross sections

The final production cross section σ_r of the different projectile residues $r = (Z,A)$ can be obtained from the production yields y_r normalized to the number of atoms per surface unit of the target (N_t) and the beam intensity (N_b) according to the equation:

$$\sigma_r = \frac{y_r}{N_b N_t} \qquad (3)$$

Target thicknesses (N_b) are known with an accuracy better than 5% and the flux of incident projectiles (N_t) is obtained from the continuous measurement provided by the SEETRAM monitor calibrated according to Ref. [22] with an accuracy also around 5%. To determine the production yield (y_r) for a given isotope we should consider not only the limited acceptance of the FRS, both in momentum and angle, but also the possible reactions in the target container (titanium windows) as well as any other layer of matter along the FRS, the ionic charge state distribution or the dead time of the data acquisition.

The limited longitudinal momentum acceptance of the FRS determines both the range of isotopes and the interval of momentum covered by a single magnetic setting of the spectrometer. The momentum dispersion of the final residues is such that most of them were measured in several magnetic settings, covering each one a part of their momentum distribution. By summing up consecutive settings we could reconstruct the whole momentum distribution of all the residues. In Fig. 4 we plot the longitudinal momentum distribution p_L, in the frame of the projectile, for the nuclide ^{160}Yb. The four different areas correspond to normalized data recorded in different magnetic settings, contributing to the reconstruction of

the whole momentum distribution. Once we have reconstructed the momentum distribution of the transmitted nuclei one has to subtract the contribution due to nuclear reactions in the windows of the target. For this purpose, an additional dummy target was used, simulating the material

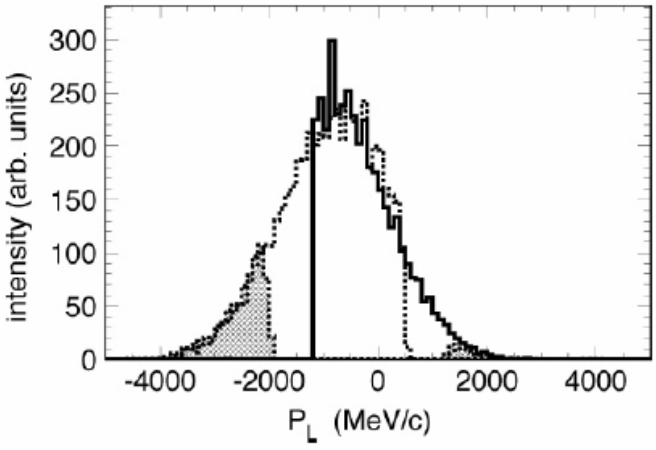

Fig. 4. Longitudinal-momentum distribution p_L, in the frame defined by the projectile in the middle of the target, for the nucleus ^{160}Yb, produced in the reaction ^{238}U(1 A GeV) + d. The different areas correspond to the momentum intervals measured in different FRS magnetic settings. The overlapping of these different measurements allows reconstructing the whole momentum distribution.

and thickness of the windows (Ti 36 mg/cm^2). The final production yield in the hydrogen was obtained using the following equation:

$$y_r = \left(y_r^{H_2} - y_r^{Ti}\right) \cdot f_Q \cdot f_{loss} \cdot f_{mr} \cdot f_{dt} \cdot f_{\varepsilon} \cdot f_{trans} \qquad (4)$$

where y_r^{H2} and y_r^{Ti} are the yields measured with the full cryogenic H_2 target and the dummy target, respectively, f_Q represents the correction due to ionic charge states, f_{loss} are the losses due to reactions in any other layers of matter along the FRS, f_{mr} are the corrections due to multiple reactions in the target, f_{dt} is the dead-time of the data acquisition, f_{ε} is the detection efficiency of the detectors and f_{trans} is the correction due to the angular acceptance of the FRS.

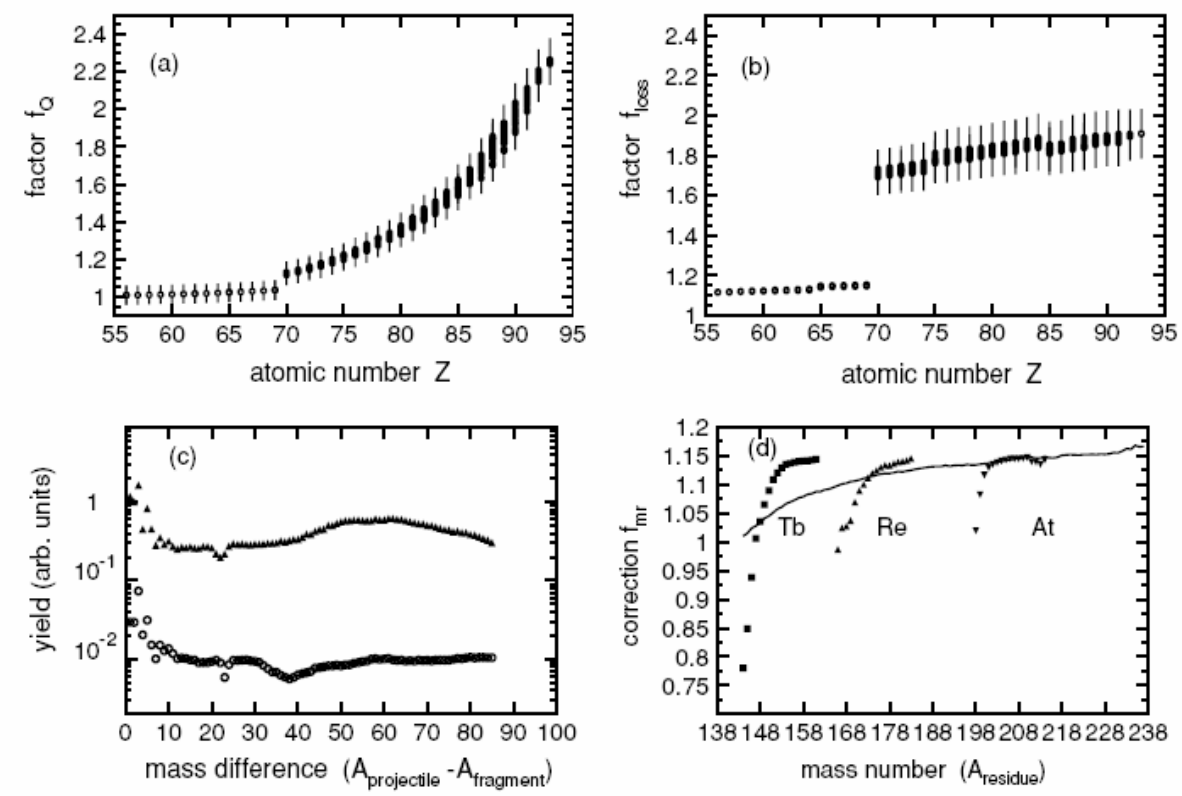

Fig. 5. Typical values for some of the corrections applied to the measured yields according to Eq. 4.

Typical values for the corrections used in Eq. 4 are shown in Fig. 5. As can be seen, the most important corrections are the ones due to ionic charge states (5.a) and secondary reactions (5.b) having both an important impact for residual nuclei above Z=70. The increase in secondary reactions above Z=70 is due to the use of a thick energy degrader at the intermediate image plane of the FRS to unambiguously separate and identify these reaction residues. Panel 5.c compares the production yields in the cryogenic target filled with D_2 (triangles) and in the dummy target (circles). Finally, panel 5.d represents the correction due to multiple reactions in the target. As can be seen, secondary reactions depopulate heavy neutron-rich nuclei and contaminate light neutron-deficient ones. The acquisition dead time was continuously monitored and was always kept below 30%. The efficiency of the detectors was evaluated as larger than 95%.

Another important correction that appears in Eq. 4 is the one due to the angular acceptance of the FRS. As already mentioned, the FRS has an angular aperture of about 15 mrad for the ions following the central trajectory of the spectrometer. The interaction between projectile and target not only slow down the former but also induces a dispersion in momentum and, therefore, in angle. In the case of spallation-evaporation channels the momentum and angular dispersion increases with the mass loss of the projectile but in general the angular transmission for these residual nuclei is generally above 80%. A particular case are spallation-fission channels since the kinematics of the reactions generates an angular distribution of the residues that largely excess the angular acceptance of the spectrometer, being the transmission between 5% and 30%.

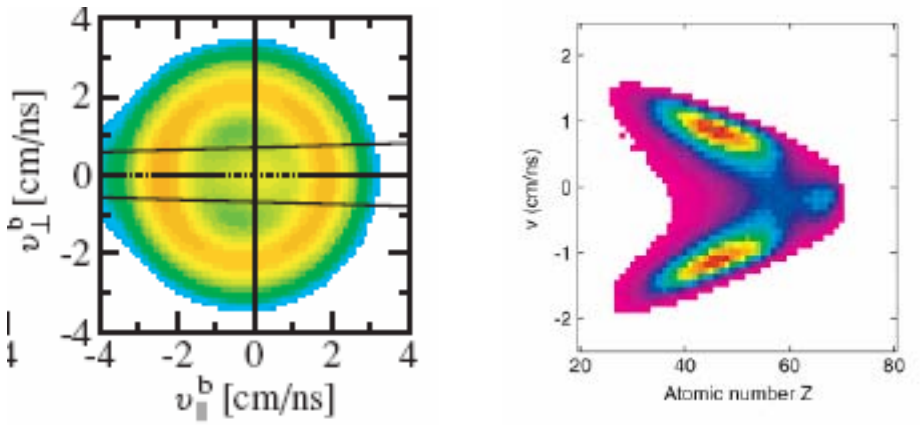

Fig. 6. Left panel: Example of the velocity distribution in the frame of the projectile for fission (outer shell) and evaporation (inner concentration around zero) residues. The two lines indicate the boundaries of the angular acceptance of the FRS. Right panel: Correlation between the longitudinal velocity in the frame of the projectile and the atomic number of the projectile residues transmitted through the FRS for the reaction ^{238}U(1 A GeV)+d.

Figure 6 illustrates the effect of the limited angular acceptance of the FRS. In the left panel we show an example of the velocity distribution in the frame of the projectile for fission (outer shell) and evaporation (inner concentration around zero) residues. The two lines indicate the boundaries of the angular acceptance of the FRS illustrating that only forward (positive longitudinal velocity) and backward (negative longitudinal velocities) emitted fission fragments are transmitted. In the right panel we show the correlation between the longitudinal velocity in the frame of the projectile and the atomic number of the projectile residues with atomic numbers between 28 and 70 transmitted through the FRS for the reaction ^{238}U(1 A GeV)+d. As can be seen, heavy projectile residues (Z>60) present an almost symmetric velocity distribution around a negative value with respect to the initial velocity of the projectile. This is a characteristic pattern for evaporation residues. However, light projectile residues present a double-hump velocity distribution with nuclei transmitted with either positive or negative velocities. This velocity distribution is understood as a consequence of the cut produced in the velocity distribution of fission residues due to the angular boundaries of the FRS as illustrated in the right panel of this figure. A detailed description of the evaluation of the angular acceptance of the FRS for any projectile residues produced either by evaporation or by fission can be found in Ref. [23].

2.6. Uncertainties

The accuracy of the measured cross sections is determined from the uncertainties of the production yields y_r, beam intensity (N_b) and target thickness (N_t). The uncertainty in beam intensity was estimated to be around 5% [22]. The uncertainty in the target thickness was evaluated including the deformation of the target walls, and the alignment of the target and beam axis. Both effects were investigated with a dedicated measurement [24]. Our evaluation of the combined effects shows that 80% of the projectiles see a target thickness variation below 1%, and the total distribution sees a target thickness variation below 3%. The influence on the density of the target of the tiny fluctuations of temperature during the experiment was observed as negligible.

The accuracy of the yields y_r is determined by the statistical uncertainty and the uncertainties of the correction factors applied in Eq. 4. The statistical uncertainty was kept well below 5% for most of the nuclides with production cross sections down to 0.01 mb. The accuracy in the

corrections applied to the yields are dominated by the two most important factors, the ionic-charge state distribution and the secondary reactions in the degrader, affecting both the yield of nuclei with Z>70. These two factors were obtained using model calculations with an accuracy around 5% for the evaluation of the ionic-charge state distributions and 10% for the reaction probability in all layers of matter inside the FRS (see Ref. [20] for details). The other correction factors were also evaluated with an accuracy between 5% and 10%. The uncertainty due to the FRS acceptance was estimated to be below 10% for evaporation residues and around 20% for fission residues.

The final statistical uncertainty of the measured production cross sections was below 5% while most of the systematic uncertainties vary between 10% and 30%. The most neutron-deficient isotopes can also show larger uncertainties due to the contribution of multiple reactions in the target.

3. Results

The technique described in this work was use to identify and determine the production cross sections and kinematic properties of the spallation residues produced in 16 different reactions summarised in table 1. All the numerical values can be found in Ref. [40].

TABLE I. LIST OF SPALLATION REACTIONS INVESTIGATED AT GSI USING THE EXPERIMENTAL TECHNIQUE DESCRIBED IN THIS WORK

Projectile	**target**	**Energies (MeV)**	**references**
^{238}U	hydrogen	1000	25, 26, 27, 28, 29
^{238}U	deuterium	1000	20, 21
^{208}Pb	hydrogen	1000, 500	30, 31, 32, 33
^{208}Pb	deuterium	1000	34
^{197}Au	hydrogen	800	35, 36
^{136}Xe	hydrogen	1400, 1000, 500, 300, 200	37, 38
^{56}Fe		1500, 1000, 750, 500, 300	39

The reactions investigated allow us to systematically investigate the nature of the residual nuclei produced in spallation reactions using target nuclei spread all along the chart of the nuclides and energies between 200 and 1500 MeV.

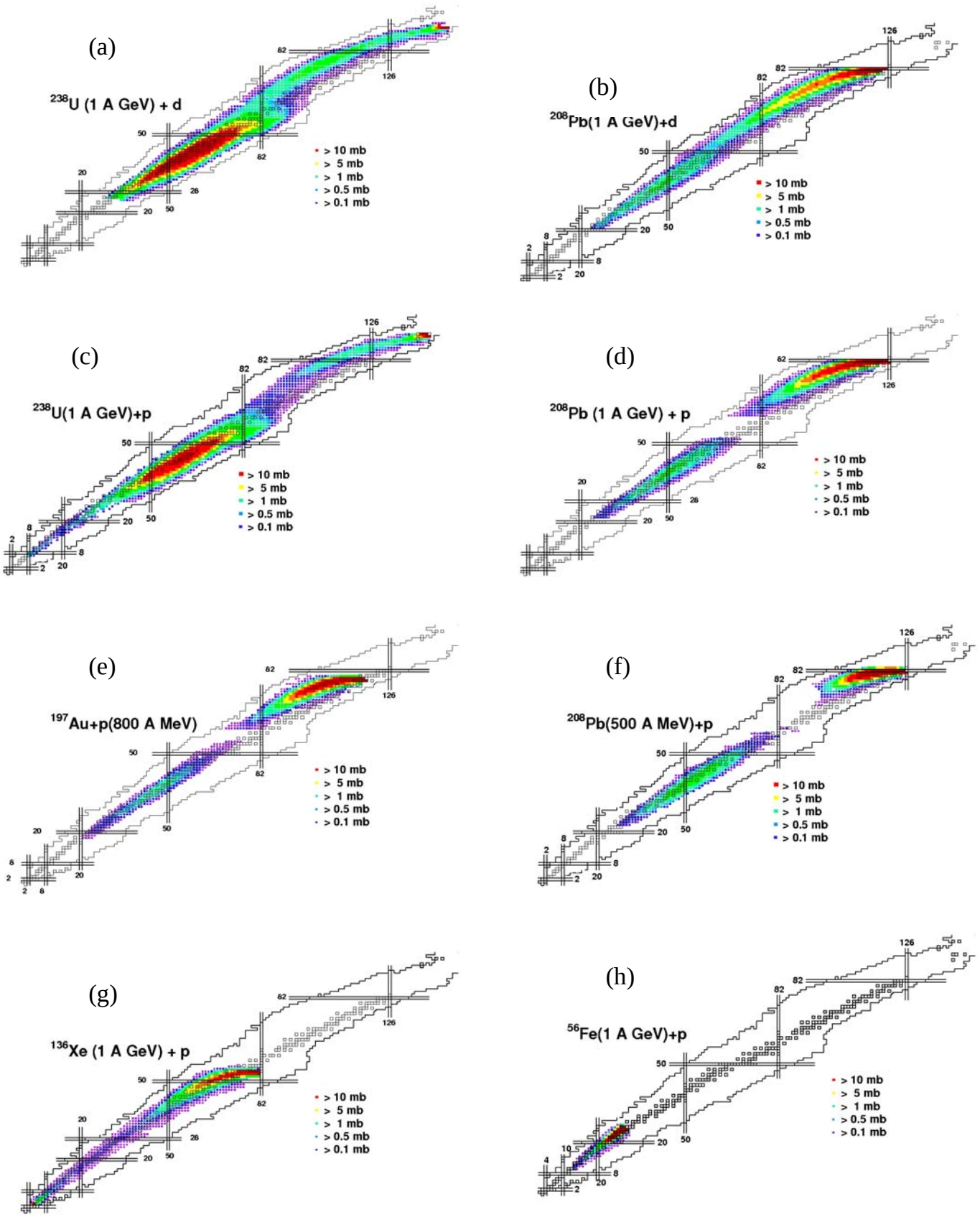

Fig. 7. Spallation residues measured in some of the reactions investigated at GSI using the technique described in this paper represented on top of a chart of the nuclides. The cluster size and color indicate the production cross sections according to the legend.

3.1. Production cross section

In Fig. 7 we show the spallation residues measured in some of the reactions investigated at SGSI using the technique described in this work, represented on top of different chart of the nuclides. The cluster size and color indicate the production cross section according to the legends. This figure allow us to discuss how residual nuclei produced in spallation reactions populate different regions of the chart of the nuclides according to the mass, atomic number and neutron excess of the target nuclei or the energy of the projectile.

The main feature in this figure is that the distribution of spallation reactions induced on heavy target nuclei shows two components while for lighter systems (^{136}Xe or lighter) we observe a single distribution. This pattern reflects the reaction mechanisms leading to the production of those nuclei. Spallation reactions are understood as a two-stage process. The first stage or intra-nuclear cascade corresponds to the fast interaction between projectile and target nuclei, where some nucleons are lost as pre-equilibrium emission and the final pre-fragments gain excitation energy and angular momentum reaching after a while a kind of thermodynamical equilibrium. During the second stage, the equilibrated pre-fragment de-excites emitting γ-rays, nucleons, clusters of nucleons or fissioning.

As seen in Fig. 7, the distribution of residual nuclei in reactions induced with heavy-target nuclei presents two components. In the first one, residual nuclei extend from the target nucleus down to lighter nuclei that we identify as produced in spallation-evaporation reactions. The second distribution is located around the same N/Z ratio and half the mass number of the target nucleus, corresponding to residual nuclei produced in spallation-fission reactions. For lighter target nuclei we observe a single distribution corresponding to evaporation residues while fission is suppressed, as expected from the increase of the fission barriers.

Spallation-evaporation residues are produced in collisions where the target pre-fragment produced in the interaction between the projectile and the target nucleus de-excites emitting neutrons, protons, clusters of protons and neutrons, and gamma rays. The total number of emitted particles depends on the excitation energy gained by the pre-fragment during the fist stage of the collision. The larger the excitation energy the longer the evaporation chain and, therefore, the lighter the final residue produced in the reaction. We can then consider the difference in mass number between the initial target nucleus and the final residue as an indirect measurement of the excitation energy induced in the collision. The excitation energy gained by the pre-fragment depends on the impact parameter but also on the initial kinetic energy of the projectile. In Figs. 7.b, 7.d and 7.f we can see the effect of the initial kinetic energy of the projectile on the length of the evaporation chain. For this comparison one should consider that deuterons, at the same kinetic energy per nucleon, induced as much as double excitation energy than protons. As can be seen in Fig. 7, and according to the limiting fragmentation concept, the evaporation chain tends to produce nuclei along the so called “evaporation corridor”. This is a universal line in the chart of the nuclides defined by those nuclides with similar probability to evaporate protons and neutrons. However, the path on the chart of the nuclides followed by the evaporation chain before reaching the “evaporation corridor” depends on the initial neutron-excess of the target nucleus (memory effect). Target nuclei with a large neutron excess (Fig. 7.g) evaporate mostly neutrons, because the “evaporation corridor” lies on the neutron-deficient side of the chart of the nuclides (left to the β-stability valley). However, systems with smaller or no neutron excess (Fig. 7.h) evaporates from the beginning a similar amount of protons and neutrons.

Some of these conclusions can also be observed in Fig. 8 where we represent the isotopic distributions of the production cross sections of spallation-evaporation residues measured at GSI for the reactions ^{238}U(1 A GeV)+p (red points) and ^{238}U(1 A GeV)+d (black points). In this figure we see that the isotopic distributions of residual nuclei close to ^{238}U present a clear "memory effect" on the initial value of the neutron excess. However, lighter residues present isotopic distributions similar in shape and centred on the position of the "evaporation corridor". We also observe the difference in excitation energy between the two systems. Collisions with deuterium produce pre-fragments with larger excitation energy leading to longer evaporation chains and then, to the production of lighter

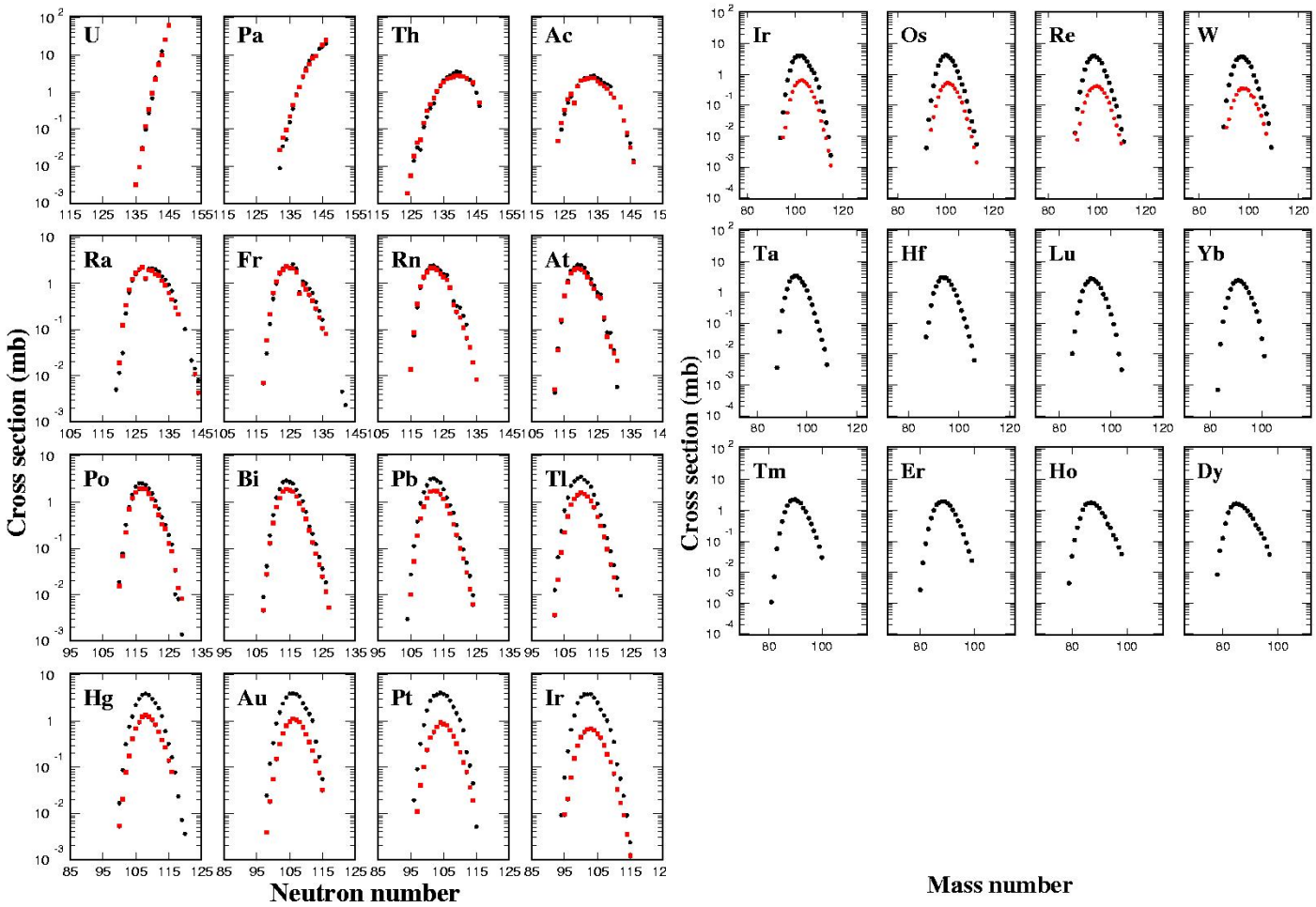

Fig. 8. Isotopic distributions of the production cross sections of spallation-evaporation residues measured at GSI for the reactions ^{238}U(1 A GeV)+p (red points) and ^{238}U(1 A GeV)+d (black points).

residual nuclei. This figure also illustrates the quality of the data. The smooth evolution of all cross sections together with the fact that error bars are for most of the nuclei smaller than the symbols are a clear indication on the quality of the data. The only deviations from the smooth evolution is observed for some N=128 isotopes of elements close to uranium which present smaller cross sections than expected. This result is explained because these nuclei are short-lived alpha emitters decaying in-flight to N=126 nuclei.

The probability and the nature of the final fission residues strongly depend on both, the energy and mass asymmetry shape of the fission potential. The height of the barrier determines the probability of this channel, indeed, light target nuclei with huge fission barriers

do not de-excite through fission. The mass-asymmetry dependence of the fission potential is determined by the forces acting between the two fission fragments, including shell effects, according to the separation distance, mass and atomic number [41]. The isotopic distributions of the fission residues produced in the spallation reactions measured in this work clearly show the effect of the fission potential. In the case of actinides, fission may occur at low excitation energies (few MeV) where shell effects are still present in the fission potential. Figures 7.c and 7.d clearly show a double-hump fission distribution produced by the double shell closure around N=82 and Z=50. At these excitation energies, the final fission residues also have a quite large neutron excess. At higher excitation energies, smaller impact parameters, shell effects disappear, the distribution of fission residues becomes single humped and these residues lose part of their neutron excess, as can also be seen in Figs. 7.c and 7.d. By contrast, pre-actinides show a single-

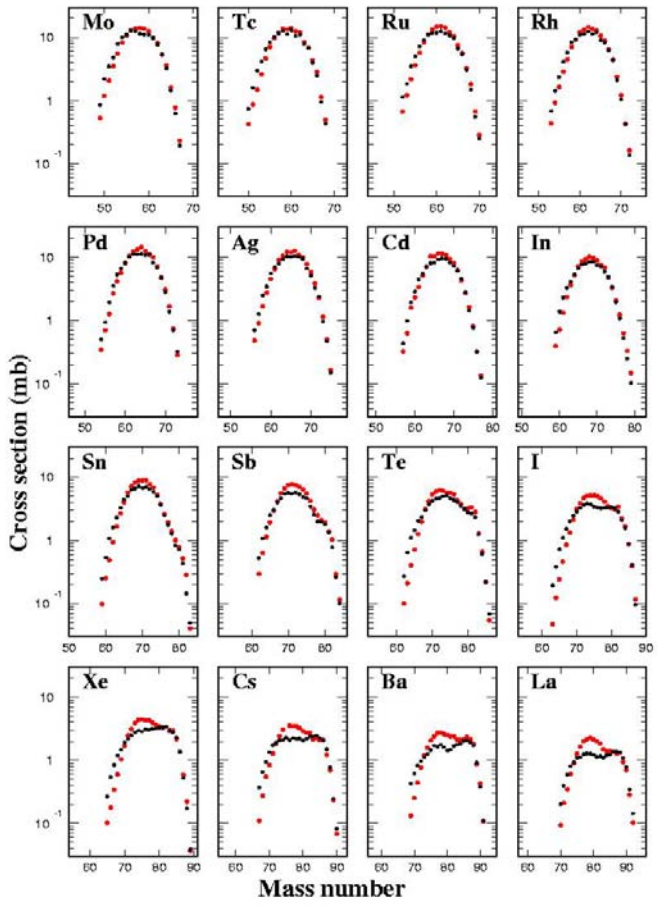

Fig. 9. Isotopic distributions of the production cross sections of spallation-fission residues measured at GSI for the reactions ^{238}U(1 A GeV)+p (red points) and ^{238}U(1 A GeV)+d (black points).

-hump distribution of fission residues, see Figs. 7.b, 7.d, 7.e and 7.f. In this case, the increase of the fission barrier strongly reduces the role of shell effects. This behaviour was already observed in dedicated experiments at GSI where the transition from double to single humped fission distributions was investigated [42].

In Figure 9 we represent the isotopic distributions of the production cross sections of spallation-fission residues measured at GSI for the reactions ^{238}U(1 A GeV)+p (red points) and ^{238}U(1 A GeV)+d (black points). In this figure we also observe the single-hump

distribution of fission residues around palladium while a double-humped distribution appears around tin in the heavy residues and molybdenum in the light ones. The comparison between the fission residues in reactions induced by protons and deuterons shows slightly wider isotopic distributions for the later. In fact, we expect that deuterons induce larger excitation energies affecting the with of the distribution of fission residues both in mass and N/Z [41].

3.2. Kinematic properties

The experimental technique used in this work allows not only the isotopic identification and the determination of the production cross sections of the residual nuclei of the projectile, but also the measurement of their longitudinal momentum with high accuracy. Indeed, once the nucleus is identified from the measurement of the magnetic rigidity, time of flight and energy loss, one can use again Eq. 1 to determine $\beta\gamma$ from the magnetic rigidity and a fix value of A and Z.

The kinematic properties of spallation residues reflect the two stages of the collision. The first stage or intra-nuclear cascade accelerates the target nucleus or decelerates de projectile nucleus in the case of reactions investigated in inverse kinematics. On average, this acceleration (deceleration) scales with the mass loss (impact parameter) induced by the collision. The second stage of the collision or de-excitation induces mostly a dispersion in the velocity distribution of the residual nuclei which strongly depends on the de-excitation mechanism, evaporation or fission. While evaporation leads to a modest dispersion around the mean velocity of the pre-fragment, the fission process populates the outer shell of a sphere with a radius defined by the Coulomb repulsion between the two fission fragments.

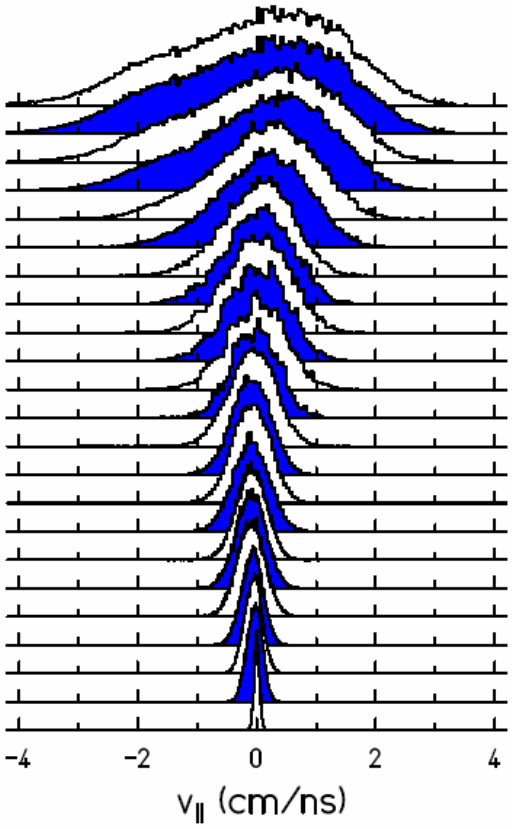

Fig. 10. Longitudinal momentum distribution of some fragments produced in the reaction ^{136}Xe(1 A GeV)+Pb in the beam frame [43]. The heavier fragments are down and the lighter up.

In Fig. 10 we report the longitudinal momentum distributions of some projectile-evaporation residues obtained for the reaction ^{136}Xe+Pb at 1000 A MeV in the frame of the beam. The distributions on the bottom correspond to heavy residues and those on the top to lighter nuclei. Although this example does not exactly correspond to a spallation reaction it helps us to illustrate the main features of the kinematic properties of the spallation residual nuclei. As can be seen, the average velocity of projectile residues decreases with the mass loss and the width of the distribution increases. A quantitative analysis of the average value and width of the velocity distributions of the residual nuclei produced in spallation reactions can be combined with the production cross sections to better characterize this reaction mechanism. A complete discussion of the kinematic properties of residual nuclei can be found in Ref. [43].

4. Physics highlights

The accurate measurements of the production cross sections and kinematic properties of the residual nuclei produced in spallation reactions shown in this paper provide not only a comprehensive data base for benchmarking different model calculations but also a useful tool for obtaining detailed information on the two stages of this reaction mechanism, the intra-nuclear cascade and the de-excitation of the pre-fragments. In this section we summarise the most outstanding results.

4.1. Investigating the intra-nuclear cascade

Most peripheral collisions constitute an extremely sensitive tool to the intra-nuclear cascade process. In particular, few nucleon knock-out or charge-exchange reactions leading to residual nuclei differing from the initial projectile nuclei in a few protons and neutrons made it possible to investigate the microscopic processes governing the intra-nuclear cascade. Indeed, the production cross sections of these residual nuclei close to the projectile are very sensitive to in-medium nucleon-nucleon interactions and Pauli blocking effects. Moreover, in the case of charge-exchange reactions, the high resolving power of the FRS allowed us to disentangle the contributions due to the quasi-elastic and inelastic processes. The latter is governed by the Δ-resonance excitation providing a sensitive probe to the inelastic nucleon-nucleon interaction. A detailed discussion of these topics can be found in Ref. [44].

4.2. Pairing correlations from the residual nuclei production cross sections

A detailed analysis of the production cross sections of spallation residues shows a clear even-odd staggering. This staggering manifest as an even-odd effect for even-mass nuclei and as an odd-even effect for odd-mass nuclei, being in both cases more pronounced for lighter nuclei. This observation was interpreted as due to pairing correlations both in the masses and the level densities of the nuclei involved in the last steps of the evaporation chain [45].

4.3. Intermediate mass fragment emission and multi-fragmentation

Although the most probable de-excitation channels are the statistical evaporation of γ-rays, nucleons or clusters of nucleons, and fission, at sufficiently high values of the excitation energies the emission of intermediate-mass fragments and even the sudden break-up of the nucleus in several pieces or multi-fragmentation becomes possible. The present data have shown that these particular de-excitation channels, intermediate-mass fragment emission and multi-fragmentation, clearly manifest in the shape of the production cross sections and in the kinematic properties of light residual nuclei produced in spallation reactions. Several works make use of these measurements to conclude on the role of these de-excitation mechanisms [46,47,48]

4.4. Fission dynamics

The accurate measurement of the fission cross sections but also the charge and mass distributions of fission fragments also allowed us to deeply investigate this reaction channel. The comparison of these observables with statistical models describing the fission process according to the transition-state picture introduced by Bohr and Wheeler clearly indicated that this model overestimate the fission rate [49,50]. However, a dynamical description of fission including dissipation, as a macroscopic parameter coupling intrinsic and collective degrees of freedom in fission, and the time the system requires to reach first the saddle point and then scission provide a much better description of the present data [51,52].

5. Conclusions

A large experimental program to investigate the production of residual nuclei in spallation reactions was performed in collaboration by several European research institutes and universities during the last years. A novel experimental technique combining inverse kinematics and a high-resolving power magnetic spectrometer made it possible the isotopic identification of all residual nuclei produced in these reactions but also to determine their production cross sections and kinematic properties with high accuracy. 16 different spallation reactions were investigated using spallation-target nuclei with different mass number and neutron excess, and projectile energies between 200 and 1500 A MeV. Around 7000 production cross sections were measured with an accuracy around 10% for spallation-evaporation residues and 20% to 30% for spallation-fission residues.

The qualitative analysis of this comprehensive data set allowed us to obtained rich information on the spallation process. The measured cross sections clearly show the role of the first (intra-nuclear cascade) and second (de-excitation) stages of the collision. The excitation energy induced by the collision defines the length of the evaporation chain and therefore the final mass number of the residual nuclei. Their neutron excess manifest as a "memory effect" at low excitation energy (low mass loss) while at sufficiently high excitation energy the limiting fragmentation regime is reached and the evaporation residues follow the so called "evaporation corridor" in the chart of the nuclides. Fission is also clearly observed with heavy spallation-target nuclei. Actinides show a typical double-hump distribution of fission residues produced in peripheral collisions inducing low excitation energy where shell effects play a major role in the mass-asymmetry dependence of the fission potential. However, we also observe a single-hump distribution of fission residues corresponding to high energy collisions at small impact parameters. Pre-actinides have only a single-hump distribution of fission fragments due to the higher fission barriers reducing the role of shell effects. Spallation target nuclei around ^{136}Xe or lighter do not show any fission.

A deeper analysis of this data is contributing to improve our understanding on spallation reactions. For example the analysis of residual nuclei very close in mass and atomic number to the spallation-target nuclei, produced in extremely peripheral collisions provide us interesting and quantitative information on the intra-nuclear cascade process. In particular in medium nucleon-nucleon cross sections, Pauli blocking effects or inelastic nucleon-nucleon processes are being investigated. Light residual nuclei are used to investigate de-excitation channels like intermediate-mass fragment emission of multi-fragmentation but also pairing correlations from the observed even-odd staggering in the final cross sections. Finally, the accurate measurement of the mass and charge distributions of fission residues provides clear indications on the role of the dynamics in the fission process. With these data we have learnt that fission can not be described as a pure statistical process, being necessary a more complete

description including the coupling of intrinsic and collective degrees of freedom through a dissipation parameter.

Finally we can conclude that this comprehensive and accurate data set on residual nuclei production in spallation reactions will be decisive for improving model calculations describing these reactions and therefore, for the design of target assemblies for the next generation spallation-neutron sources.

REFERENCES

[1] http://neutrons.ornl.gov/
[2] http://j-parc.jp/index-e.html
[3] http://www.isis.rl.ac.uk/
[4] http://neutron.neutron-eu.net/n_ess
[5] C.D. Bowman et al.: Nucl. Instrum. and Methods A \textbf{320}, 336 (1992)
[6] T. Takizuka: Proceedings of the International Conference on Accelerator-Driven Transmutation Technologies and Applications, Las Vegas, NV, 1994, AIP conference proceedings n. 346
[7] C. Rubbia et al.: preprint CERN/AT/95-44(ET), 1995
[8] R. Michel, P. Nagel, International Codes and Model Intercomparison for intermediate energy activation yields. NSC/DOC(97)-1, NEA/P\&T No 14
[9] F. Goldenbaum, contribution to the Joint ICTP-IAEA Advanced Workshop on Model Codes for Spallation Reactions, February 2008, Trieste, Italy
[10] Y. Titarenko, contribution to the Joint ICTP-IAEA Advanced Workshop on Model Codes for Spallation Reactions, February 2008, Trieste, Italy
[11] R. Michel, contribution to the Joint ICTP-IAEA Advanced Workshop on Model Codes for Spallation Reactions, February 2008, Trieste, Italy
[12] A. Junghans et al., Nucl. Instrum. Methods A 370 (1996) 312
[13] Ph. Chesny et al., GSI Annual Report 97-1, 1997, 190
[14] H. Geissel et al., Nucl. Instrum. Methods B70 (1992) 286
[15] B. Voss et al., Nucl. Instrum. Methods A364 (1995) 150
[16] M. Pfuetzner et al., Nucl. Instrum. Methods B 86 (1994) 213
[17] J.-P. Dufour et al., Nucl. Instrum Methods A 248 (1986) 267
[18] K.-H. Schmidt , Nucl. Instrum. Methods A 260 (1987) 287
[19] J. Benlliure et al., Nucl. Phys. A 660 (1999) 87
[20] E. Casarejos et al., Phys. Rev. C 74 (2006) 044612
[21] J. Pereira et al., Phys. Rev. C 75 (2007) 014602
[22] B. Jurado et al., Nucl. Instrum. Methods A 478 (2002) 493
[23] J. Benlliure et al., Nucl. Instr. and Methods A 478 (2002) 493
[24] I. Mustapha, PhD thesis, University Paris X, France, July 1999
[25] J. Taieb et al., Nucl. Phys. A 724 (2003) 413
[26] M. Bernas et al., Nucl. Phys. A 725 (2003) 213
[27] M. Bernas et al., Nucl. Phys. A 765 (2006) 197
[28] M.V. Ricciardi et al., Phys. Rev. C 73 (2006) 014607
[29] P. Armbruster et al., Phys. Rev. Lett. 93 (2004) 212701
[30] T. Enqvist et al., Nucl. Phys. A 686 (2001) 481
[31] W. Wlazlo et al. Phys. Rev. Lett. 84 (2000) 5736
[32] L. Audouin et al., Nucl. Phys. A 768 (2006) 1
[33] B. Fernandez-Dominguez et al., Nucl. Phys. A 747 (2005) 227
[34] T. Enqvist et al. Nucl. Phys. A 703 (2002) 435
[35] F. Rejmund et al., Nucl. Phys. A 683 (2001) 540
[36] J. Benlliure et al., Nucl. Phys. A 683 (2001) 513
[37] P. Napolitani et al., Phys. Rev. C 76 (2007) 064609

[38] P. Napolitani, PhD thesis, Université Paris XI, France, September 2004
[39] C. Villagrasa-Canton et al., Phys. Rev. C 75 (2007) 044603
[40] http://www-win.gsi.de/charms/data.htm
[41] J. Benlliure et al., Nucl. Phys. A 628 (1998) 458
[42] K.-H. Schmidt et al., Nucl. Phys. A 665 (2000) 221
[43] A. Bacquias, PhD thesis, University Louis Pateur, Strasbourg, France, July 2008
[44] M. Fernández, PhD thesis, University of Santiago de Compostela, Spain, January 2008
[45] M.V. Ricciardi et al., Nucl. Phys. A 733 (2004) 299
[46] M.V. Ricciardi et al., Phys. Rev. C 73 (2006) 014607
[47] P. Napolitani et al., Phys. Rev C 70 (2004) 054607
[48] E. Le Gentil et al., Phys. Rev. Lett. 100 (2008) 022701
[49] J. Benlliure et al., Nucl. Phys. A 700 (2002) 469
[50] J. Benlliure et al., Phys. Rev. C 74 (2006) 014609
[51] B. Jurado et al., Phys. Rev. Lett. 93 (2004) 072501
[52] B. Jurado et al., Nucl. Phys. A 747 (2005) 14

Role of multifragmentation in spallation reactions

A.S. BOTVINA

Institute for Nuclear Research,
Russian Academy of Sciences,
Moscow, Russia

Abstract. In nuclear reactions induced by hadrons and ions of high energies, nuclei can disintegrate into many fragments during a short time (~100 fm/c). This phenomenon known as nuclear multifragmentation was under intensive investigation last 20 years. It was established that multifragmentation is a universal process taking place in all reactions when the excitation energy transferred to nuclei is high enough, more than 3 MeV per nucleon, independently from the initial dynamical stage of the reactions. Very known compound nucleus decay processes (sequential evaporation and fission), which are usual for low energies, disappear and multifragmentation dominates at high excitation energy. For this reason, calculation of multifragmentation must be carried on in all cases when production of highly excited nuclei is expected, including spallation reactions. On the other hand, one can consider multifragmentation as manifestation of the liquid-gas phase transition in finite nuclei. This gives way for studying nuclear matter at subnuclear densities and for applications of properties of nuclear matter extracted from multifragmentation reactions in astrophysics. In this contribution, the Statistical Multifragmentation Model (SMM), which combines the compound nucleus processes at low energies and multifragmentation at high energies, is described. The most important ingredients of the model are discussed.

1. Introduction

Statistical approaches have proved to be very successful for description of nuclear reactions. According to the statistical hypothesis, initial dynamical interactions between nucleons lead to re-distribution of the available energy among many degrees of freedom, and the nuclear system evolves towards equilibrium. The most famous example of such an equilibrated nuclear source is the 'compound nucleus' introduced by Niels Bohr in 1936 [1]. It was clearly seen in low-energy nuclear reactions leading to excitation energies of a few tens of MeV. It is remarkable that the statistical concept works also for nuclear reactions induced by particles and ions of intermediate and high energies, when nuclei break-up into many fragments (multifragmentation) [2]. In the most general consideration the process may be subdivided into several stages: (1) a dynamical stage leading to formation of equilibrated nuclear system, (2) disassembly of the system into individual primary fragments, (3) de-excitation of hot primary fragments.

2. Formation of thermalized nuclear system

At present, a number of dynamical models is used for description of nuclear reactions at intermediate energies. The Intranuclear Cascade Model was the first one used for realistic calculations of ensembles of highly excited residual nuclei which undergo multifragmentation, see e.g. [3, 4, 5]. Other more sophisticated models were also used for dynamical simulations of heavy-ion reactions, such as quantum molecular dynamics (QMD), Boltzmann (Vlasov)-Uehling-Uhlenbeck (BUU, VUU) and other similar models (see e.g. refs. [6]). All dynamical models agree that the character of the dynamical evolution changes after a few rescatterings of incident nucleons, when high energy particles ('participants') leave the system. This can be seen from distributions of nucleon velocities and density profiles in remaining spectators [7, 8, 9]. However, the time needed for equilibration and transition to the statistical description is still under debate. This time is estimated around or less than 100 fm/c for spectator matter, however, it slightly varies in different models. Parameters of the

predicted equilibrated sources, i.e. their excitation energies, mass numbers and charges vary significantly with this time. In this case a reasonable strategy is to use results of the dynamical simulations as a qualitative guide line, but extract parameters of thermalized sources from the analysis of experimental data. In this case, one can avoid uncertainties of dynamical models in description of the thermalization process.

3. Break-up of nuclear system into hot primary fragments

3.1. Evolution from sequential decay to simultaneous break-up

After dynamical formation of a thermalized source, its further evolution depends crucially on the excitation energy and mass number. The standard compound nucleus picture is valid only at low excitation energies when sequential evaporation of light particles and fission are the dominant decay channels [2]. Some modifications of the evaporation/fission approach were proposed in order to include emission of fragments heavier than α -particles, see e.g. [10, 11, 12]. However, the concept of the compound nucleus cannot be applied at high excitation energies, E* $\gtrsim$ 3 MeV/nucleon. The reason is that the time intervals between subsequent fragment emissions, estimated both within the evaporation models [13] and from experimental data [14], become very short, of order of a few tens of fm/c. In this case there will not be enough time for the residual nucleus to reach equilibrium between subsequent emissions. Moreover, the produced fragments will be in the vicinity of each other and, therefore, should interact strongly. The rates of the particle emission calculated as for an isolated compound nucleus will not be reliable in this situation. There are many other theoretical arguments in favour of a simultaneous break-up at high excitation energy. For example, the Hartree-Fock and Thomas-Fermi calculations predict that the compound nucleus will be unstable at high temperatures [15]. Sophisticated dynamical calculations have also shown that a nearly simultaneous break-up into many fragments is the only possible way for the evolution of highly-excited systems [16].

On the other hand, the picture of a nearly simultaneous break-up in some freeze-out volume is more justified in this case. Indeed, the time scales of less than 100 fm/c are extracted for multifragmentation reactions from experimental data [17, 18]. Several analyses of experimental data exist, which also reject the binary decay mechanism of fragment production via sequential evaporation from a compound nucleus at high excitation energy. For example, this follows from the fact that a popular sequential GEMINI code cannot describe the multifragmentation data [19, 20, 21]. We believe that a formal reason of this failure is that the evaporation approaches always predict larger probabilities for emission of light particles (in particular, neutrons) than for intermediate mass fragments (IMFs). The GEMINI model, which assumes independent evaporation of fragments, fails also to describe angular correlations of the produced IMFs [22]. The reason is that at multifragmentation these correlations reflect Coulomb interaction of many fragments, but not a two-body kinematic.

3.2. Statistical multifragmentation model

Several versions of the statistical approach have been proposed for the description of multifragmentation reactions (see e.g. [2, 23, 24]). As the main de-excitation code we take the Statistical Multifragmentation Model (SMM), fully described in a review [2]. The reason is that this model was primary constructed for use after initial dynamical stage, and adjusted for this kind of hybrid calculations.

The model assumes statistical equilibrium of excited nuclear system with mass number A_0 , charge Z_0 , and excitation energy (above the ground state) E_0 at a low-density freezeout

volume. This volume can be parameterized as $V = V_0 + V_f$, so the baryon density is $\rho = A_0/V$. V_0 is the volume of the system at the normal nuclear density $\rho_0 \approx 0.15$ fm^{-3}. V_f is the so-called free volume available for translational motion of fragments. In the excluded volume approximation V_f may be taken as a constant for all break-up channels, however, under more realistic assumption, it depends on fragment multiplicity M in the channels [2].

The model considers all break-up channels (ensemble of partitions $\{p\}$) composed of nucleons and excited fragments taking into account the conservation of baryon number, electric charge and energy. An important advantage of the SMM is that besides these break-up channels it includes also the compound nucleus channel, and takes into account competition between all channels. In this way the SMM includes the conventional evaporation and fission processes at low excitation energy, and provides natural generalization of the de-excitation process for high excitation energy.

In the model light nuclei with mass number $A \leq 4$ and charge $Z \leq 2$ are treated as elementary stable particles with masses and spins taken from the nuclear tables ("nuclear gas"). Only translational degrees of freedom of these particles contribute to the entropy of the system. Fragments with $A > 4$ are treated as heated nuclear liquid drops. In this way one may study the nuclear liquid-gas coexistence in the freeze-out volume. Their individual free energies F_{AZ} are parameterized as a sum of the bulk, surface, Coulomb and symmetry energy contributions

$$F_{AZ} = F^B_{AZ} + F^S_{AZ} + E^C_{AZ} + E^{sym}_{AZ}. \qquad (1)$$

The standard expressions for these terms are: $F^B_{AZ} = (-W_0 - T^2/\epsilon_0)A$, where T is the temperature, the parameter ϵ_0 is related to the level density, and $W_0 = 16$ MeV is the binding energy of infinite nuclear matter; $F^S_{AZ} = B_0 A^{2/3}(\frac{T_c^2 - T^2}{T_c^2 + T^2})^{5/4}$, where $B_0 = 18$ MeV is the surface coefficient, and $T_c = 18$ MeV is the critical temperature of infinite nuclear matter; $E^C_{AZ} = cZ^2/A^{1/3}$, where $c = (3/5)(e^2/r_0)(1-(\rho/\rho_0)^{1/3})$ is the Coulomb parameter (obtained in the Wigner-Seitz approximation), with the charge unit e and r_0=1.17 fm; $E^{sym}_{AZ} = \gamma(A-2Z)^2/A$, where $\gamma = 25$ MeV is the symmetry energy parameter. These parameters are those of the Bethe-Weizsäcker formula and correspond to the assumption of isolated fragments with normal density in the freeze-out configuration, an assumption found to be quite successful in many applications. It is to be expected, however, that in a more realistic treatment primary fragments will have to be considered not only excited but also expanded and still subject to a residual nuclear interaction between them. These effects can be accounted for in the fragment free energies by changing the corresponding liquid-drop parameters. The Coulomb interaction of fragments in the freeze-out volume is described within the Wigner-Seitz approximation (see ref. [2] for details).

As is well known, the number of partitions of medium and heavy systems ($A_0 \sim 100$) is enormous (see e.g. [25]). In order to take them into account the model uses few prescriptions. At small excitation energies the standard SMM code [2] uses a microcanonical treatment, however, taking into account a limited number of disintegration channels: as a rule, only partitions with total fragment multiplicity $M \leq 3$ are considered. This is a very reasonable approximation at low temperature, when the compound nucleus and low-multiplicity channels

dominate. Recently, a full microcanonical version of the SMM using the Markov Chain method was introduced [25, 26]. It can be used for exploring all partitions without limitation. However, it is a more time consuming approach, and it is used in special cases only [26].

Within the microcanonical ensemble the statistical weight of a partition p is calculated as

$$W_{\mathrm{p}} \propto exp\ S_{\mathrm{p}}, \tag{2}$$

where S_p is the corresponding entropy, which depends on fragments in this partition, as well as on the excitation energy E_0, mass number A_0, charge Z_0, volume V of the system. In the standard treatment we follow a description which corresponds to approximate microcanonical ensemble. Namely, we introduce a temperature T_p characterising all final states in each partition p. It is determined from the energy balance equation taking into account the total excitation energy E_0 [2]. In the following we determine S_p for the found T_p by using conventional thermodynamical relations. In the standard case, it can be written as

$$S_{\mathrm{p}} = ln(\prod_{A,Z} g_{A,Z}) + ln(\prod_{A,Z} A^{3/2}) - ln(A_0^{3/2}) - ln(\prod_{A,Z} n_{A,Z}!) +$$
$$(M-1)ln(V_f/\lambda_{T_{\mathrm{p}}}^3) + 1.5(M-1) + \sum_{A,Z}(\frac{2T_pA}{\epsilon_0} - \frac{\partial F_{AZ}^S(T_p)}{\partial T_p}),$$

where $n_{A,Z}$ as the number of fragments with mass A and charge Z in the partition, $g_{A,Z} = (2s_{A,Z}+1)$ is the spin degeneracy factor, $\lambda_{T_{\mathrm{p}}} = (2\pi\hbar^2/m_N T_p)^{1/2}$ is the nucleon thermal wavelength ($m_N \approx 939$ MeV is the average nucleon mass), and the summation is performed over all fragments of the partition p. We enumerate all considered partitions and select one of them according to its statistical weight by the Monte-Carlo method.

At high excitation energy the standard SMM code makes a transition to the grandcanonical ensemble [2], since the number of partitions with high probability becomes too large. In the grand canonical formulation, after integrating out translational degrees of freedom, one can write the mean multiplicity of nuclear fragments with A and Z as

$$\langle n_{A,Z}\rangle = g_{A,Z}\frac{V_f}{\lambda_T^3}A^{3/2}\exp\left[-\frac{1}{T}\left(F_{AZ}(T,V) - \mu A - \nu Z\right)\right]. \tag{3}$$

Here the temperature T can be found from the total energy balance of the system by taking into account all possible fragments with A from 1 to A_0 and with Z from 0 to Z_0 [2]. The chemical potentials μ and ν are found from the mass and charge constraints:

$$\sum_{A,Z}\langle n_{A,Z}\rangle A = A_0, \quad \sum_{A,Z}\langle n_{A,Z}\rangle Z = Z_0. \tag{4}$$

In this case the grand canonical occupations $\langle n_{A,Z}\rangle$ are used for Monte-Carlo sampling of the fragment partitions [2]. These two methods of partition generation are carefully adjusted to provide a smooth transition from the low energy to the high energy regimes.

4. Propagation and de-excitation of hot fragments

After the Monte-Carlo generation of a partition the temperature of the hot fragments, their excitation energy and momenta can be found from the energy balance. In this approach the temperature may slightly fluctuate from partition to partition, since the total energy of the system E_0 is always conserved. At the next stage Coulomb acceleration and propagation of fragments must be taken into account. For this purpose the fragments are placed randomly in the freeze-out volume V (without overlapping), and their positions are adjusted by taking into account that their Coulomb interaction energy must be equal to the value calculated in the Wigner-Seitz approximation. We note that in the case of the Markov Chain SMM version [26] this adjustment is not necessary, since positions of fragments are sampled directly. In the freeze-out volume a possible collective flow of fragments can also be taken into account [2]. Usually it is done by adding additional radial velocities to the fragments (proportional to their distances from the centre of mass) in the beginning of Coulomb acceleration. In the following we resolve the Hamilton equations for motion of fragment from these initial positions in their mutual Coulomb field. The energy and momentum balances are strictly respected during this dynamical propagation.

The secondary de-excitation of primary hot fragments includes several mechanisms. For light primary fragments (with $A \leq 16$) produced in multifragmentation even a relatively small excitation energy may be comparable with their total binding energy. In this case we assume that the principal mechanism of de-excitation is the explosive decay of the excited nucleus into several smaller clusters (the Fermi break-up) [11, 2]. In this decay the statistical weight of the channel p containing n particles with masses m_i ($i = 1, \cdots, n$) in volume V_p can be calculated in microcanonical approximation:

$$\Delta\Gamma_p \propto \frac{S}{G}\left(\frac{V_p}{(2\pi\hbar)^3}\right)^{n-1}\left(\frac{\prod_{i=1}^{n} m_i}{m_0}\right)^{3/2}\frac{(2\pi)^{\frac{3}{2}(n-1)}}{\Gamma(\frac{3}{2}(n-1))}\cdot\left(E_{kin}-U_p^C\right)^{\frac{3}{2}n-\frac{5}{2}}, \qquad (5)$$

where $m_0 = \sum_{i=1}^{n} m_i$ is the mass of the decaying nucleus, $S = \prod_{i=1}^{n}(2s_i+1)$ is the degeneracy factor (s_i is the i-th particle spin), $G = \prod_{j=1}^{k} n_j!$ is the particle identity factor (n_j is the number of particles of kind j). E_{kin} is the total kinetic energy of particles at infinity which can be found through the energy balance by taking into account the fragment excitation energy, U_p^C is the Coulomb barrier for this decay. We have slightly modified this model [11] by including fragment excited states stable with respect to the nucleon emission as well as some long-lived unstable nuclei.

The successive particle emission from hot primary fragments with $A > 16$ is assumed to be their basic de-excitation mechanism, as in the case of the compound nucleus decay. Due to the high excitation energy of these fragments, the standard Weisskopf evaporation scheme was modified to take into account the heavier ejectiles up to ^{18}O, besides light particles (nucleons, d, t, α), in ground and particle-stable excited states [11]. The width for the emission of a particle j from the compound nucleus (A, Z) is given by:

$$\Gamma_j = \sum_{i=1}^{n}\int_0^{E^*_{AZ}-B_j-\epsilon_j^{(i)}} \frac{\mu_j g_j^{(i)}}{\pi^2\hbar^3}\sigma_j(E)\frac{\rho_{A'Z'}(E^*_{AZ}-B_j-E)}{\rho_{AZ}(E^*_{AZ})}EdE. \qquad (6)$$

Here the sum is taken over the ground and all particle-stable excited states $\epsilon_j^{(i)}$ $(i = 0, 1, \cdots, n)$ of the fragment j, $g_j^{(i)} = (2s_j^{(i)} + 1)$ is the spin degeneracy factor of the i -th excited state, μ_j and B_j are corresponding reduced mass and separation energy, E^*_{AZ} is the excitation energy of the initial nucleus, E is the kinetic energy of an emitted particle in the centre-of-mass frame. In eq. (6) ρ_{AZ} and $\rho_{A'Z'}$ are the level densities of the initial (A , Z) and final (A' , Z') compound nuclei. The cross section $\sigma_j(E)$ of the inverse reaction (A' , Z')+ j = (A , Z) was calculated using the optical model with nucleus-nucleus potential [11]. The evaporation process was simulated by the Monte Carlo method and the conservation of energy and momentum was strictly controlled in each emission step.

An important channel of de-excitation of heavy nuclei (A > 100) is fission. This process competes with particle emission, and it is also simulated with the Monte-Carlo method. Following the Bohr-Wheeler statistical approach we assume that the partial width for the compound nucleus fission is proportional to the level density at the saddle point $\rho_{sp}(E)$ [2]:

$$\Gamma_f = \frac{1}{2\pi\rho_{AZ}(E^*_{AZ})} \int_0^{E^*_{AZ}-B_f} \rho_{sp}(E^*_{AZ} - B_f - E)dE, \qquad (7)$$

where B_f is the height of the fission barrier which is determined by the Myers-Swiatecki prescription. For approximation of ρ_{sp} we used the results of the extensive analysis of nuclear fissility and Γ_n/Γ_f branching ratios, see ref. [2] for details.

All these models for secondary de-excitation were tested by numerical comparisons with experimental data on decay of compound nuclei with excitation energies less than 2–3 MeV per nucleons. It is important that after all stages the SMM provides event by event simulation of the whole break-up process and allows for direct comparison with experimental events.

5. Verification and applications of the SMM

As was shown already in first publications [2, 4] the SMM gives a very good description of experimental data in the case when fragments are emitted from equilibrated sources. Later on, many experimental groups have successfully applied SMM for interpretation of their data: ALADIN (GSI, Germany) [27], EOS (Purdue University, USA) [28], ISIS (Indiana University, USA) [22], Miniball-Multics (MSU, USA and INFN, Italy) [29], INDRA (GANIL, France) [30], FAZA (Dubna, Russia) [31], and others. In particular, the SMM describes charge (mass) distributions of produced fragments and their evolution with excitation energy, isotope distributions, multiplicities of produced particles and fragments, charge distributions of first, second, third fragments in the system, correlation functions (charge, angle, velocity ones) of the fragments, fragment kinetic energy distributions. Simultaneously, this model reproduces global characteristics of the systems, such as caloric curves, critical indexes for the phase transition, different moments of the fragment charge distribution. In other words, the model can describe nearly completely experimental events, and in some cases it can be used as event generator. Importance of multifragmentation channels for nuclear reactions is now widely recognized. The SMM is included in many complex codes designed to describe transport of particles and isotope production in matter, for example, in GEANT4 (CERN) [32].

On the other hand, systematic studies of multifragmentation have brought important information about the nuclear liquid-gas phase transition [33, 34]. Multifragmentation reaction opens the unique possibility for investigating the phase diagram of nuclear matter at temperatures $T \approx 3 - 8$ MeV and densities around $\rho \approx 0.1 - 0.3\,\rho_0$, which are expected in the freeze-out volume. Previously, only theoretical calculations without experimental verification were available for this phase diagram region. This information is crucial, for example, for the construction of a reliable equation of state of stellar matter and modelling nuclear composition in supernovae explosions, where the same thermodynamical conditions of nuclear matter exist [35].

One of the promising applications of multifragmentation reactions is investigation of properties of excited nuclei embedded in surrounding of other nuclear species. They can be modified in comparison with the properties of isolated nuclei, since in the freezeout volume fragments can interact with each other with Coulomb and residual nuclear forces. This study can not be performed in conventional nuclear reactions involving only a compound nucleus channel. However, the new properties of fragments can be extracted from analysis of experimental multifragmentation data. As was found there are essential modifications of symmetry and surface energies of hot fragments [36, 37, 38, 39]. These modified properties of fragments should be also taken into account during their secondary de-excitation [40].

6. Conclusion

Nearly 60 years ago nuclear physicers started to investigate the spallation reaction. Primary it was considered as emission of few nucleons and light charged particles (and, eventually, fission) from a heavy nucleus. Only these processes were clearly observed that time, since the accelerators could provide projectile beams with relatively low energy (few hundred MeV). During the last 15 years we have obtained solid evidences that at high projectile energies, and in heavy-ion collisions, a heavy nucleus can be completely disintegrated into light and intermediate mass fragments. This multifragmentation reaction is universal, and it is a natural fast decay taking place at high energies. The multifragmentation channels take as much as 10–15% of the total cross section in high-energy hadron-nucleus reactions, and about twice more in high-energy nucleus-nucleus collisions. Moreover, multifragmentation reactions are responsible for production of most intermediate mass fragments and some specific isotopes.

The traditional evaporation and fission models can not describe correctly this fast multifragmentation, since they are based on the hypothesis of a long-lived compound nucleus. There is a statistical approach, realized in the Statistical Multifragmentation Model (SMM), which allows for natural extension of conventional cascade-evaporation calculations for the multifragmentation reaction. At low excitation energy it includes compound nucleus processes, however, at high excitations it describes the simultaneous break-up. Already at present the SMM demonstrates very good description of experimental data, especially at high excitation energy of nuclear systems (more than 3 MeV/nucleon). The problems, which are necessary to resolve within this approach, concern mainly a better description of transition from the compound nucleus to the multifragmentation decay. This is important for calculation of reactions initiated by low energy projectiles (up to 1 GeV), when very few equilibrated nuclei have a high excitation energy sufficient for multifragmentation.

REFERENCES

[1] N. Bohr, Nature 137, 344 (1936).
[2] J.P. Bondorf, A.S. Botvina, A.S. Iljinov, I.N. Mishustin and K. Sneppen, Phys. Rep. 257, 133 (1995).
[3] Y. Yariv and Z. Fraenkel, Phys. Rev. C20, 2227 (1979).
[4] A.S. Botvina, A.S. Iljinov and I.N. Mishustin, Nucl. Phys. A507, 649 (1990).
[5] A. Boudard, J. Cugnon, S. Leray, C. Volant, Phys. Rev. C66, 044615 (2002).
[6] J. Aichelin et al., Phys. Rev., C37 2451 (1988). W. Bauer et al., Ann. Rev. Nucl. Part. Sci. 42, 77 (1992). J.Konopka et al., Prog. Part. Nucl. Phys. 30, 301 (1993).
[7] H.W. Barz et al., Nucl. Phys. A561, 466 (1993).
[8] J.P. Bondorf, A.S. Botvina, I.N. Mishustin and S.R. Souza. Phys. Rev. Lett. 73, 628 (1994).
[9] A.S. Botvina, A.B. Larionov and I.N. Mishustin, Phys. Atom. Nucl. 58, 1703 (1995).
[10] L.G. Moretto, Nucl. Phys. A247, 211 (1975).
[11] A.S. Botvina et al., Nucl. Phys. A475, 663 (1987).
[12] R.J. Charity et al., Nucl. Phys. A483, 371 (1988).
[13] R.J. Charity, Phys. Rev. C61, 054614 (2000).
[14] M. Jandel et al., J. Phys. G: 31, 29 (2005).
[15] P. Bonche, S. Levit, and D. Vautherin, Nucl. Phys. A436, 265 (1985). E. Suraud, Nucl. Phys. A462, 109 (1987).
[16] S.Das Gupta et al., Phys. Rev. C35, 556 (1987). B. Strack, Phys. Rev. C35, 691 (1987). D.H. Boal and J.N. Gloshi, Phys. Rev. C37, 91 (1988).
[17] L. Beaulieu et al., Phys. Rev. Lett. 84, 5971 (2000).
[18] V.A. Karnaukhov et al., Phys. Atom. Nucl. 66, 1242 (2003).
[19] J. Hubele et al., Phys. Rev. C46, R1577 (1992).
[20] P. Desesquelles et al., Nucl. Phys. A604, 183 (1996).
[21] P. Napolitani et al., Phys. Rev. C70, 054607 (2004).
[22] L. Pienkowski et al., Phys. Rev. C65, 064606 (2002).
[23] S.E. Koonin and J. Randrup, Nucl. Phys. A471, 355c (1987).
[24] D.H.E. Gross, Rep. Progr. Phys. 53, 605 (1990).
[25] A.S. Botvina, A.D. Jackson, I.N. Mishustin, Phys. Rev. E62, R64 (2000).
[26] A.S. Botvina, I.N. Mishustin, Phys. Rev. C63, 061601 (2001).
[27] A.S. Botvina et al., Nucl. Phys. A584, 737 (1995).
[28] R.P. Scharenberg et al., Phys. Rev. C64, 054602 (2001).
[29] M. D'Agostino, et al., Phys. Lett. B371, 175 (1996).
[30] N. Bellaize, et al., Nucl. Phys. A709, 367 (2002).
[31] S.P. Avdeyev et al., Nucl. Phys. A709, 392 (2002).
[32] S. Agostinelli et al., NIM A506, 250 (2003).
[33] J. Pochodzalla and ALADIN collaboration, Phys. Rev. Lett. 75, 1040 (1995).
[34] M. D'Agostino, A.S. Botvina, M. Bruno, A. Bonasera, J.P. Bondorf, I.N. Mishustin et al., Nucl. Phys. A650, 329 (1999).
[35] A.S. Botvina and I.N. Mishustin, Phys. Lett. B584, 233 (2004).
[36] A. Le Fevre et al., Phys. Rev. Lett. 94, 162701 (2005).
[37] J. Iglio et al., Phys. Rev. C74, 024605 (2006).
[38] A.S. Botvina et al., Phys. Rev. C74, 044609 (2006).
[39] G. Souliotis et al., Phys. Rev. C75, 011601(R) (2007).
[40] N. Buyukcizmeci et al., Eur. Phys. J. A25, 57 (2005).

GEMINI: A Code to Simulate the Decay of a Compound Nucleus by a Series of Binary Decays

R. CHARITY

Washington University at Saint Louis,
Department of Chemistry,
St. Louis, Missouri, United States of America

Abstract. The details of the statistical-model code GEMINI are discussed. It is shown that GEMINI does a reasonable job at reproducing experimental charge distributions for light compound nuclei. However for heavier systems, it overpredicts the width of the fission mass distribution. A new code GEMINI++ has been written to address this problem.

1. Introduction

The statistical-model code GEMINI was written in 1986 to address complex-fragment emission in fusion reactions. It differed from most other statistical-modes codes at the time in that it allowed not just light-particle evaporation and symmetric fission, but all possible binary-decay modes. Soon after the discovery of fission, Bohr and Wheeler borrowed the one-dimensional transition-state formalism from the study of chemical reaction rates and applied it to symmetry fission [1]. Moretto [2] generalized this formalism by adding an extra dimension associated with mass-asymmetry thus allowing it to treat binary decays of intermediate mass asymmetry. This formalism, in conjugation with barriers calculated for asymmetric fission by Arnie Sierk [3], was incorporated into GEMINI. With these ingredients, GEMINI produced rather good agreement with complex-fragment or asymmetric fission data obtained with light compound nuclei [4-6].

GEMINI is a Monte Carlo code which follows the decay of a compound nucleus by a series of sequential binary decays until such decays are impossible due to energy conservation or improbable due gamma-ray competition. For the latter, only the statistical emission of *E1* and *E2* gamma rays is considered, but these are only important at the lowest thermal energies when the particle decay width approaches zero.

As GEMINI was written to confront data from heavy-ion induced fusion reactions, the effects of large angular momenta were explicitly treated. For this reason the dichotomy between light-particle evaporation and other binary decays was still maintained. The best way of treating light-particle evaporation at high angular momentum is via the Hauser-Feshbach formalism [7]. Thus GEMINI differs from most other statistical-model codes used for modeling spallation reactions in that it uses this formalism rather than the Weisskopf-Ewing result [8]. The cost of this better treatment of angular momentum is increased CPU time. The usefulness of this aspect of GEMINI in modeling spallation reactions therefore depends on the degree to which residues with high spin are produced in the initial stages of the reaction. Angular momentum effects include anisotropic angular distributions, although these distributions still process a symmetry about $\theta_{cm} = 90^{\circ}$. To model these correctly, the input to GEMINI must also include the orientation of the spin axis of the excited residue.

For heavy systems, GEMINI simulations generally overpredict the width of the fission mass and charge distributions. Although this may be a failure of the asymmetric fission barriers used in the calculations, it probably signifies a failure of the underlying model. The Moretto formalism predicts the mass-asymmetry distributions along the ridge of conditional saddle points. However, the final mass of the fission fragments is not frozen until the scission point

is reached. For light nuclei, the saddle and scission points are almost degenerate so substantial modification during the saddle-to-scission motion is expected to be small. On the other hand for heavy systems, the saddle and scission configurations are quite different. Specifically for very heavy systems, the saddle point can no longer be approximately by two nascent fragments connect by a neck. The neck disappears and the saddle point is a deformed mononucleus and thus one cannot even define an asymmetry degree of freedom. In such cases, the mass asymmetry develops during the descent from saddle to scission. Therefore, the failure of GEMINI for these heavier systems was not unexpected.

Due to these deficiencies of the original code for heavy nuclei, as new code GEMINI++ has been written to address these problems. The new code also signals a change in language. The original version was written in Fortran77 and subsequently changed to Fortran90. The new version, GEMINI++, is written in the C++ language. In addition, a change of philosophy was made. The original GEMINI was written with lots of options to explore changes in the decay characteristics induced by the inclusion of different physics. No effort was made to systematize parameters to obtain a good overall agreement with data from a large range of compound-nucleus masses. In GEMINI++, extensive comparisons with heavy-ion induced fusion data have been used to optimize the default parameters of the model. Such data are useful for constraining statistical-model codes, as unlike spallation, the excitation energy and spin distributions of the compound nuclei can be well defined. However, this optimization is only for the regions of spin and excitation energies populated by heavy-ion fusion reaction which may not coincide with those produced in spallation.

The details of the various aspects of the two codes are given in the following sections.

2. Light-particle evaporation

In the Hauser-Feshbach formalism [7], the partial decay width of a compound nucleus of excitation energy E^* and spin S_{CN} for the evaporation of particle i is

$$\Gamma_i^{HF} = \frac{1}{2\pi\rho(E^*, S_{CN})}\int d\varepsilon \sum_{S_d=0}^{\infty} \sum_{J=|S_{CN}-S_d|}^{S_{CN}+S_d} \sum_{\ell=|J-S_i|}^{J+S_i} T_\ell(\varepsilon)\rho(E^*-B_i-\varepsilon, S_d) \qquad (1)$$

where S_d is the spin of the daughter nucleus, S_i, J, and ℓ, are the spin, total and orbital angular momenta of the evaporated particle, ε and B_i are its kinetic and separation energies, T_ℓ is its transmission coefficient or barrier penetration factor, and ρ and ρ_{CN} are the level densities of the daughter and the compound nucleus, respectively. The summations include all angular momentum couplings between the initial and final states which are computationally expensive. Evaporation channels include n, p, d, t, ^{3}He, α, ^{6}He, and $^{6\text{-}8}$Li fragments. For the heavier fragments, we include in addition all their excited states with excitation energy less than 5 MeV.

Separation energies B_i, nuclear masses, shell ΔW and ΔP corrections are obtained from the tabulations of Möller *et al*. [9]. Where available the experiment masses are used, otherwise the Finite-Range Droplet model values with shell and pairing corrections are taken.

Transmission coefficients have traditionally been obtained from the inverse reaction using the optical-model parameters obtained from global optical-model fits to elastic scattering data. Alexander *et al*. [10] have pointed out that such transmission coefficients contain the effects

of transparency in the inverse reaction which is not appropriate in evaporation. We have therefore kept the real optical-model potentials, but to ensure full absorption, used the incoming-wave boundary-condition model (IWBC) [11] to calculate T_ℓ. Global optical-model potentials were obtained from Refs. [12-18].

The transmission coefficients define the shape of the low-energy or "sub-barrier" region of the evaporation spectra. For α and heavier particles, these IWBC transmission coefficients systematically underpredict the yield of low-energy particles [19-26]. While adjusting the optical-model parameters to reduce the Coulomb barrier can reproduce some of the α-particle data, Li and Be spectra clearly show the need to a distribution of Coulomb barriers [27]. The origin of this distribution may have contributions from compound-nucleus thermal shape fluctuations [28,29] and/or fluctuations in the diffuseness of the nuclear surface. If the fluctuations are thermally induced, then we expect their variance to be proportional to temperature. In GEMINI++, a simplistic scheme was implemented to incorporate the effects of barrier distributions. The transmission coefficients were calculated as

$$T_\ell(\varepsilon) = \frac{T_\ell^{R_0-\delta r}(\varepsilon) + T_\ell^{R_0}(\varepsilon) + T_\ell^{R_0+\delta r}(\varepsilon)}{3} \tag{2}$$

which is the average of three IWBC transmission coefficients calculated with three different radii for the nuclear potential. The radii R_0 is the value from the global optical-model fits and $\Delta r = w\sqrt{T}$, consistent with thermal fluctuations. The value of the parameter w=0.9 fm was obtained from fits to experiment data.

Nuclear level densities were taken as a Fermi-gas form, i.e.

$$\rho(E^*, J) \propto (2J+1)\exp\left[2\sqrt{a(U,J)U}\right] \tag{3}$$

where a is the level-density parameter and the thermal excitation energy $U=E^*-E_{rot}(J)+\delta P$ is back shifted by the pairing correction δP and the rotational energy of the ground-state configuration $E_{rot}(J)$. The latter is taken from the Finite-Range model of Sierk [30].

Following Ignatyuk *et al.*[31,32], the fade out of shell effects is included in the level-density parameter as

$$a(U) = \tilde{a}(U)\left[1 + h(U)\frac{\delta W}{U}\right] \tag{4}$$

where the function specifying the rate of fade out is

$$h(U) = 1 - \exp(\eta_1 U) \tag{5}$$

The fadeout parameter was set to $1/\eta_1$=18.5 MeV [31-32].

From neutron resonance counting, one finds that at low excitation energies $\tilde{a} \cong A/7.3$ MeV [31]. At higher excitation energies probed by fusion reactions, smaller values are needed to reproduce the kinetic-energy spectra of evaporated particles. Thus $\tilde{a}$ must be dependent on the excitation energy. A number of studies [25,26,33] have assumed the form

$$\tilde{a}(U) = \frac{A}{k + \kappa \frac{U}{A}} \tag{6}$$

where k and κ can be obtained from fits to data and the κ term can be thought of as a first order correction to a constant value of k. For Yb compound nuclei where evaporated n, p, and α spectra were fit, values of k=7 MeV and κ=1.3 MeV were obtained [33]. For heavier systems, where only p, and α spectra were available, not unique values of k and κ were obtained from fits, but if $k \approx$ 8 MeV is assumed, then κ values of 3 MeV for ^{193}Tl [26], 2-3 MeV for ^{200}Pb [25], 4.3 MeV for ^{213}Fr [26], and 8.5 MeV for ^{224}Th [26] compound nuclei were deduced. In addition for ^{106}Cd compound nuclei, evaporation spectra were well reproduced up to high excitation energies with a constant $\tilde{a}$=A/7.5 MeV, i.e. κ=0. These results suggest that κ increases rapidly with A. To systematize this effect in GEMINI++, these data and other evaporation spectra were fit with a slightly different form which was felt to have a better asymptotic behavior,

$$\tilde{a}(U) = \frac{A}{k_\infty - (k_\infty - k_0)\exp\left(-\frac{\kappa}{k_\infty - k_0}\frac{U}{A}\right)}. \tag{7}$$

At U=0, $\tilde{a}$=A/k_0 where k_0=7.3 MeV from neutron resonance counting. For low values of U/A, this form reduces to the previously form of Eq. 6. The evolution of the level-density parameter with excitation energy is thought to be associated with the washing out of long-range correlations associated with coupling between nucleon degrees of freedom and surface vibrations. In the ground state, these long-range correlations cause the single-particle level density $g(\varepsilon)$ to be enhanced near the Fermi energy ε_F [34]. Now as $\tilde{a} \propto g(\varepsilon_F)$, so the washing out of these correlations reduces its value. The level-density parameter should therefore approach the value with no correlations which was taken as $\tilde{a} = A/k_\infty$ (k_∞=12 MeV). Experimental evaporation data can be reproduced with $\kappa = 0.00493\exp(0.0332A)$.

This strong mass dependent has significant consequences for fission of the heavier systems (see later).

The angular distributions of the evaporated fragments can be determined from the ℓ and m quantum numbers of the evaporated particles. One must provide the initial spin projection of the compound nucleus and then use Clebsch-Gordan coefficients and the predicted values of J, ℓ, and S_d to determine the m distributions of the emitted fragment. Although such an approach is implemented in GEMINI for evaporation only, we lack a quantum-mechanical model to follow the m-state distributions through fission. A more general procedure is to use a quasi-classical approach which is also implemented in GEMINI and is the only option is GEMINI++. From the values of J, ℓ, and S_d predicted by the Hauser-Feshbach formalism and the initial spin alignment of the parent nucleus, a classical vector associated with ℓ is determined. The angular distribution of the evaporated particle about this vector is then chosen from the distribution $\frac{dN}{d\Omega} = \left|P_\ell^\ell(\cos\theta)\right|^2$.

3. Fission and complex fragment decay

The Bohr-Wheeler transition-state decay width for symmetric fission [2] is

$$\Gamma_{BW} = \frac{1}{2\pi\rho_{CN}(E^*, S_{CN})}\int d\varepsilon\ \rho_{sad}\left[E^* - B_f(S_{CN}) - \varepsilon\right] \tag{8}$$

where ρ_{sad} is the level-density at the saddle-point, $B_f(S_{CN})$ is the spin-dependent saddle-point energy (fission barrier + ground-state rotational energy) and ε is the kinetic energy in the fission degree of freedom. The 2-dimension extension of this by Moretto is

$$\Gamma(y)dy = \frac{1}{2\pi\rho_{CN}(E^*, S_{CN})}\int\int \frac{dydp_y}{h} d\varepsilon\ \rho_{sad}\left[E^* - B(y, S_{CN}) - \frac{p_y^2}{2m_y}\varepsilon\right] \tag{9}$$

where y is the mass asymmetry, p_y is its conjugate momentum, m_y is the inertia associated with motion in the y coordinate, and $B(y,S_{CN})$ are the energies of the condition saddle-points. The barriers are conditional in the sense they represent a saddle-point configuration when the specified mass-asymmetry is imposed. In the potential-energy surface, these conditional saddle points represent a ridge which must be crossed in order to arrive at the scission configuration.

Simplification to this formula can be made from the expansion

$$\rho(E^* - x) \cong \rho(E^*)\exp\left(-\frac{x}{T}\right) \tag{10}$$

where the nuclear temperature is determined as

$$\frac{1}{T} = \frac{d\ln\rho(E^*)}{dE^*}. \tag{11}$$

With this expansion, the above equation can be reduced to

$$\Gamma(y)dy = \frac{1}{2\pi\rho_{CN}(E^*, S_{CN})}\frac{\sqrt{2\pi T m_y}}{h}\int d\varepsilon\ \rho_{sad}\left[E^* - B(y, S_{CN}) - \varepsilon\right]. \tag{12}$$

With this formalism, in addition to the conditional barriers, one also requires knowledge of the inertia m_y. Later Moretto suggest a new formalism [35]

$$\Gamma_Z = \frac{1}{2\pi\rho_{CN}(E^*, S_{CN})}\int d\varepsilon\ \rho_{sad}\left[E^* - B_Z(S_{CN}) - \varepsilon\right] \tag{13}$$

where here Z is the proton number of one of the nascent fragments. Basically the term $\frac{\sqrt{2\pi T m_y}}{h}$ has been eliminated and the problem has been discretized. In GEMINI this was further extended by allowing for distinct mass and charge splits:

$$\Gamma_{Z,A} = \frac{1}{2\pi\rho_{CN}(E^*, S_{CN})} \int d\varepsilon \; \rho_{sad}\left[E^* - B_{Z,A}(S_{CN}) - \varepsilon\right] \tag{14}$$

The conditional barriers now have both the mass and charge asymmetries imposed and are estimated as

$$B_{Z,A}(S_{CN}) = B_A^{Sierk}(S_{CN}) + \Delta M + \Delta E_{Coul} - \delta W - \delta P \tag{15}$$

where δW and δP are the ground-state shell and pairing corrections to the liquid drop barrier. Shell and pairing effects at the conditional saddle points are assumed to be small. The quantity B_A^{Sierk} is the interpolated Sierk barrier for the specified mass asymmetry. In the Sierk's Finite-Range calculations, the two nascent fragments have the same *Z*/*A* ratio. The correction ΔM now accounts for the different Z/A values of the two fragments, i.e.

$$\Delta M = M(Z,A) + M(Z_{CN} - Z, A_{CN} - A) - M\left(Z_{CN}\frac{A}{A_{CN}}, A\right) - M\left(Z_{CN}\frac{A_{CN} - A}{A_{CN}}\right) \tag{16}$$

where $M(Z,A)$ is the spherical Finite-Range Model mass. In addition there is Coulomb correction

$$\Delta E_{Coul} = E_{Coul}(Z, A, Z_{CN} - Z, A_{CN} - A) - E_{Coul}\left(Z_{CN}\frac{A}{A_{CN}}, A, Z_{CN}\frac{A_{CN} - A}{A_{CN}}, A_{CN} - A\right) \tag{17}$$

where $E_{Coul}(Z_1, A_1, Z_2, A_2)$ is the Coulomb energy between two fragments (Z_1,A_1) and (Z_2,A_2) estimated as two spheres separated by 2 fm with a radius parameter of 1.225 fm.

The total width requires summations over both the *Z* and *A* values of the lightest fragment.

This formalism was implemented with spin-dependent conditional barriers $B_A^{Sierk}(S_{CN})$ interpolated from the Sierk's full finite-range model calculations for ^{110}In [3], ^{149}Tb [36], and ^{194}Hg and, for lighter systems, from Sierk's finite-range calculations using a more simplistic two-spheroid shape parameterization. In the latter case, all barriers were scaled such that the symmetric barrier was consistent with the full finite-range model value. For systems which are more fissile than ^{194}Hg, the ^{194}Hg barriers are used.

This scheme works well for light systems which have a minimum in the mass distribution of the decay products for symmetric division. In these cases the saddle and scission point are almost degenerate. For heavier compound nuclei, saddle and scission points are also still expected to be approximately degenerate for asymmetric divisions [37]. Therefore in GEMINI++, for both light systems and for asymmetric divisions of heavy systems, the Moretto formalism is kept. All binary divisions are included which have asymmetries greater than the value at which the conditional barrier is a minimum, which is spin dependent.

For the more symmetric divisions in heavy nuclei, the Bohr-Wheeler formalism is used to predict the total symmetric fission yield in GEMINI++. The fission barrier is taken from Sierk's Finite-Range Model value after correcting for the ground-state shell and pairing correction, i.e.,

$$B_f(S) = B_f^{Sierk}(S) - \delta W - \delta P. \quad (18)$$

With the parameterized excitation-energy dependent level-density parameters, we find excellent agreement with experiment fission cross sections if the Bohr-Wheeler width is scaled by the factor 2.4 and the ratio of level-density parameters a_f/a_n for the saddle and ground state configuration is taken as unity. One can also obtain similar agreement if the Sierk fission barriers are reduced or if a_f/a_n is increased. The level-density formalism used in GEMINI++, predicts large enhancements in the residue cross section produced in very heavy nuclei where fission is the dominant decay mode. With a constant level-density parameter, residue cross sections are expected to be small in such nuclei. With the excitation-energy dependent level-density parameters, fission is still dominant, but the residue cross sections, though still small, are greatly enhanced. Such enhancements are observed experimentally and were previously explained by dissipation and fission delays. The present analysis suggests a much smaller role for the dependence of the fission probability on these dissipative effects and thus they are not included in the default mode of GEMINI++.

However, friction is not forgotten. Once the saddle-point is crossed, the system losses excitation energy due to light-particle evaporation during the slow saddle-to-scission motion. To estimate the magnitude of this effect, the time required for this motion was assumed to be $t=\eta\ (B_{sad}-B_{sciss})$ where B_{sad} and B_{sciss} are the symmetric saddle and scission point energies and η is the friction. The scission-point energy is determined as $B_{sciss}=Ek^{tot}-Q_f$ where Ek^{tot} is the total kinetic energy released in fission from Ref. [38] and Q_f is fission Q value. In the descent from saddle to scission, excitation energy is being increased due to dissipation and at the same being lost due to evaporation. Significant CPU time would be required to fully model this process, so instead a simple formalism was adopted. As the total number of neutrons emitted is largely determined from the statistical lifetime of the last emitted particle, we only consider evaporation from the scission-point configuration. The total change in potential between saddle and scission $B_{sad}-B_{sciss}$ is assumed to be dissipated into excitation energy at the scission point. As B_{sciss} is spin independent, the Weisskopf-Ewing formalism is used for evaporation at this stage to calculate the decay widths, i.e.,

$$\Gamma_i^{WE} = \frac{(2S_i+1)}{2\pi\rho_{sciss}^0(E^*)}\int \frac{2\mu\varepsilon\sigma_{inv}(\varepsilon)}{\pi\,\hbar^2}\rho_{sciss}(E^*-\varepsilon)d\varepsilon \quad (19)$$

where μ is the reduced mass, σ_{inv} is the inverse cross section, and

$$\frac{2\mu\varepsilon\sigma_{inv}(\varepsilon)}{\pi\,\hbar^2} = \sum_{\ell=0}^{\infty}(2\ell+1)\,T_\ell(\varepsilon). \quad (20)$$

The transmission coefficients of Eq. 2 are used, although, in principle, as we are now dealing with evaporation from a deformed system, the Coulomb barriers for charged-particle emissions should be lowered. However as charge-particle multiplicities are expected to be small, this is not a large problem. The quantities ρ_{sciss}^0 and ρ_{sciss} are the spin-independent level densities of the parent and daughter;

$$\rho_{sciss}(E^*) \propto \exp\left[2\sqrt{a(E^*-B_{sciss})}\right] \quad (21)$$

where a level-density parameter of $a = A/8$ MeV was assumed. From fitting systematics of prefission neutrons multiplicities [39] one obtained η=2 zs/MeV.

Finally, the systematics of fission mass distributions compiled by Rusanov *et al.*[38] are used to choose the mass division from the final scission temperature. Once a binary division has been selected, it is important to find the emission angle and the spins of the fragments. These are selected from the statistical treatment of angular-momentum bearing normal modes such as bending, wriggling, tilting and twisting developed by Moretto [40] and subsequently extended to asymmetric mass division by Schmitt and Pacheco [41]. Thermal fluctuations are considered in the subdivision of the total thermal excitation energy U_{tot} between the two fragments, i.e., the probability is

$$P(U_1) \propto \exp\left(2\sqrt{a_1 U_1}\right)\exp\left[2\sqrt{a_2(U_{tot}-U_1)}\right] \tag{22}$$

where U_1 is the thermal excitation energy of one fragments and a_1 and a_2 are the level-density parameters of each fragment.

4. Gamma-ray emission

At very low excitation energies, the partial decay widths for particle and gamma decay can be comparable and thus it is important to include gamma-ray emission to correctly model the termination of particle decay. However for this purpose only the *E1* and *E2* gamma rays need be considered. From Blatt and Weisskopf [42], the decay width for multipolarity ℓ is

$$\Gamma_\gamma^l = F_\ell \frac{18(\ell+1)}{\ell(\ell+3)^2\left[(2\ell+1)!!\right]^2}\frac{e^2}{\hbar c}\left(\frac{R}{\hbar c}\right)^{2l}\frac{1}{D_0}\sum_{s_d=|S_{CN}-\ell|}^{S_{CN}+\ell}\int \varepsilon^{2\ell+1}\frac{\rho(E^*-\varepsilon,S_d)}{\rho(E^*,S_{CN})}d\varepsilon \tag{23}$$

where ε is the gamma-ray energy, $R = 1.2A^{1/3}$ fm, D_0 is 1 MeV, and F_l accounts for deviations from the Weisskopf estimates. Values of F_1=0.025 and F_2=9.0 were taken from Ref. [43].

5. Conclusion

The statistical-model code GEMINI follows the decay of a compound nucleus by a series of binary divisions. The partial decay widths are taken from the Hauser-Feshbach formalism for light-particle evaporation and from Moretto's generalized transition-state formalism for more symmetry divisions. This prescription provides an adequate description of the decay process for light compound nuclei. For heavier systems, the predicted mass distributions are too wide. A new code GEMINI++, was written to overcome this problem. For heavy systems, the Bohr-Wheeler formalism is now used for symmetric fission and the width of the mass distributions of the fission fragments is interpolated from systematics.

This work was supported by the U.S. Department of Energy, Division of Nuclear Physics under grant DE-FG02-87ER-40316.

REFERENCES

[1] N. Bohr and J.A. Wheeler, Phys. Rev. **56,** 426 (1939).
[2] L.G. Moretto, Nucl. Phys. **A247,** 221 (1975).
[3] A.J. Sierk, Phys. Rev. Lett. **55,** 582 (1985).
[4] R.J. Charity, D.R. Bowman and Z.H. Liu, R.J. McDonald, M.A. McMahan, G.J. Wozniak, L.G. Moretto, S. Bradley, W.L. Kehoe, and A.C. Mignerey, Nucl. Phys. **A476**, 516 (1988).
[5] R.J. Charity, M.A. McMahan, G.J. Wozniak, R.J. McDonald, L.G. Moretto, D.G. Sarantites, L.G. Sobotka, G. Guarino, A. Panteleo, L. Fiore, A. Gobbi, and K. Hildenbrand, Nucl. Phys. **A483**, 371 (1988).
[6] R.J. Charity, K.X. Jing, D.R. Bowman, M.A. McMahan, G.J. Wozniak, L.G. Moretto, N. Colonna, G. Guarino, A. Pantaleo, L. Fiore, A. Gobbi, and K.D. Hildenbrand, Nucl. Phys. **A511**, 59 (1990).
[7] W. Hauser and H. Feshbach, Phys. Rev **87**, 366 (1952).
[8] V.F. Weisskopf and D.H. Ewing, Phys. Rev. **57**, 472 (1940).
[9] P. Möller, J.R. Nix, W.D. Myers, and W.J. Swiatecki, Atomic Data Nucl. Data Tables **59**, 185 (1995).
[10] J.M. Alexander, M.T. Magda, and S. Landowne, Phys. Rev. C **42,** 1092 (1990).
[11] G.H. Rawitscher, Nucl. Phys. **85**, 337 (1966).
[12] C.M. Perey and F.G. Perey, Phys. Rev. **132**, 755 (1963).
[13] F.G. Perey, Phys. Rev. **131**, 745 (1963).
[14] D. Wilmore and P.E. Hodgson, Nucl. Phys. **55**, 673 (1964).
[15] L. McFadden and G.R. Satchler, Nucl. Phys. **84**, 177 (1966).
[16] F.D. Becchetti , Jr. and G.W. Greenlees, *Polarization Phenomena in Nuclear Reactions* (University of Wisconsin Press, Madison, 1971).
[17] J. Cook, Nucl. Phys. **A388**, 153 (1982).
[18] R. Balzer, M. Hugi, B. Kamys, J. Lang, R. Müller, E. Ungricht, J. Unternährer, L. Jarczyk, and A. Strzałkowski, Nucl. Phys. **A293**, 518 (1977).
[19] N.G. Nicolis, D.G. Sarantites, L.A. Adler and F.A. Dilmanian, K. Honkanen, Z. Majka, L.G. Sobotka, Z. Li, T.M. Semkow, J.R. Beene, M. Halbert, D.C. Hensley, J.B. Natowitz, R.P. Schmitt, D. Fabris, G. Nebbia and G. Mouchaty, Phys. Rev. C **41**, 2118 (1990).
[20] M. Gonin, L. Cooke, K. Hagel, Y. Lou, J.B. Natowitz, R.P. Schmitt, S. Shlomo, B. Srivastava, W. Turmel, H. Utsunomiya, R. Wada, G. Nardelli, G. Nebbia, G. Viesti, R. Zanon, B. Fornal, G. Prete, K. Niita, S. Hannuschke, P. Gonthier, and B. Wilkins, Phys. Rev. C **42**, 2125 (1990).
[21] M. Kildir, G. LaRana, R. Moro, A. Brondi, A. D'Onofrio, E. Perillo, V. Roca, M. Romano, F. Terrasi, G. Nebbia, G. Viesti, and G. Prete, Phys. Rev. C **46**, 2264 (1992).
[22] J. Boger, J.M. Alexander, R.A. Lacey, and A. Narayanan, Phys. Rev. C **49**, 1587 (1994).
[23] R.J. Charity, M. Korolija, D.G. Sarantites, and L.G. Sobotka, Phys. Rev. C **56**, 873 (1997).
[24] J.F. Liang, J.D. Bierman, M.P. Kelly, A.A. Sonzogni, R. Vanderbosch, and J.P.S van Schagen, Phys. Rev. C **56**, 908 (1997).
[25] A.L. Caraley, B.P. Henry, J.P. Lestone, and R. Vandenbosch, Phys. Rev. C **62**, 054612 (2000) .
[26] B.J. Fineman, K.-T. Brinkmann, A.L. Caraley, N. Gan, R.L. McGrath, and J. Velkovska, Phys. Rev. C **50**, 1991 (1994).

[27] R.J. Charity, L.G. Sobotka, J. Cibor, K. Hagel, M. Murray, J.B. Natowitz, R. Wada, Y. El Masri, D. Fabris, G. Nebbia, G. Vieste, M. Cinausero, E. Fioretto, G. Prete, A. Wagner, and H. Xu, Phys. Rev. C **63**, 024611 (2001).
[28] R.J. Charity, Phys Rev. C **61**, 054614 (2000).
[29] R.J. Charity, Phys. Rev. C **64**, 064610 (2001).
[30] A.J. Sierk, Phys. Rev. C **33**, 2039 (1986).
[31] A.V. Ignatyuk, G.N. Smirenkin, and A.S. Tishin, Sov. J. Nucl. Phys. **21**, 255 (1975).
[32] A.V. Ignatyuk, K.K. Istekov, and G.N. Smirenkin, Sov. J. Nucl. Phys. **29**, 450 (1979).
[33] R.J. Charity, L.G. Sobotka, J.F. Dempsey, M. Devlin, S. Komarov, D.G. Sarantites, A.L. Caraley, R.T. deSouza, W. Loveland, D. Peterson, B.B. Back, C.N. Davids, and D. Seweryniak, Phys. Rev. C **67**, 044611 (2003).
[34] C. Mahaux and R. Sartor, Adv. Nucl. Phys. **20**, 1 (1991).
[35] L.G. Moretto and G.J. Wozniak, Prog. In Part. And Nucl. Phys. **21**, 401 (1988).
[36] N. Carjan and J.M. Alexander, Phys. Rev. C **38**, 1692 (1998).
[37] K. Thomas, R. Davies, and A.J. Sierk, Phys. Rev. C **31**, 915 (1985).
[38] A.Y. Rusanov, M.G. Itkis, and V.N. Okolovich, Phys. At. Nucl. **60**, 683 (1997).
[39] D. Hilscher and H. Rossner, Ann. Phys. (Paris) **17**, 471 (1992).
[40] L.G. Moretto and R.P. Schmitt, Phys Rev. C **21**, 204 (1980).
[41] R.P. Schmitt, Nucl. Phys. A379, 313 (1982).
[42] J.M. Blatt and V.F. Weisskopf, *Theoretical Nuclear Physics*,(Wiley, New York, 1958)
[43] D.E. DiGregorio, M. diTada, D. Abriola, M. Elgue, A. Ecthegoyen, J.O. Fernández Niello, A.M. Ferrero, S. Gil, A.O. Macchiavelli, A.J. Pacheo, J.E. Testoni, P.R. Silveira Gomes, V.R. Vanin, R. Liguori Neto, E. Crema, and R.G. Stokstad, Phys. Rev. C **39**, 516 (1989)

The ITEP Experiments with Targets exposed to up-to 2.6 GeV Protons

Y.E. TITARENKO, V.F. BATYAEV

ITEP,
Moscow, Russia

Abstract. The thin target experiments carried out using the ITEP proton synchrotron (Moscow, Russia) during the last decade are reviewed in detail. The experiments were aimed at determining the independent and cumulative yields of radioactive residuals in 0.04-2.6 GeV proton-irradiated thin targets. In total, 144 targets made of 22 materials ranging from ^{nat}Cr to ^{nat}U have been irradiated. Particular emphasis was laid to single-isotopic and isotope-enriched materials, such as $^{206\text{-}208}$Pb, ^{56}Fe, $^{182\text{-}186}$W, and ^{99}Tc. All in all, by the beginning of 2005 more than 10,000 yields had been determined, published, and then introduced into the EXFOR database. A fresh run of experiments with structural materials (^{56}Fe, ^{nat}Cr, ^{nat}Ni, ^{93}Nb, ^{181}Ta, and ^{nat}W) is under way. The experiments are expected to complete in 2009. The experimental procedure is described together with the techniques for, and results of, comparing with the similar data obtained at GSI (Darmstadt) and ZSR (Hannover).

1. Introduction

The thin target experiments[1] are aimed at verifying the interactions of primary beam protons of a given energy with target nuclei, i.e. the primary processes. The purpose of the verification is to check out the adequacy of describing the INC only, namely, to check on the accuracy of calculating the cross section that characterize the nuclear interactions of of high-energy particles in term s of the models used in the transport code systems.

As early as 1990, The ITEP began experimenting to determine the independent and cumulative yields of residual products in thin targets via direct γ-spectrometry [1]. An Al foil - ^{59}Co sample sandwich was exposed to 2 GeV proton beam at the booster of the U-70 accelerator at the Institute for High-Energy Physics (Protvino, Russia). The Al foil was used to monitor the proton beam. After that, the sandwich was delivered at ITEP to be measured using a γ-spectrometer. The long period that elapsed between the irradiation end and the calculation start made the short-lived nuclides decay, so the information about production of the lattes went astray.

During the same period, the ITEP U-10 synchrotron was provided with the task-oriented extraction channel for high-energy protons of ~$1\cdot10^{11}$ proton/pulse intensity. Besides, a high-resolution γ-spectrometer was purchased.

The techniques developed, the equipment purchased, and the external beam extraction realized in the ITEP U-10 synchrotron made it possible to implement ISTC Projects Nos. 839, 2002, and 3266 supported financially by EC, Norway, and Japan and to carry out the batch measurements of the independent and cumulative yields of residuals from the thin experimental samples of different materials right at ITEP.

2. Review of experiments with thin targets

The experiments to determine the cross sections for nuclide production in thin targets were and are made under ISTC Projects Nos. 839-0 (1997-1998) [2,3], 839 (1999-2000) [4], 2002 (2002-2004) [5], and 3266 (2006-2009) [6]. Tables 1-4 list the targets and proton energies

[1] We call a target thin if it satisfies the following two criteria: (1) the energy loss of an incident particle as it traverses the target is negligible compared with its initial energy and (2) the free path of an incident particle is much in excess of the target length.

used in the Projects. The numerals in Tables 1 and 2 for Projects 839 and 2002 that have been implemented indicate the numbers of the residual nuclide production cross sections determined. The Technical reports on the Projects are accessible in the IAEA and OECD databases [4,5].

TABLE I. THE TARGETS AND PROTON ENERGIES USED IN ISTC PROJECT NO. 839

Proton Energy [GeV]	Targets																			
	^{56}Fe	^{58}Ni	^{59}Co	^{63}Cu	^{65}Cu	^{93}Nb	^{99}Tc	^{182}W	^{183}W	^{184}W	^{186}W	^{nat}W	^{nat}Hg	^{206}Pb	^{207}Pb	^{208}Pb	^{nat}Pb	^{209}Bi	^{232}Th	^{nat}U
0.1			25	11	6		18						44	22	22	20		26	87	108
0.2			29	29	29		39	32	35	36	36		65						128	123
0.8							72	70	76	77	60								130	195
1.0*							64									114				
1.2*			41	47	54		67						103						214	226
1.5				35	36									92	93	94	93	99		
1.6			41	42	47		78	109	111	114	119		141						212	231
2.6	36	38	41	42	48	85	85					129								

* - Additionally, ^{208}Pb were exposed to 1000 MeV protons.

* - The ^{63}Cu and ^{65}Cu samples were involved in the intercalibration measurements between ITEP and JAERI [3].

TABLE II. THE TARGETS AND PROTON ENERGIES USED IN ISTC PROJECT NO. 2002

Targets	Proton Energy (GeV)										
	0.04	0.07	0.1	0.15	0.25	0.4	0.6	0.8*	1.2	1.6	2.6
^{nat}Pb	18	28	43	63	95	116	141	154	171	181	178
^{208}Pb	8	28	36	63	94	113	141	154	170	182	172
^{207}Pb	9	29	42	65	94	112	140	152	170	180	171
^{206}Pb	13	28	46	65	94	112	139	156	170	180	171
^{209}Bi	13	35	50	71	106	128	147	162	183	192	198

* - Additionally, ^{197}Au was exposed to 800 MeV protons.

TABLE III. LIST OF IRRADIATION RUNS FOR BETA-ACTIVE NUCLIDE PRODUCTION MEASUREMENTS IN ISTC PROJECT NO. 3266

Targets	Proton Energy (GeV)										
	0.04	0.07	0.1	0.15	0.25	0.4	0.6	0.8	1.2	1.6	2.6
^{56}Fe$^{(*)}$	X	x	p	p	27	30	32	30	31	32	32
^{nat}Cr	X	x	p	p	33	32	38	38	39	38	40
^{nat}Ni	X	x	p	p	p	40	43	43	42	46	46
^{93}Nb	X	x	i	i	p	p	p	105	110	123	128
^{181}Ta	X	x	p	p	p	p	p	P	p	p	p
^{nat}W	X	x	i	i	p	p	p	P	p	p	p

(*) - Additionally, ^{56}Fe was irradiated by 300, 500, 750, 1000 and 1500 MeV proton,

x – to be irradiated in June 2008

i – irradiated (γ-spectra processing in progress),

p - γ-spectra processed,

numbers – quantities of residual nuclides cross sections determined.

TABLE IV. LIST OF IRRADIATION RUNS FOR A-ACTIVE NUCLIDE (^{148}GD) PRODUCTION MEASUREMENTS IN ISTC PROJECT NO. 3266

Targets	Proton energies (GeV)			
	0.6	0.8	1.6	2.6
^{181}Ta	x	x	x	x
^{nat}W	x	x	x	x

3. Techniques for experimental determining reaction product yields

The techniques for experimental determining the yields (cross sections for production) of residuals is based on direct γ-spectrometry without any chemical separation of the radioactive nuclei produced by irradiation.

3.1. The spectrometer characteristics

The radioactive nuclei produced in the irradiated sampled were recorded with a GC-2518 coaxial Ge detector-based standard spectrometering circuit of a 1.8 keV resolution in the ^{60}Co 1332 keV γ-line. Figs 1 and 2 show examples of the γ-spectra of the Pb and Al foils irradiated.

3.2. The mathematical formalism used to determine the sought parameters

The formalism of presenting and, correspondingly, the techniques for experimental determining the reaction product yields (cross sections) are based on the fact that any of the recorded reaction products of different-energy proton interactions with matter can be generated in both an examined reaction and decays of its "parent" precursors.

This approach permits introducing the concepts of independent production rate R_i^{ind} if a reaction product is generated by nuclear reaction only and of cumulative production rate R_i^{cum} if a reaction product is generated by all processes (both in the reaction directly and in the decays of its parent precursors produced independently) [4,5]:

$$R_i^{cum/ind} = \sigma_i^{cum/ind} \cdot \hat{\Phi} \qquad i=1,2,st \tag{1}$$

where $\sigma_1^{cum/ind}$ and $\sigma_2^{cum/ind}$ are, respectively, the cumulative and independent production cross sections of nuclides N_1 and N_2, in experimental sample N_{Tag} exposed to protons of neutrons [barn]; $\sigma_{st}^{cum/ind}$ are the cumulative or independent monitor reaction cross sections used to calculate the mean proton flux density [barn]; $\hat{\Phi}$ is the area- and time-averaged proton or neutron flux density [particle/(cm^2·s)].

The reaction rate definition (1) permits the double-link-chain of nuclide "parentage" ($N_1 \xrightarrow{\lambda_1} N_2 \xrightarrow{\lambda_2}$) to be presented as a set of differential equations that describe the production and decay of the nuclides.

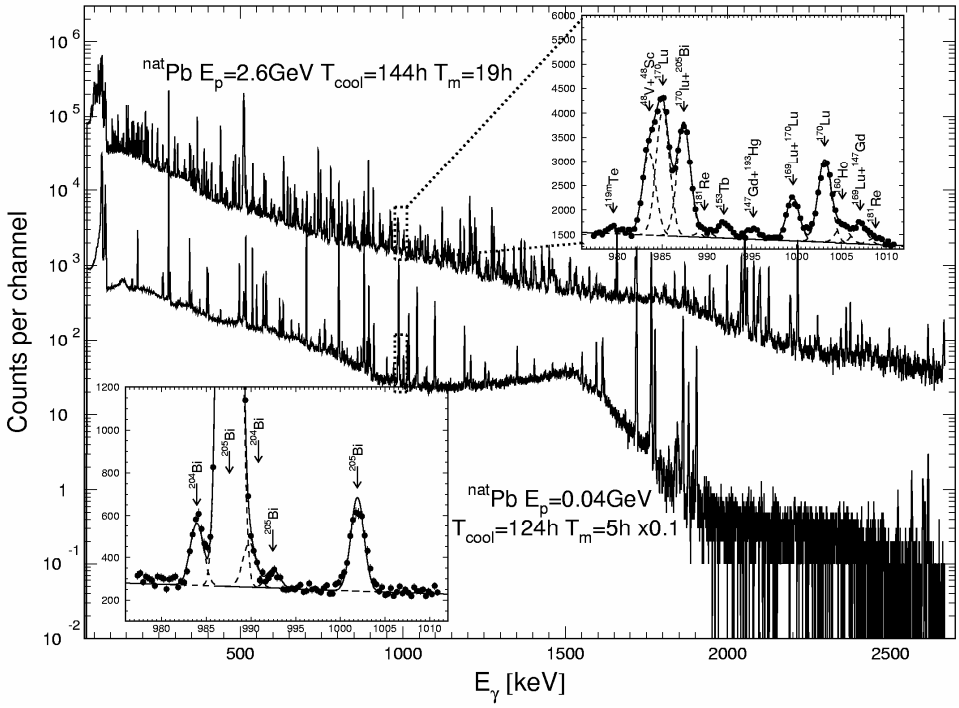

Fig. 1. Spectra of γ-emission from Pb foils exposed to 2.6 u 0.04 GeV protons.

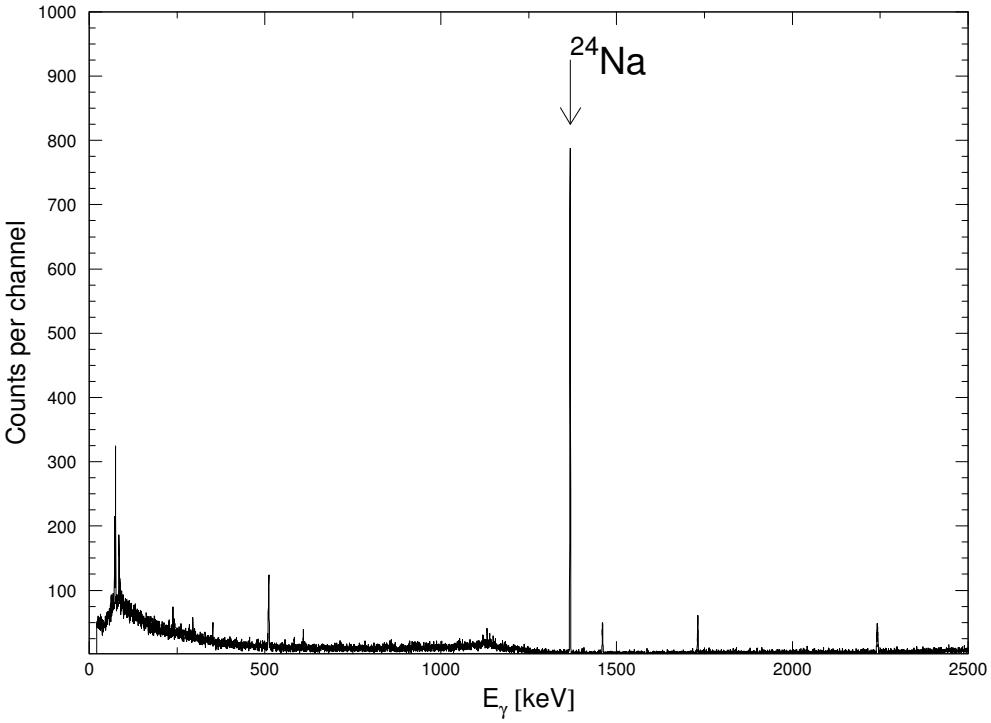

Fig. 2. Spectrum of γ-emission from Al foil exposed to 2.6 GeV protons.

The least squares techniques were used to fit the measured points of the first and second nuclide decay curves to the decay onset (irradiation stop moment). The condition that numbers of nuclei of the first and second nuclides in the samples irradiated should be the same at the irradiation stop (i.e. the decay onset) permits the reaction rates to be obtained from the sets of differential equations that describe their production and decay:

$$R_1^{cum/ind} = \frac{\hat{A}_1}{N_{Tag} \cdot \eta_1 \cdot \varepsilon_1} \cdot \frac{1}{F_1} \tag{2}$$

$$R_1^{cum/ind} = \frac{\hat{A}_2^1}{N_{Tag} \cdot \eta_2 \cdot \varepsilon_2 \cdot \nu_{12}} \cdot \frac{\lambda_2 - \lambda_1}{\lambda_2} \cdot \frac{1}{F_1} \tag{3}$$

$$R_2^{ind} = \left(\frac{\hat{A}_2^2}{F_2} + \frac{\hat{A}_2^1}{F_1} \cdot \frac{\lambda_1}{\lambda_2} \right) \cdot \frac{1}{N_{Tag} \cdot \eta_2 \cdot \varepsilon_2} \tag{4}$$

$$R_2^{cum} = R_2^{ind} + \nu_{12} \cdot R_1^{cum/ind} = \left(\frac{\hat{A}_2^1}{F_1} + \frac{\hat{A}_2^2}{F_2} \right) \cdot \frac{1}{N_{Tag} \cdot \eta_2 \cdot \varepsilon_2} \tag{5}$$

where $\hat{A}_1 = A_1 \cdot k_{\mu_1}$, $\hat{A}_2^1 = A_2^1 \cdot k_{\mu_2}$, and $\hat{A}_2^2 = A_2^2 \cdot k_{\mu_2}$ are the parameters determined by least-squares fitting the experimental points of the decay curves of the mother and daughter nuclides (super- and subscripts 1 and 2 stand for mother and daughter, respectively); N_{Tag} is the number of nuclei in an irradiated sample; η_1 and η_2 are γ-abundancies ; λ_1, and λ_2 are decay constants; ε_1 and ε_2 are absolute spectrometer efficiencyes at γ-quantum energies E_1 the first nuclide)and E_2 (the second nuclide); v is the branching factor, i.e. the probability for mother to become daughter; F_1 and F_2 are functionals calculated via formulae (13) permitting nuclide decay during the irradiation time.

The corrections k_μ that allow for γ-quantum absorption in an experimental sample are determined as

$$k_{\mu_j} = \frac{k \cdot \sigma_{tot_j} \cdot h}{1 - e^{k \cdot \sigma_{tot_j} \cdot h}} \tag{6}$$

where h is experimental sample thickness (g/cm^2); σ_{tot_j} is the total interaction cross section of γ-quanta of the j-th energy with matter (barn/atom); $k = \frac{N_{A_v}}{M} \cdot 10^{-24}$ is the coefficient of transition from dimension [barn/atom] to dimension [cm^2/g], where N_{A_v} is Avogadro number; M is molecular weight.

The yields (production cross sections) of the independent and cumulative yields of residual product nuclei in an identified double-link nuclear transformation chain are calculated by normalizing the respective reaction rates to the mean proton flux density:

$$\sigma_1^{cum/ind} = \frac{R_1^{cum/ind}}{\hat{\Phi}} \qquad \sigma_2^{cum/ind} = \frac{R_2^{cum/ind}}{\hat{\Phi}} \tag{7}$$

In some cases where the fitting of experimental points fails to permit determination of $\hat{A}_2^1$, it is expedient to introduce the concept of supracumulative reaction rate and, accordingly, of supracumulative cross section [4]

$$R_2^{cum*} = R_2^{ind} + \frac{\lambda_1}{\lambda_1 - \lambda_2} \cdot \nu_1 \cdot R_1^{ind} = \frac{\hat{A}_2^2}{N_{Tag} \cdot \eta_2 \cdot \varepsilon_2 \cdot F_2} \tag{8}$$

$$\sigma_2^{cum^*} = \frac{R_2^{cum*}}{\hat{\Phi}} \tag{9}$$

3.3. The mean proton flux density

3.3.1. The monitor reaction techniques

B The pioneer works determined the mean flux density of protons that irradiate a target using the ^{27}Al(p,x)^{24}Na reaction rate. However, the proton channel of ^{24}Na production exists alongside with the neutron channel (^{27}Al(n,α)^{24}Na), so the use of the latter reaction underestimates the mean proton flux density. Therefore, the ^{27}Al(p,x)^{22}Na monitor reaction was used in the later works. The geometric dimensions of Al foils are always the same as those of the irradiated foils, so the expression of the mean proton flux density can be presented as

$$\hat{\Phi} = \frac{R_{st}^{cum}}{\sigma_{st}^{cum}} \tag{10}$$

$$\frac{\Delta\hat{\Phi}}{\hat{\Phi}} = \sqrt{\left(\frac{\Delta R_{st}^{cum}}{R_{st}^{cum}}\right)^2 + \left(\frac{\Delta\sigma_{st}^{cum}}{\sigma_{st}^{cum}}\right)^2} \tag{11}$$

The R_{st}^{cum} value s calculated by formula (6).

Simultaneously, the ^{27}Al(p,x) ^{24}Na and ^{27}Al(p,x)^{7}Be reaction cross sections are calculated together with the ^{27}Al(n,p)^{27}Mg reaction rate in the Al foil. The latter reaction is used to estimate the neutron component rather than to monitor the proton beam.

Fig. 3 is the plot of ^{27}Al(p,x)^{22}Na reaction cross section versus energy. That reaction was examined in many works, so its excitation function is well known

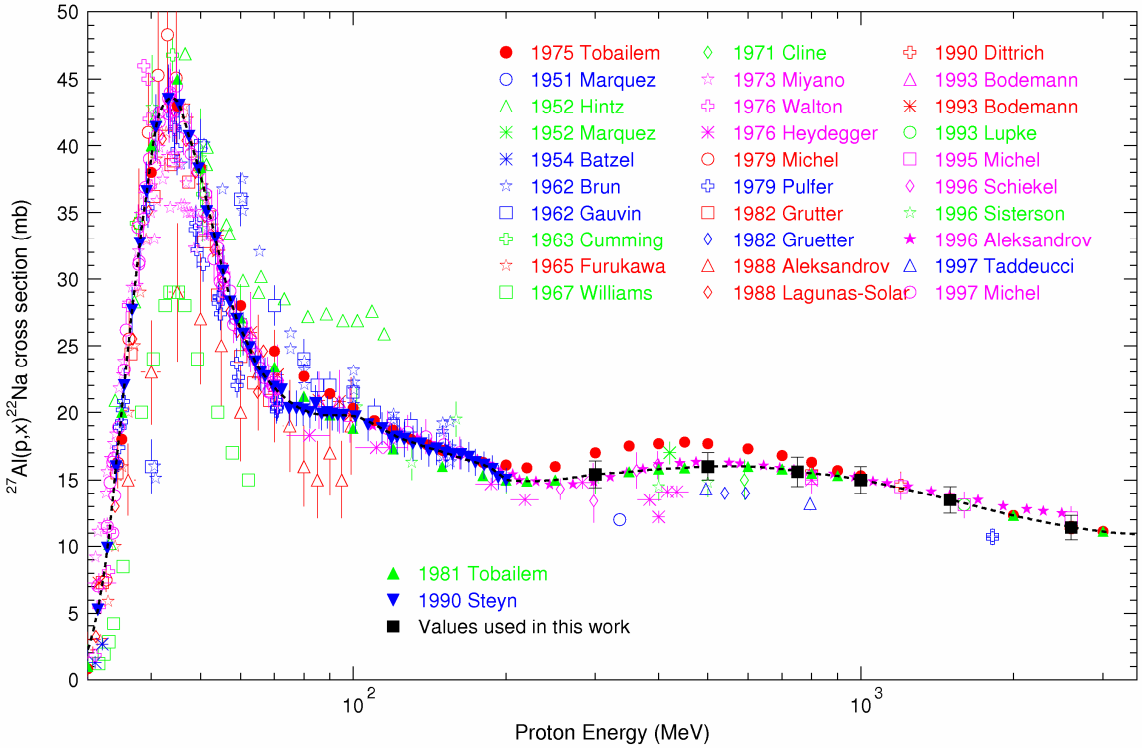

Fig. 3. The $^{27}Al(p,x)^{22}Na$ monitor reaction cross section versus energy.

3.3.2. The current transformer techniques

Given a certified current transformer that produces a pulse, whose shape repeats the longitudinal shape of the proton beam pulse, and using a processor board to digitize the signal, the proton flux density can be calculated as

$$\Phi_{FCT} = \frac{I \cdot t \cdot k_{flux}}{K \cdot z \cdot e \cdot T_{irr} \cdot S}, \qquad (12)$$

where I is the channel-by-channel sum expressed in pulses of summary oscillograms, B; t is the oscillograph channel (digitization) width, c; k_{flux} is the ratio of the number of ions or protons that traversed a microcircuit die to their total number in a beam, K is the conversion factor of the current transformer signal, B/A; z is charge number of the accelerated ions; e is elementary charge, Coul; T_{irr} is irradiation time, s; S is the cross section of the chip die and, hence, of monitor, cm^2.

The charged particle fraction through the monitor is found by determining the ratio of the rates of reactions in ^{24}Na produced in the "large" monitor that completely overlaps the beam cross section to that in the "small" monitor , whose cross section is the same as that of the experimental sample.

The current transformer-measured pulse amplitudes are also used to calculate the corrections $k_{f(t)}$ that allow correctly for the decays of the produced nuclides during irradiation, especially of short-lived nuclides:

$$F_i = \left(1 - e^{-\lambda_i \cdot t_{irr}}\right) \cdot \sum_{j=1}^{K} V_j \Big/ \sum_{j=1}^{K} V_j \cdot e^{-\lambda_i \cdot \left(t_{irr} - t_j\right)}, \qquad (13)$$

where t_j is the time of the j-th pulse; V_j is amplitudes sum in the *i-th* time interval; t_{irr} is the irradiation time.

Shown as an example in Fig. 4 is the minute structure of a sample irradiation run, and in Fig 5 the summary oscillogram of the bunch structure of proton beam.

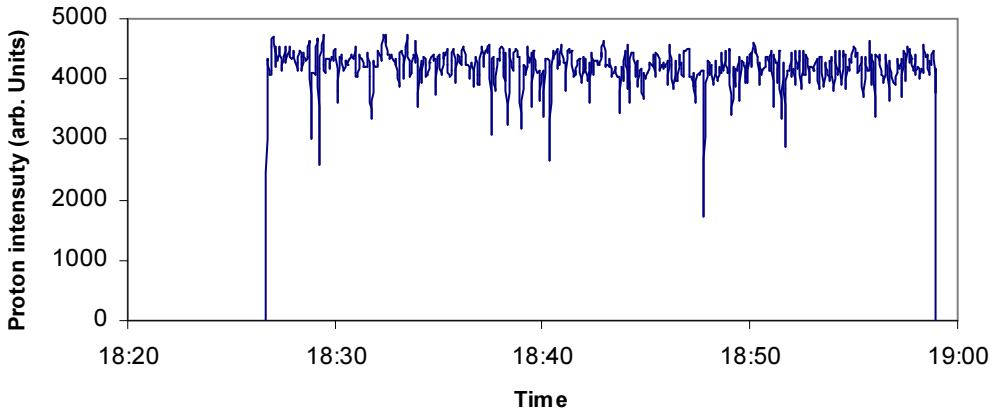

Fig. 4. The minute time structure of an experimental sample exposure cycle.

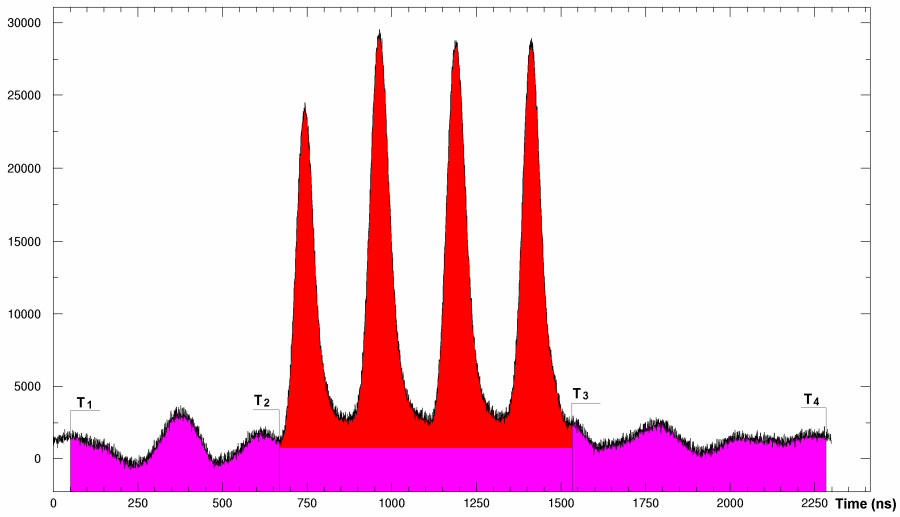

Fig. 5. The summary oscillogram of the proton beam bunch structure.

TABLE V. EXAMPLE OF COMPARISON OF PROTON NUMBERS MEASURED BY CURRENT TRANSFORMER AND MONITOR REACTIONS

Target / Energy (GeV)	Proton number through target (10^{14})		CT/MR ratio
	current transformer (CT)	monitor reactions (MR)	
W / 1.2	1.07±0.03	1.03±0.08	1.04±0.09
Nb / 1.2	1.07±0.03	1.02±0.08	1.05±0.09
Fe / 1.2	0.96±0.03	0.91±0.07	1.05±0.09
W / 0.8	0.85±0.03	0.81±0.07	1.05±0.10
Nb / 0.8	0.47±0.02	0.47±0.04	1.00±0.10

3.4. The measurement errors

Since a few $(R_{ij}^{ind/cum} \pm \Delta R_{ij}^{ind/cum})$ values calculated for k different γ-lines $(i = 1,2;\ \ 1 < j < k)$ may be averaged when calculating the mean reaction rates, it is expedient to introduce definitions for relative quantum yield and relative spectrometer efficiency that are related to one another as

$$\eta_{ij} = k_{\gamma_i} \cdot \eta_{ij}^{rel} \qquad \varepsilon_{ij} = k_{\varepsilon} \cdot \varepsilon_{ij}^{rel} \tag{14}$$

The $k_{\gamma i} \pm \Delta k_{\gamma i}$ values were borrowed from [7], while the procedure of determining the $k_{\varepsilon} \pm \Delta k_{\varepsilon}$ value can be found in [8]. In this case, the relative reaction rate for each nuclide via the factors $k_{\gamma i}$ and k_{ε} introduced, as well as the absolute reaction rates calculated via (2)-(5), can be presented as

$$^{rel}R_{ij}^{cum/ind} = R_{ij}^{cum/ind} \cdot k_{\gamma j} \cdot k_{\varepsilon} \cdot N_{tag}, \tag{15}$$

The errors in the relative reaction rates $\Delta\,^{rel}R_1^{cum/ind}$, $\Delta\,^{rel}R_2^{cum/ind}$, $\Delta\,^{rel}R_2^{ind}$,and $\Delta\,^{rel}R_2^{cum}$ are calculated via the error transfer formulas allowing for errors in all values that enter (2)-(5), (8).

The mean values of the relative independent or cumulative rates of the i-th nuclide production as inferred from j γ-lines were calculated as

$$^{rel}\overline{R}_i^{cum/ind} = \frac{\sum_{j=1}^{k} {}^{rel}R_{ij}^{cum/ind} \cdot {}^{rel}W_{ij}}{\sum_{j=1}^{k} {}^{rel}W_{ij}} \qquad {}^{rel}W_{ij} = \frac{1}{\left(\Delta\,^{rel}R_{ij}^{cum/ind}\right)^2} \tag{16}$$

$$\Delta\,^{rel}\overline{R}_i^{cum/ind} = \max\left\{\left(\Delta\,^{rel}\overline{R}_i^{cum/ind}\right)';\left(\Delta\,^{rel}\overline{R}_i^{cum/ind}\right)''\right\} \tag{17}$$

$$\left(\Delta^{rel}\overline{R}_i^{cum/ind}\right)' = \sqrt{\frac{\sum_{j=1}^{k} {}^{rel}W_{ij}\left({}^{rel}\overline{R}_i^{cum/ind} - {}^{rel}\overline{R}_{ij}\right)^2}{(k-1)\sum_{j=1}^{k} {}^{rel}W_{ij}}} \tag{18}$$

$$\left(\Delta^{rel}\overline{R}_i^{cum/ind}\right)'' = \sqrt{\frac{1}{\sum_{j=1}^{k} {}^{rel}W_{ij}}} \tag{19}$$

Following (13), the mean absolute independent of cumulative rates of the *i*-th nuclide production were calculated together with their errors from the respective relative reaction rates:

$$\overline{R}_i^{cum/ind} = \frac{{}^{rel}\overline{R}_{ij}^{cum/ind}}{k_{\gamma_i} \cdot k_{\varepsilon} \cdot N_{tag}} \tag{20}$$

$$\Delta\overline{R}_i^{cum/ind} = \overline{R}_i^{cum/ind} \cdot \sqrt{\left(\frac{\Delta^{rel}\overline{R}_i^{cum/ind}}{{}^{rel}\overline{R}_i^{cum/ind}}\right)^2 + \left(\frac{\Delta k_{\gamma_i}}{k_{\gamma_i}}\right)^2 + \left(\frac{\Delta k_{\varepsilon}}{k_{\varepsilon}}\right)^2 + \left(\frac{\Delta N_{tag}}{N_{tag}}\right)^2} \tag{21}$$

In case but a single γ-line is involved in calculating a reaction rate (possibly, a single line is chosen among j γ-lines, or else a nuclide shows but a single line (j=1)), the γ-abundance of a that line $\left(\eta_i \pm \Delta\eta_i\right)$ and the absolute detection efficiency $\left(\varepsilon_i \pm \Delta\varepsilon_i\right)$ were used in formulas (2)-(5), (8), so the absolute independent/cumulative reaction rate can be calculated at once.

3.5. Extra errors

The measurements were made simultaneously with the supplementary researches to reduce the errors in the eventual results, namely

- the extracted proton beam neutron component was specified;
- the spectrometer efficiency was studied as a function of the irradiated sample position geometry
- the γ-spectrum processing codes were optimized;
- the laboratory room background was monitored.

3.5.1. Neutron component

The neutron component was estimated as

$$\frac{\overline{\Phi}_n}{\overline{\Phi}_p} = \frac{\sigma_{p,x}^{^{24}Na} / \overline{\sigma}_{n,p}^{^{27}Mg}}{N^{^{24}Na} / N^{^{27}Mg} - \overline{\sigma}_{n,\alpha}^{^{24}Na} / \overline{\sigma}_{n,p}^{^{27}Mg}} \quad (22)$$

where $\overline{\sigma}_{n,p}^{^{27}Mg}$, $\overline{\sigma}_{n,\alpha}^{^{24}Na}$ are the neutron spectrum-weighted cross sections; $\sigma_{p,x}^{^{24}Na}$ is the ^{27}Al(p,x)^{24}Na, reaction cross sections; N_{24Na} and N_{27Mg} are numbers of the ^{24}Na and ^{27}Mg nuclei produced in the Al samples with due allowance for their decays under irradiation.

Figs. 4.1 and 4.2 show the measured neutron component of the proton beams extracted under different conditions.

3.5.2. Spectrometer efficiency

The analytical height-energy detection efficiency can be presented as

$$\varepsilon(E,H) = \varepsilon_{base}(E) \cdot \left[\frac{(q_1 + q_2 \cdot \ln E + H_{base})}{(q_1 + q_2 \cdot \ln E + H)} \right]^2 \quad (23),$$

where q_1 and q_2 are the parameters determined by fitting the experimental data.

The error in the absolute spectrometer efficiency is ranging from 4.0% to 4.5%.

Figs. 5.1 and 5.2 show the results of measuring the height-energy dependence and the basic relative detection efficiency at a 40-mm height.

3.5.3. Processing of gamma-spectra; calculations of cross sections

The γ-spectra were processes by GENIE-2000 code. The sets of spectra measured having been computer-processed by interactive fitting their peaks, the code examines also the pre-processing results for each of the spectra. Figs 6.1 and 6.2 show the results of pre-processing sets of spectra by GENIE-2000 in automatic mode (a) and the results of additional manual processing in interactive fitting mode (b).

The identification of γ-lines and the calculations of cross sections for production of residuals by formulas (1)-(21) are realized via the ITEP-devised SIGMA code combined with the PCNUDAT database. The Fig. 7 shows the characteristic decay curves.

3.5.4. Background of the laboratory room

The occurrences of the background γ-spectral lines in the measured spectra due to the natural radioactive background of the laboratory were allowed for by analyzing the spectra from the irradiation-intact samples. Fig. 8 shows the radioactive laboratory background (measured for ~4 days) that shows occurrences of natural radionuclides from the ^{238}U, ^{235}U, and ^{232}Th decay chains, except for the 661 keV (^{137}Cs) and 344.9, 722.9 keV (^{108}Ag) γ-line energies. The ^{137}Cs and ^{108}Ag occurrences are due probably to many years' heavy-water reactor operation in the ITEP territory.

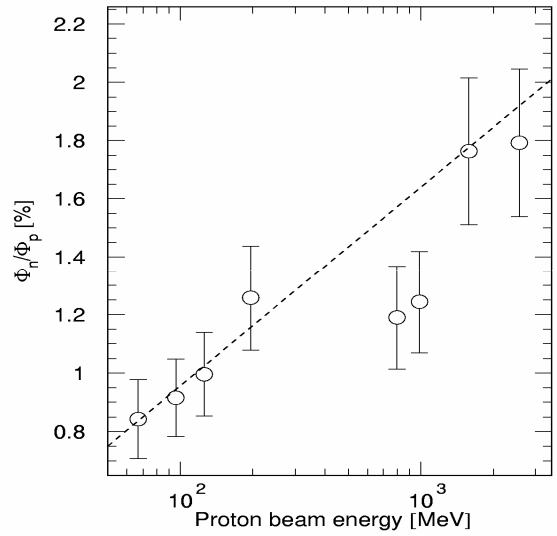

Fig. 4.1. Neutron component in the proton beams of different energies extracted under Project 839.

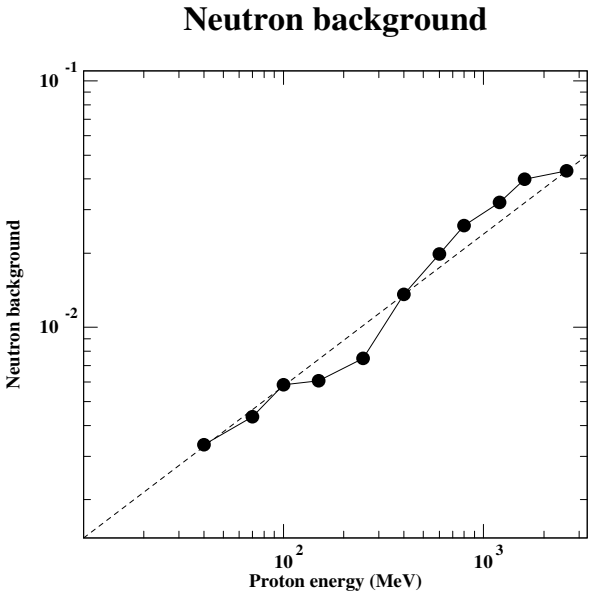

Fig. 4.2. Neutron component in the proton beams of different energies extracted under Project 2002.

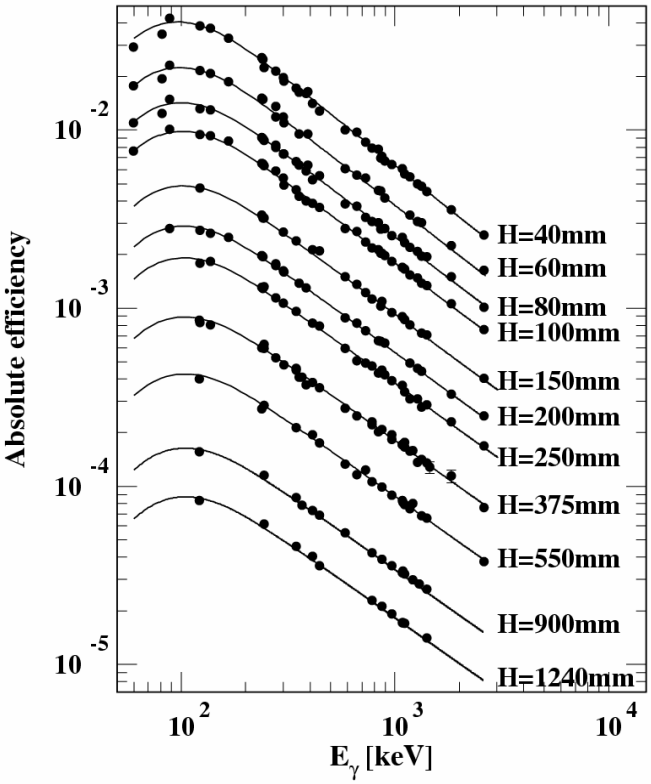

Fig. 5.1. The computational height-energy simulation of the absolute detection efficiency of the spectrometer.

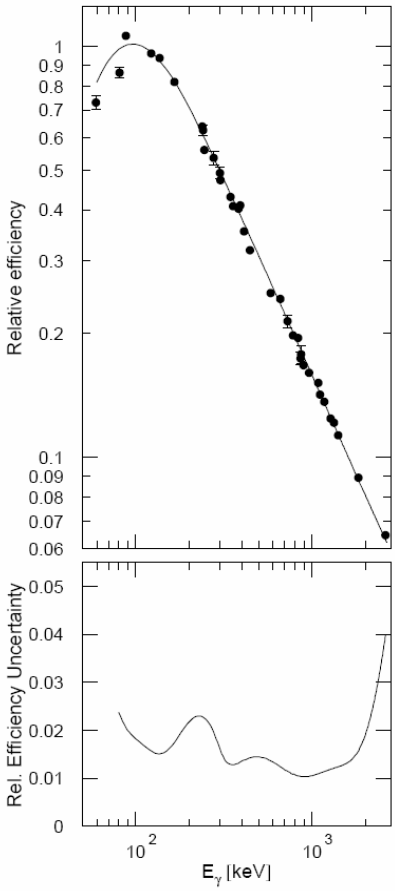

Fig. 5.2. The basic relative detection efficiency of the spectrometer at the height of 40 m and its error.

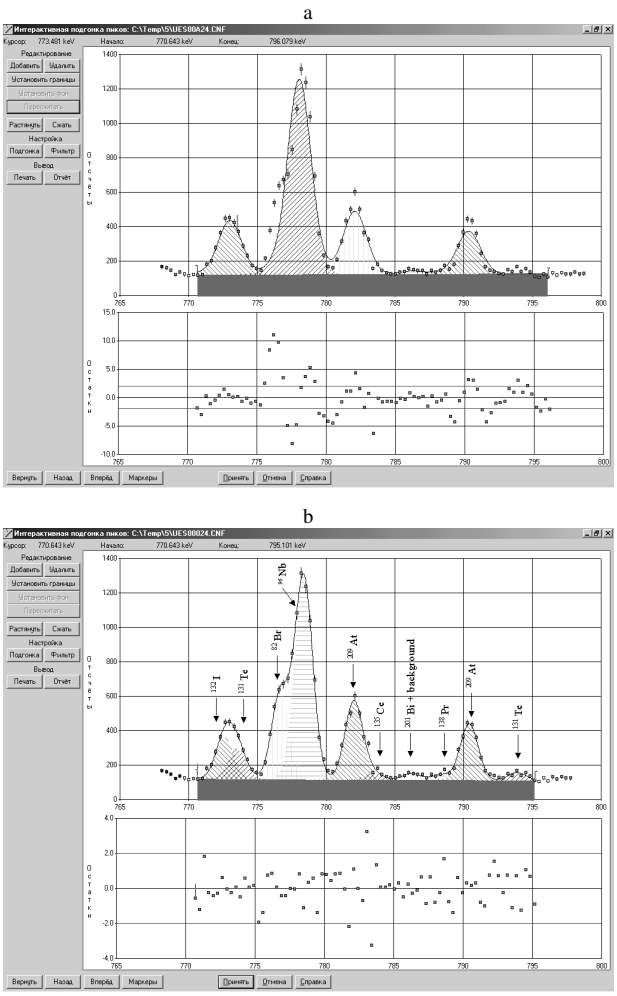

Fig. 6.1. The results of primary processing a γ-spectrum by GENIE-2000 code (a) and of additional manual processing in interactive fitting mode (b).

a

Отчёт по области

Начало: 770.643 keV Итерации: 15
Конец: 796.079 keV Хи-квадрат: 10

№	Энергия	Центр	Площадь	Ошибка	ПШПВ	Отношение
1	772.947	2369.06	2131.15	2.70	2.018	1.36
2	777.997	2384.55	7648.76	1.17	2.021	1.36
3	782.030	2396.92	2472.26	2.44	2.023	1.35
4	786.244	2409.84	131.60	28.94	2.025	1.35
5	790.306	2422.30	1680.24	3.25	2.027	1.35

Закрыть Справка

b

Отчёт по области

Начало: 770.643 keV Итерации: 10
Конец: 795.101 keV Хи-квадрат: 1.1

№	Энергия	Центр	Площадь	Ошибка	ПШПВ	Отношение
1	772.581	2367.94	1212.98	18.57	1.531	1
2	773.477	2370.69	884.47	25.27	1.531	1
3	776.644	2380.40	2467.32	3.28	1.533	1
4	778.327	2385.56	5918.96	1.66	1.533	1
5	781.964	2396.72	2310.83	3.31	1.535	1
6	783.428	2401.21	194.08	31.01	1.536	1
7	786.146	2409.54	203.98	17.46	1.537	1
8	788.248	2415.98	154.91	24.02	1.538	1
9	790.340	2422.40	1661.15	3.25	1.539	1
10	793.820	2433.07	235.75	15.15	1.541	1

Закрыть Справка

Fig. 6.2. The GENIE-2000 report on the processing parameters. (a) and (b) stand for the same as in Fig. 6.1.

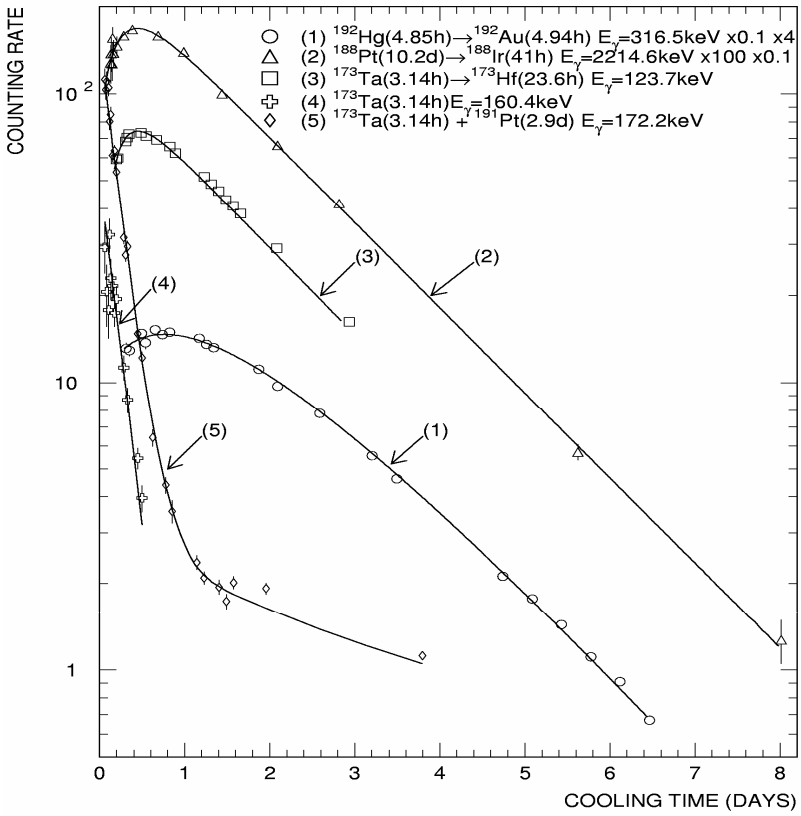

Fig. 7. Characteristic examples of the decay curves of the $^{192}Hg \rightarrow {}^{192}Au$ (1), $^{188}Pt \rightarrow {}^{188}Ir$ (2), and $^{173}Ta \rightarrow {}^{173}Hf$ (3) parentages and of the independent ^{173}Ta (4) and $^{173}Ta + {}^{191}Pt$ (5). To facilitate visualization, the scaling factors x along Y axis and x along X axis have been introduced.

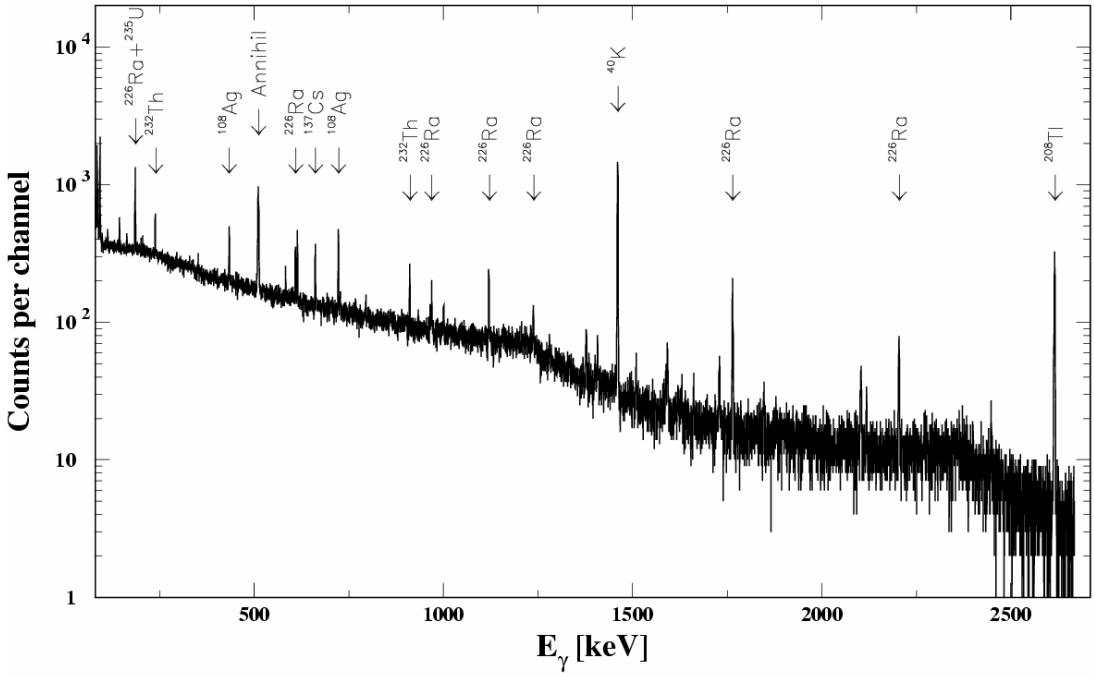

Fig. 8. The laboratory room radioactive background.

4. Irradiation of experimental samples

At ITEP, the above experiments are being made using the U-10 accelerator, which is a ring facility with a 25 MeV energy of proton injection into a ring and a 9.3 GeV maximum proton acceleration energy. At present, the external beams of fast and slow extraction are available with the parameters listed in Table 6.

Under ISTC Project#839 (1997-2000), the samples were exposed to the, thereby permitting high-intensity slow-extracted proton beam, thereby permitting (in combination with the available medical beam) them to be independently exposed to 2.6 – 0.8 GeV and 0.2 – 0.07 GeV protons, respectively (Figs. 9 and 10).

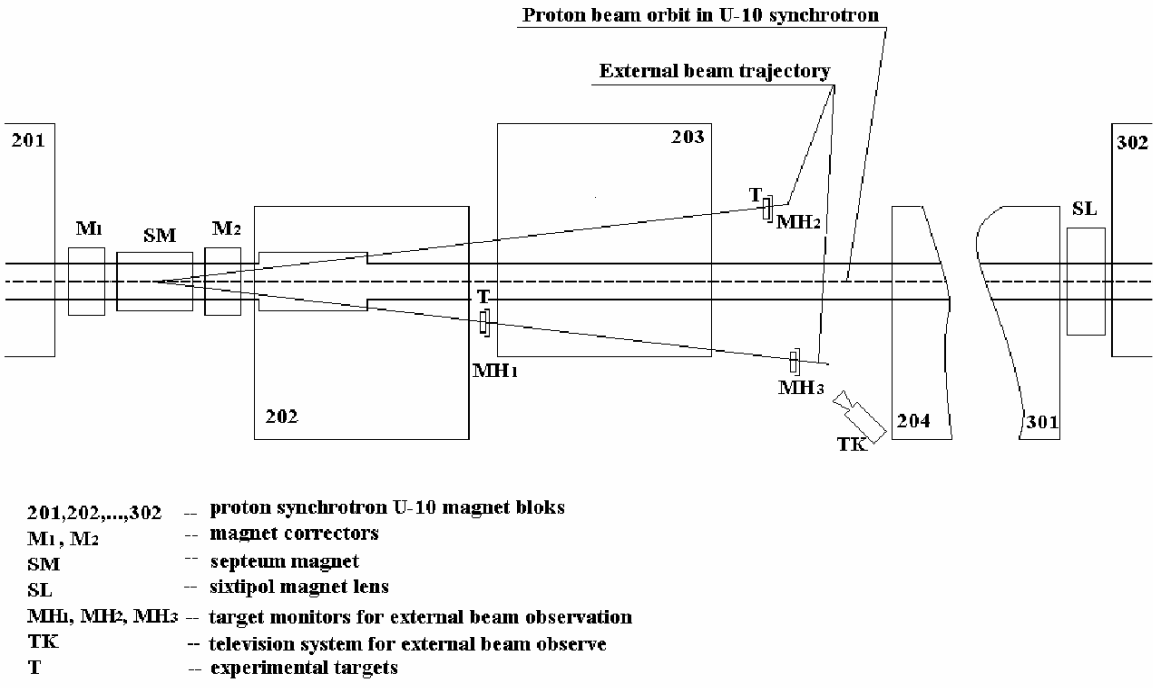

Fig. 9. The schematics of the facility and of the 2.6 – 0.8 GeV proton beam slow extraction elements.

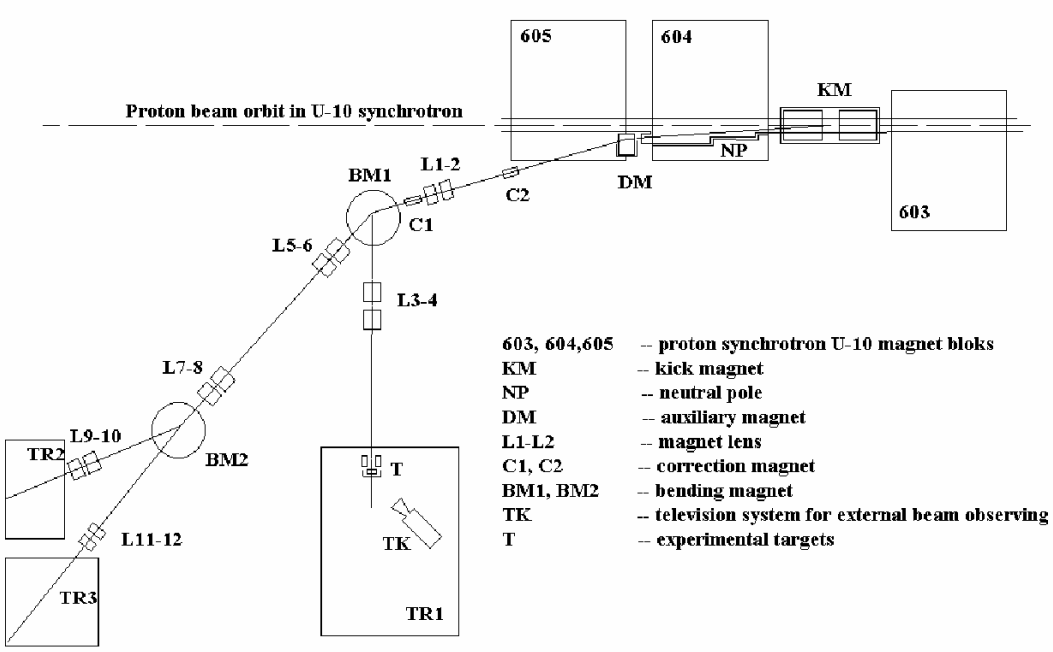

Fig. 10. The schematics of the facility and of the 0.2 – 0.07 GeV medical proton beam fast extraction elements.

Under ISTC Project#2002 (2002-2005) the samples were exposed to the task-oriented high-intensity fast-extracted proton beam, thereby permitting them to be exposed to 0.04 - 2.6 GeV protons (Fig. 11).

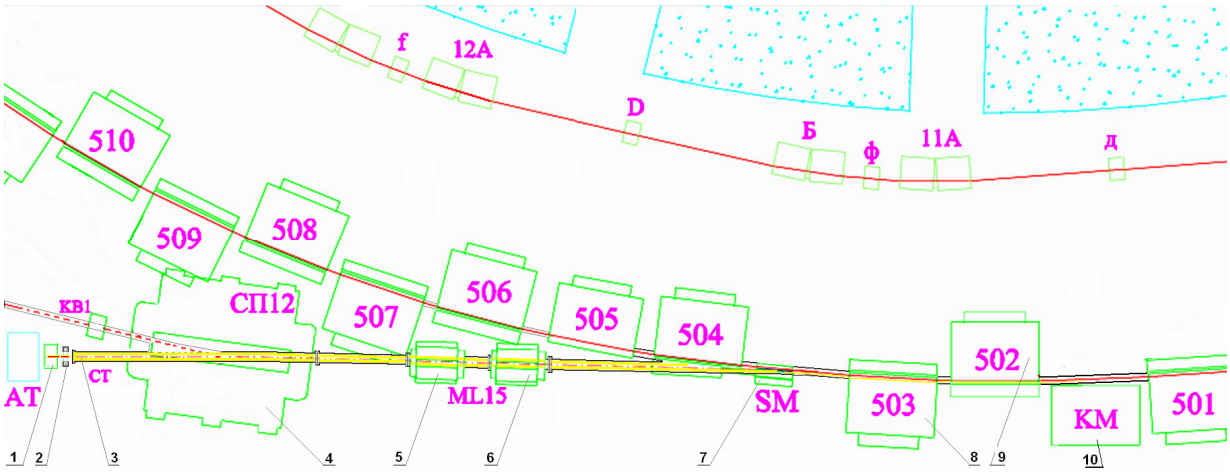

Fig. 11. The schematics of the facility and of the 0.04 – 2.6 GeV proton beam fast extraction elements: 1 – table to place the samples to be irradiated; 2 – current transformer; 3 – output flange of vacuumized proton guide; 4. – rotary magnet; 5, 6 – doublet of quadrupole lenses; 7 – septum magnet; 8, 9 – magnetic blocks pf accelerator ring; 10 - kicker magnet.

TABLE VI. THE EXTERNAL BEAM PARAMETERS OF THE ITEP PROTON ACCELERATOR

Parameter	Fast extraction (medical beam)	Slow extraction (204 gap)	Fast extraction (503 gap)
Энергия, (ГэВ)	0.07 – 0.20	0.8 -- 2.6	0.04 -- 2.6
Intensity (proton/pulse)	~ $2 \cdot 10^{9}$	~ $1 \cdot 10^{11}$	~ $2 \cdot 10^{11}$
Pulse duration (s)	~$0.25 \cdot 10^{-6}$	~ 0.3	~$1 \cdot 10^{-6}$
Pulse repetition rate (pulse/min)	~ 15	~ 15	~ 15
Section (mm)	Circle Ø 20	Ellipsis ~ 15x20	Ellipsis ~ 10x15

5. Proton beam energies

The extracted proton beam energies must be known because the experiments were aimed eventually at determining the excitation functions of the independent and cumulative yields of residuals and, in particular, at finding the proton flux densities via the excitation functions of the respective monitor reactions.

Considering the invariability of the proton orbit circumference (that is of one of the main synchrotron characteristics), the proton energy can be calculated by measuring the rotation frequency of protons f_r

$$E_0 = \frac{m_p \cdot c}{\sqrt{c^2 - L^2 \cdot f_r^2}} \quad - \quad m_p \tag{24}$$

where E_0 is the kinetic energy of a circulating proton; m_p=938.26 МэВ is proton mass; L=251.21 m is the closed orbit length; c=2.99776 $\cdot 10^8$ m/s is speed of light.

The f_r value is multiple to the accelerating radio frequency:

$$f_a = h \cdot f_r \tag{25}$$

where h=4 is number of harmonics; f_a is the accelerating radio frequency that varies from 1.07 MHz to 4.85 MHz. The f_a signal is formed safely, so the f_a values can well be measured up to 10^{-4} and even better.

6. The techniques for the calculation-experiment and experiment-experiment comparisons

As a rule, the theoretical calculations are made to simulate the independent yields of reaction products. To get the correct comparison or a general representation of the excitation functions for cumulative and supracumulative yields, it is expedient to consider the procedure of calculating them from independent calculated or experimental values of their precursors.

The general form of the radioactive nuclide transformation chain is

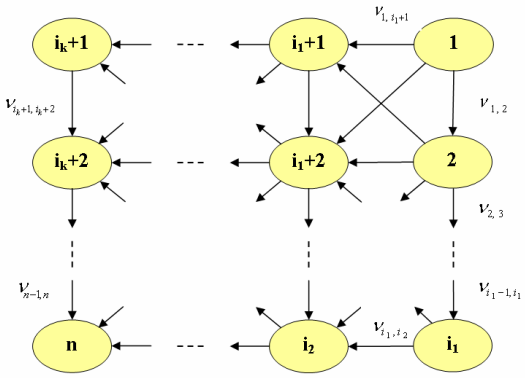

Fig.10. Radioactive transformation chain pattern.

Consider a chain composed of n nuclides interconnected via β^-, ε, n, p, and α transitions. Let all the chain nuclides be so numbered that a nuclide labeled a lower number will always be transformed into nuclide labeled a higher number.

Then, having known the independent cross sections for production of all the chain nuclides, we can calculate their cumulative cross sections as

$$\sigma_k^{cum} = \sum_{j=1}^{k} m_{kj} \cdot \sigma_j^{ind}, \qquad k = 1,2,...,n \tag{26}$$

where m_{kj} is a matrix, whose elements re calculated as

$$\sigma_k^{cum} = \begin{cases} \sum_{j=1}^{k} \nu_{ik} \cdot m_{ik} & \text{, для} \quad \kappa > j \\ 1 & \text{, для} \quad \kappa = j \\ 0 & \text{, для} \quad \kappa < j \end{cases} \tag{27}$$

where ν_{ik} –are the branching factors, i.e. the probabilities for the i-th nuclide to turn into the k-th nuclide

The vectorial form of the expression to calculate the cumulative yields is

$$\vec{\sigma}^{cum} = M \cdot \vec{\sigma}^{ind} \tag{28}$$

where M is a matrix with elements m_{kj}; $\vec{\sigma}^{cum}$ and $\vec{\sigma}^{ind}$ are vectors, whose elements are, respectively, cumulative and independent cross sections of the chain elements:

$$\vec{\sigma}^{cum} = \begin{cases} \sigma_1^{cum} \\ \sigma_2^{cum} \\ . \\ . \\ \sigma_n^{cum} \end{cases}, \qquad \vec{\sigma}^{ind} = \begin{cases} \sigma_1^{ind} \\ \sigma_2^{ind} \\ . \\ . \\ \sigma_n^{ind} \end{cases} \tag{29}$$

The branching factors v_{ik} were borrowed from the ENSDF database of 18 decay modes of radioactive nuclide decays: β^-, $\beta^- n$, *IT*, ε, $\varepsilon + \beta^+$, p, α, $\beta^+ p$, $\beta^+ \alpha$, $\beta^+ 2p$, εp, $\varepsilon\alpha$, 2 ε, n, β^+, 2 β^-, 2 β^+, 2 | e [8]. All modes that lead to identical variations of nuclear charge and mass were united into 12 groups of decays. The branching factors were taken for ground states or, if they are absent, for the first metastable state.

In case a branching factor is known inaccurately and is presented as (<0 or (>) than some limit, the branching factor value was taken to equal that limit, i.e. (<0 or (>) was replaced with (=).

If a branching factor value was indicated to be unknown (?), it was taken to be zero in case the numerical values of other branching factors are presented (allowing for the above remark),or else was taken to equal 1 in case other decay modes are not indicated. If other decay modes are presented and the sum of their indicated values is below 100%, the value of the unknown branching factor was taken to be 100% less the sum of the presented remaining decay modes.

If a few decay modes with unknown branching factors are presented, their values were taken to be a ratio of 100% to the number of such decay modes. If but a single decay mode is presented and its branching coefficient value is below 100%, the lacking difference was ascribed to mode β^+ (for neutron-deficient nuclides) and to mode β^- (for neutron-excessive nuclides).

If a delayed decay mode (say, ($\beta^+ \alpha$)) is indicated, the delayed decay mode value (α) was subtracted from the basic mode (β^+).

The decay mode *SF* is inapplicable to the given problem and was not used.

In total, 2470 nuclides with their branching factors were taken from the ENSDFdata.exe file. Out of that set, 75 nuclides were used to construct the simulated decay chains.

It should be noted that the branching factors obtained in such a way from the ENSDFdata.exe file are sometimes different from the data of other sources.

The comparison between the calculated and experimental excitation functions is presented both qualitatively as plots and quantitatively as mean-squared deviation factors *F* or mean ratios *S* calculated as

$$\langle F \rangle = 10^{\sqrt{A}}, \tag{30}$$

where $A = \left\langle \left(\log\left(\sigma_{ITEP,i} / \sigma_{X,i} \right) \right)^2 \right\rangle$, X=GSI, ZSR, calc.

$$\langle S \rangle = \frac{\sum_{i=1}^{n} \left(\sigma_{ITEP_i} / \sigma_{X_i} \right)}{n} \qquad (31)$$

7. Analysis of the experiments made

The ITEP results are expedient to analyze starting from

- the results of the ITEP and JAERI intercalibration measurements of the residual product nuclides from ^{63}Cu and ^{65}Cu samples by the direct kinematics techniques;
- the results of five experiments with measuring the residual nuclide yields in ^{56}Fe samples exposed to 0.3, 0.5, 0.75, 1.0, 1.5 GeV protons made using direct (ITEP, ZSR) and inverse (GSI) kinematics;
- the results of four experiments with measuring the residual nuclide yields in ^{197}Au, ^{208}Pb, and ^{238}U samples exposed to 0.8, 0.5, and 1.0 GeV protons made using direct (ITEP, ZSR) and inverse (GSI) kinematics;

The data obtained at ITEP and elsewhere were quantitatively intercompared as sets of independent experimental data by calculating the cumulative yields via independent yields as described above (Item 5) and using the mean squared deviation factor <*F*> that was calculated from (28) and used to analyze the theoretical and experimental results.

7.1 Intercalibration measurements of residual product yields from 1.2 GeV proton-irradiated ^{63}cu and ^{65}cu samples

The results of measuring the residual product yield in ^{63}Cu and ^{65}Cu samples exposed to 1.2 GeV protons at ITEP (GS-2518 detector) and JAERI (VHTRC and FNS detectors) are presented in [3] and displayed in Fig. 12. A good agreement is seen between the product yields obtained at the two laboratories. Table presents the values of factors <F> and <S>. The data presented have been obtained via $^{27}Al(p,x)^{24}Na$ monitor reaction and, hence, are considered tentative. The results presented in the Final Report on Project 839 have been measured once again using the $^{27}Al(p,x)^{22}Na$ reaction.

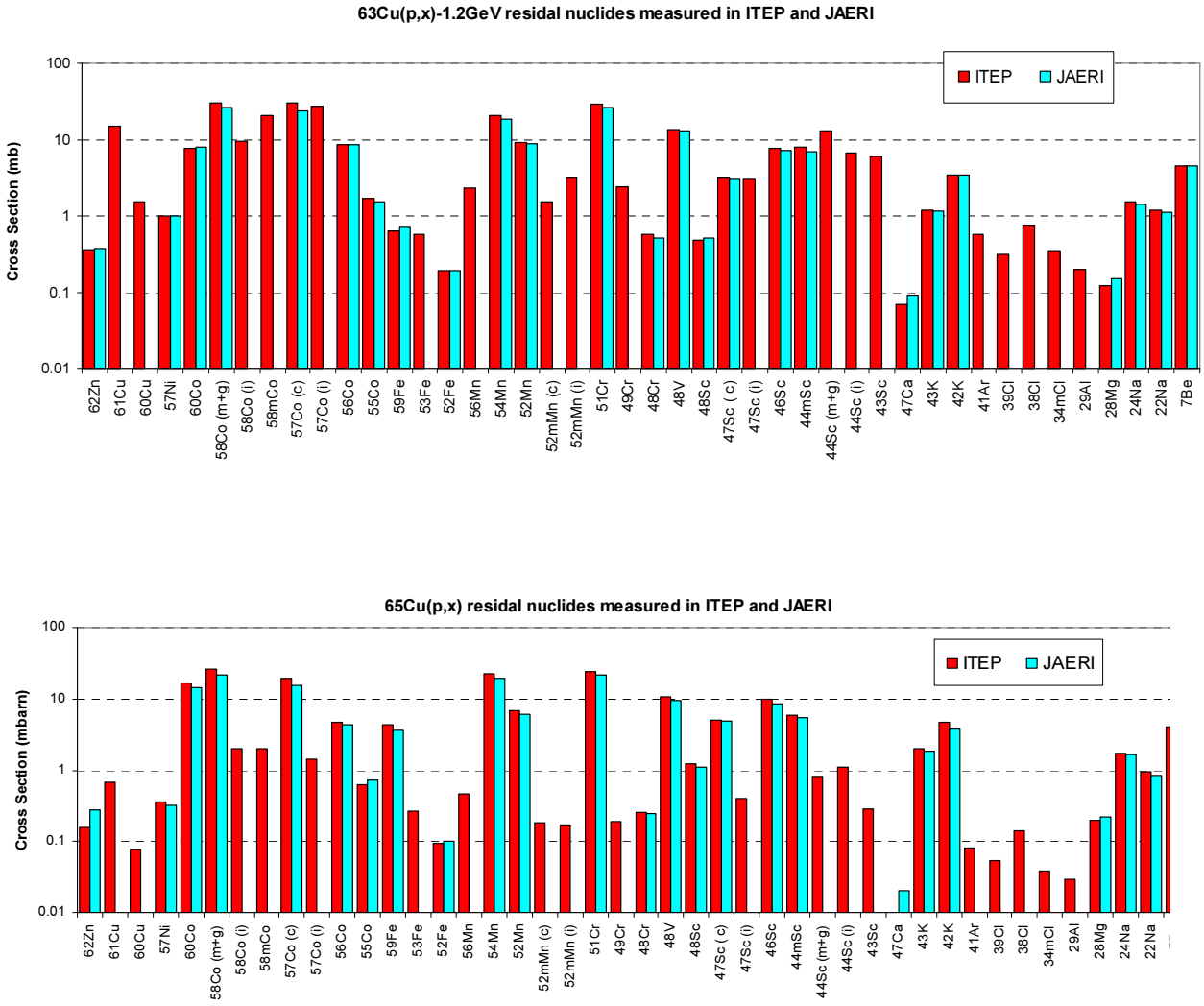

Fig. 12. The ITEP and JAERI-measured yields (barn) in ^{63,65}Cu exposed to 1.2 GeV protons.

TABLE VII. COMPARISON BETWEEN THE PRODUCT YIELDS (MB) IN ^{63,65}CU EXPOSED TO 1.2 GEV PROTONS AS MEASURED AT ITEP AND JAERI

	^{63}Cu	^{65}Cu
<F>	1.11	1.03
<S>	1.22	1.02

7.2. The results of measuring residual product yields in the samples with mean mass number by direct and inverse kinematics techniques

The 0.3, 0.5, 0.75, 1.0, and 1.5 proton irradiations of the mean-mass-number samples prepared by pressing the ^{56}Fe-enriched fine iron power (0.3% 0f ^{54}Fe, 99.5±0.1% of ^{56}Fe, 0.2% of ^{57}Fe, and <0.05% of ^{58}Fe) have given 218 independent and cumulative yields of radioactive residual product nuclei with halflives from 6.6 min to 312 days.

The comparisons with the data obtained elsewhere were realized by analyzing 41 works from EXFOR international nuclear database, in which the cross sections for producing secondary products of nuclear reactions in ^{56}Fe exposed to different-energy protons were determined. A lot of the experimental works were broken into the following four groups:

- the data cited in the present work (the black dots),
- the data obtained at GSI by inverse kinematics techniques (the white dots),
- the data obtained by R. Michel (the white crosses), Th. Schiekel (the white triangles), and M. Fassbender (the white diamonds) because the datasets obtained at those Laboratories are the closest to the dataset presented here,
- the data of the remaining 32 works constitute a separate group (the black asterisks)

Fig. 13 shows 6 examples of comparing the data on the residual product yields from ^{56}Fe measured at ITEP, GSI, and ZSR. To facilitate the comparisons, the said Figures present the plots of excitation functions simulated via different codes.

All the products were broken into two groups of products of Spallation (A>30) and fragmentation (A<30). Table 8 present the comparison results.

TABLE VIII. MEAN SQUARED DEVIATION FACTOR F OF THE ITEP AND GSI DATA FOR EACH ENERGY AND EACH COMBINATION OF PRODUCT GROUPS

	Product mass (A). Proton energy (GeV)						
	300	500	750	1000	1500	2600	All energies, all products
ITEP- GSI (A<30)	1.23	1.36	1.19	2.36	1.56	1.57	1.36
ITEP– GSI (A>30)	1.39	1.27	1.34	1.34	1.27	1.25	

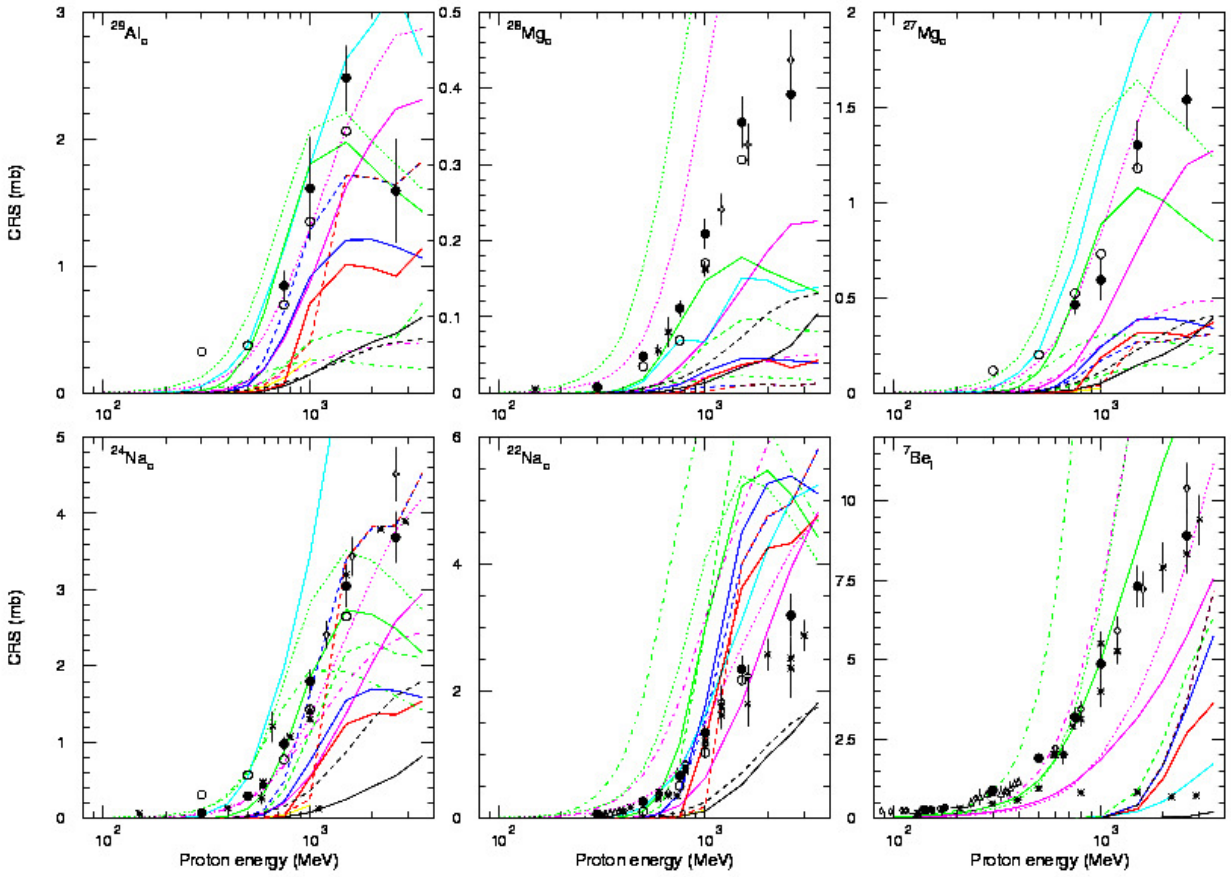

Fig. 13. An example of comparisons among the yields of residual product nuclei from ^{56}Fe measured at ITEP (the black dots), GSI (the white dots), and elsewhere. Also shown are the simulation results of various computational codes.

7.3. The results of measuring the yields of residual product nuclei in samples of high mass numbers obtained by direct and inverse kinematics techniques

In the high-mass range, the direct and inverse kinematics data were compared for ^{197}Au (E_p = 0.8 GeV), ^{208}Pb (E_p = 0.5 and 1.0 GeV), and ^{238}U (E_p = 1.0 GeV). The ITEP team used U of natural composition as a ^{238}U-containing sample, and Pb enriched with ^{208}Pb (97.2% of ^{208}Pb, 1.93% of ^{207}Pb, <0.01% of ^{206}Pb and, <0.001% of ^{204}Pb) as a ^{208}Pb-containing sample. The ZSR team used Pb of natural composition.

Since the ITEP team did not measured the residual product yields in ^{238}U exposed to 1 GeV protons, the relevant results to be compared with the GSI data were obtained by linear nterpolation of the logarithms of the known experimental cross section values for proton energies E_1=0.8 GeV and E_2=1.2 GeV:

$$\sigma_E^i = \exp\left[\frac{E_2 - E}{E_2 - E_1}\cdot\ln\left(\sigma_{E_1}^i\right) + \left(1 - \frac{E_2 - E}{E_2 - E_1}\right)\cdot\ln\left(\sigma_{E_2}^i\right)\right],$$

where $\sigma^i_{E_1}$ and $\sigma^i_{E_2}$ are cross sections of the i-th nuclide for proton energies E_1 and E_2.

The errors in the cross sections obtained by interpolation were calculated as

$$\Delta_{\sigma^i_{1.0}} = \sigma^i_{1.0} \cdot \sqrt{(\delta_{st})^2 + 0.25(\delta^i_{0.8})^2 + 0.25(\delta^i_{1.2})^2},$$

where δ_{st} is the relative error of monitor; $\delta^i_{0.8}$ and $\delta^i_{1.2}$ are relative errors in cross sections $\sigma^i_{0.8}$ and $\sigma^i_{1.2}$ of the i-th nuclide (without the monitor error) or 0.8 GeV and 1.2 GeV, respectively.

Table 8 and Figs. 14-15 present the comparisons between ITEP and ZSR (direct γ-spectrometry) and between ITEP and GSI (direct and inverse kinematics) for ^{197}Au [9].

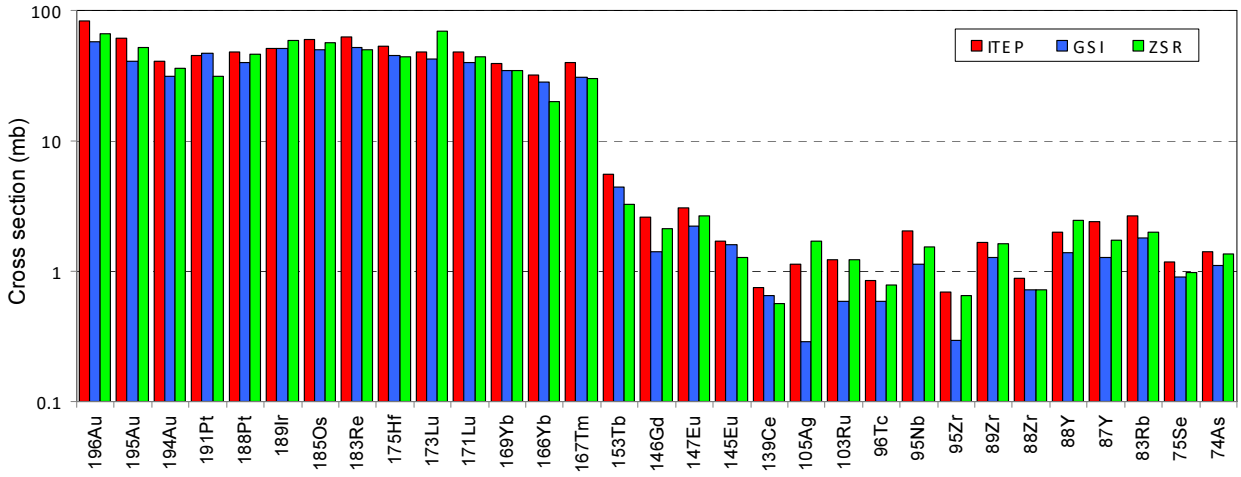

Fig. 14. Reaction product yields in ^{197}Au exposed to .8 GeV protons and measured at ITEP, ZSR, and GSI.

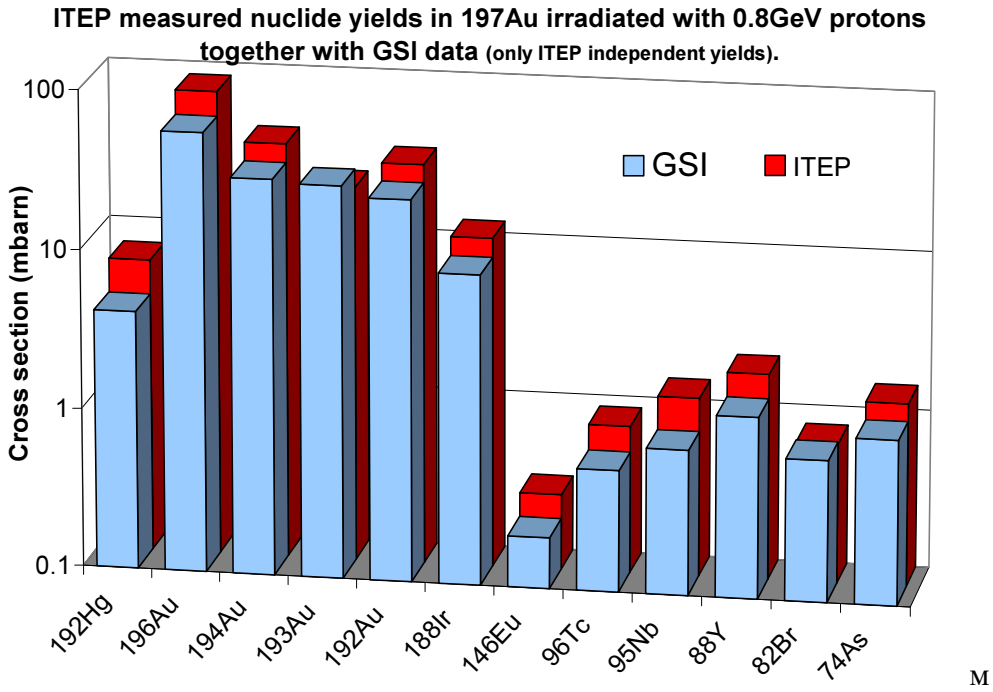

Fig. 15. Comparison of the ITEP-measured ^{197}Au(p,x) reaction yields at E_p = 0.8 GeV with the GSI measurement data.

TABLE IX. COMPARISON OF THE ITEP-MEASURED ^{197}AU(P,X) REACTION YIELDS AT E_P = 0.8 GEV WITH THE GSI AND ZSR MEASUREMENT DATA

Comparison	<F>	<S>
ITEP/GSI	1.54	1.45
GSI/ZSR	1.56	0.88
ITEP/ZSR	1.28	1.17

The ITEP-ZSR (direct gamma-spectrometry), ITEP-GSI, and ZSR-GSI (direct and inverse kinematics) comparisons among the yields in 1.0 GeV proton-irradiated ^{208,nat}Pb are presented in Fig. 16 and Table 10 [10]

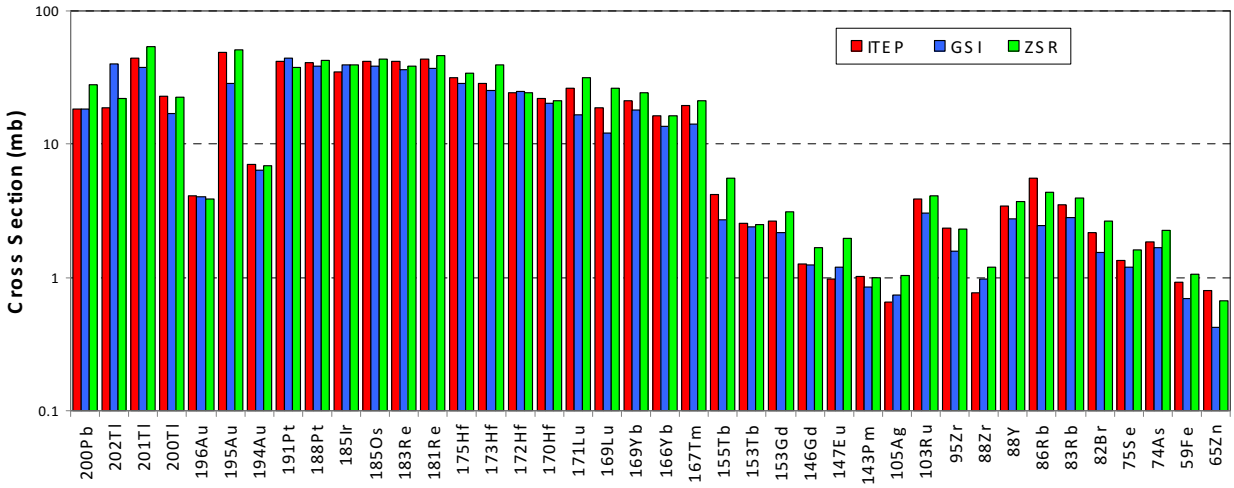

Fig. 16. The product yields (barn) in ^{208}Pb exposed to 1.0 GeV protons at ITEP, ZSR and GSI.

TABLE X. COMPARISON AMONG THE YIELDS IN ^{208,NAT}PB EXPOSED TO 1.0 GEV PROTONS AT ITEP, GSI, AND ZSR

Comparison	<F>	<S>
ITEP/GSI	1.35	1.20
GSI/ZSR	1.45	0.79
ITEP/ZSR	1.25	0.90

Table 11 and Figs. 17 and 18 present the ITEP-GSI comparison results for ^{208}Pb exposed to 0.5 GeV protons.

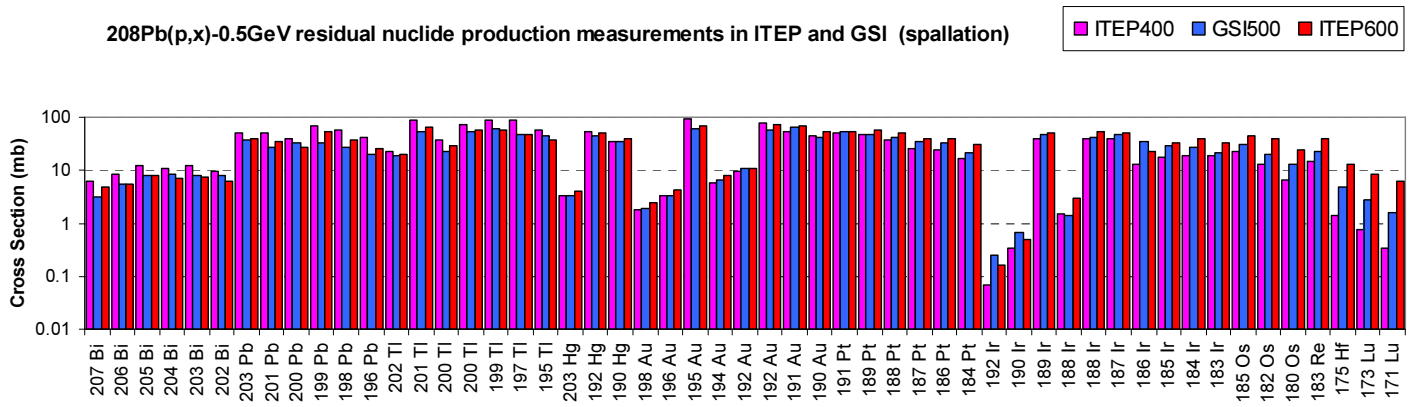

Fig. 17. The product yields in ^{208}Pb exposed to 0.5 GeV protons at ITEP and GSI (spallation products).

TABLE XI. COMPARISON BETWEEN THE ITEP- AND GSI-MEASURED YIELDS IN ^{208}PB EXPOSED TO 0.5 GEV PROTONS

	<F>	<S>
All products	1.51	0.98
Spallation pr.	1.32	1.12
Fission pr.	1.81	0.71

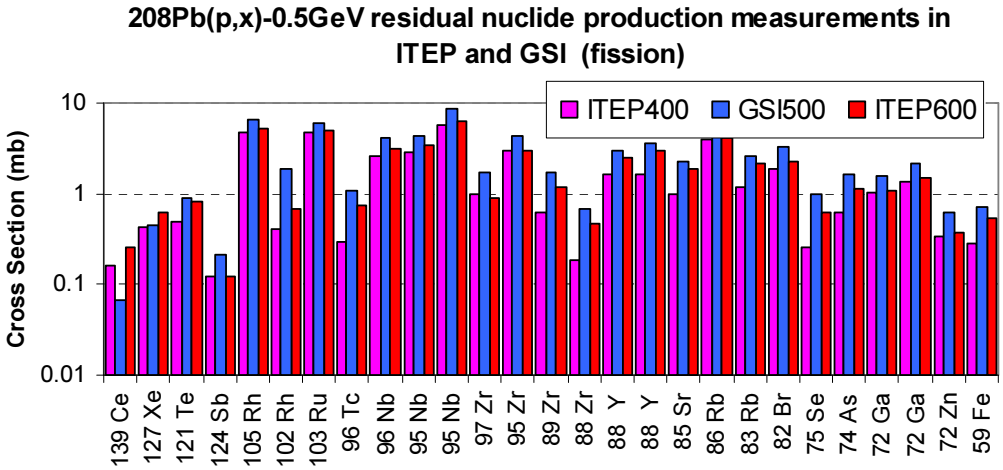

Fig. 18. The product yields in ^{208}Pb exposed to 0.5 GeV protons at ITEP and GSI (fission products).

Comparisons between the ITEP and GSI results for ^{238,nat}U exposed to 1.0 GeV protons are presented in Fig. 19 and in Tables 12 and 13 [11].

TABLE XII. THE ITEP- AND GSI-MEASURED INDEPENDENT YIELDS OF ^{NAT}U(P,X) REACTION AT E_P = 1.0 GEV

Product	$T_{1/2}$	Type	ITEP	GSI, Darmstadt
232Pa	1.31d	i	8.40 ± 0.48	6.13 ± 0.92
230Pa	17.4d	i	3.28 ± 0.26	2.88 ± 0.43
226Ac	29.37h	i	2.26 ± 0.18	1.53 ± 0.23
203Pb	51.873h	$i_{(m1+m2+g)}$	1.29 ± 0.23	0.06 ± 0.0060
201Pb	9.33h	$i_{(m+g)}$	4.67 ± 0.69	0.19 ± 0.02
200Tl	26.1h	i	1.43 ± 0.12	0.044 ± 0.0044
146Eu	4.61d	i	0.698 ± 0.048	0.514 ± 0.026
144Pm	363d	i	1.41 ± 0.14	1.02 ± 0.15
140La	1.6781d	i	2.89 ± 0.17	2.49 ± 0.15

…

88Y	106.65d	i	8.57 ± 0.46	6.51 ± 0.52
86Rb	18.631d	$i_{(m+g)}$	17.1 ± 0.84	11.2 ± 0.6
82Br	35.30h	$i_{(m+g)}$	11.5 ± 0.56	8.49 ± 0.51
78As	90.7m	i	7.64 ± 0.87	5.33 ± 0.32
76As	1.0778d	i	6.79 ± 0.40	5.93 ± 0.36
74As	17.77d	i	3.77 ± 0.26	2.84 ± 0.28
72Ga	14.10h	i	5.31 ± 0.30	3.68 ± 0.22

TABLE XIII. COMPARISON OF THE ITEP-MEASURED INDEPENDENT YIELDS OF ^{NAT}U(P,X) REACTION AT E_P = 1.0 GEV WITH THE GSI MEASUREMENT DATA

	<F>	<S>
All products	2.77	3.54
All except ^{203}Pb, ^{201}Pb, ^{200}Tl	1.39	1.35

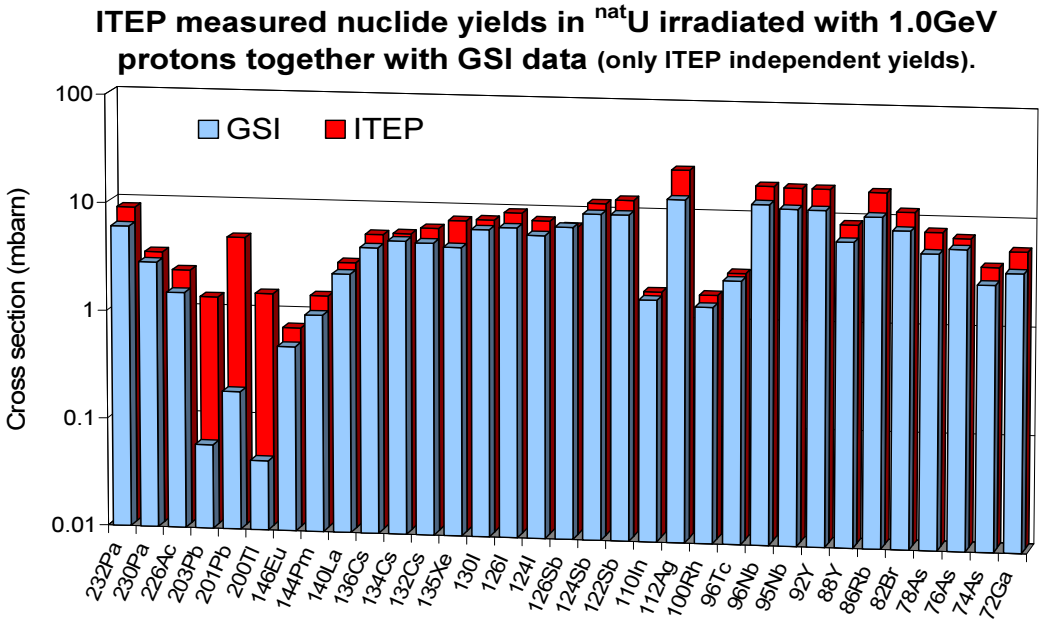

Fig. 16. Comparison of the ITEP-measured independent yields of ^{nat}U(p,x) reaction at E_p = 1.0 GeV with the GSI measurement data.

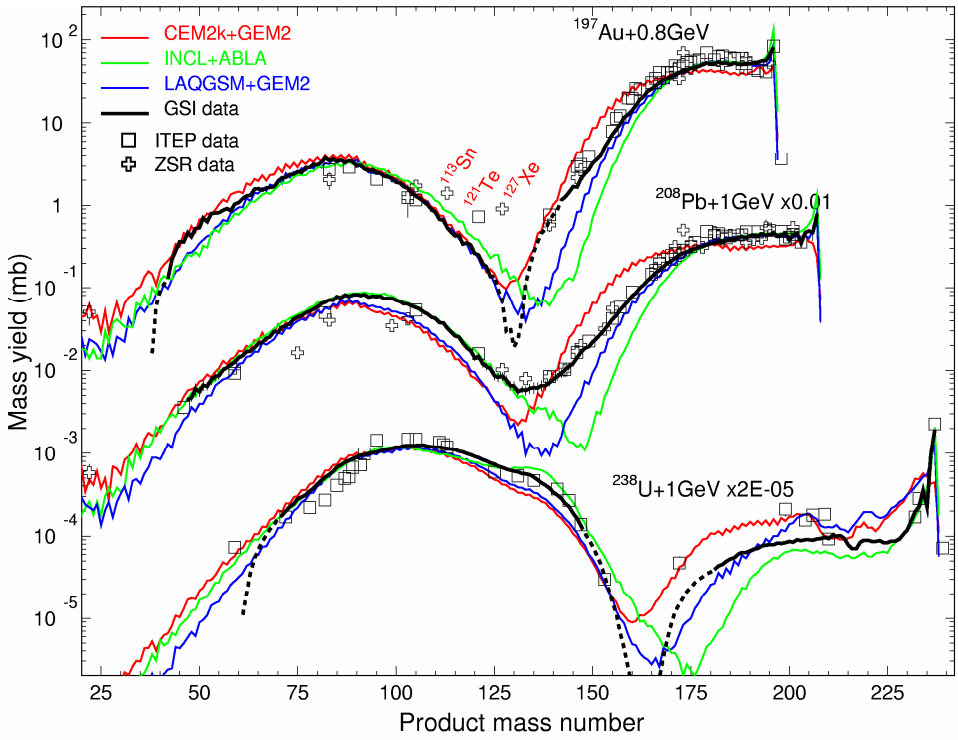

Fig. 17. Comparison among the ITEP, ZSR, and GSI-measured mass yields of $^{197}Au(p,x)$ reaction at E_p = 0.8 GeV together with theoretical predictions.

8. Conclusions

Table 14 presents the complete set of comparisons between the reaction product yields measured at ITEP and the JAERI, GSI, and ZSR measurements results.

TABLE XIV. COMPARISONS OF THE REACTION PRODUCT YIELDS MEASURED AT ITEP WITH THE GSI AND ZSR MEASUREMENTS RESULTS

Target	Energy (GeV)	set	<F>	<S>
^{63}Cu ^{65}Cu	1.2	ITEP/JAERI	1.11 1.22	1.03 1.02
^{56}Fe	0.3, 0.5, 0.75,1.0, 1.5	ITEP/GSI	1.36	
^{197}Au	0.8	ITEP/GSI GSI/ZSR ITEP/ZSR	1.54 1.56 1.28	1.45 0.88 1.17
^{208}Pb	0.5	ITEP/GSI	1.51 – all products 1.32 – spallation pr. 1.81 – fission pr.	0.98 – all products 1.12 – spallation pr. 0.71 – fission pr.
	1.0	ITEP/GSI GSI/ZSR ITEP/ZSR	1.35 1.45 1.25	 0.79 0.90
^{238}U	1.0	ITEP/GSI	1.39	1.35

Analysis of comparisons among the experimental data has shown that

- As a whole, the convergence among three datasets is quite satisfactory (at least much better than the convergences between experiment and calculations), so all three

datasets (ITEP, GSI, and ZSR) must be used to verify the simulated results. At the same time, the minute comparison has revealed some systematic differences. For instance, The GSI data are systematically10-15% below the ITEP data that, in turn, are systematically ~10% below the ZSR data, with the GSI data being systematically ~20% below the ZSR data.

- With the view of verifying the codes, the calculation-experiment comparisons are expedient to make using the data on a broad energy range (from ~20 MeV to 2-3 GeV) instead of the data on separate energies, i.e. the excitation function concept must be played.
- With the above approach, each of the experimental datasets shows its own significance, namely
    1. The ZSR and ITEP data will be especially useful I the lower range of energies (~500MeV), wherein experimenting at GSI is impossible or else the experimental results will contradict the direct kinematics data. In this case those ZSR datasets are particularly important that were obtained using the stacks, thereby permitting the near-threshold excitation functions to be obtained in some cases.
    2. The GSI data are especially important when updating the methodological approaches to perfecting models and codes because those data concern the total isobaric distributions of reaction products (it should be remembered, however, that the said methodology fails to separate the ground and isomeric states of nuclei). It is also of importance that the number of the GSI experiments is restricted and, therefore cannot fully satisfy the demands of theoreticians (the GSI experiments disregard the low-energy range (up to 300 MeV) completely).
- The ITEP experience in comparing the results (both experiment-calculations and experiment-experiment) may underlie verification of codes.
- The ITEP team is prepared to continue studying the proton-induced reaction yields in thin targets and suggests the following target compositions to be discussed (Table 15). The list may be altered and extended.

TABLE XV. LIST OF TARGETS AND PROTON ENERGIES IN THE NEXT PROJECT #3880 [12]

List of irradiation runs for beta-active nuclide production measurements.											
Targets	Proton Energy (GeV)										
	0.04	0.07	0.1	0.15	0.25	0.4	0.6	0.8	1.2	1.6	2.6
^{nat}Mo	x	x	x	x	x	x	x	x	x	x	x
^{nat}Zr	x	x	x	x	x	x	x	x	x	x	x
^{nat}Ti	x	x	x	x	x	x	x	x	x	x	x
^{nat}In	x	x	x	x	x	x	x	x	x	x	x
^{115}In	x	x	x	x	x	x	x	x	x	x	x
^{nat}Sn	x	x	x	x	x	x	x	x	x	x	x
^{112}Sn	x	x	x	x	x	x	x	x	x	x	x
^{124}Sn	x	x	x	x	x	x	x	x	x	x	x

REFERENCES

[1] Yu.E.Titarenko, V.D.Kazaritsky, V.F.Batyaev, Yu.V.Kochevalin, N.V.Stepanov, Experimental and computational researches into cross sections for 1.2 GeV proton-induced deep spallation reactions in Co-59, Parts 1 and 2, Moscow, Preprints ITEP No. 81, 1993, 1-15 and No. 30, 1994, 1-25.

[2] Yu.E. Titarenko, O.V. Shvedov, M.M. Igumnov, S.G. Mashnik, E.I. Karpikhin, V.D. Kazaritsky, V.F. Batyaev, A.B. Koldobsky, V.M. Zhivun, A.N. Sosnin, R.E. Prael, M.B. Chadwick, T.A. Gabriel, M. Blann. Experimental and Computer Simulation Study of the Radionuclides Produced in Thin 209Bi Targets by 130 MeV and 1.5 GeV Proton-Induced Reactions. Nucl. Instr. Meth. A (1998), v. 414, No. 1, p. 73-99.

[3] Yu.E. Titarenko, O.V. Shvedov, V.F. Batyaev, E.I. Karpikhin, V.M. Zhivun, A.B. Koldobsky, M.M. Igumnov, I.S. Sklokin, R.D. Mulambetov, A.N. Sosnin, H. Yasuda, H. Takada, S. Chiba, Y. Kasugai, S.G. Mashnik, R.E. Prael, M.B. Chadwick, T.A. Gabriel, and M. Blann. Experimental and Computer Simulation Study of Radionuclide Yields in the ADT Materials Irradiated with Intermediate Energy Protons. Proc. 3d Specialists' Meeting on High Energy Nuclear Data, March 30-31, 1998, JAERI, Tokai, Ibaraki-ken, Japan, Ed., T. Fukahori JAERI-Conf 98-016, November 1998, pp. 125-135.

[4] Yu.E. Titarenko et al. Experimental and Theoretical Study of the Yields of Residual Product Nuclei in Thin Targets Irradiated by 100 – 2600 MeV Protons, IAEA, Nuclear Data Section, INDC(CCP)-434, September, 2002, http://www-nds.iaea.org/reports/indc-ccp-434.pdf.

[5] Yu.E. Titarenko, V.F. Batyaev, E.I. Karpikhin, R.D. Mulambetov, V.M. Zhivun, A.V. Ignatyuk, V.P. Lunev, N.N. Titarenko, Yu.N. Shubin, V.S. Barashenkov, S.V. Mulambetova, K.A. Lipatov, A.V. Belkin, N.N. Alexeev, V.A. Schegolev, Yu.M. Goryachev, V.O. Kudryashov: "Experimental and theoretical studies of the yields of residual product nuclei produced in thin Pb and Bi targets irradiated by 40-2600 MeV protons", Final Technical Report on the ISTC Project #2002, 2005 http://www.nea.fr/html/science/egsaatif/ISTC2002-final-report.pdf

[6] ISTC Project #3266: http://tech-db.istc.ru/ISTC/sc.nsf/html/projects.htm?open&id=3266

[7] R.B.Firestone, in: Tables of Isotopes, 8th ed.: 1998 Update (with CD ROM) edited by S.Y.Frank Chu (CD-ROM Ed.), C.M.Baglin (Ed.), V.S.Shirley (Ed.), (Wiley Interscince, New York, 1996).

[8] J. K. Tuli, Evaluated Nuclear Structure Data File. A Manual for Preparation of Data Sets, BNL-NCS-51655-01/02-Rev, February 2001, http://ie.lbl.gov/databases/ENSDF-Manual.pdf. ENSDF database is available at: http://ie.lbl.gov/databases/ENSDFdata.exe.

[9] Yu.E. Titarenko, V.F. Batyaev, V.M. Zhivun, A.B. Koldobsky, Yu.V. Trebukhovsky, E.I. Karpikhin, R.D. Mulambetov, S.V. Mulambetova, Yu.V. Nekrasov, A.Yu Titarenko, K.A. Lipatov, S.G. Mashnik, R.E. Prael, K. Gudima, M. Baznat. Cross Sections for Nuclide Production in 1 GeV Proton-Irradiated 208Pb and 0.8 GeV Proton-Irradiated 197Au. // Imbedded topical AccApp'03 (Nuclear Applications of Accelerator Technology) 2003 Annual Meeting of the American Nuclear Society (ANS) in San Diego, 1-5 June 2003, California, USA, ANS Proceedings, pp. 1070-1073.

[10] Yu. E. Titarenko, O. V. Shvedov, V. F. Batyaev, E. I. Karpikhin, V. M. Zhivun, A. B. Koldobsky, R. D. Mulambetov, S.V. Kvasova, A. N. Sosnin, S. G. Mashnik, R. E. Prael, A. J. Sierk, T. A. Gabriel, M. Saito, H. Yasuda, Cross sections for nuclide production in 1 GeV proton-irradiated 208Pb, Phys. Rev. C **65**, 064610 (2002).

[11] Yu.E. Titarenko, V.F. Batyaev, E.I.Karpikhin, V.M.Zhivun, A.B.Koldobsky, R.D. Mulambetov, S.V. Mulambetova, S.G.Mashnik, R.E.Prael. Nuclide Production in 197Au, 208Pb and natU Irradiated with 0.8-1 GeV Protons: Comparison with other

Experiments and with Theoretical Predictions. // Workshop on Nuclear Data for the Transmutation of Nuclear Waste, September 1-5, 2003 at GSI-Darmstadt, Germany. Proceedings of the International Workshop on Nuclear Data for the Transmutation of Nuclear Waste, ISBN 3-00-012276-1 http://www-w2k.gsi.de/tramu/proceedings/titarenko2.pdf

[12] ISTC Project #3880: http://tech-db.istc.ru/ISTC/sc.nsf/html/projects.htm?open&id=3880

ABLA07 - Towards a Complete Description of the Decay Channels of a Nuclear System from Spontaneous Fission to Multifragmentation

A. KELIĆ, M.V. RICCIARDI, K.-H. SCHMIDT

Gesellschaft für Schwerionenforschung,
Darmstadt, Germany

Abstract. The physics and the technical algorithms of the statistical de-excitation code ABLA07 are documented. The new developments of ABLA07 have been guided by the empirical knowledge obtained in a recent experimental campaign on the nuclide distributions measured at GSI, Darmstadt. Besides distinct signatures of very asymmetric binary splits, lighter systems show clear features of multifragmentation, while heavy systems reveal the influence of dynamics and microscopic structure on the fission process. ABLA07 includes elaborate but efficient descriptions of all these processes, with one set of the model parameters fixed for all systems and all energies.

1. Introduction

Nuclear reactions represent an excellent tool to study static and dynamical properties of nuclear matter. For example, while fission at low excitation energies can be used to extract information on the heights and curvatures of the fission barriers [1] or on pairing and shell correlations at large deformations [2,3], fission at high excitation energies (above ~100 MeV) can give insight into dissipative properties of nuclear matter, see e.g. [4]. Other examples are spallation reactions and heavy-ion reactions at and above the Fermi energy, which are best suited for studying thermal instabilities and the liquid-gas phase transition in nuclear matter [5,6,7,8,9,10]. Unfortunately, most of the needed information cannot be directly obtained from the experimental observables. Usually, one needs to use some reaction model, and only by comparing the predictions of a considered model with measured observables one can gain more insight into the physical processes. For this purpose, of course, reaction models as realistic as possible are mandatory.

In recent years, reaction models became important not only for the basic research but also for different applications. Fusion, fission, fragmentation or spallation reactions are used in order to produce beams of secondary, radioactive ions. Spallation reactions are used as a neutron source [11,12] and considered for different applications such as for example nuclear-waste management [13,14]. To these purposes, many facilities are being built or being planned all around the world. For the proper functioning of these facilities, cross sections of different particles produced in considered nuclear reactions have to be known. Due to the variety of the involved systems, i.e. different target/projectile/beam-energy combinations, not all production cross sections can be measured, and one has to rely on model calculations. Therefore, reliable and fast reaction models are also mandatory for technological applications.

Usually, nuclear-reaction models consist of two stages: In the first stage, it is assumed that due to the interaction between a target and a projectile nucleus, an excited thermally equilibrated nuclear system is formed. After the thermalised system is formed, in the second stage its decay is described in the frame of the statistical model [15]. Usually, two realisations of the statistical model are employed: The Weisskopf-Ewing approach [16] and the Hauser-Feshbach approach [17]. While in the former a direct consideration of angular momentum and parity is neglected, in the latter approach they are explicitly taken into account. Many different deexcitation codes based on these two approaches have been developed. They mostly differ according to different descriptions of the physics concepts involved, e.g. level density, nuclear potential, nuclear viscosity or number of considered decay channels. In order to be used for the description of the deexcitation process of residues formed in different types

of interactions (i.e. different target/projectile/energy combinations) a deexcitation code has to be adapted to some specific needs:

- A consistent treatment of level densities as a function of excitation energy and nuclear shape is mandatory. The treatments of shell effects [18] and collective excitations [19] are particularly important.

- The dynamics of the fission process and the onset of thermal instabilities at the highest temperatures have to be considered.

- Modelling of fission requires considering a large variety of fissioning nuclei in a wide range of excitation energies. Available empirical formulations of nuclide distributions in fission of specific nuclei should be replaced by a model, which is based on more fundamental properties, like the potential-energy landscape around saddle and scission.

- For application purposes, inclusion in complex transport codes demands for short computing times.

In the following, we will describe the deexcitation code ABLA07, which complies with the above-mentioned requirements.

2. Description of the model

ABLA07 is a dynamical code that describes the de-excitation of the thermalised system by simultaneous break-up, particle emission and fission. Simultaneous break-up is considered as the cracking of the hot nucleus into several fragments due to thermal instabilities. The description of particle evaporation is based on the Weißkopf-Ewing formalism [20], while the fission decay width is calculated taking into account dynamical effects [21]. The basic ingredients of the model are[1]:

1. Emission of neutrons, light charged particles (Z=1, 2), intermediate-mass fragments IMF (Z>2) and gamma rays is considered.

2. In calculating the particle decay widths the following effects are considered:

    - Energy dependent inverse cross sections based on nuclear potential using the ingoing-wave boundary condition model [22].

    - Barriers for charged particles are calculated using the Bass potential [23].

    - Thermal expansion of the source [24] is taken into account.

    - Change of angular momentum due to particle emission is considered.

3. The fission decay width is described by including:

    - An analytical time-dependent approach [25,26] to the solution of the Fokker-Planck equation,

[1] Comparison with the previous version of the model ABLA is given in Annex I.

- The influence of the initial deformation on the fission decay width,
- The double-humped structure in the fission barriers of actinides,
- Symmetry classes in low-energy fission.

4. Particle emission on different stages, i.e. between ground state and saddle point, between the saddle and scission point, and from two separate fission fragments, of the fission process is calculated separately.

5. Kinetic-energy spectra of the emitted particles are directly calculated from the inverse cross sections.

6. A stage of simultaneous break-up [9] in the decay of hot excited systems is explicitly treated.

In the following, these different steps will be discussed in more details.

2.1 Particle emission

Following the Weißkopf-Ewing formalism [20,27], the decay width of a specific initial nucleus, characterised by its excitation energy E_i into a daughter nucleus with excitation energy E_f by emission of particle ν with kinetic energy ε_ν is given as:

$$\Gamma_\nu(E_i) = \frac{2\cdot s_\nu + 1}{2\cdot\pi\cdot\rho_i(E_i)}\cdot\frac{2\cdot m_\nu}{\pi\cdot\hbar^2}\cdot\int_0^{E_i - S_\nu - B_\nu}\sigma_c(\varepsilon_\nu)\cdot\rho_f(E_f)\cdot(\varepsilon_\nu - B_\nu)\mathrm{d}E_f \qquad (1)$$

In the above equation, s_ν is the spin of the emitted particle, ρ_i and ρ_f are the level densities in the initial and the daughter nucleus, respectively, σ_c is the cross section for the inverse process, B_ν is the Coulomb barrier for charged-particle emission and m_ν the mass of the emitted particle.

In order to calculate the probability of a certain decay channel, i.e. $P_\nu = \Gamma_\nu / \sum\Gamma_i$, one needs, therefore, several important parameters: the level density, the Coulomb barrier and the inverse cross section. Below, we discuss them in more details.

2.1.1. Level density

The total level density used in Eq. (1) is calculated as the product of the intrinsic level density $\rho_{in}(E)$ and the vibrational and rotational enhancement factors, $K_{vib}(E_{corr})$ and $K_{rot}(E_{corr})$, respectively [28]:

$$\rho(E) = \rho_{in}(E)\cdot K_{vib}(E)\cdot K_{rot}(E). \qquad (2)$$

The intrinsic density of excited states, ρ_{in}, is calculated with the well-known Fermi-gas formula:

$$\rho_{in}(E) = \frac{\sqrt{\pi}}{12}\frac{\exp(S)}{\tilde{a}^{1/4}E_{eff}^{\ 5/4}}, \qquad (3)$$

with the exponent S:

$$S = 2 \cdot \sqrt{\tilde{a} \cdot E_{corr}} = 2 \cdot \sqrt{\tilde{a} \cdot \left(E_{eff} + \delta U \cdot k\left(E_{eff}\right) + \delta P \cdot h\left(E_{eff}\right)\right)}, \quad (4)$$

and the asymptotic level-density parameter $\tilde{a}$ as given in Ref. [18]:

$$\tilde{a} = 0.073 \cdot A + 0.095 \cdot B_S \cdot A^{2/3}, \quad (5)$$

where A is the mass of the nucleus, and B_s is the ratio between the surface of the deformed nucleus and a spherical nucleus. δU is the shell-correction energy, which is for the ground state calculated according to Ref. [29]. At the fission saddle point, the shell-correction energy is assumed to be negligible [30,31]. The function $k(E_{eff})$ describes the damping of the shell effect with excitation energy, and is calculated according to Ref. [18] as $k(E_{eff}) = 1 - \exp(-\gamma E_{eff})$, with the parameter γ determined by $\gamma = \tilde{a} / (0.4 \cdot A^{4/3})$ [32].

The parameter δP of equation (4), which is identical to the pairing condensation energy in odd-odd nuclei, is calculated as:

$$\delta P = -\frac{1}{4} \cdot \Delta^2 \cdot g + 2 \cdot \Delta, \quad (6)$$

with an average pairing gap $\Delta = 12 / \sqrt{A}$, and the single-particle level density at the Fermi energy $g = 6 \cdot \tilde{a} / \pi^2$. The function $h(E_{eff})$ parameterises the superfluid phase transition [33] at the critical energy $E_{crit} = 10$ MeV [34]:

$$h(E_{eff}) = \begin{cases} 1 - \left(1 - \dfrac{E_{eff}}{E_{crit}}\right)^2, & E_{eff} < E_{crit} \\ 1, & E_{eff} > E_{crit} \end{cases}. \quad (7)$$

The effective energy E_{eff} is shifted with respect to the excitation energy E to accommodate for the different energies of even-even, odd-mass, and odd-odd nuclei:

$E_{eff} = E$ odd Z – odd N

$E_{eff} = E - \Delta$ odd A

$E_{eff} = E - 2\Delta$ even Z – even N.

In order to calculate the intrinsic level density at very low excitation energies, we switch from the Fermi-gas level density to the constant-temperature level density [35]. The calculation is based on the work performed in Ref. [36], where the values of the parameters of the constant-temperature level density approach were obtained from the simultaneous analysis of the neutron resonances and the low-lying levels in the framework of the Gilbert-Cameron approach [35].

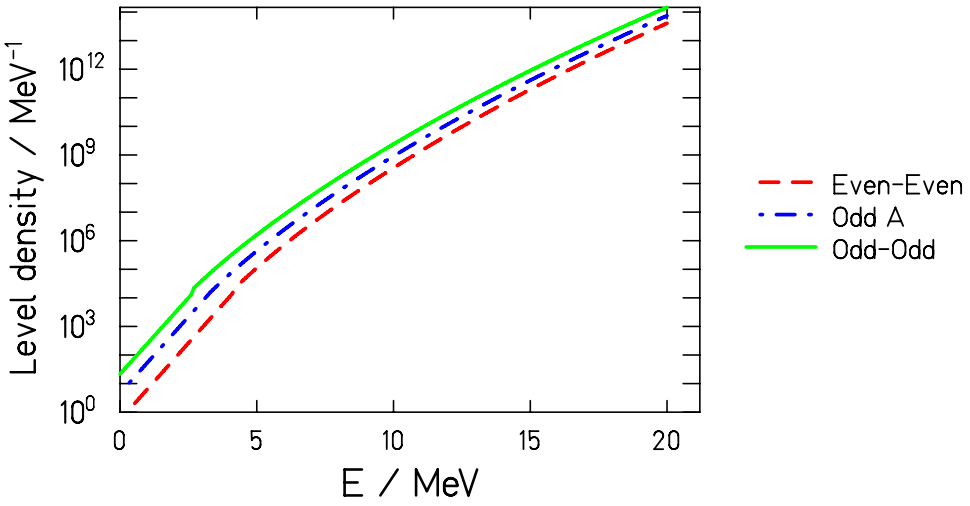

Fig. 1. Intrinsic level density $\rho_{in}(E)$ for three nuclei – ^{242}Cf, ^{241}Bk and ^{240}Bk – calculated in ABLA07 using combined Fermi-gas – constant-temperature level density approach.

As it was shown in Ref. [19], collective excitations can contribute considerably to the total nuclear level density. In deformed nuclei, the most important contribution to the collective enhancement of the level density originates from rotational bands, while in spherical nuclei the collective enhancement is caused by vibrational excitations.

In ABLA07, the contribution of collective excitations to the level density is described in the following way (for more details, see Ref. [19]): For nuclei with a quadrupole deformation $|\beta_2|$ > 0.15, the rotational enhancement factor $K_{rot}(E_{corr})$ is calculated in terms of the spin-cutoff parameter $\sigma_\perp$:

$$K_{rot}(E_{corr}) = \begin{cases} \left(\sigma_\perp^2 - 1\right)\cdot f(E_{corr}) + 1, & \sigma_\perp^2 > 1 \\ 1, & \sigma_\perp^2 < 1 \end{cases} \tag{8}$$

$$\sigma_\perp^2 = \frac{\Im_\perp \cdot T}{\hbar^2}, \quad f\left(E_{corr}\right) = \left(1 + \exp\left(\frac{E_{corr} - E_c}{d_c}\right)\right)^{-1}, \tag{8a}$$

where E_{corr} is defined in Eq. (4), $\Im_\perp = \frac{2}{5} m_0 \cdot A \cdot R^2\left(1 + \beta_2 / 3\right)$ is the rigid-body moment of inertia perpendicular to the symmetry axis, and m_0 is the mass unit. The ground-state quadrupole deformation β_2 is taken from the finite-range liquid-drop model including microscopic corrections [29], while the saddle-point deformation is taken from the liquid-drop model as given in Ref. [37]. The damping of the collective modes with increasing excitation energy is described by a Fermi function $f(E)$ with parameters E_c = 40 MeV and d_c = 10 MeV. The vibrational enhancement for spherical nuclei is generally smaller than the rotational enhancement for deformed nuclei. For nuclei with a quadrupole deformation $|\beta_2|$ < 0.15, the vibrational enhancement factor is calculated by using the same formula as for the rotational enhancement (Eq. (8)), but with the spin-cutoff parameter which is, in order to simulate the vibrational motion, calculated assuming irrotational flow: $\sigma'^2_\perp = 70 \cdot \beta_{eff}^2 \cdot \sigma_\perp^2$, where $\sigma_\perp$ is

given by Eq. (8a), and β_{eff} is a dynamical deformation parameter: $\beta_{eff} = 0.022 + 0.003 \cdot \Delta N + 0.005 \cdot \Delta Z$; ΔN and ΔZ are the absolute values of the number of neutrons and protons, respectively, above or below the nearest shell closure.

2.1.2 Influence of angular momentum

In the standard Weisskopf-Ewing approach, the change of angular momentum in the evaporation process due to particle emission is not treated. To overcome this limitation, we have developed a dedicated formalism, which calculates the distribution of orbital angular momentum in the emission of nucleons and fragments from excited nuclei with finite angular momentum.

The emitting (mother) nucleus with mass number A_m has the angular momentum l_m and the excitation energy E_m^*. After the emission of a fragment with mass number A_f, separation energy S_f , kinetic energy K_f, excitation energy E_f^* and angular momentum l_f , the daughter nucleus with mass number A_d, angular momentum l_d and excitation energy E_d^* is formed.

In the classical approximation, the probability for the emission of the fragment with a given orbital angular momentum is determined by the phase space available for the daughter nucleus and the fragment after the fragment emission. Due to energy conservation, we have the following relation:

$$E_d^* + E_f^* = E_m^* + E_m^{rot} - E_d^{rot} - E_f^{rot} - E_{orb} - S_f \,. \tag{9}$$

Here, only E_d^{rot} , E_f^{rot} and E_{orb} depend on the orbital angular momentum of the fragment. The optimum combination of final intrinsic and orbital angular momentum is defined by the collinear combination of the angular momenta:

$$| l_{orb} | = | l_m | - | (l_d + l_f) | ,$$

which leads to the final configuration with the largest number of states in the final nucleus.

The number of final states is approximately given by:

$$\rho \propto (l_d + l_f) \cdot \exp\left(2 \cdot \sqrt{a\left(E_m^* - S_f - \frac{{l_{orb}}^2}{2\Theta_{orb}} - \frac{(l_d + l_f)^2}{2\Theta_m} \right)} \right). \tag{10}$$

Renaming $(l_d + l_f) = l_{final}$, we get

$$\ln(\rho) \propto \ln(l_{final}) + 2 \cdot \sqrt{a\left(E_m^* - S_f - \frac{{l_{orb}}^2}{2\Theta_{orb}} - \left(\frac{{l_m}^2 - 2 l_m l_{orb} + {l_{orb}}^2}{2\Theta_m} \right) \right)} \tag{11}$$

- *The most probable value of the orbital momentum:*

To obtain the most probable value of l_{orb} we search for the maximum of the function in Eq. (11). The full distribution given by Eq. (11) is well approximated by a Gaussian function, whose width is related to the second derivative of the distribution in (11).

For relativistic nucleus-nucleus and nucleon-nucleus collisions, mostly considered here, the value of l_{final} is expected to be very close to l_m. This is why we expand the above function around l_m:

$$\ln\left(\rho_{approx}\right) \propto \frac{l_{orb}}{l_m} + 2\cdot\sqrt{S_4}\cdot\left(1 - \frac{a}{2\cdot S_4}\left(\frac{{l_{orb}}^2}{2\Theta_{orb}} - \frac{l_m l_{orb}}{\Theta_m} + \frac{{l_{orb}}^2}{2\Theta_m}\right)\right),$$

with $S_4 = a\left(E_m^* - S_f - \frac{{l_m}^2}{2\Theta_m}\right)$, which does not depend on l_{orb}.

Since $\Theta_m >> \Theta_{orb}$, we can approximate:

$$\ln\left(\rho_{approx}\right) \propto \frac{l_{orb}}{l_m} + 2\cdot\sqrt{S_4}\cdot\left(1 - \frac{a}{2\cdot S_4}\left(\frac{{l_{orb}}^2}{2\Theta_{orb}} - \frac{l_m l_{orb}}{\Theta_m}\right)\right).$$

The maximum of this function is given by requiring the first derivative to be zero:

$$\frac{1}{l_m} - \frac{2\sqrt{S_4}}{2}\frac{a}{2}\frac{2l_{orb}}{S_4\Theta_{orb}} + \frac{2\sqrt{S_4}}{2}\frac{a l_m}{S_4\Theta_m} = 0$$

or

$$\frac{1}{l_m} - \frac{a}{\sqrt{S_4}}\frac{l_{orb}}{\Theta_{orb}} + \frac{a}{\sqrt{S_4}}\frac{l_m}{\Theta_m} = \frac{1}{l_m} - \frac{a}{\sqrt{S_4}}\left(\frac{l_{orb}}{\Theta_{orb}} - \frac{l_m}{\Theta_m}\right) = 0$$

From this we determine the optimum value of l_{orb}:

$$l_{orb} = \Theta_{orb}\cdot\left(\frac{l_m}{\Theta_m} + \frac{\sqrt{S_4}}{a}\cdot\frac{1}{l_m}\right) \tag{12}$$

The values of Θ_m and Θ_{orb} can be estimated as follows:

$$\Theta_m = \frac{2}{5}m_0 A_m r^2 = \frac{2}{5}m_0 {r_0}^2 A_m^{5/3}$$

$$\Theta_{orb} = m_0\left(A_1{d_1}^2 + A_2{d_2}^2\right) = m_0\left(A_1\left(\frac{A_2}{A_m}d\right)^2 + A_2\left(\frac{A_1}{A_m}d\right)^2\right) = m_0\left(\frac{d}{A_m}\right)^2\left({A_1}^2 A_2 + A_1{A_2}^2\right)$$

with $d = r_0\left(A_1^{1/3} + A_2^{1/3}\right)$ in the touching-sphere configuration.

- *The width of the orbital-momentum distribution:*

To estimate the width of the orbital-momentum distribution in one evaporation step, we first write down the second derivative of ln(ρ):

$$\frac{\partial^2(\ln\rho)}{\partial l_{orb}^2} = \frac{a}{\sqrt{S_4}\cdot\Theta_{orb}} .$$

From this we conclude that the orbital-momentum distribution can be approximated by Gaussian with the standard deviation:

$$\sigma = \sqrt{\frac{\sqrt{S_4}\Theta_{orb}}{a}} . \tag{13}$$

In an evaporation code, the emission of a particle induces a change in angular momentum of the mother nucleus. This change is calculated by randomly picking the angular-momentum value from a Gaussian distribution with the mean value l_{orb} (Eq. (12)) and the standard deviation σ (Eq.(13)).

The most severe approximation in the above consideration is the restriction to collinear angular momenta in the evaporation process. This approximation is most crucial for the estimation of the widths of the orbital angular-momentum distribution, which may be underestimated. However, the most important value for the evaporation process is the most probable orbital angular momentum, which is only little affected, due to the dominant influence of the strong energy dependence of the level density.

2.1.3. Inverse cross sections

In calculating the inverse cross section for the emission of particles one has to consider several effects: The existence of the Coulomb barrier for charged particles (especially at low energy), the tunnelling through it (especially for light particles), and the energy-dependent quantum-mechanical cross section.

At energies well above the Coulomb barrier the shape of the barrier does not play any role. σ_c is then calculated without taking into account the tunnelling:

$$\sigma_c(\varepsilon_\nu) = \pi\cdot R^2\cdot\left(1-\frac{B_\nu}{\varepsilon_\nu}\right), \quad R = R_{geom} + R_\lambda \tag{14}$$

$$R_{geom} = 1.16\cdot\left(A_1^{1/3} + A_2^{1/3}\right), \quad \text{and} \quad R_\lambda = \sqrt{\frac{\hbar^2}{2\cdot\mu\cdot E_{cm}}} ,$$

where μ is the relative mass (= $M_1 \cdot M_2/(M_1+M_2)$) and $E_{cm} = \varepsilon_\nu \cdot (A_1-A_2)/A_1$. R_λ is obtained for the square-well potential and is responsible for the dependence of the capture cross section on the particle energy[2].

[2] For low particle kinetic energy the wavelength associated to the particle becomes comparable to the nuclear dimensions, which results in the dependence of the cross section on particle energy.

2.1.4. Barriers for charged-particle emission

To calculate the Coulomb barrier, we use the nuclear potential for $l = 0$ ($V(r) = V_N(r) + V_C(r)$) and then numerically search for the position of the maximum that corresponds to the barrier.

- *The empirical nuclear potential of R. Bass* [38,39]:

$$-V_N(s) = \frac{C_1 \cdot C_2}{C_1 + C_2} \cdot \frac{1}{A \cdot \exp\left(\frac{s}{d_1}\right) + B \cdot \exp\left(\frac{s}{d_2}\right)}, \tag{15}$$

with the parameters:

$A = 0.333$ MeV^{-1} fm, $B = 0.007$ MeV^{-1} fm,

$d_1 = 3.5$ fm, $d_2 = 0.65$ fm.

C_1 and C_2 are the half-density radii of the daughter nucleus and emitted particle, respectively, calculated as:

$$C_i = R_i \cdot \left(1 - \frac{(0.9984\text{fm})^2}{R_i^2}\right), \quad R_1 = \left(1.28 \cdot A_f^{1/3} - 0.76 + \frac{0.8}{A_f^{1/3}}\right)\text{fm},$$

$$R_2 = \left(1.28 \cdot A_2^{1/3} - 0.76 + \frac{0.8}{A_2^{1/3}} + d\right)\text{fm}, \quad d = \begin{cases} 3\text{ fm}, & 1\text{H} \\ 0\text{ fm}, & 2\text{H} \\ 0\text{ fm}, & 3\text{H} \\ 0\text{ fm}, & 3\text{He} \\ 1\text{ fm}, & 4\text{He} \end{cases}.$$

The variable $s = r - C_1 - C_2$ gives the distance between the two surfaces based on half-density radii.

- *Coulomb potential* [39]:

$$V_C = \begin{cases} 1.44 \cdot \dfrac{Z_1 \cdot Z_2}{r}, & r > R_C \\ 1.44 \cdot \dfrac{Z_1 \cdot Z_2}{2 \cdot R_C} \cdot \left(3 - \dfrac{r^2}{R_C^2}\right) & r \le R_C \end{cases}, \text{ with } R_C = 1.3 \cdot \left(A_1^{1/3} + A_2^{1/3}\right) \text{ fm}. \tag{16}$$

Please note that inclusion of Eqs. (14-16) into the expression (1) for the particle decay width implies the use of numerical tools for solving the integral in Eq. (1) which can considerably increase the computational time. In order to overcome this problem, we have approximated the integrand in the Eq. (1) with a function, which allows us to analytically solve the integral. Details are given in Annex B.

2.1.5. Tunnelling through the barrier

At energies below and just above the Coulomb barrier, the tunnelling of charged particles through the barrier plays an important role, and, consequently, the expression for the inverse

cross section given by Eq. (14) is not any more applicable. In order to incorporate the effect of the tunnelling through the potential barrier, we follow the work done by Avishai in Ref. [40]. He considered two different energy ranges for calculating the inverse cross sections:

- *Energy below the Coulomb barrier:*

Avishai [40] showed that the nucleus-nucleus fusion cross section at sub-barrier energies can be predicted by the simple theory of Wong based on the barrier-penetration technique [41], where it is assumed that the reaction occurs whenever the two nuclei have penetrated through the potential barrier. For every angular momentum, i.e. every impact parameter, the penetration probability can be calculated by the Hill-Wheeler formula [42], after approximating the shape of the barrier by an inverted (half) parabola plus a Coulomb slope (V~1/r).

If R_l is the position of the top of the barrier, E_l is the value of the effective interaction at its maximum and $\hbar\omega_L$ the curvature, the transmission coefficient for angular momentum l can be calculated as:

$$P(l,\varepsilon_\nu)=\left\{1+\exp\left[\pi\cdot\frac{E_l-\varepsilon_\nu}{\hbar\omega_l}+C(\varepsilon_\nu)\right]\right\}^{-1}. \tag{17}$$

C(E) express the penetration through the Coulomb part. Once the penetration coefficients of Eq. (17) are summed over all the possible angular momenta, one obtains the inverse cross section:

$$\sigma(\varepsilon_\nu)=\frac{\hbar\omega_{l=0}R_0^2}{2\varepsilon_\nu}\cdot\ln\left(1+\exp\left(\pi\cdot\frac{\varepsilon_\nu-E_{l=0}}{\hbar\omega_{l=0}}-C(\varepsilon_\nu)\right)\right). \tag{18}$$

- *Energy just above the Coulomb barrier:*

When the energy is just above the barrier, Avishai's formulation reduces to Wong's prediction [41] in which the barrier is assumed to have the form of an inverted (full) parabola. The cross section is in this case not so much affected by the Coulomb slope and the calculation of the tunnelling only through the (full) parabola gives a satisfactory result:

$$\sigma(\varepsilon_\nu)=\frac{\hbar\omega_{l=0}R_0^2}{2\varepsilon_\nu}\cdot\ln\left(1+\exp\left(2\pi\cdot\frac{\varepsilon_\nu-E_{l=0}}{\hbar\omega_{l=0}}\right)\right). \tag{19}$$

Again, inclusion of expressions (18-19) into Eq. (1) would imply the use of numerical tools for solving the integral. To overcome this problem, in ABLA07 the effect of tunnelling on the particle decay width has been determined by fitting the numerical results of a complete calculation with the Avishei formula for the transmission coefficients: Firstly, the numerical solution of Eq. (1) is obtained without considering the tunnelling, resulting in the so-called classical decay width Γ_{class}. In the second step, Eq. (1) is integrated numerically with taking the tunnelling into account; this results in the so-called exact particle decay width Γ_{exact}. The ratio Γ_{exact} / Γ_{class} is shown in Fig. 2 for several different systems. This ratio is then fitted, and the obtained fitting function $f(E_f, A_f, A_\nu, V)$ is used in ABLA07, so that the exact solution of Eq. (1) can be approximated by $\Gamma_{ABLA} = f(E_f, A_f, A_\nu, V)\cdot\Gamma_{class}$.

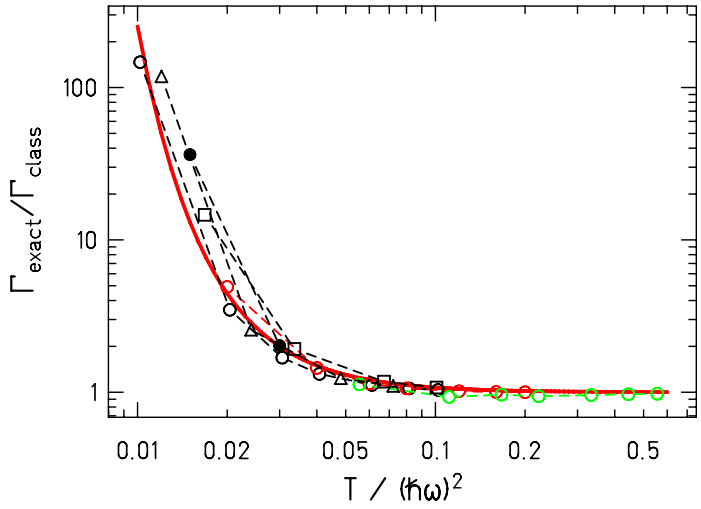

Fig. 2. Enhancement of the particle decay width due to tunnelling through the potential barrier for different particles and emitting systems (different symbols) together with a functional form given by Eq. (17) (full red line).

The function $f(E_f, A_f, A_v, V)$ that fits best the ratio $\Gamma_{exact} / \Gamma_{class}$ has the following form:

$$f(E_f, A_f, A_v, V) = 10^{\left(4\cdot10^{-4}\cdot x^{-\frac{4.3}{\ln(10)}}\right)} \quad \text{with} \quad x = \left(\frac{T}{(\hbar\omega)^2}\frac{1}{\mu^{1/4}}\right), \tag{20}$$

where x is the ratio between the temperature (T) of the daughter nucleus (A_f) and the energy ($\hbar\omega$) of the inverse parabola at the potential barrier (V), divided by the forth root of the reduced mass (μ) of the system. $\hbar\omega$ is calculated from the second derivative of the potential given in Section II.1.4.

2.1.6. Expansion

In order to correctly describe the de-excitation of a heated nucleus, changes in the nuclear density of the compound nucleus with thermal energy have to be considered. A nucleus tends to expand when it is heated, until it reaches a status of thermal equilibrium, where the level density is maximal for the given total excitation energy. The increase of volume has three possible consequences which may affect the following de-excitation process: Firstly, it lowers the Coulomb barrier. Secondly, it changes the level density of the compound nucleus. Thirdly, and most important, the nucleus can enter the region of spinodal instabilities. In this section we discuss the first and second aspects, while the third aspect will be discussed in section III.

The radius of the expanded nucleus is derived from the analytical expression for the density at thermal equilibrium presented in Ref. [24]. There, the decrease of the density, ρ_{eq}/ρ_o, relatively to the normal density of the nucleus, is calculated according to the following formula:

$$\frac{\rho_{eq}}{\rho_o} = \frac{1}{4}\cdot\left(1+\sqrt{9-8\frac{\varepsilon^*_{tot}}{\varepsilon_b}}\right), \tag{21}$$

where $\varepsilon^*_{tot} = E^*_{tot} / A$ is the excitation energy per nucleon (E^*_{tot} is the total excitation energy of the system of mass number A) and ε_b is the ground-state binding energy per nucleon of the system. Assuming a spherical nucleus, we obtain the relative increase of the radius, r_{eq} / r_o, due to thermal expansion:

$$\frac{r_{eq}}{r_o} = \left(\frac{1}{4} \cdot \left(1 + \sqrt{9 - 8\frac{\varepsilon^*_{tot}}{\varepsilon_b}} \right) \right)^{-\frac{1}{3}}, \tag{22}$$

The elongated nuclear radius at thermal equilibrium is used to calculate the nuclear potential (using the empirical formula of Bass [38]), and, finally the reduced Coulomb barrier.

The second effect of the thermal expansion is to change the level density. The level density is related to the thermal energy through the level density parameter, a. The dependence of a on the nuclear matter density is given by the Fermi-gas model:

$$\frac{a_{eq}}{a_o} = \left(\frac{r_{eq}}{r_o} \right)^2 . \tag{23}$$

In Ref. [24] it is demonstrated that the above equation can apply for finite nuclei; specifically:

$$\frac{\tilde{a}_{eq}}{\tilde{a}_o} = \left(\frac{r_{eq}}{r_o} \right)^2 . \tag{24}$$

In reality, we do not make use of the above formula (24) in ABLA07. Since the deexcitation cascade is ruled by the decay widths, which in turn depend on the relative weight of the level densities of the mother and daughter nuclei, the change on the density of levels due to thermal expansion will not reflect perceptibly on the decay widths. This is particularly true for heavy nuclei – where the difference in level density between mother and daughter is minimal – and at high excitation energy – where the density of levels is anyhow very high. For this reason, the effect of thermal expansion on the level density is not considered in ABLA07.

As an example of ideas described in the above sections, we show in Fig. 3 a comparison between calculated and measured production cross sections of ^{3}He and ^{4}He in proton-induced reaction on ^{56}Fe at several proton-beam energies. Calculations show only the contribution of the particle emission from the thermalised system, i.e. no production from the first stage of interaction (e.g. intra-nuclear cascade) is included.

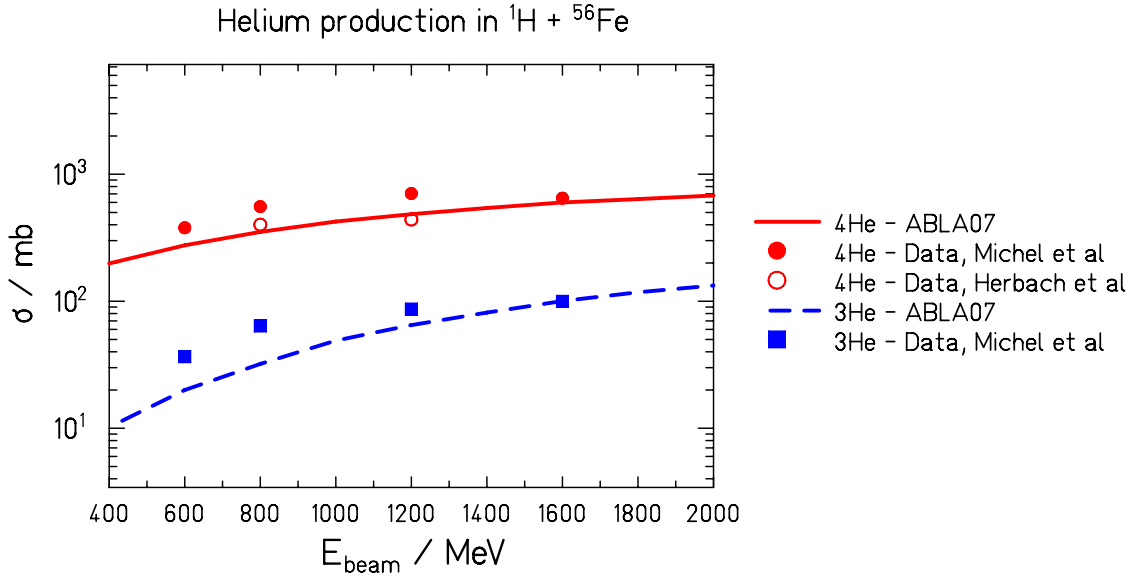

Fig. 3. Comparison between measured and calculated production cross sections of ^{3}He and ^{4}He – full (^{4}He) and dashed (^{3}He) lines: ABLA07 predictions; dots (^{4}He) and squares (^{3}He): data from Refs. [43,44]. Please note, that in the calculated cross sections no contribution from the first stage of the reaction is taken into account.

2.1.7. Kinetic-energy spectra

The kinetic energy of the emitted particle in the frame of the emitting source is sampled from the Maxwell-Boltzmann distribution at the corresponding temperature taking into account the effects of the Coulomb barrier for charged particles.

For generating random numbers following others than a rectangular function, different techniques are available. The option which is fastest in the application is based on the integration and the inversion of the function. In case of Maxwell distributions this procedure cannot be performed analytically, and usually one is performing this operation numerically, which has of course consequences on the computing time. To avoid this problem, we use in ABLA07 an appropriate random generator by a folding method. We demonstrate the procedure on the example of the Maxwellian energy distribution:

$$\frac{dI_{Maxwell}}{dE} \propto E \cdot e^{-E/T} . \tag{25}$$

The intensity I is given as the product of the energy E and an exponential decrease with a slope given by the temperature T.

A random generator for the exponential function

$$\frac{dI_{\exp}}{dE} = e^{-E/T}$$

is readily given by:

$$E_i = -T \cdot \ln(PRN),$$

where *PRN* is pseudo-random generator that produce numbers in the interval I={0,1} with uniform probability.

The Maxwell distribution can be obtained by the following folding expression of two exponential distributions:

$$\frac{dI_{Maxwell}}{dE} \propto \int_0^E e^{-\varepsilon/T} \cdot e^{-(E-\varepsilon)/T} d\varepsilon = e^{-E/T} \int_0^E d\varepsilon = E \cdot e^{-E/T}$$

Consequently, a random generator for the Maxwell distribution can be constructed by adding the results of two independent calls of the exponential random generator:

$$E_i = -T[\ln(PRN) + \ln(PRN)]. \tag{26}$$

In case of charged particles one has also to consider the influence of the Coulomb barrier. In this case, the Eq. (25) is read as:

$$\frac{dI_{Maxwell}}{dE} \propto \frac{E^2}{E+B} \cdot e^{-E/T}. \tag{27}$$

Due to the factor *(E+B)* in Eq. (27), one cannot obtain an exact formulation of the random number generator. In this case, we introduce an approximation: We start from the function:

$$dI/dE \propto E^2 \cdot e^{-E/T}, \tag{28}$$

for which one can obtain an exact formulation. The modification introduced by the additional Coulomb term (*B*+*x*) in Eq. (27) is small when *T*<*B*, and in this case Eqs. (27) and (28) are very close to each other. The difference between these two functions becomes more important for larger values of *T*/*B*, which is not often the case as the Coulomb barriers for light-charged particles are in most of the cases ~ 5 – 10 MeV.

For the function given by Eq. (28), according to the same ideas leading from Eq. (25) to Eq. (26) one obtains as the exact formulation the following expression:

$$E_i = -T(\ln(PRN) + \ln(PRN) + \ln(PRN)). \tag{29}$$

The same form can then be used for creating the spectra according to Eq. (27). Please note, that the logarithmic slope of the high-energy tail is correctly reproduced by this event generator.

In order to realistically calculate particle kinetic-energy spectra, functional forms given by Eqs. (25) and (27) have to be corrected for the quantum-mechanical effects at low particle kinetic energies, which lead to an additional factor proportional to $1/\upsilon$, where υ is the particle velocity [45]. In this case, Eqs. (25) and (27) have the following forms:

$$\frac{dI}{dE} \propto \begin{cases} \sqrt{E} \cdot \exp\left(-\frac{E}{T}\right), & \text{neutrons} \\ \frac{E^{3/2}}{E+B} \cdot \exp\left(-\frac{E}{T}\right), & \text{charged particles} \end{cases} \cdot \tag{30}$$

For these two functions, one cannot get exact formulations of the random-number generator, but similar as in case of Eq. (27) an approximation, which enables fast calculations of kinetic energy spectra:

$$E_i = \begin{cases} 2 \cdot T \cdot \sqrt{\ln(PRN) \cdot \ln(PRN)}, & \text{neutrons} \\ 3 \cdot \mathrm{T} \cdot \left(-\ln(\mathrm{PRN}) \cdot \ln(PRN) \cdot \ln(PRN)\right)^{1/3}, & \text{charged particles} \end{cases} . \tag{31}$$

Equation (31) is then used for obtaining the kinetic energies of emitted particles. In Fig. 4, a comparison between neutron and proton kinetic-energy spectra calculated according to Eqs. (30) and (31) is shown.

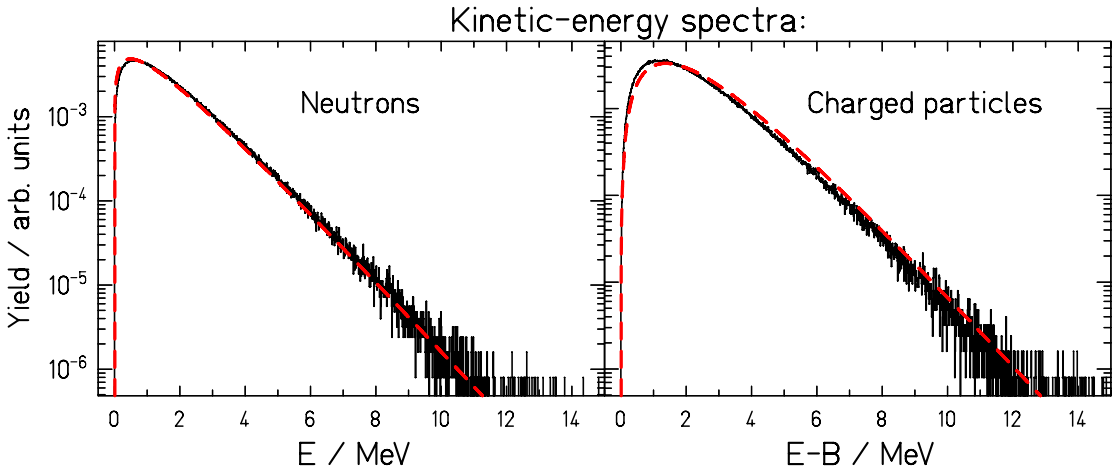

Fig. 4. Comparison between analytical functions specified by Eq. (30) (dashed line) and the corresponding random generators specified by Eq. (31) (full histogram). The parameters are T = 1 MeV and B = 10 MeV.

After determining the kinetic energy of the emitted particle, its velocity vector is determined assuming isotropic emission[3] in the frame of the emitting source. Using this information, at every de-excitation step the recoil of the excited nucleus due to particle emission is then calculated.

2.2. Gamma emission

In several evaporation codes, γ-radiation is not included as a possible channel, because the particle decay channels dominate above the particle-emission threshold. However, in the last de-excitation step of the evaporation cascade, gamma emission becomes competitive to particle decay for heavy compound nuclei. Normally, the emission of gammas is much less probable than the particle decay (about 10^5 times less favourable). Since the level density

[3] This approximation is valid for moderate angular momentum or high excitation energies.

depends on the mass (heavier nuclei have denser energy levels) the number of levels between the ground state and the particle separation energy of a heavy nucleus can be as high as 10^5 or even exceed this value. If the excitation energy of the compound nucleus is slightly higher than its particle separation energy, it can decay only into the ground state or into the first excited states of the daughter nucleus (if the daughter nucleus is an even-even nucleus, then only the ground state is energetically accessible due to the pairing gap – see Ref. [46] for a wider discussion). In this situation, gamma emission and particle decay can become two competitive channels.

As the emission of statistical γ-rays occurs predominantly via the giant dipole resonance, the γ-radiation rate can be calculated according to Ref. [36] as:

$$\Gamma_\gamma(E) = \sum_{I=|J-1|}^{J+1} \int_0^E \varepsilon_\gamma^3 \cdot k(\varepsilon_\gamma) \cdot \frac{\rho(E-\varepsilon_y, I)}{\rho(E, I)} d\varepsilon_\gamma \quad , \tag{32}$$

where E is the excitation energy of the mother nucleus and $k(\varepsilon_\gamma)$ is the radiative strength function for a dipole electric transition. As already said, for high excitation energy the probability for γ emission is negligible compared to the probability for particle emission and it becomes important only at the energies around and below the particle separation energies. As indicated in Ref. [36], taking $E = S_n$, and using the power approximations for the radiative strength function [47] and the constant temperature model [36], equation (32) can be parameterised as:

$$\Gamma_\gamma(S_n) = 0.624 \cdot 10^{-9} \cdot A^{1.60} \cdot T^5 \,\mathrm{MeV}, \tag{33}$$

where A is the mass of a mother nucleus and T is the nuclear-temperature parameter of the constant-temperature model [36].

The effects of gamma decay are especially visible in the strength of the even-odd staggering of the final products [46]. As an example, the production cross sections of different isotopes of $_{71}$Lu in the reaction ^{208}Pb (1A GeV) + ^{1}H are shown in Fig. 5. The experimental data from [48] are shown as full dots and compared with two sets of calculation: without including γ emission (open squares) and with including it (open triangles). One can observe that the γ competition tends to reduce the even-odd structure in the isotope cross sections to a great extent.

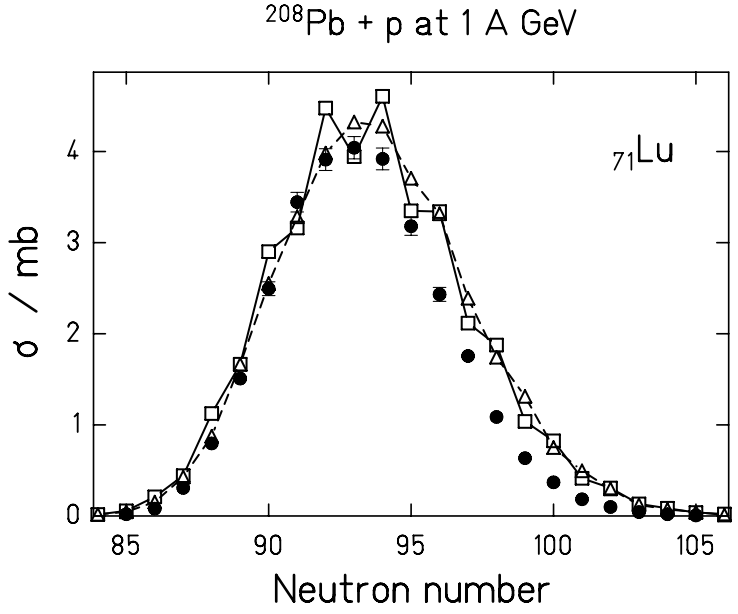

Fig. 5. Production cross sections of the isotopes of lutetium produced in the reaction ^{208}Pb+H at 1 A GeV, calculated with the statistical code ABRABLA with (Δ) and without (□) the inclusion of the γ-radiation decay channel, and compared to the experimental data (●) from Ref. [48]. The errors on the experimental data are shown only if the error bars are larger than the symbol size.

2.3. Fission

Fission plays an important role in the decay of heavy nuclei. At each de-excitation step a competition between fission and other decay channels is calculated. The fission decay width is calculated in a time-dependent approach as developed in Refs. [21,25,26]. If fission occurs, the ABLA07 code calls a program called PROFI where masses, atomic charges, excitation energies and velocities of two fission fragments are calculated. In the PROFI code, only binary fission is considered. The original version of the PROFI model has been published in Refs. [49,50]; recent developments and improvements are given in Refs. [51,52].

2.3.1. Time-dependent fission width

The modelling of the fission decay width at high excitation energies requires the treatment of the evolution of the fission degree of freedom as a diffusion process, determined by the interaction of the fission collective degree of freedom with the heat bath formed by the individual nucleons [53,4]. Such process can be described by the Fokker-Planck equation (FPE) [54], where the variable is the time-dependent probability distribution $W(x, p; t, \beta)$ as a function of the deformation in fission direction x and its canonically conjugate momentum p. The parameter β is the reduced dissipation coefficient. The solution of the FPE leads to a time-dependent fission width $\Gamma_f(t)$. However, these numerical calculations are too much time consuming to be used in nuclear-reaction codes.

To avoid this problem, an analytical approximation to the solution of the one-dimensional Fokker-Planck equation for the time-dependent fission-decay width for the initial condition of a Gaussian distribution centred at the spherical shape has been developed in Refs. [25,26]. The mean values and the widths of the initial Gaussian distributions in space and momentum

are given by the entrance channel. In this approximation, the time dependence of the fission width is expressed as [25,26]:

$$\Gamma_f(t) = K \cdot \Gamma_{BW} \cdot \frac{W_n(x = x_b; t, \beta)}{W_n(x = x_b; t \to \infty, \beta)}, \tag{34}$$

where $K = \left[1 + (\beta/(2\omega_0))^2\right]^{1/2} - \beta/(2\omega_0)$ is the Kramers factor [53] with ω_0 corresponding to the frequency of the harmonic oscillator describing the potential at the saddle-point deformation and β is the reduced dissipation coefficient. In the above equation, Γ_{BW} is the fission width given by the statistical approach of Bohr and Wheeler [55] and *Wn(x=xb;t,β)* is the normalized probability distribution at the saddle-point deformation x_b.. The saddle-point deformations are calculated according to Ref. [56].

In case of a nuclear potential approximated by a parabola, the solution of the Fokker-Planck equation for the probability distribution *W(x=x_b;t,β)* at the saddle-point deformation has a Gaussian form with a time-dependent width. For a special case of initial conditions, namely zero mean deformation and zero mean velocity, this solution has the following form [57]:

$$W_n(x = x_b; t, \beta) = \frac{1}{\sqrt{2\pi}\sigma} \cdot \exp\left(-\frac{x_b^2}{2\sigma^2}\right), \tag{35}$$

with σ^2 given as [57]:

$$\sigma^2 = \frac{\mathrm{kT}}{\mu\omega_1^2}\left\{1 - \exp(-\beta \cdot \mathrm{t}) \cdot \left[\frac{2\beta^2}{\beta_1^2}\sinh^2\left(\frac{1}{2}\beta_1 \mathrm{t}\right) + \frac{\beta}{\beta_1}\sinh(\beta_1 \mathrm{t}) + 1\right]\right\}, \tag{36}$$

where k is Boltzmann´s constant, T is the nuclear temperature, μ is the reduced mass associated to the deformation degree of freedom, ω_1 describes the curvature of the potential at the ground state and $\beta_1 = (\beta^2 - 4\omega_1^2)^{1/2}$.

Due to the classical nature of the Fokker-Planck equation, the initial behaviour predicted by this solution is wrong since for $t = 0$ equation (36) leads to $\sigma = 0$. Therefore, in Refs. [25,26] the zero-point motion at the spherical shape has been chosen as the initial condition of the problem. The zero-point motion is taken into account by shifting the time scale $t \to t + t_0$ in Eq. (36) by a certain amount t_0, where t_0 is the time needed for the probability distribution to reach the width of the zero-point motion in deformation space. The value of t_0 is calculated as [21]:

$$t_0 = \frac{1}{\beta}\ln\left(\frac{2T}{2T - \hbar\omega_1}\right), \text{ in the under-damped regime } (\beta < 2\omega_1), \text{ and}$$

(37)

$$t_0 = \frac{\hbar\beta}{4\omega_1 T}, \text{ in the over-dumped regime } (\beta \geq 2\omega_1).$$

In Fig. 6 a comparison between the numerical solution of the one-dimensional Langevin equation of motion (full histogram) and the analytical approximation for case of ^{248}Cf starting

from spherical initial conditions is shown. The agreement between these two solutions is very satisfactory. For more details, see [25,26].

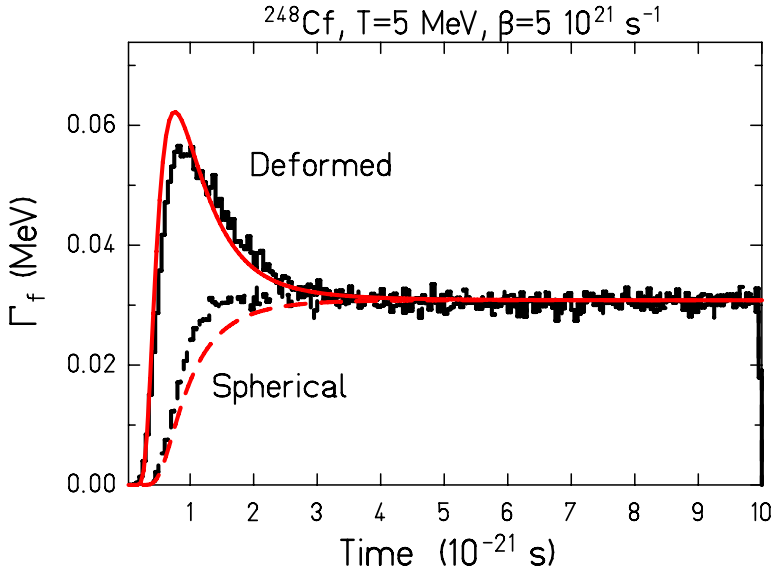

Fig. 6. Time-dependent fission decay width $\Gamma_f(t)$ as obtained from the solution of the one-dimensional Langevin equation of motion (histograms) assuming that the excited ^{248}Cf system starts from either a spherical ($\beta_2=0$) or a deformed ($\beta_2=0.235$) configuration. Dashed and full lines correspond to the result obtained with the described analytical approximations for spherical [25,26] and deformed [59] initial conditions, respectively. The figure shows the case T=5 MeV and $\beta = 5 \cdot 10^{21} s^{-1}$.

By introducing the time-dependent fission decay width, the ABLA07 code can be considered as a dynamical code with the explicit treatment of the system time evolution. Technical details on the inclusion of the time evolution are given in the Appendix 1 of Ref. [26].

2.3.2. Influence of initial conditions

In the previous section we gave a brief overview on the analytical approximation of the time-dependent fission width developed in Refs. [25,26] for spherical initial conditions. On the other hand, it is very difficult to create a fissioning system under such ideal initial conditions [58], and, therefore, the influence of initial deformation on the fission decay width has to be taken into account in order to have a realistic description of this decay channel [58, 59,60]. In Ref. [59], we extended the above-described approach, which has been derived for the initial condition of a Gaussian distribution centred at the spherical shape, to more general initial conditions; here, a short overview will be given.

In order to take into account non-spherical initial conditions, we introduced into the approximation (34) - (37) the solution of the dynamic Langevin equation of the system without considering the fluctuating term, assuming that the system starts at the finite initial deformation x_{init}. For this case, we calculate the mean deformation of the system at each time t. We get two solutions, one for the over-damped and one for the under-damped regime.

In the over-damped regime, the mean deformation of the system at time t follows the equation:

$$x_{mean} = x_{init} \cdot \exp\left[-\frac{1}{2}(\beta - \beta_1)\cdot t\right]. \tag{38}$$

In the under-damped regime, the mean deformation of the system is described by the equation:

$$x_{mean} = x_{init} \cdot \cos\left(\frac{1}{2}\beta_2 \cdot t\right)\cdot \exp(-\beta \cdot t), \text{ with } \beta_2 = \sqrt{4\omega_0{}^2 - \beta^2}\,. \tag{39}$$

The solutions (38) and (39) are then included into the solution of the Fokker-Planck equation given in (34) by performing the transformation $x_b \rightarrow x_b - x_{mean}$.

This then leads to the following analytical approximation to the solution of the Fokker-Planck equation for the time-dependent fission width:

$$\Gamma_f(t) = K \cdot \Gamma_{BW} \cdot \frac{kT}{\mu\omega_1^2 \cdot \sigma^2} \cdot \frac{\exp\left(-\frac{(x_b - x_{mean})^2}{2\sigma^2}\right)}{\exp\left(-\frac{\mu\omega_1^2 \cdot x_b^2}{2kT}\right)}, \tag{40}$$

$$\sigma^2 = \frac{kT}{\mu\omega_1^2}\left\{1 - \exp(-\beta\cdot(t+t_0))\cdot\left[\frac{2\beta^2}{\beta_1^2}\sinh^2\left(\frac{1}{2}\beta_1(t+t_0)\right) + \frac{\beta}{\beta_1}\sinh(\beta_1(t+t_0)) + 1\right]\right\},$$

where t_0 is given by Eq. (37) and x_{mean} by Eqs. (38) and (39). This is the formula used in ABLA07 to calculate the fission decay width.

In Fig. 6, we compare the results of this analytical approximation for the time-dependent fission width with the numerical results of the Fokker-Planck equation calculated for the nucleus ^{248}Cf starting from deformed initial conditions (full line and full histogram). The agreement between the analytical approximation for more general initial conditions and one-dimensional numerical calculations is quite satisfactory.

2.3.3. Low-energy fission

In case of low-energy fission, the double-humped structure in the fission barrier as a function of elongation and the symmetry classes at different saddle points are of importance for a proper description of the process. These effects have been included in the ABLA07 code, following the ideas developed in Refs. [1,61,62]: Assuming that the vibrational states in the second well are completely damped into all the other compound states, i.e. the system found in the second minimum can either fission via passage over the second (B) barrier or return to the initial deformation via passage over the first (A) barrier, the fission decay width can be calculated as [1,61]:

$$\Gamma_f = \frac{\Gamma_A \cdot \Gamma_B}{\Gamma_A + \Gamma_B}, \tag{41}$$

where, Γ_A and Γ_B represent the partial decay widths for fission over barrier A and B, respectively. These partial widths are calculated as:

$$\Gamma_{A,B} = \frac{1}{2\pi \cdot \rho_g(E)} \int_0^{E-B_f^{A,B}} \rho_{A,B}(\varepsilon) d\varepsilon \,. \tag{42}$$

In the above equation, ρ_g is the level density at the initial deformation, $\rho_{A,B}$ level density above the barrier A and B, respectively, and $B_f^{A,B}$ the height of the barrier A and B, respectively.

In order to calculate the level density at a specific deformation, one has to take into account the symmetry class of the corresponding configuration. Following the ideas of Refs. [1,62,63] we assume that the barrier A is mirror symmetric and axially symmetric for nuclei with $N \leq 144$, while axially asymmetric for nuclei with $N > 144$. The barrier B is axially asymmetric, and mirror symmetric for nuclei with mass smaller than 226, while mirror asymmetric for larger masses. We also assume, that for nuclei with Z^2/A less than 34 only barrier B plays a role, while for heavy nuclei with Z^2/A larger than 40.6 only barrier A is important. In the intermediate region both barriers have to be considered.

Another important input in the Eq. (42) is the height of the corresponding barrier. In ABLA07 we assume that these two barriers have the same height and that it is given by the prediction of the finite-range liquid drop model of Sierk [64] with ground-state shell-correction energies of Ref. [29] included. We make this assumption for the following two reasons: Firstly, experimental information on the fission-barrier height is available for a very limited number of nuclei (see e.g. [65]), with large uncertainties for the barrier which is the lowest between the two A and B. Moreover, different theoretical calculations predict often very different values of the barrier heights, and sometimes they over/under-predict the experimental barrier by few MeV. This all makes it quite difficult, or even impossible, to perform the calculations in regions where the experimental data are scarce or even not existing. Secondly, several studies [30,31,66] have shown that the shell-correction energy at the fission saddle point is very small, and, thus, considering the uncertainties in model predictions, can be neglected. Due to all this, we assume that $B_A = B_B = B_{FRLDM} - \delta U_{GS}$, where δU_{GS} is ground-state shell correction energy, and B_{FRLDM} macroscopic fission barrier calculated according to Ref. [64]. We have decided to use the model of Ref. [64] as according to a recent study performed in [67], this model gives very realistic predictions of fission-barrier heights in experimentally unexplored regions.

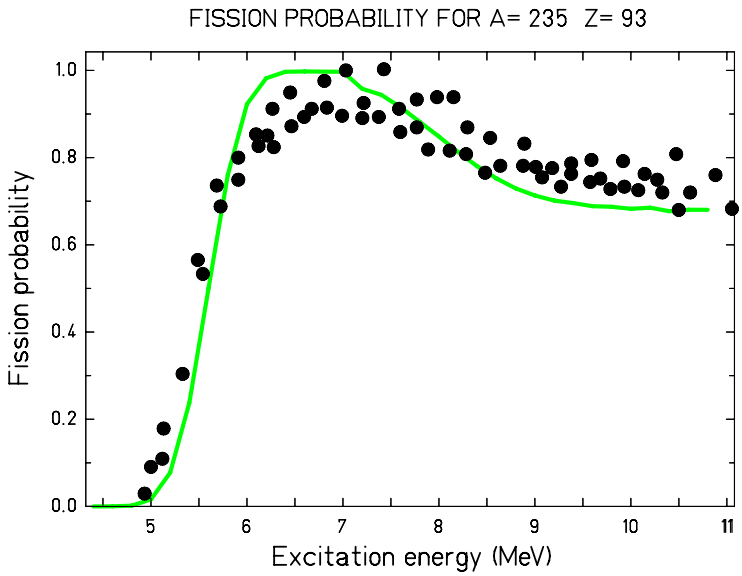

In Fig. 7, we compare the prediction of ABLA07 with measured fission probability as a function of excitation energy for the compound system ^{235}Np. The agreement between the data and calculations is very satisfactory.

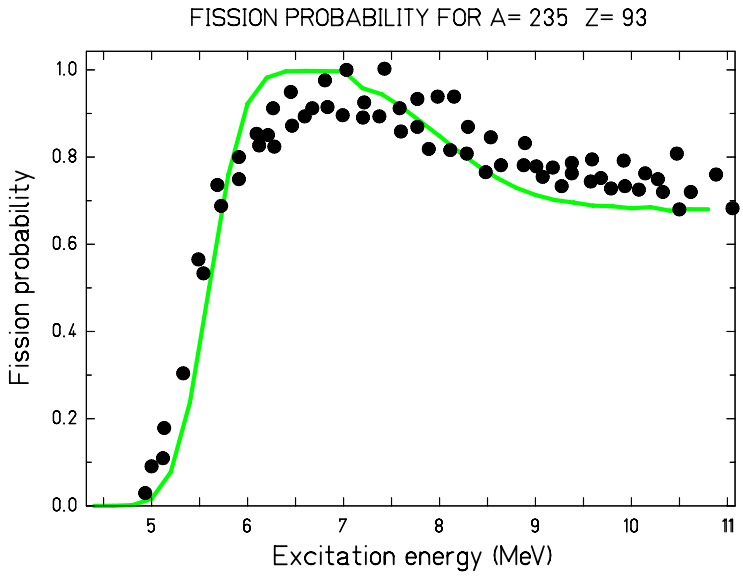

Fig. 7. Energy-dependent fission probability for the compound system ^{235}Np: full symbols – experimental data from Ref. [1], full line – results of ABLA07.

2.3.4. Fragment production in fission

Properties of fission fragments, i.e. masses, atomic numbers, excitation and kinetic energies, are calculated based on the macro-microscopic approach and the separability of compound-nucleus and fragment properties on the fission path [51]. The original technical description of the fragment-formation model – PROFI – was published in Refs. [49,50], while the updated description will be the subject of a forthcoming publication.

In the PROFI model it is assumed that different splits in mass are basically determined by the number of available transition states above the potential energy surface behind the outer saddle point. The macroscopic properties of the potential-energy landscape of the fissioning system are attributed to the strongly deformed fissioning system, which are deduced from mass distributions at high excitation energy [68] and Langevin calculations [69]. The microscopic properties of the potential-energy landscape of the fissioning system are given by the qualitative features of the shell structure in the nascent fragments. They are determined from the observed features of the fission channels [70] according to the procedure described in [51].

In case of spontaneous fission, the mass distribution is not determined by the phase space but by the variation of the tunnelling probability through the outer barrier as a function of mass asymmetry. The tunnelling probability is calculated using the Hill-Wheeler approach.

The dynamics of the fission process responsible for the fragment formation is considered in an approximate way: Since a variation of the mass asymmetry is connected with a substantial transport of nucleons and, consequently, the inertia of this collective degree of freedom should be large, we assume that the phase space near the outer saddle point determines the mass asymmetry of the system, which is more or less frozen during the descent to scission. On the other hand, the *N/Z* collective degree of freedom can be considered as a fast degree of freedom, as it is enough to exchange very few neutrons or protons between the two nascent fragments in order to explore the full *N/Z* range observed in the final fragments. Therefore, we assume that the *N/Z* degree of freedom is determined, opposite to mass asymmetry, near the scission point, and we calculate its value taking into account the charge-polarisation effects [71].

The excitation energies of the created fragment are calculated from the available excitation energy at the scission point and the deformation energies of the fragments at scission. The deformation energies of the fragments are assumed to be specific to the individual fission channels. They are deduced from experimental data on total kinetic energies and neutron yields. Kinetic energies are then calculated applying the energy conservation law.

2.3.5. Particle emission in fission

In ABLA07, particle emission is calculated at different stages of the fission process – (i) up to the saddle point, (ii) from the saddle up to the scission point, and (iii) from the two separated fission fragments. In order to calculate the particle emission on the way from the saddle to the scission point, we have parameterized the saddle-to-scission times obtained by solving the three-dimensional Langevin equation of motion using the one-body dissipation tensor with the reduction coefficient K_s=0.25 [72]. Then, at each time step, the probability to emit a neutron or some of the light charged particles is calculated. IMF emission is not considered as a decay channel between saddle and scission. This procedure is repeated as long as the cumulative particle emission time (i.e. sum of the particle emission times emitted after the saddle point) is shorter than the saddle-to-scission time.

After scission, two fission fragments are formed, and their decay is followed as described in Section II.1.

In Fig. 8 a comparison between measured and calculated fission-fragment mass and neutron-multiplicity distributions in case of spontaneous fission of ^{252}Cf is shown. Please note that there was no special adjustment of model parameters in order to reproduce the data.

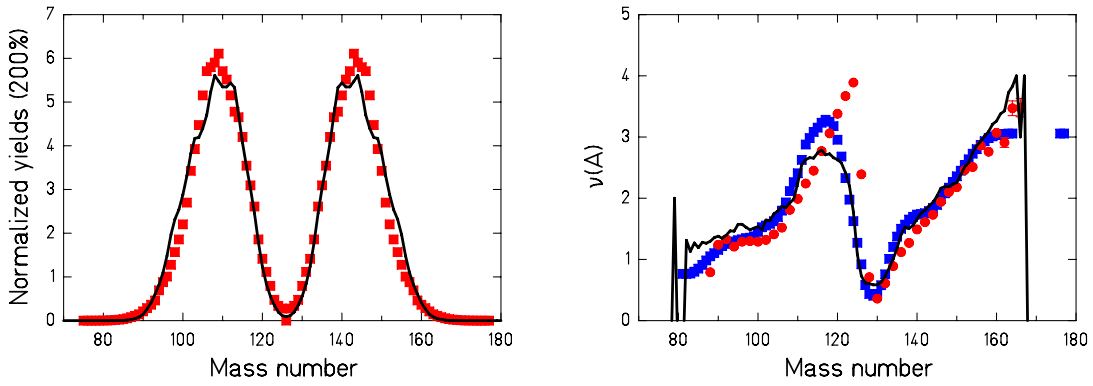

Fig. 8. Spontaneous fission of ^{252}Cf – Left: comparison between measured mass distribution [73] (symbols) and ABLA07 prediction (full line); Right: comparison between measured [74] (dots) and evaluated [75] (squares) neutron multiplicities as a function of the fission-fragment mass and the result of an ABL07 calculation (full line).

2.4. IMF emission

The range of emitted fragments in the ABLA07 code has been extended to above $Z = 2$ in order to obtain a more realistic description of the production of intermediate-mass fragments (IMFs), which was strongly underestimated in the previous version of ABLA. Two models for the production of IMFs are implemented: In the first scenario, all nuclei below the Businaro-Gallone maximum of the mass-asymmetry dependent barrier, see Fig. 9, are taken into account in the evaporation process. The barriers are given by the Bass nuclear potential. Thermal expansion of the compound nucleus is considered. In the second scenario, which will be described in Section III, if the excitation energy of the system exceeds the corresponding threshold, the simultaneous break-up of the system is modelled according to a power-law distribution, which is suggested by several theoretical models.

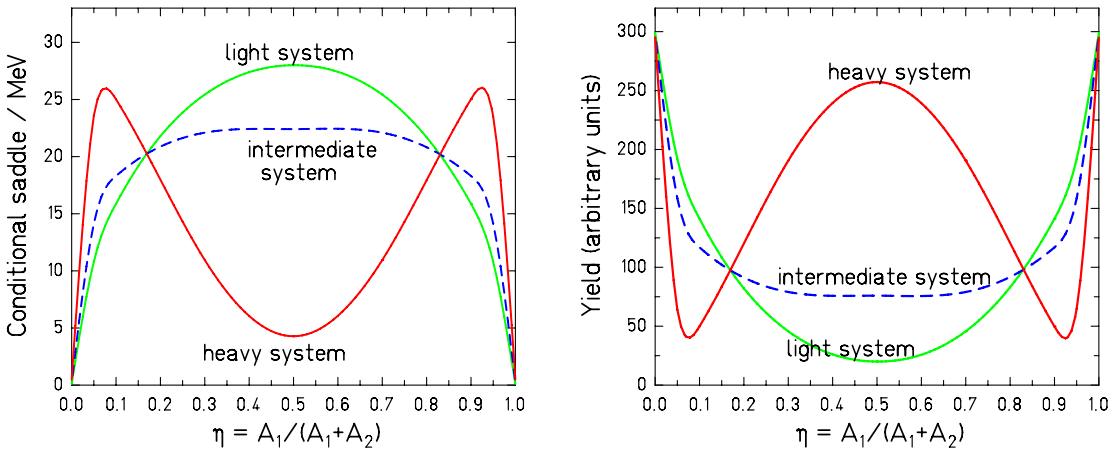

Fig. 9. Energies above the ground state in the touching-sphere configuration (left) and corresponding mass distributions (right) given by the available phase space above corresponding configuration in the left part of the figure.

In the case of sequential IMF emission, in order to have a fast calculation scheme, the different decay channels are divided into a few groups: The emission of neutrons, light charged particles and gammas is treated explicitly. The same is true for fission. The emission

of IMFs with $Z \geq 3$, on the other hand, is treated as one class of events in the first step, in order not to increase the computational time. The idea is the following:

To calculate the probability P_i of a given decay channel i, we need the corresponding decay width Γ:

$$P_i = \frac{\Gamma_i}{\Gamma_{tot}}, \quad \Gamma_{tot} = \sum_k \Gamma_k = \Gamma_{neutron} + \sum_{lcp} \Gamma + \Gamma_{gamma} + \Gamma_{fission} + \sum \Gamma_{IMF} \ , \tag{43}$$

In the above equation, the sum over *lcp* goes over all light-charged particles with Z=1, 2, while the sum over IMF goes over all intermediate-mass fragments that can be emitted in a given reaction. Therefore, the explicit calculation of the last term in Eq. (43) would be very time consuming. On the other hand, from the experimental observations we know that the element distribution of IMF fragments follows a power law. Thus, we can well estimate the total decay width for IMF production ($\Gamma_{IMF}^{tot} = \sum \Gamma_{IMF}$) by determining the slope in the double-logarithmic presentation by calculating the decay width for the isotopes of two elements (e.g. Z = 3 and Z = 5) and integrating the adapted power-law function:

$$\Gamma_{IMF}(Z) = a \cdot Z^b \Leftrightarrow \log\left(\Gamma_{IMF}(Z)\right) = a + b \cdot \log(Z) \quad \Rightarrow$$

$$b = \frac{\log\left(\Gamma_{IMF}(Z=5)/\Gamma_{IMF}(Z=3)\right)}{\log(5/3)}, \ a = \frac{\Gamma_{IMF}(Z=5)}{5^b}$$

$$\Gamma_{IMF}(Z=i) = \sum_A \Gamma_{IMF}(Z=i, A), \ \ i = 3{,}5 \, , \tag{44}$$

where A is the mass of a selected IMF. $\Gamma_{IMF}(Z=3)$ and $\Gamma_{IMF}(Z=5)$ are then explicitly calculated according to the procedure described below.

Once the parameters a and b are obtained, one can determine the total decay width for IMF emission by performing the following integration:

$$\Gamma_{IMF}^{tot} = \int_3^{Z_{CN}} a \cdot Z^b dZ = a \cdot \left(Z_{CN}^{b+1} - 3^{b+1}\right). \tag{45}$$

Only if the emission of IMFs is realised, the competition between the individual IMFs is to be considered, as described below.

Since long time, it has been discussed whether the emission of an IMF from a heavy nucleus (above the Businaro-Gallone point) is better described as an evaporation process or as a fission process with very asymmetric mass-split. Both approaches were already used in the past in nuclear de-excitation codes, e.g. in GEMINI [76] as very asymmetric fission or in GEM2 [77] as evaporation. Already in 1975 it was pointed out that there is a continuous transition between the two processes [78]. Recently [79] it was shown that even for such a heavy nucleus as ^{238}U the lightest IMFs are produced in a rather compact configuration, indicating that there is gradual transition from the standard fission process towards evaporation. From the physical point of view an extremely asymmetric binary split into two compact nuclei corresponds to an evaporation of a light nucleus from a heavy compound nucleus. In ABLA07 we based the fission-to-evaporation changeover on the M-shaped

potential energy as a function of the mass asymmetry. At the point were the M-shaped potential reaches it maximum, the fission model smoothly fades away in favour of the evaporation process.

In ABLA07, the statistical weight for the emission of IMFs is calculated, similarly as in case of any other particle-decay channel, on the basis of the detailed-balance principle, except that in this case also the available nuclear levels in the IMF have to be considered The decay width (Γ) as a function of the excitation energy (E) depends on the inverse cross section (σ_{inv}), on the level densities of the two daughter nuclei (ρ_{imf} and $\rho_{partner}$) and on the level density of the mother nucleus above the ground state (ρ_C):

$$\Gamma \approx \int_0^{E_{imf}^{max}} \int_0^{E_{partner}^{max}} \sigma_{inv} \frac{\rho_{imf}(E_{imf}) \cdot \rho_{partner}(E_{partner})}{\rho_C(E)} \, dE_{imf} \, dE_{partner} , \tag{46}$$

with the following relation that guaranties the energy conservation:

$$E = E_{imf} + E_{partner} + Q + \varepsilon . \tag{47}$$

Here E, E_{imf} and $E_{partner}$ represent the initial excitation energy of the mother nucleus, and the excitation energies of the two daughter nuclei, respectively. Q is the Q-value, and ε is the total kinetic energy in the centre of mass of the system. The barrier (B) which is also playing the role is calculated using the fusion nuclear potential of Bass [38] (see also Section II.1.4). The inverse cross section (σ_{inv}) is calculated using the ingoing-wave boundary condition model [22], where only the real potential is used to describe the transmission probability of particles. An analytical approximation to Equation (46) is used in order to avoid the numerical calculation of the two integrals, which is rather time-consuming: We assume that in order to calculate the phase space available for the IMF emission, we can, instead of folding the level densities (Eq. (46)) of the two fragments at the saddle point for IMF emission, calculate the level density of the compound nucleus at the same intrinsic excitation energy, using a modified level-density parameter to consider the increased surface of the configuration at the barrier In other words, instead, as described by Eq. (46), considering the system in a moment of the IMF emission as two systems (IMF and its partner) in the touching-sphere configuration, we describe it as a single system in the given configuration, i.e. deformation, angular momentum and excitation energy given by the touching-sphere configuration. To test this assumption, we have calculated the decay width for the ^{16}O emission from several different compound systems, using either the Eq. (46) or assumption of a single system in the touching-sphere configuration, resulting in Γ_2 and Γ_1, respectively. In Fig. 10, we show the ratio between Γ_2 and Γ_1 as a function of excitation energy above the touching-sphere configuration.

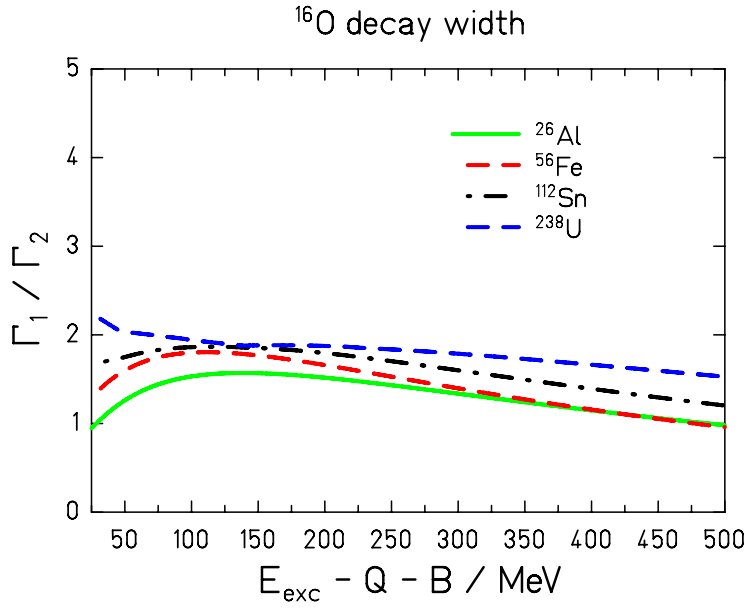

Fig. 10. Ratio between ^{16}O decay widths, Γ_1 and Γ_2, calculated assuming one system in the touching-sphere configuration or two systems (^{16}O and its partner) in the same configuration, respectively.

The kinetic energies of sequentially emitted IMFs and their partners are calculated, similar as in case of fission, from Coulomb repulsion using the momentum conservation in the frame of the decaying mother nucleus.

In Fig. 11 experimental data measured in the reaction $^{238}U+^{1}H$ at 1 *A* GeV [79,80,81,82] are compared with the predictions of ABLA07 coupled to the reaction model BURST [79]. In this reaction, the largest contribution to the production of residual nuclei is coming from fission. On the other hand, nuclei with atomic number smaller than ~15 are produced as intermediate-mass fragments, while those with atomic number larger than ~70 are residues after the sequential emission of neutrons, light-charged particles and/or IMFs. Cross sections, as well as first and second moments of the isotopic distributions are compared, and agreement between the data and the calculations is very satisfactory.

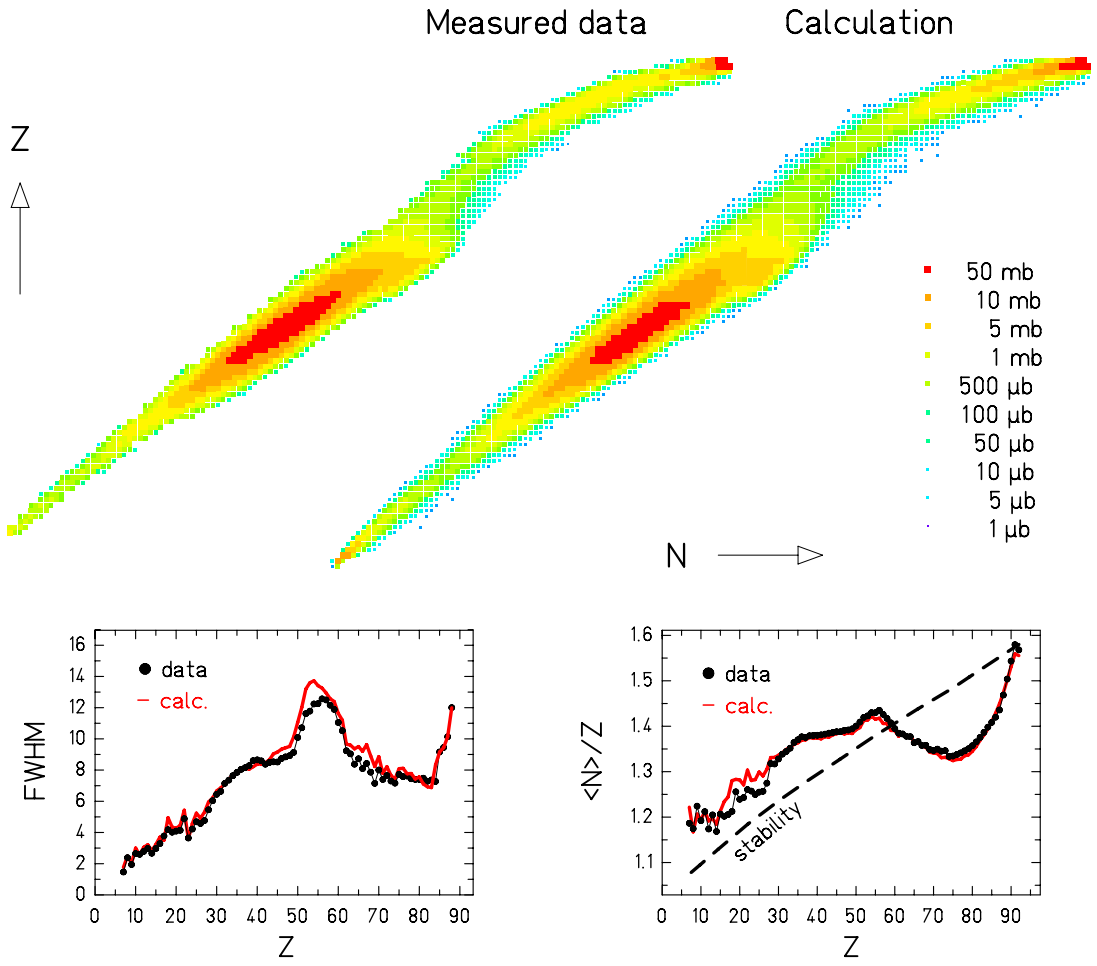

Fig. 11. Up – Cross sections for the nuclei produced in 1 GeV p on ^{238}U: Measured cross sections [79,80,81,82] (left) and prediction of BURST [79] + ABLA07 (right) presented on the chart of the nuclides. Down – Right: Mean neutron-to-proton ratio of isotopic distributions as a function of the atomic number, compared with the stability line (dashed line) and to the BURST + ABLA07 prediction (solid line). Left: FWHM of the isotopic distributions compared to the prediction of the BURST + ABLA07 code (solid line).

3. Break-up stage

If the excitation energy acquired during the first, collision, stage is high enough, the increase of volume has a dramatic consequence: The nucleus enters the spinodal region [83] characterized by negative incompressibility. In this region, an increase in the system volume due to expansion is connected with the increase in pressure, and, consequently, any local fluctuation in density is strongly amplified leading to a mixed phase consisting of droplets represented by a small amount of light nuclei at normal nuclear density, and the nuclear gas represented by individual nucleons. This process is often called “break-up”. The fragments formed in this process undergo deexcitation process and cool down. What is finally experimentally observed are the cold fragments, normally called IMFs. The entire multifragmentation process is scientifically very interesting for its relation to the equation-of-state of nuclear matter, in particular to the liquid-gas phase transition.

The starting point of the break-up stage in ABLA07 is a hot nuclear system –so-called "spectator"[4], leftover of the initial collision stage. We assume that, if the excitation energy per nucleon of the spectator exceeds a limiting value [9], the system undergoes the break-up stage; otherwise we assume that it will directly de-excite through sequential evaporation and/or fission.

About the limiting excitation energy per nucleon, two options are possible in ABLA07. The default option is that the limiting excitation energy per nucleon is constant for all nuclei; its value is fixed to 4.2 MeV. Another possible option is to use a mass-dependent value of the limiting excitation energy, deduced from the mass dependence of the temperature in the plateau of the caloric curve as pointed out by Natowitz in [84].

Please note that in the description of the break-up stage we do not consider any effect of compression, which could play a role in case of central heavy-ion collisions at Fermi energies. In case of nucleus-nucleus collisions at relativistic energies or of spallation reactions, the heating of the system is purely thermal without any influence of compression; for these reactions, the break-up stage in ABLA07 is adapted.

3.1. IMF formation by break-up

It is not trivial to determine theoretically the size distribution of the break-up fragments. Models that evaluate it just by phase-space arguments, considering all possible partitions and weighted them by the number of available states, are considered to be inadequate since they neglect the dynamic of the expansion. On the other hand, the dynamics of the break-up process is far to be fully understood. In this context, in order to have an estimate of the production cross-sections of the IMFs, we based our model on the following considerations:

At the starting point of ABLA07, the spectator nucleus has mass $A_{init}^{spectator}$ and excitation energy $E_{init}^{spectator} = A_{init}^{spectator} \cdot \varepsilon_{init}$. If ε_{init} is larger than some limiting value ε_{freeze_out} [9], the system will enter the break-up stage, where the excitation energy of the spectator is partially consumed to break up the spectator into several hot fragments. In the light of this picture, the break-up process in ABLA07 is technically divided into two steps.

As the first step, it is calculated how much of the initial energy is removed through the loss of mass to form nucleons or fragments (which are, at this stage, not specified). Specifically, it is calculated to which amount the mass of the spectator has to be reduced, down to $A_{freeze-out}^{spectator}$, in order to get to an excitation energy per nucleon corresponding to ε_{freeze_out}. The energy consumed to lose one mass unit varies from 10 MeV for an initial excitation energy of 2.9 A MeV to 5 MeV for an initial excitation energy of 11.8 A MeV. These values have been deduced from the comparison with the experimental data in the reaction ^{238}U+Pb at 1 A GeV [85]. In the model, we assume that in the break-up stage the N/Z ratio is conserved, so the break-up product has the same N/Z ratio as the initial spectator nucleus. In this way, we obtain the mass $A_{freeze-out}^{spectator}$, nuclear charge $Z_{freeze-out}^{spectator}$ and excitation energy of the spectator residue after the break-up stage.

In order to calculate mass and atomic number of light clusters emitted in the break-up process, the following considerations are taken:

---

[4] The term spectator is derived from fragmentation reactions, but the following description of the break-up process is valid for the decay of any hot thermalised system regardless of the way how it was produced.

Many experimental observations established that the production cross-sections in the domain of multifragmentation follow a power law:

$$\frac{d\sigma}{dA} \propto A^{-\tau}, \tag{48}$$

whose slope is rather well described by an exponent $\tau \approx 2$. The value of $\tau \approx 2$ turned to be rather universal, although a more accurate investigation of experimental data [86] showed a certain dependence on Z_{bound}, a quantity often associated to the impact parameter and therefore to the total excitation energy. In ABLA07, the mass of nucleons and fragments produced at break-up is sampled from an exponential distribution with slope parameter $\tau(E^*/A)$, providing that the sampled mass is rejected when exceeding the maximum available mass given as $A^{left}_{freeze-out} = A^{spectator}_{init} - A^{spectator}_{freeze-out}$. The value of τ is calculated assuming a linear dependence on the excitation energy per nucleon in the temperature regime of interest as discussed in Refs. [87,86]. The sampling is performed several times until the entire mass $A^{left}_{freeze-out}$ is consumed. Each time, the charge Z_{IMF} of the fragment is sampled from a Gaussian distribution centred at Z_{mean}, where Z_{mean} is determined by imposing that the ratio A/Z is the same of the hot remnant. The width of the distribution is given by the relation [88]:

$$\sigma_Z^2 = \frac{T_{freeze-out}}{C_{symm}}, \tag{49}$$

where C_{sym} is the symmetry term of the nuclear equation of state. C_{sym} is set to depend on E^*/A, as reported in Refs. [89,90,87].

Each of the break-up-fragments greater than an α particle will then enter the evaporation cascade.

In Fig. 12 we compare the excitation function for the production of ^{7}Be in the reaction ^{93}Nb+^{1}H calculated with BURST [79] + ABLA07 with experimental data (see [91] and references therein). At lowest proton-beam energies, ^{7}Be is produced only via sequential decay from the excited nuclei, while at highest energies also the simultaneous break-up process contributes to its production.

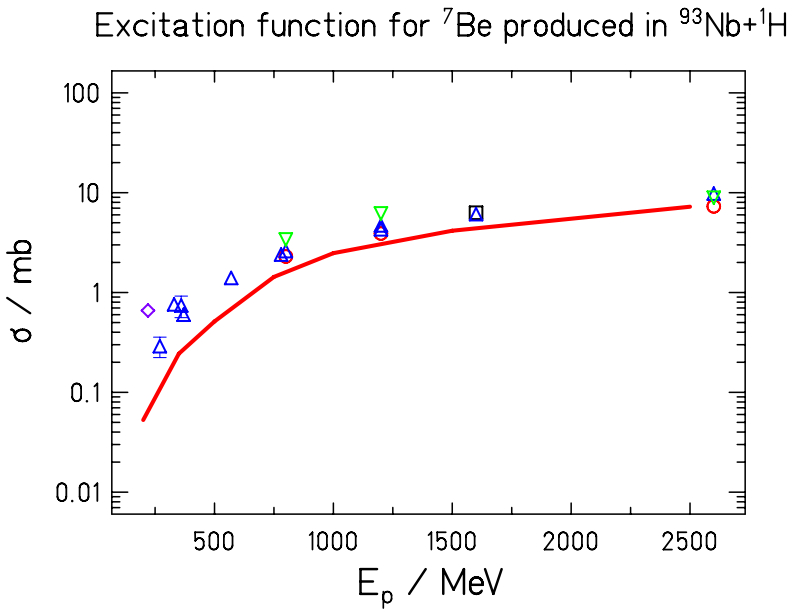

Fig. 12. Excitation function fort the production of ^{7}Be in the reaction of ^{93}Nb+^{1}H – symbols: experimental data (see [92] and references therein), full line: predictions of ABLA07 coupled to BURST [79].

3.2. Kinetic-energy spectra

The question on how the fragments acquire their kinetic energies in the multifragmentation process is still vividly discussed, and is closely related to the time scale of the break-up process. If this time scale is very short compared to the time the system needs to reach thermal equilibrium (which at intermediate and high energies is < 100 fm/c [93,94,95]), the break-up system will not reach the thermal equilibrium and dynamical effects play a decisive role, see e.g. [96]. On the contrary, if this time scale is long enough for thermal equilibrium to establish, one can apply statistical considerations as done for example in Ref. [97].

In the first case, the kinematic properties of the created fragments during the break-up are mostly given by the Fermi motion of nucleons in the break-up system. In this case, one can apply the Fermi-gas model [98] for calculating the width σ of the momentum distribution of a created fragment:

$$\sigma^2 = \sigma_0^2 \cdot \frac{A_{frag} \cdot \left(A_{init}^{spectator} - A_{frag}\right)}{A_{init}^{spectator} - 1}, \tag{50}$$

where A_{frag} is the fragment mass, and σ_0 a parameter amounting to ~118 MeV/c for heavy nuclei. For calculating the kinematical properties, one has to consider two additional effects – influence of thermal motion of nucleons inside the fragment [99] and thermal expansion of the break-up source [24]. Both of these effects will influence the value of the parameter σ_0 entering Eq. (50).

In the second case, created fragments are in thermal equilibrium with the surrounding gas, and the kinematical properties are mostly given by the thermal motion of fragments inside the break-up volume. In this case, Eq. (50) can be written as [98]:

$$\sigma^2 = m_n \cdot A_{frag} \cdot T_{freeze-out} \cdot \frac{\left(A_{init}^{spectator} - A_{frag}\right)}{A_{init}^{spectator}}, \quad (51)$$

where m_n is the nucleon mass. Additionally, one has to include the effects of Coulomb repulsion between the nascent fragments in order to calculate their velocities. This is done according to Ref. [100] (see Eq. (4) in Ref. [100]).

Both of these options, i.e. Eqs. (50) and (51) are incorporated in the ABLA07 code, and can be used for calculating kinetic energies of fragments produced in multifragmentation.

4. Conclusions

Guided by the empirical knowledge obtained in a recent experimental campaign on the nuclide distributions measured at GSI, Darmstadt, the ABLA code has been subject to important developments. By including the new analytical approximation to the solution of the Fokker-Planck equation for the time dependent fission width, ABLA07 is transformed from a pure statistical code to a dynamical code. It is coupled to the improved semi-empirical fission model PROFI that calculates the characteristics of fragments formed in fission over a large range of energies – from spontaneous fission up to high-energy fission. Apart from neutrons, light charged particles and gammas, also the emission of intermediate-mass fragments is consistently described in ABLA07, thus overcoming the limitation of the previous version of the model in which IMF emission was not considered. The code was originally developed for describing the de-excitation stage of heavy-ion collisions and spallation reactions at relativistic energies. However, coupled to a suitable model for the first stage of the reaction, ABLA07 can also be used to model the de-excitation phase of any kind of nuclear reaction if the approximations of ABLA07 are not considered to be crucial. The parameters of the ABLA07 code are fixed and are the same for all systems and all incident energies, rendering to the code a high predictive power.

ACKNOWLEDGEMENTS

We acknowledge the financial support of the European Community under the FP6 Integrated Project EUROTRANS Contract no. FI6W-CT-2004-516520 and “Research Infrastructure Action – Structuring the European Research Area” EURISOL DS Project Contract no. 515768 RIDS. The EC is not liable for any use that may be made of the information contained herein.

Annex A

In the table below, a comparison between the major physics input of the previous version of the model (ABLA [101,19]) and of the present version (ABLA07) is given.

	ABLA	ABLA07
Physics Processes	Deexcitation process of a thermalised system – emission of neutrons, protons and ^{4}He, and fission	Deexcitation process of a thermalised system – simultaneous break-up, emission of gammas, neutrons, Z=1 and 2 particles and intermediate-mass fragments, and fission)
Method	Statistical model, Weisskopf formalism	Statistical model, extended Weisskopf formalism
Monte Carlo Technique	« timelike »	« timelike »
Nuclear level density	Fermi-gas model; Deformation dependence [18]; Energy dependence [18]; Collective enhancement [19]	Fermi-gas model + Constant-temperature model [35,36]; Deformation dependence [18]; Energy dependence [18]; Collective enhancement [19]
Coulomb barriers	For protons and ^{4}He empirical barriers	For LCP and IMF (all possible species) by nuclear potential [23] plus Coulomb potential; Thermal expansion of the source [102] included
Nuclear binding energies	Finite-range liquid-drop model including shell and pairing [29]	Finite-range liquid-drop model including shell and pairing [29]
Particle-decay width	Geometrical inverse cross sections	Energy-dependent inverse cross sections based on nuclear potential using the ingoing-wave boundary condition model [22]; Tunnelling for LCP included
Fission barriers	Finite-range liquid-drop model [64] plus ground-state shell effect [29]	Finite-range liquid-drop model [64] plus ground-state shell effect [29]
Angular momentum	Influence of angular momentum on fission barrier	Influence of angular momentum on fission barrier

	is considered	and particle-decay width is considered; Change of angular momentum due to particle evaporation is considered
Dissipation in fission	Transient effect considered by step function	Transient effect considered by approximated solution of the Fokker-Planck equation [25,26]; Influence of initial conditions included [58,59]
Low-energy fission probability	Not included	Included according to [1,61]
Fission-fragment nuclide distribution	Conditional transition-state model [49,50]	Conditional transition-state model [49,50,51]

Annex B

As mentioned above, the correct description of the inverse cross section would lead to the numerical integration of the Eq. (1) and would considerably slow down the calculations.

In fact, using expression (11) the Eq. (1) can be rewritten in the following way:

$$\Gamma_\nu\left(E_i,J_i\right)=\frac{2\cdot s_\nu+1}{2\cdot\pi\cdot\rho\left(E_i,J_i\right)}\cdot\frac{2\cdot m_\nu\cdot\pi}{\pi\cdot\hbar^2}\int_0^{E_i-S_\nu-B_\nu}\cdot\left(R_{geom}+R_\lambda\right)^2\cdot\frac{\left(\varepsilon_\nu-B_\nu\right)^2}{\varepsilon_\nu}\rho\left(E_f,J_f\right)\cdot\mathrm{d}E_f\ . \quad \text{(A1)}$$

Following Moretto [103], we can approximate the level density by the constant-temperature formula, with T determined by the inverse logarithmic slope of the level density at the maximum excitation energy of the daughter nucleus. After changing the variable $E_f \rightarrow \varepsilon=\varepsilon_\nu= E_i - E_f - S_\nu$, Eq. (A1) becomes[5]:

$$\Gamma\left(E_i,J_i\right)=\frac{2\cdot s+1}{2\cdot\pi\cdot\rho\left(E_i,J_i\right)}\cdot\frac{2\cdot m\cdot\pi}{\pi\cdot\hbar^2}\int_B^{E_i-S_\nu}\cdot\left(R_{geom}+R_\lambda\right)^2\cdot\frac{\left(\varepsilon-B\right)^2}{\varepsilon}\rho\left(E_i-S_\nu-B\right)\cdot\exp\left(-\frac{\varepsilon-B}{T}\right)\cdot\mathrm{d}\varepsilon,$$

$$T=\left.\frac{d\ln\rho\left(E_f\right)}{dE_f}\right|_{E_f=E_i-S-B}\cdot \quad \text{(A2)}$$

This results in three integrals to be solved:

$$I_1=\int_B^{E_i-S}R_{geom}^2\cdot\frac{\left(\varepsilon-B\right)^2}{\varepsilon}\cdot\exp\left(-\frac{\varepsilon-B}{T}\right)d\varepsilon\,, \quad \text{(A3)}$$

$$I_2=\int_B^{E_i-S}2\cdot R_{geom}\cdot R_\lambda\cdot\frac{\left(\varepsilon-B\right)^2}{\varepsilon}\cdot\exp\left(-\frac{\varepsilon-B}{T}\right)d\varepsilon\,, \quad \text{(A4)}$$

$$I_3=\int_B^{E_i-S}R_\lambda^2\cdot\frac{\left(\varepsilon-B\right)^2}{\varepsilon}\cdot\exp\left(-\frac{\varepsilon-B}{T}\right)d\varepsilon\,, \quad \text{(A5)}$$

---

[5] For comparison, in the previous version of ABLA the particle decay width was given as:

$$\Gamma\left(E_i,J_i\right)=\frac{2\cdot s+1}{2\cdot\pi\cdot\rho\left(E_i,J_i\right)}\cdot\frac{2\cdot m\cdot\pi}{\pi\cdot\hbar^2}\int_B^{E_i-S}\cdot R_{geom}^2\cdot\varepsilon\cdot\rho\left(E_i-S-B\right)\cdot\exp\left(-\frac{\varepsilon-B}{T}\right)\cdot\mathrm{d}\varepsilon$$

B.1 Inclusion of the Coulomb factor

The first task is to formulate the decay width for charged particles with the Coulomb factor included in an approximate closed analytical expression (integral I_1 in Eq. (A3)). This means that one needs finding the solution of the integral:

$$Y = \int x \frac{x}{x+B} \exp\left(-\frac{x}{T}\right) dx$$

Here, only the general forms are given in order to illustrate the mathematical idea. The variable $x=\varepsilon-B$ is the energy above the barrier, T is the temperature and B is the barrier.

Our basic idea is to calculate the decay width with the combination of two functions:

$$Y = \frac{1}{\frac{1}{Y_1}+\frac{1}{Y_2}}, \quad \text{with} \quad Y_1 = \int x \cdot \exp\left(-\frac{x}{T}\right) dx \qquad \text{and} \qquad Y_2 = \int \frac{x^2}{B} \cdot \exp\left(-\frac{x}{T}\right) dx \,.$$

Both integrals can be solved analytically:

$$\int x \cdot e^{ax} dx = \frac{e^{ax}}{a^2}(ax-1) \qquad \text{and} \quad \int x^2 \cdot e^{ax} dx = e^{ax}\left(\frac{x^2}{a} - \frac{2x}{a^2} + \frac{2}{a^3}\right), \text{ with } \quad a = -\frac{1}{T} \,.$$

resulting in:

$$I_1 = R_{geom}^2 \cdot \frac{2T^3}{2T+B} \,. \tag{A6}$$

Justification:

With $y = x\frac{x}{x+B} exp\left(-\frac{x}{T}\right)$, $y_1 = x \cdot exp\left(-\frac{x}{T}\right)$ and $y_2 = \frac{x^2}{B} \cdot exp\left(-\frac{x}{T}\right)$ we get

$$y = \frac{1}{\frac{1}{y_1}+\frac{1}{y_2}} \,.$$

Since both curves (y_1 and y_2) are similar in shape, this relation also holds approximately for the integrals.

B.2 Inclusion of the energy-dependent quantum-mechanical cross section

In order to include the energy-dependent quantum-mechanical cross section one has to solve the integrals I_2 (Eq. (A4)) and I_3 (Eq. (A5)).

After replacing R_λ in Eq. (A4) with the expression given in Eq. (11), I_2 becomes:

$$I_2 = \int_B^{E_i - S} 2 \cdot R_{geom} \cdot k \cdot \frac{1}{\sqrt{\varepsilon}} \cdot \frac{(\varepsilon - B)^2}{\varepsilon} \cdot \exp\left(-\frac{\varepsilon - B}{T}\right) d\varepsilon \,, \; k = \sqrt{\frac{\hbar^2 \cdot (M_1 + M_2)}{2 \cdot M_2 \cdot (M_1 - M_2)}} \,. \tag{A7}$$

The integral $\int \frac{(\varepsilon - B)^2}{\varepsilon^{3/2}} \cdot \exp\left(-\frac{\varepsilon - B}{T}\right) d\varepsilon$ can be solved analytically [104][6], resulting in:

$$I_2 = 2 \cdot R_{geom} \cdot k \cdot \left[\frac{2\sqrt{T}\left(2B^2 + TB\right) + \exp\left(\frac{B}{T}\right)\sqrt{\pi B}\left(4B^2 + 4BT - T^2\right)\mathrm{erf}\left(\sqrt{\frac{B}{T}}\right)}{2\sqrt{TB}} - \frac{\exp\left(\frac{B}{T}\right)\sqrt{\pi}\left(4B^2 + 4BT - T^2\right)}{2\sqrt{T}} \right] \tag{A8}$$

The third integral in Eq. (A5) can be solved analytically in an approximate way like the integral I_1:

$$I_3 = \frac{k^2}{\frac{1}{Y_1} + \frac{1}{Y_2} + \frac{1}{Y_3}},$$

where $Y_1 = \int \exp\left(-\frac{x}{T}\right) dx, \quad Y_2 = \int \frac{x}{2B} \exp\left(-\frac{x}{T}\right) dx$ and $Y_3 = \int \frac{x^2}{B^2} \exp\left(-\frac{x}{T}\right) dx$

Finally:

$$I_3 = k^2 \cdot \frac{2T^3}{2T^2 + 4BT + B^2} \,. \tag{A9}$$

In case of neutrons ($B = 0$), these integrals become:

$$I_1^{neutrons} = R_{geom}^2 \cdot T^2 \,. \tag{A10}$$

$$I_2^{neut} = R_{geom} \cdot k \cdot \sqrt{\pi} T^{3/2} \,. \tag{A11}$$

$$I_3^{neut} = k^2 \cdot T \,. \tag{A12}$$

In Figure A.2 we show the ratio between the analytical approximation of Eq. (1), given by Eqs. (A6 – A9) for light charged particles and Eqs. (A10 – A12) for neutrons, and the result

---

[6] $$\int \frac{(\varepsilon - B)^2}{\varepsilon^{3/2}} \cdot \exp\left(-\frac{\varepsilon - B}{T}\right) d\varepsilon = -\frac{\exp\left(\frac{B - \varepsilon}{T}\right)\left[2\sqrt{T}\left(2B^2 + T\varepsilon\right) + \exp\left(\frac{\varepsilon}{T}\right)\sqrt{\pi\varepsilon}\left(4B^2 + 4BT - T^2\right)\mathrm{erf}\left(\sqrt{\frac{\varepsilon}{T}}\right)\right]}{2\sqrt{T\varepsilon}}$$

of the numerical integration of Eq. (1). This ratio is shown for several different nuclei. We see that in case of neutron there is no difference between the analytical and the numerical solutions. In case of light charged particles, the analytical approximation over-estimates the particle width by less than 10 % as compared to the numerical solution. Thus, we can conclude that the analytical approximation to the Eq. (1) is quit realistic in calculating the particle-decay width.

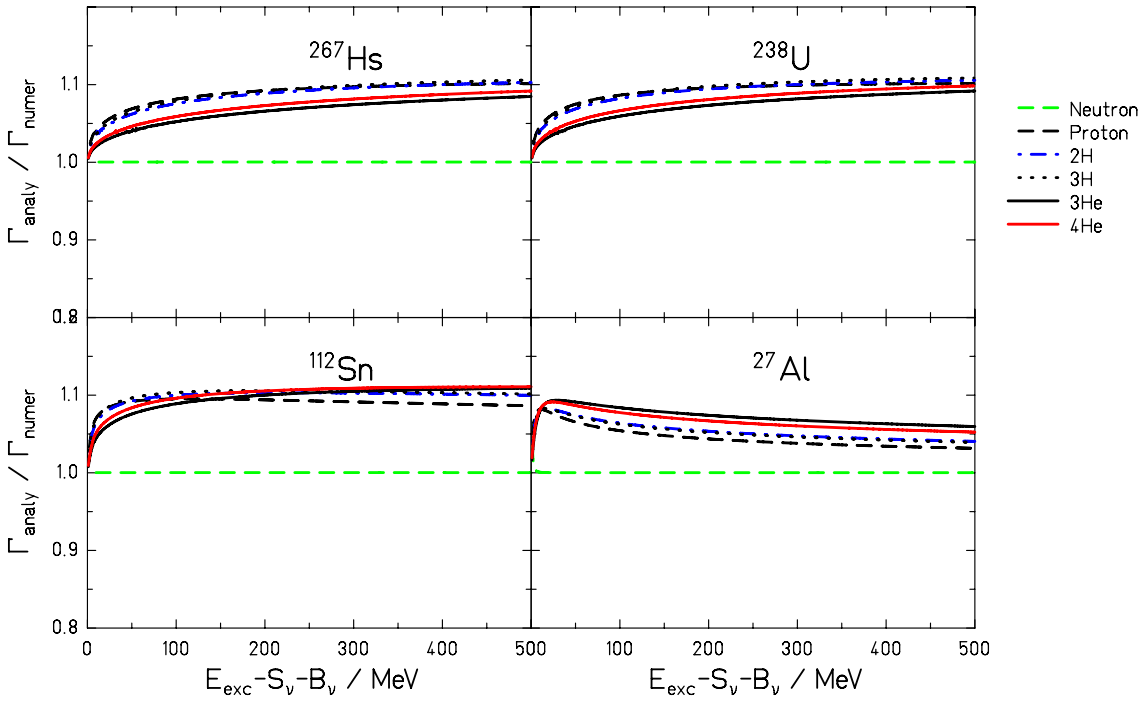

Fig. A.1. Ratio between numerical and analytical solution of Eq. (A.1) as a function of excitation energy for the case of neutron and light-charged particle emission from different nuclei.

REFERENCES

[1] A. Gavron et al, Phys. Rev. C13 (1976) 2374
[2] F. Rejmund et al, Nucl. Phys. A678 (2000) 215
[3] K.-H. Schmidt et al, Nucl. Phys. A665 (2000) 221
[4] P. Grangé, L. Jun-Qing, and H.A. Weidenmüller, Phys. Rev. C 27 (1983) 2063
[5] J. Pochodzalla et al, Phys. Rev. Lett. 75 (1995) 1040
[6] L. G. Moretto et al, Ann. Rev. Nucl. Part Sci. 43 (1993) 379
[7] B. K. Srivastava et al, Phys. Rev. C65 (2002) 054617
[8] M.-V. Ricciardi et al, Phys. Rev. Lett. 90 (2003) 212302
[9] K.-H. Schmidt, M. V. Ricciardi, A. Botvina, T. Enqvist, Nucl. Phys. A 710 (2002) 157
[10] V. A. Karnaukov, Phys. of Part. and Nuclei 37 (2006) 165
[11] http://www.sns.gov
[12] http://neutron.neutron-eu.net/n_ess
[13] C. Rubbia et al, Report CERN/AT/95-44/(ET) (1995)
[14] C. D. Bowmann et al, Nucl. Instr. Meth. A320 (1992) 336
[15] R. G. Stokstad, "The use of statistical models in heavy-ion reaction studies", published in "Treatise on heavy-ion science", Volume 3, edited by D. A. Bromely, Plenum Press, New York, ISBN 0-306-41573-9 (v. 3)
[16] V. F. Weisskopf and D. H. Ewing, Phys. Rev. 57 (1940) 472; ibid 935
[17] W. Hauser and H. Feschbach, Phys. Rev. 87 (1952) 366
[18] A.V. Ignatyuk, G.N. Smirenkin and A.S. Tishin, Sov. J. Nucl. Phys. 21 (1975), 255.
[19] A. R. Junghans et al, Nucl. Phys. A 629 (1998) 635.
[20] V.F. Weisskopf and D.H. Ewing, Phys. Rev. 57 (1940) 472
[21] B. Jurado, K.-H. Schmidt and J. Benlliure, Phys. Rev. B 533 (2003) 186
[22] M. Kildir et al, Phys. Rev. C 51 (1995) 1873.
[23] R. Bass, Proc. Of the Symposium on Deep-Inelastic and Fusion Reactions with Heavy Ions, Berlin 1979, Springer Verlag, Berlin.
[24] J. Tõke, J. Lu and W. Udo Schröder, Phys. Rev. C 67, 034609 (2003)
[25] B.Jurado et al, Nucl. Phys. A 747 (2005) 14
[26] B. Jurado, C. Schmitt, K.-H. Schmidt, J. Benlliure and A. R. Junghans, Nucl. Phys. A 757 (2005) 329
[27] L. G. Moretto, Proc. of the 3rd IAEA symposium on the physics and chemistry of fission, Rochester, New York, 13-17 August 1973, p. 329.
[28] S. Bjørnholm, A. Bohr and B.R. Mottelson, Proc. Int. Conf. on the Physics and Chemistry of Fission, Rochester 1973 (IAEA Vienna 1974) Vol. 1, p. 367
[29] P. Moller et al, At. Data Nucl. Data Tables 59 (1995) 185
[30] W.D. Myers and W.J. Swiatecki, Nucl. Phys. A 601 (1996) 141
[31] A.V. Karpov, A. Kelić and K.-H. Schmidt, J. Phys. G 35 (2008) 035104
[32] K.-H. Schmidt et al, Z. Phys. A 308 (1982) 215.
[33] A. V. Ignatyuk, K. K. Istekov and G. N. Smirenkin, Yad. Fiz. 29 (1979) 875 (Sov. J. Nucl. Phys. 29 (1979) 450)
[34] A. V. Ignatyuk, M. G. Itkis, V. N. Okolovich, G. R. Ruskina, G. N. Smirenkin, A. S. Tishin, Yad. Fiz. 25 (1977) 25 (Sov. J. Nucl. Phys. 25 (1977) 13)
[35] A. Gilbert, A. Cameron, Can. J. Phys., 43, 1446 (1965)
[36] A.V. Ignatyuk, in: G.C. Bonsignori, M. Bruno, A. Ventura, D. Vretenar (Eds.), Proceedings on of the Conference Bologna 2000: Structure of the Nucleus at the Dawn of the Century, Bologna, Italy 29 May–3 June 2000, World Scientific, Singapore, 2001
[37] S. Cohen, W. J. Swiatecki, Ann. Phys. 22 (1963) 406.
[38] R. Bass, Proc. Of the Symposium on Deep-Inelastic and Fusion Reactions with Heavy Ions, Berlin 1979, Springer Verlag, Berlin.

[39] M. de Jong, „Experimentalle Untersuchungen und Modellrechnungen zur Projektilfragmentation schwerer Kerne am Beispiel von 208Pb“, TU Darmstadt, 1998.
[40] Y. Avishai, Z. Physik A286 (1978) 285.
[41] C. Y. Wong, Phys. Rev. Lett. 31 (1973) 766.
[42] D. L. Hill, J. A. Wheeler, Phys. Rev. 89 (1953) 1102.
[43] R.Michel et al., Nucl.Inst. Meth.B 103 (1995) 183
[44] C.M.Herbach et al., Proc. of the SARE-5meeting, OECD, Paris, July 2000
[45] A. S. Goldhaber, Phys. Rev. C 17 (1978) 2243
[46] M. V. Ricciardi et al, Nucl. Phys. A 733 (2004) 299-318
[47] P. Axel, Phys. Rev. 126 (1962) 271
[48] T. Enqvist et al., Nucl. Phys. A 686 (2001) 481
[49] J. Benlliure, A. Grewe, M. de Jong, K.-H. Schmidt, S. Zhdanov, Nucl. Phys. A 628 (1998) 458
[50] K. Kruglov, A. Andreyev, B. Bruyneel et al., Europ. Phys. J. A 14 (2002) 365
[51] K.-H. Schmidt, A. Kelić and M.V. Ricciardi, accepted in Eur. Phys. Lett; arXiv nucl-ex/0711.3967v1
[52] A. Kelić and K.-H. Schmidt, *to be submitted*
[53] H.A. Kramers, Physika VII 4 (1940) 284
[54] H. Risiken, Springer-Verlag, Berlin Heidelberg, 1989, ISBN 0-387-50498-2
[55] N. Bohr and J.A. Wheeler, Phys. Rev. 56 (1939) 426
[56] R. W. Hasse and W. D. Myers, “Geometrical Relationships of Macroscopic Nuclear Physics” Springer-Verlag Berlin Heidelberg (1988) ISBN 3-540-17510-5
[57] S. Chandrasekhar, Rev. Mod. Phys. 15 (1943) 1
[58] C. Schmitt, P.N. Nadtochy, A. Heinz, B. Jurado, A. Kelić, K.-H. Schmidt, Phys. Rev. Lett. 99 (2007) 042701
[59] C. Schmitt et al, *in preparations*.
[60] R.J.Charity, arXiv:nucl-th/0406040v1 (2004)
[61] V.M. Strutinsky and S. Bjørnholm, Proc. of International Symposium on Nuclear structure, 4-11 July 1968, Dubna; published by IAEA, Vienna 1968.
[62] S. Bjørnholm and J.E. Lynn, Rev. Mod. Phys. 52 (1980) 725
[63] K.-H. Schmidt et al, Nucl. Phys. A 665 (2000) 221
[64] A. Sierk, Phys. Rev. C 33 (1986) 2039
[65] M. Dahlinger, D. Vermeulen, K.-H. Schmidt, Nucl. Phys. A 376 (1982) 94
[66] W.J. Swiatecki, K. Siwek-Wilczynska and J. Wilczynski, Acta Phys. Pol. B 38 (2007)1565
[67] A. Kelić and K.-H. Schmidt, Phys. Lett. B 643 (2006) 362
[68] Ya. Rusanov et al., Phys. At. Nucl. 60 (1997) 683
[69] P. N. Nadtochy, G. D. Adeev and A. V. Karpov, Phys. Rev. C 65 (2002) 064615
[70] U. Brosa, S. Grossmann and A. Müller, Phys. Rep. 197 (1990) 167
[71] P. Armbruster, Nucl. Phys. A 140 (1970) 385
[72] P.N. Nadtochy, *private communication*
[73] F.-J. Hambsch and S. Oberstedt, Nucl. Phys. A 617 (1997) 347
[74] R. L. Walsh and J. W. Boldeman, Nucl. Phys. A 276 (1977) 189
[75] A. Wahl, At. Data Nucl. Data Tabels 39 (1989) 1
[76] R. J. Charity et al., Nucl. Phys. A 483 (1988) 371.
[77] S. Furihata, Nucl. Instrum. Methods B 171 (2000) 251
[78] L. G. Moretto, Nucl. Phys. A 247 (1975) 211
[79] M. V. Ricciardi et al., Phys. Rev. C 73 (2006) 014607
[80] P. Armbruster et al, Phys. Rev. Lett. 93 (2004) 212701
[81] M. Bernas et al, Nucl. Phys. A 765 (2006) 197
[82] M. Bernas et al, Nucl. Phys. A 725 (2003) 213

[83] Ph. Chomaz, M. Colonna and J. Randrup, Phys. Rep. 389 (2004) 263
[84] J. B. Natowitz et al, Phys. Rev. C 65 (2002) 034618
[85] T. Enqvist et al, Nucl. Phys. A 658 (1999) 47
[86] C. Sfienti et al., Nuclear Physics A 787 (2007) 627
[87] N. Buyukcizmeci, R. Ogul and A.S. Botvina, Eur. Phys. J. A25 (2005) 57
[88] A. Raduta and F. Gulminelli, Phys. Rev. C 75 (2007) 024605
[89] G.A. Souliotis et al, PRC 75 (2007) 011601R
[90] A.S. Botvina et al., Phys. Rev. C 74 (2006) 044609
[91] R. Michel et al, Nucl. INstr. Meth. B 129 (1997) 153
[92] R. Michel et al, Nucl. INstr. Meth. B 129 (1997) 153
[93] A. Boudard, J. Cugnon, S. Leray and C. Volant, Phys. Rev. C 66 (2002) 044615
[94] Th. Ghaitanos, H. Lenske and U. Mosel, Phys. Lett. B 663 (2008) 197
[95] W. Cassing, Z. Phys. A 327 (1987) 447
[96] W. Nörenberg, G. Papp and P. Rozmej, Eur. Phys. J. A 9 (2000) 327
[97] J.P. Bondorf et al, Phys. Rep. 257 (1995) 133
[98] A.S. Goldhaber, Phys. Lett. B53 (1974) 306
[99] W. Bauer, Phys. Rev. C51 (1995) 803
[100] K.C. Chung, R. Donangelo and H. Schechter, Phys. Rev. C36 (1987) 986
[101] J.-J. Gaimard, K.-H. Schmidt, Nucl. Phys. A 531 (1991) 709
[102] J. Tõke, J. Lu, and W. Udo Schröder, Phys. Rev. C 67, 034609 (2003)
[103] L. G. Moretto, Proc. of the 3rd IAEA symposium on the physics and chemistry of fission, Rochester, New York, 13-17 August 1973, p. 329
[104] http://integrals.wolfram.com/index.en.cgi

Conclusions of the workshop and specifications of the future benchmark

S. LERAY

CEA Saclay,
IRFU/SPhN,
Gif-sur-Yvette, France

Abstract. A summary of the workshop is presented, and the specifications for a benchmark of the spallation models are given as defined during the workshop.

1. Outcome of the workshop

As recalled in the introductory talk by D. Filges, spallation reactions play an important role in a wide domain of applications such as neutron sources for condensed matter and material studies, transmutation of nuclear waste and rare isotope production, astrophysics, simulation of detector set-ups in nuclear and particle physics experiments, and radiation protection near accelerators or in space. For all these applications, there is a need for reliable simulation tools in which the event generators used to compute the production yields and characteristics of the particles and nuclei generated in the interactions are built on solid nuclear physics and validated against experimental data. The first goal of this workshop was to bring together experts in spallation models in order to discuss the models used in high-energy transport codes, in particular their validity and deficiencies, but also to consider other, often more sophisticated models that could either be implemented in transport codes in the future or serve as references calculations. Since over the previous ten years, there has been an important effort, especially in Europe, to collect new high quality experimental data on spallation reaction products, the second goal was to establish a set of experimental data that could serve as the basis for a benchmark of the models. Finally, the third goal was to discuss the possible objectives of such a benchmark and define the rules. All these goals can be considered as having been achieved during the course of the workshop.

1.1. Spallation models

The Monte-Carlo event generators used to compute the production yields and characteristics of all the particles and nuclei generated in spallation reactions are generally a coupling of an Intra-Nuclear Cascade (INC) model followed by a de-excitation (principally evaporation/fission) model. Sometimes a pre-equilibrium stage is inserted in between. Specific presentations of INC and de-excitation models were given by authors of the models. The sessions on models began by a talk recalling the basic assumptions of intranuclear cascade models, which define their domain of validity, by Y. Yariv who also introduced the Isabel model and its future follow-up ETGAR. Then the other major INC models used in transport codes were presented, namely INCL4 by A. Boudard, CEM and LAQGSM by S. Mashnik, PEANUT by A. Ferrari, JAM by K. Niita, sometimes inside the more general context of the associated transport code such as FLUKA for PEANUT, or PHITS for JAM. Generally, a comprehensive description of the model was given which allowed an understanding of the assumptions made, the parameters used and the domain of applicability. Most of the main ingredients of intranuclear cascade models, such as the nucleon-nucleon interactions, target nucleus modelling and nucleon trajectory calculations appeared to be very similar in all models. Significant differences are found in the INC stopping criterion, with sometimes the addition of a pre-equilibrium stage before de-excitation, the possibility of

emitting clusters during the INC stage and the treatment of pions. There were discussions about the necessity to adjust parameters to reproduce specific data or to fix the parameters on a physics basis with the risk of poorer agreement with some experimental data. The consensus was that the second option should be favoured in order to have a general good predictive power.

While in INC models nucleons follow straight-line classical trajectories, there are more sophisticated models based on a semi-classical N-body theory, which in principle should give more precise results, especially at low energies. Depending on the numerical mean adopted to solve the problem, these are the Vlasov-Uehling-Uhlenbeck (VUU), Boltzmann-Uehling-Uhlenbeck (BUU), Landau-Vlasov (LV), or Quantum Molecular Dynamics (QMD) models. Three examples were presented during the workshop: the BUU model by Z. Rudy, IQMD by C. Hartnack, and JQMD, implemented into PHITS by K. Niita - their results seem promising. It appeared that these models sometimes face questions similar to those encountered in INC models, such as the treatment of Pauli blocking or the way to coalesce nucleons into fragments. Because of the large computing time needed for one calculation, these models have generally not been compared to an extensive set of experimental data on nucleon-induced reactions. In view of their potential and the further increase of computing capabilities, their participation in the benchmark would be most welcome.

As regards de-excitation models, new versions of ABLA and GEMINI were presented by K.-H. Schmidt and R. Charity, respectively. ABLA is now able to predict intermediate mass fragment production and barriers for light charged particle emission have been improved. The Bohr and Wheeler formalism is now used in GEMINI to describe the symmetric fission of heavy system, which was not well predicted up to now. A. Botvina introduced the SMM model, which treats multifragmentation as a possible decay channel at high excitation energies. Although probably not very important in proton-induced reaction, this channel could play a role in the production of intermediate mass fragments, which are generally underpredicted by available models. The GEM model from S. Furihata was not presented but its main features were discussed in S. Mashnik's talk.

In order to check the abilities of the various codes to predict reliably the different quantities relevant for applications, it is necessary to first validate the physics models on elementary experimental data. Therefore, it has been agreed to organise an international benchmark of the different models developed by different groups in the world against a selected set of differential experimental data to be defined during this workshop.

1.2. Experimental data

Important efforts in Europe over the past 10-15 years have resulted in the accumulation of high-quality experimental data covering all the reaction channels of spallation reactions. This workshop provided an opportunity to review the most important experimental results that can be used for model validation. Comparisons with some of the models presented in this workshop were sometimes shown.

F. Goldenbaum presented an extensive set of data obtained by the NESSI and PISA collaborations on light charged-particle and intermediate mass fragment double-differential cross-sections. J. Benlliure gave a review of the results obtained at GSI using the reverse kinematics technique at the Fragment Separator (FRS). This programme allowed the determination of the isotopic distributions of residues produced with different beams from U to Fe impinging on a liquid hydrogen target. While all produced residues can be measured at the FRS at a few given incident energies, γ- or mass-spectrometry measurements are used to

obtain the incident energy dependence (excitation functions) of some specific residue production. Results from the two main groups performing this kind of measurements were summarized by R. Michel and Y. Titarenko. Y. Titarenko also showed systematic comparisons between the production yields obtained by the different groups. Some significant discrepancies were observed, and a suggestion was made that experts on residue measurement should meet and investigate the reasons for these discrepancies in order to select the correct data for the benchmark. Neutron production measurements were also briefly discussed.

Discussion sessions were organized to define the set of experimental data that could serve as a basis for the benchmark. The decision was made to select a limited number of experimental data while representing the full range in energy and target mass, and the different reaction channels. This set of data should be compulsorily calculated by the participants in the benchmark. An additional optional set of experimental data was also defined, which would allow a better meshing of the energy or mass ranges.

The agreed data sets would contain experimental data on the production of the following:

- neutrons: double-differential cross-sections (DDXS), multiplicity distributions, average multiplicities,
- protons and light charged particles: DDXS, multiplicity distributions, average multiplicities,
- pions: DDXS, multiplicity distributions, average multiplicities,
- residues (including IMFs): isotopic distributions, excitation functions, recoil velocities,
- coincidence measurements were mentioned, but because of the frequent complicated detection filter will not be part of the mandatory set of data.

Some not (yet) existing data should be included within the benchmark if possible. The mandatory set of data concentrates mainly on Pb and Fe targets. A detailed list of both the mandatory and additional sets of experimental data will be given on the web site devoted to the benchmark.

2. Specifications of the benchmark

The specifications of the benchmark, including the set of selected experimental data to be compared to models, were fixed during the workshop. The benchmark will be organised under the auspices of the International Atomic Energy Agency (IAEA) in 2008-2009, and the first results discussed at the next Accelerator Applications conference (AccApp'09) to be held in Vienna, May 2009.

2.1. Participation

Anyone responsible for a model describing spallation reactions can participate in the benchmark provided that he/she complies with **all the rules** listed below, otherwise their contribution will not be considered.

- The code used by the participants should be able to treat **the complete reaction mechanism**, i.e. contain a description of the first stage of the reaction by an intranuclear cascade, a QMD or a BUU model followed by a de-excitation stage, with an optional intermediate pre-equilibrium stage. Code developers working on a model describing only

one stage of the interaction could contact the organizers to have their code coupled to a code describing the other stage of the reaction mechanism, if this is possible.

- Participants should provide a short but complete write-up of their model(s) with references to the most relevant published papers, and **give a comprehensive description of all the physics ingredients and parameters used for the present benchmark.**
- Participants should **provide the organizers with the source code** in the version used for the benchmark. The organizers commit themselves not to distribute the source codes to anyone else.
- Participants should calculate the complete mandatory set of experimental data which has been chosen to be as limited as possible, while covering the full range of energy, mass and reaction channels.
- An additional set of experimental data will be provided for participants who wish a more thorough comparison of their model. Participants are encouraged to calculate these data.
- Additionally, information will be requested that characterizes the remnant nucleus at the end of the first stage of the reaction (INC, INC+PE, QMD or BUU) to serve as inputs for the de-excitation stage. These data are required in order to understand the physical behavior of the different models.
- Calculations with one model should be undertaken **with the same set** (default preferentially) **of parameters**. Participants can provide calculations with several versions of their model, but should calculate complete sets of mandatory data and provide detailed descriptions of the parameters for each version.
- Participants should provide the organizers with the results of the calculations in the **requested format**. Results should be given along with the statistical uncertainty of the calculation.

2.2. Domain

The benchmark is restricted to nucleon-induced reactions on nuclei from carbon to uranium between 20 MeV and 3 GeV. Since intranuclear cascade models are based on physics assumptions, which are in principle not valid below a hundred MeV, most data comparisons will be above 100 MeV with, nevertheless, a few sets at low incident energies. This approach has been adopted because simulation code users perform many calculations in which the models are applied down to 20 MeV, at least for certain isotopes. This situation arises because

- 20-150 MeV libraries are not available for all isotopes;
- when using libraries below 150 MeV, residue production can be calculated only through activation libraries not available or not totally reliable over the complete energy range for all isotopes;
- the libraries do not allow correlations between particles to be taken into account.

The goal of the benchmark is to test the physics models currently used or potentially usable in the future in high-energy transport codes to compute the production yields and properties of particles and nuclei emitted in a fundamental spallation interaction. Therefore, only comparisons with **elementary experimental data on thin targets** will be considered.

2.3 Information to be provided by participants

- **List of model ingredients and parameters**

Parameters of first stage model (INC, INC+PE, QMD, BUU...)

- *N-N* interaction elastic and inelastic cross-sections
- Nuclear medium description (continuous medium, individual nucleons, pseudo-particles…)
- In-medium corrections of *N-N* interaction (or not)
- Nuclear average potential V_N,V_π
- Nuclear shape description
- Production of composite particles during the cascade stage (or not) - if yes, parameters describing the coalescence mechanism
- Implementation of the Pauli blocking and related parameters
- Pre-equilibrium or not – if yes, parameters of the pre-equilibrium model, and criterion to switch from INC to pre-equilibrium and from pre-equilibrium to de-excitation
- If no-pre-equilibrium, criterion to switch from INC to de-excitation
- Range of validity in energy and mass
- Computational time (time per event for a typical case and indication of the platform)

...

Parameters of de-excitation models

- Level densities
- Inverse reaction cross-sections: σ_{inv} including Coulomb barriers for the different types of evaporated particles
- Fission barriers
- Fission fragment generation
- List of de-excitation channels and related parameters

...

- **Additional information**

Additional information to be provided by the participant for each calculated system:

- Reaction cross-section
  - given by the model, σ_R (σ_{geom} x N_{inel} / N_{evts})
  - used for normalisation, σ'_R (if different from σ_R)
- Characteristics of the remnant nucleus at the end of the first stage of the reaction (INC, INC+PE, QMD or BUU) that will serve as inputs for the de-excitation stage, mean values and distributions:

- excitation energy, E*
- charge, Z_R
- mass, A_R
- excitation energy per nucleon, E^*/A_R
- bi-dimensional plot of E* versus A_R (if possible)
- recoil velocity, p_R
- angular momentum, J_R

- Multiplicities of all types of particles emitted in each stage of the reaction (INC, QMD or INC+pre-eq and de-excitation)
  - neutron multiplicities
  - proton multiplicities
  - light charged particles (deuterons to alphas)
  - pion multiplicities
  - PAW ntuples (if possible)

3. Organization of the benchmark

The organizers of the present workshop will organize the benchmark under the auspices of IAEA. A website will be set up that describes and defines the benchmark, including the format of the data to be delivered by the participants and the sets of experimental data selected for comparison with the models.

The deadline for providing the calculated sets of data will be January 31st, 2009. A first preliminary analysis of the results could be discussed by participants at the next Accelerator Applications international conference (AccApp'09) to be held in Vienna, May 2009.

Appendix 1

LIST OF PARTICIPANTS

BATYAEV Viacheslav Feliksovich
Institute of Theoretical and Experimental Physics
(I.T.E.P.)
B. Cheremushkinskaya ul. 25
117259 Moscow
RUSSIAN FEDERATION
E-mail: vfb@itep.ru

BENLLIURE Jose
Universidade de Santiago de Compostela
Facultade de Fisica
Campus Universitario Sur a Coruna
E-15706 Santiago de Compostela
SPAIN
E-mail: j.benlliure@usc.es

BOTVINA Alexander Stepanovich
Russian Academy of Sciences
Institute for Nuclear Research
60th October Anniversary Av.
Prospect 7A
117312 Moscow
RUSSIAN FEDERATION
E-mail: a.botvina@gsi.de

BOUDARD Alain
CEA Saclay
IRFU/SPhn
F-91191 Gif-sur-Yvette Cedex
FRANCE
E-mail: alain.boudard@cea.fr

CHARITY Robert J.
Washington University at Saint Louis
Department of Chemistry
One Brookings Drive, Campus Box 1134
MO-63130 Saint Louis
UNITED STATES OF AMERICA
E-mail: charity@wustl.edu

CHHANTBAR Manishaben Chimanlal
Saurashtra University
Faculty of Science
Department of Physics
University Campus
Gujarat (360 005), Rajkot
INDIA
E-mail: manisha_chhantbar@yahoo.com

DAVID Jean Christophe
CEA Saclay
IRFU/SPhN
F-91191 Gif-sur-Yvette Cedex
FRANCE
E-mail: jean.christophe.david@cea.fr

DUCRET Jean Eric
CEA Saclay
IRFU/SPhn
F-91191 Gif-sur-Yvette Cedex
FRANCE
E-mail: jean-eric.ducret@cea.fr

FERRARI Alfredo
CERN, European Organization for Nuclear Research
CH-1211 Geneva 23
SWITZERLAND
E-mail: alfredo.ferrari@cern.ch

FILGES Detlef
Forschungszentrum Jülich Gmbh
Institut für Kernphysik
Postfach 1913
D-52425 Jülich
GERMANY
E-mail: d.filges@fz-juelich.de

GALLMEIER Franz X.
Oak Ridge National Laboratory
Spallation Neutron Source Project
Bethel Valley Road, Bldg 8600
P.O. Box 2008, MS-6466
Oak Ridge TN 37831-6466
UNITED STATES OF AMERICA
E-mail: gallmeierfz@ornl.gov

GALOYAN Aida
Joint Institute for Nuclear Research
Laboratory of Information Technologies
Joliot-Curie 6
141980 Dubna
Moscow Region
RUSSIAN FEDERATION
E-mail: GALOYAN@lxpub01.jinr.ru

GOLDENBAUM Frank
Forschungszentrum Jülich GmbH
Institut für Kernphysik
Postfach 1913
D-52425 Jülich
GERMANY
E-mail: f.goldenbaum@fz-juelich.de

GULIK Volodymyr Ivanovych
National Academy of Sciences of Ukraine
Institute for Nuclear Research
pr. Nauky, 47
03680 Kyiv
UKRAINE
E-mail: gulik@kinr.kiev.ua

HARTNACK Christoph
Laboratoire de Physique Subatomique et des
Technologies Associées, Ecole des Mines
La Chantrerie
4 rue Alfred Kastler, BP 20722
44307 Nantes Cedex 3
FRANCE
E-mail: hartnack@subatech.in2p3.fr

HELLA Khalid Mohamed Magdy El-wafaey
Atomic Energy Authority
Nuclear Research Center
Experimental Nuclear Physics Department
P.O. Box 13759
Cairo
EGYPT
E-mail: khalidhella@maktoob.com, khalidhella@yahoo.com

IBRAHIM Abdullahi Mohamed
Sudan University of Science & Technology
College of Science, Department of Physics
P.O. Box 3045
11113 Khartoum
SUDAN
E-mail: kalabalg@yahoo.com

KAITANIEMI Pekka Juhani
University of Helsinki
Helsinki Institute of Physics (HIP)
P.O. Box 64
00014 Helsinki
FINLAND
E-mail: kaitanie@cc.helsinki.fi

KUMAR Vinod
University of Rajasthan
High Energy Nuclear Physics Laboratory
302004 Jaipur
INDIA
E-mail: vkumarv1@sancharnet.in

KUMAWAT Harphool
Bhabha Atomic Research Centre
Nuclear Physics Division
Trombay
400085 Mumbai
INDIA
E-mail: harphool@barc.gov.in,
kumawat77@yahoo.com

LERAY Sylvie
CEA Saclay
IRFU/SPhN
F-91191 Gif-sur-Yvette Cedex
FRANCE
E-mail: Sylvie.Leray@cea.fr

MAHMOUD GAD ALLAH Imbaby Ismail
Atomic Energy Authority
Nuclear Research Centre, Engineering Department
101 Kasr El Aini Street, P.O.13759
Cairo
EGYPT

MANK Guenter
International Atomic Energy Agency
Division of Physical & Chemical Sciences - Physics Section
Wagramerstraße 5
P.O. Box 100
A-1400 Vienna
AUSTRIA
E-mail: G.Mank@iaea.org

MASHNIK Stepan
Los Alamos National Laboratory
Applied Physics Division, X 3 MCC, M.S. P365
Los Alamos NM 87545
UNITED STATES OF AMERICA
E-mail: mashnik@lanl.gov

MENGONI Alberto
ENEA
Applied Phyisics Section
V. Don Fiammelli 2
I-40128 Bologna
ITALY
E-mail: A.Mengoni@iaea.org

MICHEL Rolf
Universität Hannover
Zentrum für Strahlenschutz und Radioökologie
Herrenhauser Str. 2
D-30419 Hannover
GERMANY
E-mail: michel@zsr.uni-hannover.de

NANDY Maitreyee
Saha Institute of Nuclear Physics
Nuclear Chemistry Division
Sector 1. Block Af, Bidhannagar
700064 Kolkata
INDIA
E-mail: mnandy98@yahoo.com,
maitreyee.nandy@saha.ac.in

NIITA Koji
RIST, Research Organization for
Information Science and Technology
2 - 4 Shirane, Shirakata
Tokai, Naka
Ibaraki 319 1106
JAPAN
E-mail: niita@tokai.rist.or.jp

RUDY Zbigniew
Jagiellonian University
Faculty of Physics, Astronomy and Applied Computer Science
Cracow
POLAND
E-mail: ufrudy@cyf-kr.edu.pl

SALSAC Marie Delphine
CEA Saclay
IRFU/SPhN
F-91191 Gif-sur-Yvette Cedex
FRANCE
E-mail: mariedelphine.salsac@cea.fr

SCHMIDT Karl Heinz
Gesellschaft für Schwerionenforschung (Gsi)
Nuclear Physics 2
Planckstrasse 1
D-64291 Darmstadt
GERMANY
E-mail: k.h.schmidt@gsi.de

STANCULESCU Alexander
IAEA International Atomic Energy Agency
Nuclear Power Division
Nuclear Power Technology Development Section
Wagramer Straße 5
P.O. Box 100
A-1400 Vienna
AUSTRIA
E-mail: A.Stanculescu@iaea.org

STERZENBACH Guenter
Forschungszentrum Jülich Gmbh
Institut für Festkörperforschung
Theorie 1
Leo-Brand-Straße
D-52425 Jülich
GERMANY
E-mail: g.sterzenbach@fz-juelich.de

TITARENKO Yuri
Institute of Theoretical and Experimental Physics
(I.T.E.P.)
B. Cheremushkinskaya ul. 25
117259 Moscow
RUSSIAN FEDERATION
E-mail: TITAREN@VITEP3.ITEP.RU

WOHLMUTHER Michael
Paul Scherrer Institut, PSI
CH-5232 Villigen
SWITZERLAND
E-mail: michael.wohlmuther@psi.ch

YARIV Yair
Soreq Nuclear Research Center
Israel Atomic Energy Commission
81800 Yavne
ISRAEL
E-mail: yariv@soreq.gov.il

YEMELE David
University of Dschang
Faculty of Science
Dept. of Physics
P.O. Box 67
Dschang
REPUBLIC OF CAMEROON

Appendix 2

MEETING AGENDA

Monday, 4th February, INC Models
Chairperson: G. Mank
Room: Adriatico Guest House Giambiagi Lecture Hall

08:30
09:45
Registration and Administrative formalities
01h15
Room: Adriatico Guest House (Lower Level 1)
09:45
10:30
Introduction and Aim of the Meeting
45 min
lecture_notes

D. Filges
Forschungszentrum Jülich GmbH, Germany

10:30
11:00
Coffee Break
30 min
Room: Adriatico Guest House (Lower Level 1)
11:00
12:30
ISABEL - INC Model for High-Energy Hadron-Nucleus Reactions
01h30
lecture_notes

Y. Yariv
Soreq, Israel

12:30
14:00
Lunch Break
01h30
Room: Adriatico Guest House Cafeteria
14:00
15:30
Detailed description of the Intra Nuclear Cascade from Liege: INCL4
01h30
lecture_notes

A. Boudard
CEA, France

15:30
16:00
Coffee Break
30 min
Room: Adriatico Guest House (Lower Level 1)
16:00
18:00

General Meeting:

Spallation Data and Applications, A. Mengoni, A. Stanculescu, IAEA, Goals of the intercomparison
02h00
lecture_notes
19:15
21:15

Official Reception
02h00
Room: Adriatico Guest House Cafeteria

Tuesday, 5th February INC/PE Models
Chairperson: S. Leray
Room: Adriatico Guest House Giambiagi Lecture Hall
5 February 2008
09:00
10:30
CEM03.03 and LAQGSM03.03 Event Generators for MCNP6, MCNPX and MARS15
01h30
lecture_notes

S. Mashnik
LANL, USA

10:30
11:00
Coffee Break
30 min
Room: Adriatico Guest House (Lower Level 1)
11:00
12:30
Models in FLUKA
01h30
lecture_notes

A. Ferrari
CERN, Geneva, Switzerland

12:30
14:00
Lunch Break
01h30
Room: Adriatico Guest House Cafeteria
14:00
15:00
Proton Induced Spallation Reactions Investigated Within the Framework of BUU Model
01h00
lecture_notes

Z. Rudy
Jagiellonian University, Cracow, Poland

15:00
15:30
Discussion of Intercomparison
30 min
15:30
16:00
Coffee Break
30 min
Room: Adriatico Guest House (Lower Level 1)
16:00
18:00

Expert Meeting on Intercomparison:

Choice of Experimental Data (including Neutron Data)
02h00
Room: Adriatico Guest House Informatics Lab.
20:30
21:45
Discussion
01h15

Wednesday, 6th February QMD Models
Chairperson: D. Filges
Room: Adriatico Guest House Giambiagi Lecture Hall
6 February 2008
09:00
10:30
The Description of Nuclear Collision Within the Quantum Molecular Dynamics Model
01h30
lecture_notes

C. Hartnack
Subatech, France

10:30
11:00
Coffee Break
30 min
Room: Adriatico Guest House (Lower Level 1)
11:00
12:30
Nuclear Reaction Models (JAM and JQMD) in PHITS
01h30
lecture_notes

K. Niita
RIST, Japan

12:30
14:00
Lunch Break
01h30

Room: Adriatico Guest House Cafeteria
14:00
14:45
Experimental Data on Evaporation and Pre-equilibrium Emission in GeV p-induced Spallation Reactions
45 min
lecture_notes

F. Goldenbaum
Forschungszentrum Jülich GmbH, Germany

14:45
15:30
Detailed Investigation of Residual Nuclei Produced in Spallation Reactions at GSI
45 min
lecture_notes

J. Benlliure
University of Santiago de Compostela, Spain

15:30
16:00
Coffee Break
30 min
Room: Adriatico Guest House (Lower Level 1)
16:00
16:15
QMD Approach to Spallation Reactions
15 min
lecture_notes

M. Nandy
Saha Inst. of Nuclear Physics, Kolkata, India

16:15
18:00
Expert Meeting on Intercomparison: Figures of Merit
01h45
Room: Adriatico Guest House Informatics Lab.

Thursday, 7th February De-excitation Models
Chairperson: S. Mashnik
Room: Adriatico Guest House Giambiagi Lecture Hall
7 February 2008
09:00
10:30
The Role of Multifragmentation in Spallation Reactions
01h30
lecture_notes

A. Botvina
INR, Russia

10:30
11:00
Coffee Break
30 min
Room: Adriatico Guest House (Lower Level 1)

11:00
12:00
GEMINI: De-excitation of Excited Compound Nuclei Through a Series of Binary Decays
01h00
lecture_notes

R. Charity
Washington Univ. in St. Louis, USA

12:00
12:15
Multiplicity Fluctuations in Interactions of Light Nuclei with Carbon Nuclei at Momentum of 4.2 GeV/c per Nucleon and their Theoretical Interpretation
15 min
lecture_notes

A. Galoyan
JINR, Dubna, Russian Federation

12:15
12:30
Discussion
15 min
12:30
14:00
Lunch Break
01h30
Room: Adriatico Guest House Cafeteria
14:00
14:45
ITEP Experiments with Thin Targets Irradiated by up to 2.6 GeV Protons
45 min
lecture_notes

Y. Titarenko, V. Batyaev
ITEP, Russia

14:45
15:30
Experimental Cross Sections for the Production of Residual Nuclides at Medium Energies: Status, Recent Progress and Challenges for Modelling
45 min
lecture_notes

R. Michel
Univ. of Hannover, Germany

15:30
16:00
Coffee Break
30 min
Room: Adriatico Guest House (Lower Level 1)
16:00
18:00

Expert meeting on Intercomparison:

Data and Results Format, General Discussion
02h00
Room: Adriatico Guest House Informatics Lab.

Friday, 8th February De-excitation Models
Chairperson: Y. Yariv
Room: Adriatico Guest House Giambiagi Lecture Hall
8 February 2008
09:00
10:30
The De-excitation Code ABLA07
01h30
lecture_notes

K. H. Schmidt
GSI, Germany

10:30
11:00
Coffee Break
30 min
Room: Adriatico Guest House (Lower Level 1)
11:00
12:30
Summary and Perspectives (intercomparison description)
01h30
lecture_notes

S. Leray
CEA, France

12:30
14:00
Lunch Break
01h30
Room: Adriatico Guest House Cafeteria
14:00
16:00
Closing Session (Report)
02h00

Nuclear Data Section
International Atomic Energy Agency
P.O. Box 100
A-1400 Vienna
Austria

e-mail: services@iaeand.iaea.org
fax: (43-1) 26007
telephone: (43-1) 2600-21710
Web: http://www-nds.iaea.org